ABSTRACT

Title of Dissertation: SIDEROPHILE ELEMENTS AND MOLYBDENUM, TUNGSTEN, AND OSMIUM ISOTOPES AS TRACERS OF PLANETARY GENETICS AND DIFFERENTIATION: IMPLICATIONS FOR THE IAB IRON METEORITE COMPLEX

Emily Anne Worsham, Doctor of Philosophy, 2016

Dissertation directed by: Professor Richard Walker, Department of Geology

Isotopic and trace element abundance data for iron meteorites and chondrites are presented in order to investigate the nature of genetic relations between and among meteorite groups. Nebular and planetary diversity and processes, such as differentiation, can be better understood through study of IAB complex iron meteorites. This is a large group of chemically and texturally similar meteorites that likely represent metals with a thermal history unlike most other iron meteorite groups, which sample the cores of differentiated planetesimals. The IAB complex contains a number of chemical subgroups. Trace element determination and modeling, Re/Os isotopic systematics, nucleosynthetic Mo isotopic data, and ^{182}Hf-^{182}W

geochronology are used to determine the crystallization history, genetics, and relative metal-silicate segregation ages of the IAB iron meteorite complex.

Highly siderophile element abundances in IAB complex meteorites demonstrate that diverse crystallization mechanisms are represented in the IAB complex. Relative abundances of volatile siderophile elements also suggest late condensation of some IAB precursor materials.

Improvements in the procedures for the separation, purification, and high-precision analysis of Mo have led to a ~2 fold increase in the precision of $^{97}Mo/^{96}Mo$ isotope ratio measurements, compared to previously published methods. Cosmic ray exposure-corrected Mo isotopic compositions of IAB complex irons indicate that at least three parent bodies are represented in the complex. The Hf-W metal-silicate segregation model ages of IAB complex subgroups suggests that at least four metal segregation events occurred among the various IAB parent bodies.

The IAB complex samples reservoirs that were isotopically identical, but chemically distinct, and reservoirs that were chemically similar in some respects, yet isotopically different. Some IAB subgroups are genetically distinct from all other iron meteorite groups, and are the closest genetic relations to the Earth. The chemical differences between magmatic iron meteorite groups and some IAB subgroups likely originated as a result of their formation on undifferentiated parent bodies where impacting and mixing processes were important. This, in addition to the genetic difference between some IAB irons and magmatic groups, implies that these IAB parent bodies and magmatic parent bodies formed in a different location and/or time in the protoplanetary disk.

SIDEROPHILE ELEMENTS AND MOLYBDENUM, TUNGSTEN, AND OSMIUM ISOTOPES AS TRACERS OF PLANETARY GENETICS AND DIFFERENTIATION: IMPLICATIONS FOR THE IAB IRON METEORITE COMPLEX

by

Emily Anne Worsham

Dissertation submitted to the Faculty of the Graduate School of the
University of Maryland, College Park, in partial fulfillment
of the requirements for the degree of
Doctor of Philosophy
2016

Advisory Committee:
Professor Richard Walker, Chair
Dr. Conel Alexander
Professor James Farquhar
Professor William McDonough
Professor Jessica Sunshine

Preface

Much of the research presented in this dissertation is submitted or previously published in peer-reviewed journals as standalone articles. I made significant contributions to co-authored works. Following is a summary of the contributions from each author.

Chapter 2

Worsham E. A., Bermingham K. R., and Walker R. J. (2016) Siderophile element systematics of IAB complex iron meteorites: New insights into the formation of an enigmatic group. *Geochimica et Cosmochimica Acta* **188**, 261-283.

I collected ~60% of the highly siderophile element data and Os isotope data. I conducted all of the numerical trace element modeling of various crystallization processes. Katherine Bermingham and I collected ~ 40% of the data together, and she contributed to the discussion. Rich Walker helped interpret the results. I wrote the first draft of the manuscript, and co-authors provided edits.

Chapter 4

Worsham E. A., Walker R. J., and Bermingham K. R. (2016) High-precision molybdenum isotope analysis by negative thermal ionization mass spectrometry. *International Journal of Mass Spectrometry* **407**, 51-61.

I improved the chemical separation procedures of Mo, and developed the loading and analytical routine, with input and suggestions from both co-authors. I made the spike-standard mixtures with help from Katherine Bermingham. I collected all data reported here, and I wrote the first draft of the manuscript, which was later reviewed by the co-authors.

Chapter 5

Worsham E. A., Bermingham K. R., and Walker R. J., Molybdenum and tungsten isotope evidence for diverse genetics and chronology among IAB iron meteorite complex subgroups. *Earth and Planetary Science Letters.* **In review.**

I conducted the chemistry and collected the Mo and W isotope analyses. I collected ~ 70% of the Osmium isotope data, and Katherine Bermingham and I collected the other 30%. I wrote the first draft of the manuscript and incorporated edits from the co-authors.

Acknowledgements

First of all, thank you to Rich Walker for all the advice, direction, humor, and patience. I want to thank my committee, Conel Alexander, James Farquhar, Bill McDonough, and Jessica Sunshine for your constructive comments and support. I was financially supported by a research and teaching assistantships, the ESSIC travel grant and the Goldhaber travel award, which I am also grateful for. Thanks to Tim McCoy and Linda Welzenbach for several tours of the Smithsonian meteorite collection and for trusting me to dissolve valuable meteorites to obtain valuable data. Thanks also to Katherine Bermingham, who has been my collaborator and confidant throughout my studies. I want to thank Greg Archer for many laughs and enlightening discussions. Other people who have supported me throughout this process, both in the lab and out, include Igor Puchtel, Richard Ash, Jingao Liu, James Day, Miriam and Nick Sharp, and Andi Mundl. I also want to acknowledge my supportive office mates past and present, Jeremy Bellucci, Kristy Long, Ming Tang, Kang Chen, Mitch Haller, and Connor Hilton. For guiding me in my early professional development, I thank Hap McSween, Larry Taylor, Paul Niles, and Linda Kah.

I've had a lot of fun at Maryland and made a lot of great friends, and for that I thank all of the UMD Geology faculty, staff, and gradtuate students. I truly appreciate getting to know so many great people. I was lucky to have my some of my best friends, Ena Djordjevic and Austin Duck, independently choose to come to the University of Maryland as well. You've been invaluable emotional support and I know we will reminisce together about that time we all lived in Mount Rainier often. Thanks to my farther flung friends, Bonnie Buckles, Stephanie Riggs, Kurt McIntosh,

Tammy Chamberlin, and Amber Hall for your support. Finally, thank you and I love you to my extended family; my mom and dad, Lesa and Paul Worsham; my sister, Rebecca Worsham; and my brother in law, Hans Hansen. You all inspired me to work hard in school and to be curious, you encouraged debate, and you indulged my love of science and space and rocks.

I wouldn't be who or where I am without you all. Thank you.

Table of Contents

List of Tables

List of Figures

List of Abbreviations

AGB – asymptotic giant branch

CAI – Calcium-Aluminum-rich inclusion

CRE – cosmic ray exposure

CS – crystal segregation

CS-FC – crystal segregation-fractional crystallization

FC – fractional crystallization

HSE – highly siderophile element

ID – isotope dilution

INAA – instrumental neutron activation analysis

LA – laser ablation

MC-ICP-MS – multicollector inductively coupled plasma mass spectrometry

MSWD – mean square weighted deviation

N-TIMS – negative-thermal ionization mass spectrometry

PGE – platinum group element

P-TIMS – positive thermal ionization mass spectrometry

TFL – terrestrial fractionation line

TIMS – thermal ionization mass spectrometry

USNM# - United States national museum number

Chapter 1: Introduction

1.1 Motivating questions

Characterizing the origin, nature, and evolution of the chemical and isotopic heterogeneity that existed in the early solar system is a fundamental pursuit of planetary science. Because the heat budgets available to planetary bodies were likely primarily controlled by when and where they formed in the protoplanetary disk, nebular heterogeneity has bearing on the question of why some asteroids differentiated into a core, mantle, and crust, and why some did not. Moreover, linking different types of planetary bodies to one another through shared isotopic nebular reservoirs will give new insights into the origins of both nebular and planetary diversity.

1.2 Overview of early solar system history recorded in meteorites

Meteorites allow for the investigation of the chemical, isotopic, and chronologic evolution of the earliest solar system, leading to the formation of terrestrial planets. Evidence obtained from meteorites, along with astronomical observations, has led to the understanding that the solar nebula formed when a portion of a giant molecular cloud composed of presolar gas and dust collapsed (e.g., Cameron and Truran, 1977).

Most of the gas and dust coalesced into the proto-sun, around which the remaining gas and dust formed a protoplanetary disc, from which planetary bodies formed through accretion (Chambers, 2004). As cooling of the nebular gas progressed,

refractory elements and minerals condensed from the nebula, and condensates evolved to include increasingly more volatile phases. The condensed materials and presolar dust grains clumped together, until gravitational forces took over and larger planetesimals and planetary embryos formed (Chambers, 2004). Ultimately the terrestrial planets were built from multiple collisions of planetary embryos, the frequency of which decreased exponentially with advancing time.

Primitive meteorites, termed "chondrites", did not experience sufficient heating to cause partial melting or wholesale differentiation, and consequently retained primitive chemical and mineralogical compositions. Chondrites are aggregates of materials, including matrix, chondrules, refractory metal grains, and Ca-Al rich inclusions (CAIs). The CAIs represent the earliest condensates from the planetary nebula and, thus, the oldest known materials formed in the early solar system (e.g., Grossman, 1972; Amelin et al. 2002; Bouvier and Wadhwa, 2010). Other meteorites, termed "achondrites", generally originated on planetary bodies that experienced heating sufficient to melt and differentiate into metallic cores and silicate mantles and crusts early in solar system history (e.g., Lovering, 1957; Fish et al., 1960; Goldstein and Short, 1967).

Major heat sources for the thermal evolution of early planetesimals include the decay of short-lived radionuclides, such as ^{26}Al, latent heat from accretion, and impact heating (e.g., Fish et al., 1960; Lee et al., 1977). Whether or not a given planetesimal differentiated likely depended primarily on the abundance of short-lived, heat-producing isotopes at the time it accreted. Early melting and differentiation is evidenced, for example, by "magmatic" iron meteorites, which represent the cores of differentiated planetary bodies. Evidence from the short-lived ^{182}Hf-^{182}W isotope system, which can be

used to date the relative ages of metal-silicate segregation, indicates that the parent bodies of most magmatic iron meteorite groups differentiated within the first 2-3 Myr of solar system formation, consistent with heating from the decay of ^{26}Al (e.g., Kruijer et al., 2014a).

The distributions of siderophile elements in magmatic iron meteorite groups indicate that the cores of their parent bodies crystallized primarily by fractional crystallization (e.g., Scott, 1972; Wasson, 1999; Wasson and Richardson, 2001; Wasson et al., 2007; Walker et al., 2008; McCoy et al., 2011). By contrast, "non-magmatic" or "silicate-bearing" groups, including the IAB complex and the IIE group, have complicated formational histories and chemical compositions that cannot be explained by simple fractional crystallization (e.g., Wasson et al., 1980; Wasson and Kallemeyn, 2002). "Ungrouped" iron meteorites have chemical compositions that do not fall into any recognized groups. In some instances they may sample asteroidal cores, whereas other ungrouped irons may have formed by other processes. This variety of iron meteorites and the mechanisms by which they crystallized have implications for the thermal evolution of the iron meteorite parent bodies. It has been suggested that the chemical and textural differences between the non-magmatic and magmatic iron meteorites may be related to the degree of differentiation that their parent bodies experienced (e.g., Kracher, 1985). It is, therefore, useful to study non-magmatic irons to assess whether their parent bodies were partially or fully differentiated.

1.3 IAB complex of iron meteorites

The IAB complex is a large, non-magmatic group of iron meteorites that is chemically and texturally distinct from the magmatic iron meteorite groups. For example, some members of the complex contain abundant silicate clasts, whereas silicates are rare among magmatic irons. Wasson and Kallemeyn (2002) most recently categorized the IAB complex and subdivided it into a main group (MG) and several chemical subgroups. The chemical diversity of the MG and subgroups suggest that these iron meteorites formed in separate parental melts, either on the same parent body, or on separate parent bodies by similar processes (Wasson and Kallemeyn, 2002).

The highly siderophile elements (HSE) are useful for examining the crystallization history of metal-rich asteroids due to their generally well-understood partitioning behavior in metallic systems (e.g., Jones and Drake, 1983; Jones and Malvin, 1990; Chabot and Jones, 2003). A comprehensive study of HSE characteristics and Re-Os isotope systematics was conducted here to examine whether or not meteorites within and between the MG and subgroups could be related to one another by crystal-liquid fractionation processes. Trace element modeling within subgroups was conducted to explore different crystallization mechanisms to elucidate the thermal history and degree of differentiation of the IAB parent body(ies). The long-lived ^{187}Re-^{187}Os isotope system was also used to assess late-stage open system behavior of siderophile elements (e.g., Chen et al., 1998; Becker et al., 2001). The new HSE and ^{187}Re-^{187}Os data are presented, along with discussion of the formation of the IAB complex, in Chapter 2 of this dissertation.

Magmatic iron meteorite groups are distinguished from one another in part by variable depletions/enrichments in volatile siderophile elements (e.g., Ga, Ge) and redox-sensitive elements (e.g., Fe, W), when compared to one another and chondritic relative abundances of siderophile elements (Scott and Wasson, 1975; Kelly and Larimer, 1977). Therefore, siderophile element data were obtained *in situ* to investigate volatility- and oxidation-related trends within and between the IAB MG and subgroups. These results are reported in Chapter 3. This allowed for further assessment of chemical differences within the IAB complex, and between the IAB complex and magmatic iron meteorite groups.

The relations between IAB subgroups, and how they fit into the larger context of iron meteorites in general, can also be evaluated using mass-independent and radiogenic isotopes of siderophile elements. This kind of investigation takes advantage of the various types of isotopic heterogeneity recorded in meteorites.

1.4 Isotope heterogeneity in the early solar nebula

Numerous studies have shown isotopic variability in a variety of elements in chondrite components and bulk meteorites (e.g., Clayton and Mayeda, 1976). The anomalous isotopic compositions of an element are measured relative to some reference; normally the terrestrial bulk silicate Earth isotopic composition, represented by standard reference materials. Isotopic anomalies can either be primary or secondary features of a cosmochemical sample. Primary isotopic compositions are inherited from the original materials or source from which the samples formed. Secondary isotopic anomalies can originate from a variety of processes, including the decay of radioactive parent isotopes,

such as those in the short-lived ^{182}Hf-^{182}W isotope system and the long-lived ^{187}Re-^{187}Os isotope system. Cosmic ray exposure can also modify the original isotopic composition of most elements, due to neutron capture processes (e.g., Os – Walker, 2012). Additionally, physical or chemical processes (e.g., vaporization/condensation) can produce mass-dependent or mass-independent isotopic fractionation in many isotope systems. Both primary and secondary isotopic features have been observed in Mo and W, for instance (e.g., Dauphas et al., 2002a; Fujii et al., 2006; Masarik, 1997; Qin et al., 2008b; Weiser and DeLaeter, 2009; Burkhardt et al., 2014).

Primary isotopic heterogeneity is evidenced in presolar grains, preserved in some chondritic meteorites. These refractory grains contain elements synthesized in various stellar nucleosynthetic processes (e.g., *s*-, *r*-, and *p*-process) that occur in distinct types of stars and in different stages of stellar evolution (e.g., Cameron, 1957; Burbidge et al., 1957; Nittler et al., 2003; José and Iliadis, 2011). The *p*-process occurs either by photodisintegration (a process by which a nucleus sheds a neutron) or by proton capture during supernovae. The slow neutron capture (*s*-) process occurs primarily in asymptotic giant branch stars, while the rapid neutron capture (*r*-) process occurs in supernovae with high neutron fluxes (Burbidge et al., 1957; José and Iliadis, 2011). Therefore, the isotopic compositions of presolar grains, such as SiC, reflect the isotopic signatures of the particular nucleosynthetic processes that occurred in their parent stars (Nicolussi et al., 1998; Nittler, 2003; **Fig. 1.1**). The highly variable isotopic compositions of presolar grains require that multiple generations of stars created them and injected them into the interstellar medium where they were mixed and ultimately incorporated into the giant molecular cloud from which our solar system formed (e.g., Nittler, 2003).

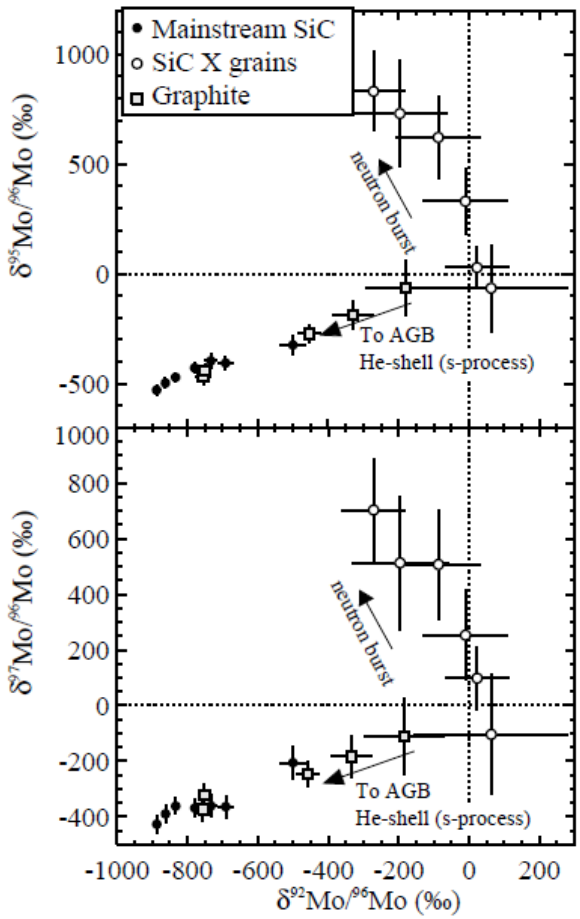

Fig. 1.1. Molybdenum isotopic compositions of presolar graphite and two types of presolar SiC grains. Note the large isotopic variations, relative to the terrestrial isotopic composition, defined as the origin. Figure from Nittler (2003); data from references therein.

Primary heterogeneity is also present in bulk materials. Primary variability in $^{17}O/^{16}O$, relative to $^{18}O/^{16}O$ in meteorites was first demonstrated by Clayton et al. (1976). Oxygen isotopes have since been used as a genetic tracer of solar system materials (e.g., Clayton, 1993). Other elements which display isotopic heterogeneities at the bulk meteorite scale include Sm and Nd (Andreasen and Sharma, 2006), Ba (e.g., Ranen and Jacobsen, 2006; Bermingham et al., 2016a), Ni (Regelous et al., 2008), Ti (Niemeyer and Lugmair, 1984; Trinquier et al., 2009), Cr (Trinquier et al., 2007; Qin et al., 2010), Ru

(Chen et al., 2010; Fischer-Gödde et al., 2015), and Mo (Dauphas et al., 2002a; Burkhardt et al., 2011). With the exception of O isotopic variability, primary isotopic features in these elements among planetary bodies are most likely nucleosynthetic in origin (Niemeyer and Lugmair, 1984; Dauphas et al., 2002a).

Why primary nucleosynthetic isotopic effects in some elements are exhibited at the bulk meteorite scale is an open question. The solar nebula may have been poorly mixed initially with respect to isotopically diverse presolar material, leading to nucleosynthetic isotope effects that were simply dependent on the variable degrees of homogenization (e.g., Andreasen and Sharma, 2007). Alternately, selective thermal processing of thermally labile presolar carriers in a homogenized solar nebula may have created isotopic heterogeneity (e.g., Trinquier et al., 2009). In this case, the presence and nature of nucleosynthetic effects would depend on the types of presolar carriers and the degree of thermal processing. It has also been proposed that late injections of material from nearby supernovae imparted isotopic heterogeneity, and may have also supplied short-lived radionuclides to the solar nebula (e.g., Cameron and Truran, 1977). These various scenarios are not mutually exclusive.

1.5 Introduction to Mo cosmochemistry

The Mo isotopic system is uniquely suited to address current outstanding questions in cosmochemistry because it consists of seven stable isotopes that are synthesized by a variety of nucleosynthetic processes. Molybdenum is also moderately siderophile, so it is abundant in most types of meteorites (e.g., Kuroda and Sandell, 1954). Though the cosmochemical applications for Mo isotopes are the primary focus of

this dissertation, the application of mass-dependent Mo isotope effects as indicators of paleoredox conditions has been the focus of numerous studies of Mo in bulk samples of terrestrial rocks and sediments (e.g., Barling et al., 2001; Seibert et al., 2003; Anbar, 2004). In cosmochemistry, "mass-independent" nucleosynthetic Mo isotope anomalies have been used primarily to evaluate the extent of mixing and/or thermal processing in the solar nebula, and to test genetic relations amongst solar system materials (e.g., Dauphas et al., 2002a; Burkhardt et al., 2011).

Nucleosynthetic anomalies in Mo were first reported by Dauphas et al. (2002a) using multi-collector inductively coupled plasma mass spectrometry (MC-ICP-MS) and Yin et al. (2002) using thermal ionization mass spectrometry (TIMS). Both studies showed evidence for endemic isotope anomalies in carbonaceous chondrites. Dauphas et al. (2002a) also reported similar effects in iron meteorites, mesosiderites, and pallasites. Using TIMS, Becker and Walker (2003) reported the Mo isotopic compositions of chondrites and iron meteorites that were indistinguishable from terrestrial standards. The disagreement between the various studies was likely a result of insufficient analytical resolution (Yokoyama and Walker, 2016). Most recently, Burkhardt et al. (2011) reported Mo isotopic compositions of CAIs, carbonaceous, ordinary, and enstatite chondrites, magmatic and non-magmatic iron meteorites, pallasites, angrites, and shergottites, using MC-ICP-MS.

Because the nucleosynthetic anomalies observed in the Mo isotopic compositions of bulk meteorite samples are parent-body-specific (e.g., Dauphas et al., 2002a; Burkhardt et al., 2011), Mo is a valuable genetic tracer of the materials that comprise early solar system planetesimals. By merging groups or incorporating ungrouped or

anomalous meteorites into existing groups, the formation histories of meteorite parent bodies can be made more comprehensive. As a corollary, by demonstrating that certain solar system objects are unrelated, the evolutionary histories of the meteorite parent bodies can be clarified. Importantly, genetic links can only be rejected and not confirmed.

It is only possible to reject genetic linkages among meteoritic material if isotopic differences can be resolved. The current state-of-the-art precision of the measured $^{97}Mo/^{96}Mo$ isotope ratio is ± 13 ppm by thermal ionization mass spectrometry operated in negative mode (N-TIMS) (Nagai and Yokoyama, 2016a) and ± 21 ppm by MC-ICP-MS (Burkhardt et al., 2011). In an effort to increase the resolving power of the Mo isotopic system, procedures were developed for this study that allowed for the separation, purification, and high-precision analysis of Mo using a *Thermo-Fisher Triton Plus* N-TIMS at the University of Maryland. The new methodology, which is capable of achieving ± 5.4 ppm (2SD) precision for $^{97}Mo/^{96}Mo$, is presented in Chapter 4.

1.6 Genetics and chronology of IAB meteorites

Molybdenum isotopes were used to investigate how IAB complex meteorites may be genetically related to one another. In addition, the short-lived ^{182}Hf-^{182}W chronometer was employed to obtain relative metal-silicate segregation ages of the subgroups, and to evaluate whether the major heat source(s) responsible for metal-segregation was internal (e.g., ^{26}Al) or external (e.g., impact). Molybdenum isotope data, ^{182}W data, and Os data, which were used to correct Mo and W isotopes for CRE effects, are presented in Chapter 5. New Mo isotope data for magmatic iron meteorites, ungrouped iron meteorites,

ordinary chondrites, and an enstatite chondrite are also reported in Chapter 5 to make comparisons with IAB complex iron meteorites.

Trace element modeling of HSE abundances, used in concert with the Mo and W isotopic compositions, of IAB complex iron meteorites gives insight into an enigmatic group of iron meteorites that may represent more than one parent body. The complex may also represent a type of partially differentiated parent body intermediate between chondrite and magmatic iron meteorite parent bodies, either in time or space. Chapter 6 of this dissertation summarizes the previous chapters and discusses the outstanding questions and future directions of this research.

Chapter 2: Siderophile element systematics of IAB complex iron meteorites: New insights into the formation of an enigmatic group

2.1 Abstract

Siderophile trace element abundances and the ^{187}Re-^{187}Os isotopic systematics of the metal phases of 58 IAB complex iron meteorites were determined in order to investigate formation processes and how meteorites within the IAB chemical subgroups may be related. Close adherence of ^{187}Re-^{187}Os isotopic data of most IAB iron meteorites to a primordial isochron indicates that the siderophile elements of most members of the complex remained closed to elemental disturbance soon after formation. Minor, presumably late-stage open-system behavior, however, is observed in some members of the sLM, sLH, sHL, and sHH subgroups. The new siderophile element abundance data are consistent with the findings of prior studies suggesting that the IAB subgroups cannot be related to one another by any known crystallization process. Equilibrium crystallization, coupled with crystal segregation, solid-liquid mixing, and subsequent fractional crystallization can account for the siderophile element variations among meteorites within the IAB main group (MG). The data for the sLM subgroup are consistent with equilibrium crystallization, combined with crystal segregation and mixing. By contrast, the limited fractionation of siderophile elements within the sLL subgroup is consistent with metal extraction from a chondritic source with little subsequent processing. The limited data for the other subgroups were insufficient to draw robust conclusions about crystallization processes involved in their formation. Collectively, multiple formational processes are represented in the IAB complex, and

modeling results suggest that fractional crystallization within the MG may have been a more significant process than has been previously recognized.

2.2 Introduction

"Magmatic" iron meteorite groups, such as IIAB, IIIAB, and IVA, are so termed because members of each group have relative and absolute trace element abundances that can largely be accounted for by the fractional crystallization of metallic melts. They have commonly been interpreted to sample the metallic cores of differentiated planetesimals (Lovering, 1957; Fish et al., 1960; Goldstein and Short, 1967; Scott, 1972; Scott and Wasson, 1975). By contrast, the IAB complex is a large group of iron meteorites that is chemically and texturally distinct from the magmatic iron groups.

The members of the IAB complex have major and trace element relationships that cannot be accounted for by simple fractional crystallization (e.g., Scott 1972; Kelly and Larimer, 1977; Wasson et al., 1980; Pernicka and Wasson, 1987; Wasson and Kallemeyn, 2002; Goldstein et al., 2009). Particularly, the ranges in the concentrations of elements that are not strongly fractionated by fractional crystallization, such as Ni, Ge, and Ga, are much greater in the IAB complex than in magmatic groups (**Fig. 2.1**). Further, some meteorites within the IAB complex contain abundant silicate clasts, which are rare in magmatic groups. Consequently, IAB complex meteorites were once termed "non-igneous", but are now referred to as "non-magmatic" or "silicate-bearing" (e.g., Wasson, 1970; Willis, 1981; McCoy et al., 1993). The presence of much lower density silicates, most of which are roughly chondritic in both their mineralogy and chemical composition, remains difficult to reconcile with the enveloping, once-molten Fe-Ni metal

(Benedix et al., 2000; Wasson and Kallemeyn, 2002). The chemical and isotopic similarity of some silicate inclusions to winonaites, a group of primitive achondrites, has led to the suggestion that at least some IAB meteorites are from the same parent body as the winonaites (Bild, 1977; Clayton and Mayeda, 1996).

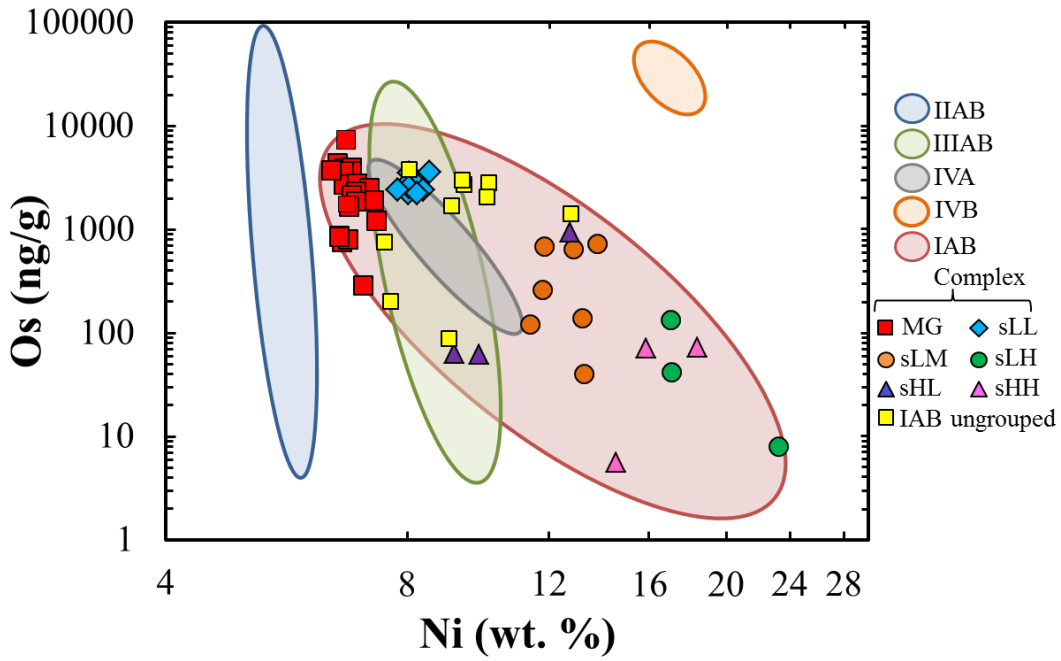

Fig. 2.1. Ni vs. Os for the IIAB, IIIAB, IVA, and IVB magmatic iron meteorite groups and the IAB complex. Fields represent the range of each group. Data symbols for the magmatic groups are omitted for clarity, but are shown for the IAB complex subgroups. The magmatic groups have more linear Ni vs. Os, and smaller ranges in Ni than the IAB complex as a whole. Os data for the IAB complex are from this study. Other Os data are from Cook et al. (2004), Walker et al. (2008), and McCoy et al. (2011), and Ni data are from Wasson (1974), Buchwald (1975), Rasmussen et al. (1984), Wasson, (1999), Wasson and Richardson (2001), and Wasson and Kallemeyn (2002).

The IAB iron meteorite group was initially divided into four separate groups, then consolidated into IAB and IIICD groups, and was later designated group IAB-IIICD as evidence for a compositional continuum accumulated (e.g., Wasson and Schaudy, 1971; Scott et al., 1973; Kracher et al., 1980; Choi et al., 1995). Wasson and Kallemeyn (2002) gathered these meteorites into what is now termed the “IAB complex”, and subdivided it

into a main group (MG) and five subgroups based primarily on the clustering of Ni and Au concentrations. The MG comprises the traditional IAB group, whereas the subgroups include the previously defined groups IIIC and IIID. The complex also contains a number of "ungrouped IAB" iron meteorites that bear chemical similarities to the complex, but do not clearly fall into any of the subgroups. It remains unclear what, if any, common processes relate meteorites from the different subgroups, or even whether all IAB complex meteorites come from the same parent body. The processes by which meteorites within a subgroup are related are also debated.

In an attempt to explain the unusual chemical and textural characteristics of the IAB complex, various authors have proposed formation scenarios that invoke melting and/or mixing on either a partially differentiated or undifferentiated parent body. There is, however, currently no consensus on the formation scenario(s) for the IAB complex. Kracher (1985) proposed that the IAB complex irons sample the fractionally crystallized, S-rich core of an internally heated, partially differentiated parent body. By contrast, the trace element modeling of other authors led to the suggestion that the IAB complex originated in impact-generated melt pools in the mega-regolith of a chondritic parent body or bodies (Wasson et al., 1980; Choi et al., 1995; Wasson and Kallemeyn, 2002). This scenario can potentially better account for the presence of silicates that are suspended in the metal of some IAB complex irons. Conversely, arguments made by Keil et al. (1997) against the efficiency of impact melting and the longevity of melts led Benedix et al. (2000) to suggest that radioactive decay was a more likely source of heat than impacts. That study, using evidence from silicate inclusions, proposed a model by which partial differentiation of an internally heated chondritic parent body was followed

by impact-induced breakup and reassembly. Studies investigating the petrography and Ar-Ar and I-Xe ages of IAB silicates (McCoy et al., 1993; Bogard et al., 2005; Vogel and Renne, 2008; Ruzicka and Hutson, 2010; Tomkins et al., 2013), and Hf-W and Pd-Ag model ages of the IAB metals (Schulz et al., 2012; Theis et al., 2013) have supported different aspects of each of the major formational models.

In order to further constrain the formation and crystallization history of IAB complex iron meteorites, we report ^{187}Re-^{187}Os isotopic systematics and highly siderophile element abundances (HSE; Re, Os, Ir, Ru, Pt, and Pd are measured here) for bulk samples of 58 IAB complex iron meteorites. The ^{187}Re-^{187}Os isotope system is used to assess the extent of open-system behavior of the HSE in the IAB complex. The new HSE data are then used to re-examine the classification of meteorites within the complex, and to examine processes that have been previously proposed to relate meteorites within the subgroups. The absolute and relative abundances of the HSE are particularly well suited for this task because their behaviors, resulting from crystal-liquid fractionation and mixing processes, are generally well understood (e.g., Jones and Drake, 1983; Jones and Malvin, 1990; Chabot and Jones, 2003).

2.3 Samples

All samples examined in this study were obtained from the Smithsonian Institution National Museum of Natural History (**Table 2.1**). Each of the IAB subgroups is represented by at least three samples. The MG samples examined here represent ~25% of recognized MG iron meteorites and span the range of MG compositions reported by Wasson and Kallemeyn (2002) (low to high Au contents). Detailed petrographic

descriptions of IAB silicates can be found in Bild (1977), McCoy et al. (1993); Takeda et al. (2000), Benedix et al. (2000), Ruzicka and Hutson (2010), and Ruzicka (2014). Silicate-metal relationships are discussed in Wasson and Kallemeyn (2002) and Tomkins et al. (2013). The fraction of IAB iron meteorite samples which contain silicates was estimated by Wasson and Kallemeyn (2002) to be ~ 42% (**Tables 2.1 and A2.2** – Buchwald, 1975; McCoy et al., 1993; and Benedix et al., 2000). Silicates occur either as visible inclusions on the mm to cm scale, or as finely disseminated grains on the order of 100 μm across (Wasson and Kallemeyn, 2002). Abundances of silicate clasts in silicate-bearing IAB irons can range from a few vol. % to 40-60 vol. % (e.g., McCoy et al., 1996; Tomkins et al., 2013). For example, in Hope, Bogou, and Smithville, silicates were observed as rare phases in association with troilite and graphite (and only as a single grain in Hope) (Buchwald, 1975). In contrast, Landes and Campo del Cielo, have abundant silicate clasts (e.g., Bunch et al., 1972; Tomkins et al., 2013). The majority of the silicates are broadly chondritic in terms of both their chemical composition and mineralogy, though Benedix et al. (2000) also described sulfide-rich, graphite-rich, and phosphate-rich, non-chondritic silicates. In terms of the metal, many IAB complex irons display a Widmanstätten pattern upon etching with dilute acid, with kamacite and taenite lamellae ranging from sub-mm to mm scale. Samples from the IAB complex represent the range of textural types present in iron meteorites from hexahedrite to ataxite (Benedix et al., 2000).

2.4 Analytical methods

2.4.1 HSE chemistry

Highly siderophile element concentrations and Os isotopic compositions were obtained using methods previously described (Cook et al., 2004; Walker et al., 2008; McCoy et al., 2011). The meteorites were cut into 30 to 300 mg pieces using a water-cooled *Leco "Vari-cut"* saw with a 12.7 cm diamond wafering blade, which was cleaned with carborundum between each sample. For some silicate-bearing meteorites (e.g., Landes and Woodbine), it was impossible to separate pure metal from silicate for digestion, although silicate inclusions were avoided as much as possible. All samples were mechanically abraded using carborundum paper, and sonicated in ethanol three times to remove any adhering rust, fusion crust, or saw blade contamination. Masses of the samples digested are given in **Table 2.1**. Each sample was spiked prior to digestion with a combined platinum-group element (PGE) spike (^{191}Ir, ^{99}Ru, ^{194}Pt, and ^{105}Pd) and a combined Re-Os spike (^{185}Re and ^{190}Os) for isotope dilution. Occasionally, it was necessary to spike with an additional individual ^{105}Pd spike to supplement the combined PGE spike because it was too dilute in ^{105}Pd for some of the Pd-enriched samples.

Samples and spikes were digested and equilibrated in *Pyrex*® Carius tubes at 220°C for at least 24 hours, using 5 ml of concentrated HNO_3 and 2.5 ml of concentrated HCl. The metal phase was completely digested using this technique, but any silicates present were not dissolved. Upon opening the tubes, oxidized volatile Os was immediately extracted into carbon tetrachloride (CCl_4) and then back-extracted and reduced using concentrated HBr (Cohen and Waters, 1996). The Os was further purified via microdistillation (Birck et al., 1997). The Os total analytical blank was negligible for

all samples, comprising < 0.1% of the total Os extracted, averaging 4 ± 2 pg, with an isotopic composition of $^{187}Os/^{188}Os = 0.15 \pm 0.04$ (n=7).

The HSE remaining in the aqueous phase following Os extraction were separated and purified using anion exchange chromatography (Rehkämper and Halliday, 1997). Samples were centrifuged to separate and allow removal of silicate residue. Each sample was loaded onto a disposable 2 ml Biorad column filled with 1.7 ml of AG1X8 100-200 mesh resin in 1M HCl. After most non-analytes were rinsed off the column with 1M HCl, 0.8M HNO_3, and 1M HCl-1M HF, Re and Ru were eluted in 6M HNO_3, followed by Pt and Ir in concentrated HNO_3. Finally, Pd was eluted in concentrated HCl. Rhenium and Ru cuts were further purified using a smaller version of the primary anion column that was made using disposable transfer pipettes and 250 µl of resin. The Re-Ru, Pt-Ir, and Pd cuts were then evaporated to dryness and re-dissolved in a small amount of *aqua regia* to reduce resin-derived organics. The HSE cuts were dried again and taken up into solution in 0.8 M HNO_3 for analysis. The total analytical blanks for Re, Ir, Ru, Pt, and Pd were 1 ± 2, 3 ± 10, 30 ± 40, 300 ± 600, and 40 ± 80 pg, respectively (n=7). These blanks were typically less than 1% of the total element analyzed, with the exception of the Pt blank, which accounted for 2-3% of the Pt separated from some lower abundance samples (i.e., Mount Magnet, Freda, Dayton, Edmonton (KY)). The Re blank accounted for ≤ 0.1% of the total Re extracted for nearly all samples. The exceptions are Dayton and Freda, where the blank accounted for 0.2% and 0.9% of the total Re, respectively. All blanks are sufficiently low as to have an inconsequential effect on the isotope systematics.

2.4.2 Mass spectrometry

Osmium was analyzed using a *VG Sector 54* thermal ionization mass spectrometer in negative ion mode (N-TIMS). Loading procedures were similar to those reported by Cook et al. (2004). Samples were dissolved in concentrated HBr and 1 to 50 ng of Os were loaded onto an outgassed Pt filament. The sample was dried by applying a 0.5 A current through the filament. Once dry, ~0.8 µl of a saturated solution of $Ba(OH)_2$ was deposited on top of the sample and used as an electron activator. For samples and standards, the Os isotope beams were collected in multiple Faraday cups using a static analytical routine. The external reproducibility of $^{187}Os/^{188}Os$ for an Os reference material was ± 0.03% (2σ). For samples, however, the average internal uncertainty on the $^{187}Os/^{188}Os$ measurement was ± 0.04% ($2\sigma_m$). Because the blank correction for $^{187}Os/^{188}Os$ was negligible, we assigned an uncertainty of ± 0.04% to $^{187}Os/^{188}Os$. In cases where lower signal intensity made the statistics of the individual measurement > 0.04%, the standard error of the mean of the measurement is reported ($2\sigma_m$) (low-abundance samples Freda and Mount Magnet). The uncertainties for Os concentrations are estimated to be ± 0.1%.

Rhenium, Ir, Ru, Pt, and Pd concentrations were determined using a *Nu Plasma* multi-collector inductively coupled plasma mass spectrometer (MC-ICP-MS). Sample solutions were introduced into the plasma using a *Cetac Aridus*^{TM} desolvating nebulizer. Analyses were conducted in static mode using multiple Faraday cups. Spiked ratios were measured to better than ± 0.1% (2σ). For Ir, Ru, Pt, and Pd, instrumental mass bias was corrected using a fractionation factor obtained by comparing isotope ratio measurements of standards with the accepted isotope ratios. Rhenium cuts were doped with W in order

to correct for instrumental mass bias, normalizing to $^{184}W/^{186}W = 1.0780$ (Kleine et al., 2004). The uncertainties of Ir, Ru, Pt, and Pd concentrations were estimated to be better than ± 3%, based on repeated analyses of spiked aliquots of previously well-characterized iron meteorites which were used as reference materials (Walker et al., 2008). Uncertainties for Re concentrations are estimated to be ± 0.18%. For $^{187}Re/^{188}Os$ ratios, the uncertainties were estimated to be ± 0.2%.

2.5 Results

2.5.1 ^{187}Re-^{187}Os isotopic systematics

Rhenium-187 decays to ^{187}Os via β^- decay with λ for $^{187}Re = 1.666 \times 10^{-11}$ yr^{-1} (Smoliar et al., 1996). The siderophile element systematics of meteorites that do not plot on a primordial ^{187}Re-^{187}Os isochron must be considered with caution, as non-isochronous samples may reflect post-formation gain or loss of Re and/or Os, and likely other HSE. Rhenium-Os isotopic data are presented in **Table 2.1** and **Fig. 2.2**. The moderate fractionation of Re from Os in the MG produces a range in $^{187}Re/^{188}Os$ from 0.346 (Magura) to 0.909 (Hope). The corresponding range in $^{187}Os/^{188}Os$ is 0.12270 to 0.16727. If the other subgroups are included in the range, the lowest $^{187}Re/^{188}Os$ and $^{187}Os/^{188}Os$ ratios are for Carlton (sLM) and the highest are for Georgetown (ungrouped).

Table 2.1. Highly siderophile element abundances and Re-Os isotope data. Samples are listed in order of decreasing Re concentration. Sample weights are given in grams. †Ni, in wt. %, data are from Wasson and Kallemeyn (2002). All other concentrations are reported as ng/g.

Sample	Wt.	Ni†	Re	Os	Ir	Ru	Pt	Pd	$^{187}Re/^{188}Os$	$^{187}Os/^{188}Os$	Δ_{Os}[b]
IAB main group											
Landes[a]	0.025	6.55	354.8	4368	4293	9805	10500	3581	0.3912	0.12627	-0.3
Seligman	0.195	6.67	308.7	3891	3293	7754	8886	3502	0.3822	0.12563	0.5
Yenberrie	0.108	6.82	290.6	3926	3463	5536	6359	3647	0.3565	0.12365	1.0
Ballinger	0.011	6.78	279.9	3153	3137	6782	7179	3402	0.4278	0.12905	-1.4
Duplicate	0.039		274.1	3138	3111	6341	7352	3382	0.4209	0.12868	0.3
Cranbourne	0.074	6.82	275.0	3670	3614	9662	11380	3398	0.3608	0.12377	-1.2
Campo del Cielo[a]	0.053	6.68	274.1	3632	3308	6725	8213	3403	0.3635	0.12418	0.8
New Leipzig	0.097	6.68	272.4	2723	2904	8626	9898	3527	0.4824	0.13353	0.1
Magura[a]	0.049	6.44	269.2	3743	3648	9892	11430	3254	0.3464	0.12270	-0.4
Canyon Diablo[a]	0.071	6.93	231.7	2780	2560	5579	6959	3494	0.4016	0.12723	1.1
Odessa[a]	0.016	7.19	224.3	2501	2572	5392	6749	3795	0.4321	0.12931	-2.3
Jenkins[a]	0.129	6.92	211.6	2327	2207	5403	6772	3585	0.4382	0.13008	0.6
ALHA 77283	0.065	7.28	210.2	1891	2327	5687	6867	4526	0.5362	0.13777	-0.1
Youndegin[a]	0.092	6.83	202.4	2134	2217	6354	6960	4010	0.4572	0.13156	0.4
Smithville[a]	0.033	6.92	191.4	1884	2028	6096	6422	3734	0.4898	0.13415	0.5
Seymour	0.100	6.78	166.5	1673	1807	5636	6383	3627	0.4799	0.13340	0.7
Bogou[a]	0.091	7.33	158.9	1219	1747	5178	5999	3754	0.6291	0.14510	-0.3
Burgavali	0.078	6.64	132.1	759.2	1217	9283	10120	3305	0.8422	0.16195	-0.5
Morasko	0.084	6.76	106.8	799.0	1141	9612	10260	3306	0.6456	0.14649	0.5
Seeläsgen	0.040	6.59	104.3	863.4	1143	9643	10340	3314	0.5831	0.14148	0.0
Sarepta	0.122	6.59	100.7	845.1	1131	9372	10190	3287	0.5748	0.14099	1.5
Duplicate	0.140		103.3	849.2	1136	9995	10270	3432	0.5873	0.14183	0.1
Hope[a]	0.203	7.06	54.26	288.9	753.1	6584	5893	3449	0.9094	0.16727	-0.6
IAB sLL (low Au, low Ni) subgroup											
Pine River[a]	0.261	8.04	268.1	3515	3085	3812	4925	4286	0.3674	0.12451	1.0
Shrewsbury[a]	0.113	8.53	226.5	3588	2729	3384	4840	4539	0.3038	0.11949	1.1
Duplicate	0.035		226.6	3641	2717	4254	4897	4413	0.2995	0.11912	0.8
Comanche[a]	0.071	8.24	226.4	2698	2614	4577	5738	4499	0.4043	0.12740	0.7
Bahjoi[a]	0.140	7.94	220.2	2598	2429	4659	5739	4370	0.4084	0.12771	0.5
Toluca[a]	0.141	8.02	215.9	2232	1962	4351	5426	4283	0.4663	0.13228	0.4
Deport	0.124	8.05	215.8	2587	2429	4633	5613	4389	0.4018	0.12721	0.7
Balfour Downs[a]	0.098	8.38	212.0	2422	2302	4148	5613	4809	0.4218	0.12870	-0.2
Bischtübe[a]	0.236	7.78	201.6	2432	2326	3554	4870	3932	0.3994	0.12639	-5.5
Duplicate	0.117		204.8	2425	2338	3822	4890	4257	0.4068	0.12764	1.1
Goose Lake[a]	0.045	8.24	188.2	2217	2139	4509	6094	4056	0.4092	0.12779	0.7
IAB sLM (low Au, medium Ni) subgroup											
Persimmon Creek[a]	0.194	13.79	80.73	730.6	840.2	1360	2026	5585	0.5330	0.13755	0.3
Duplicate	0.113		71.03	671.7	829.6	1314	1919	5184	0.5101	0.13577	0.6
Mungindi	0.197	11.86	47.86	678.4	570.3	426.2	610.7	5881	0.3397	0.12235	1.4
Edmonton (KY)	0.064	12.90	38.86	650.6	508.4	521.8	586.9	5769	0.2874	0.11817	1.0
Duplicate	0.284		38.74	649.7	502.0	516.1	584.4	5647	0.2869	0.11816	1.3
Maltahöhe[a]	0.198	11.40	16.42	121.4	165.0	641.0	626.2	5390	0.6533	0.14731	2.6
Anoka	0.309	11.80	13.84	260.2	167.9	256.2	224.5	5722	0.2558	0.11566	0.8
Duplicate	0.072		14.05	260.8	162.2	253.1	221.1	5847			
Carlton[a]	0.190	13.23	7.113	140.0	92.49	97.70	101.9	6689	0.2444	0.11494	2.7
Lamesa	0.268	13.28	4.582	39.78	48.14	142.6	138.6	6639	0.5559	0.14070	14
Duplicate	0.199		4.706	39.65	47.86	142.7	139.0	6632	0.5727	0.14120	5.3

Table 2.1. (continued)

Sample	Wt.	Ni†	Re	Os	Ir	Ru	Pt	Pd	$^{187}Re/^{188}Os$	$^{187}Os/^{188}Os$	Δ_{Os} [b]
IAB sLH (low Au, high Ni) subgroup											
Tazewell	0.180	17.06	7.512	134.7	87.84	62.04	85.93	8687	0.2683	0.11692	3.6
Dayton[a]	0.252	17.10	2.594	41.82	31.37	49.13	48.66	8262	0.2985	0.12035	14
Duplicate	0.225		2.590	40.53	28.68	48.21	46.73	8194	0.3077	0.12036	6.8
Freda	0.278	23.21	0.6164	8.043	7.500	30.00	23.02	12210	0.3692	0.12662	21
IAB sHL (high Au, low Ni) subgroup											
Quarat al Hanish	0.150	12.75	86.75	943.4	957.6	2214	2671	6066	0.4432	0.13048	0.6
Chebankol	0.238	9.17	8.632	63.31	102.9	1328	1711	4578	0.6587	0.14680	-6.7
Sombrerete[a]	0.264	9.84	6.099	61.87	73.80	537.6	468.2	5369	0.4753	0.13297	0.2
IAB sHH (high Au, high Ni) subgroup											
Kofa	0.231	18.39	8.218	72.38	99.22	2554	3671	9650	0.5478	0.13872	0.2
ALHA 80104	0.295	15.86	7.584	70.94	90.42	2597	3225	8641	0.5157	0.13669	5.4
Mount Magnet[a]	0.299	14.57	0.6252	5.650	6.176	142.6	59.90	9212	0.5340	0.13922	16
IAB ungrouped											
TIL 91725[a]	0.131	8.04	285.3	3784	3244	5151	5934	3743	0.3631	0.12412	0.5
Caddo County[a]	0.260	9.42	254.0	2728	2515	4696	6058	4267	0.4488	0.13091	0.5
Zagora[a]	0.123	9.36	243.0	3026	2655	4520	5413	3981	0.3867	0.12607	1.3
Mertzon[a]	0.088	9.08	188.0	1701	2160	3959	7395	3540	0.5332	0.13760	0.6
EET 84300[a]	0.093	10.11	183.4	2839	2161	1995	2768	4710	0.3109	0.12022	2.8
Duplicate	0.127		176.8	2769	2085	1876	2694	4094	0.3070	0.11982	2.0
Woodbine[a]	0.230	10.05	177.9	2062	1984	2389	3053	6181	0.4156	0.12834	1.2
Pitts[a]	0.158	12.81	117.9	1433	1244	1780	2447	6954	0.3962	0.12682	1.3
Duplicate	0.097		105.8	1423	1392	1724	2450	6486	0.3582	0.12405	3.7
Duplicate	0.111		114.1	1491	1373	1790	2346	6433	0.3685	0.12418	-3.2
Mundrabilla[a]	0.060	7.50	81.62	751.9	998.0	3232	3825	3925	0.5237	0.13754	7.5
Duplicate	0.078		89.40	785.5	971.6	3243	3627	3828	0.5491	0.13830	-5.0
Waterville	0.116	7.63	34.86	203.2	366.8	3278	3187	3874	0.8303	0.16061	-4.6
Duplicate	0.126		33.33	186.0	348.4	3395	2804	3908	0.8671	0.16255	-14
Georgetown[a]	0.109	9.03	17.33	88.47	190.4	2105	1750	3601	0.9488	0.16983	-6.1
IAB unclassified, classified here as MG											
Osseo	0.068	6.71	510.3	7313	5934	8769	10690	3368	0.3360	0.12204	1.2
Sardis	0.137	6.73	185.3	1760	2022	7588	8292	3424	0.5078	0.13551	-0.2
Duplicate	0.075		185.8	1765	2024	7546	8289	3421	0.5074	0.13558	0.9

[a]IAB irons in which silicate inclusions have been observed by Buchwald (1975) and McCoy et al. (1993). A more detailed summary of silicate occurences is provided in Table S2.

[b]Δ_{Os} is calculated by, $\Delta_{Os} = 10^4(^{187}Os/^{188}Os_{IAB} - (0.09532 + 0.07918 \times {}^{187}Re/^{188}Os_{IAB}))$, where 0.09532 is the initial $^{187}Os/^{188}Os$ and 0.07918 is the slope of the MG isochron (Table 2.2).

Rhenium-Os isotopic data were regressed for the MG and individual IAB subgroups using ISOPLOT (Ludwig, 2003) (**Table 2.2**). Because it is represented by the largest number of samples in this study and in the IAB complex, the MG isochron is used for comparison to the other subgroups. The MG isochron gives an age of 4574 ± 20 Ma and an initial $^{187}Os/^{188}Os$ of 0.09532 ± 0.00017 (MSWD = 4.2). This age and initial $^{187}Os/^{188}Os$ overlap, within uncertainties, the composite group IAB age and initial ratio of 4537 ± 21 and 0.09556 ± 0.00016 reported by Horan et al. (1998). The age and initial ratio are also similar to results for magmatic iron meteorite groups (Smoliar et al., 1996; Shen et al., 1996; Walker et al., 2008; McCoy et al., 2011). The isochrons for most of the individual subgroups yield ages and initial $^{187}Os/^{188}Os$ that overlap with those of the MG, although the precision of the regressions vary considerably, in part due to the limited range in Re/Os for some subgroups (sLH, sHH). The sHL isochron yields an apparent age ~100 Myr younger than isochrons for the MG, sLL, and sLM subgroups; however, it was generated with data from three meteorites, and is not considered to be meaningful.

Parts in 10,000 deviations of data for individual samples, relative to the slope and initial $^{187}Os/^{188}Os$ of the MG isochron, are given as Δ_{Os} values in **Table 2.1** (Walker et al., 2002). The Δ_{Os} values are calculated by $\Delta_{Os} = 10^4(^{187}Os/^{188}Os_{sample} - (0.09532 + 0.07918 \times {}^{187}Re/^{188}Os_{sample}))$, where 0.09532 is the initial $^{187}Os/^{188}Os$ and 0.07918 is the slope of the MG isochron (**Table 2.2**). The 13 samples of the 58 IAB meteorites examined here that do not plot within uncertainty of the MG isochron are Carlton and Lamesa (sLM); Tazewell, Dayton, and Freda (sLH); Chebankol (sHL); ALHA 80104 and Mount Magnet (sHH); and Pitts, EET 84300, Mundrabilla, Waterville, and Georgetown (ungrouped).

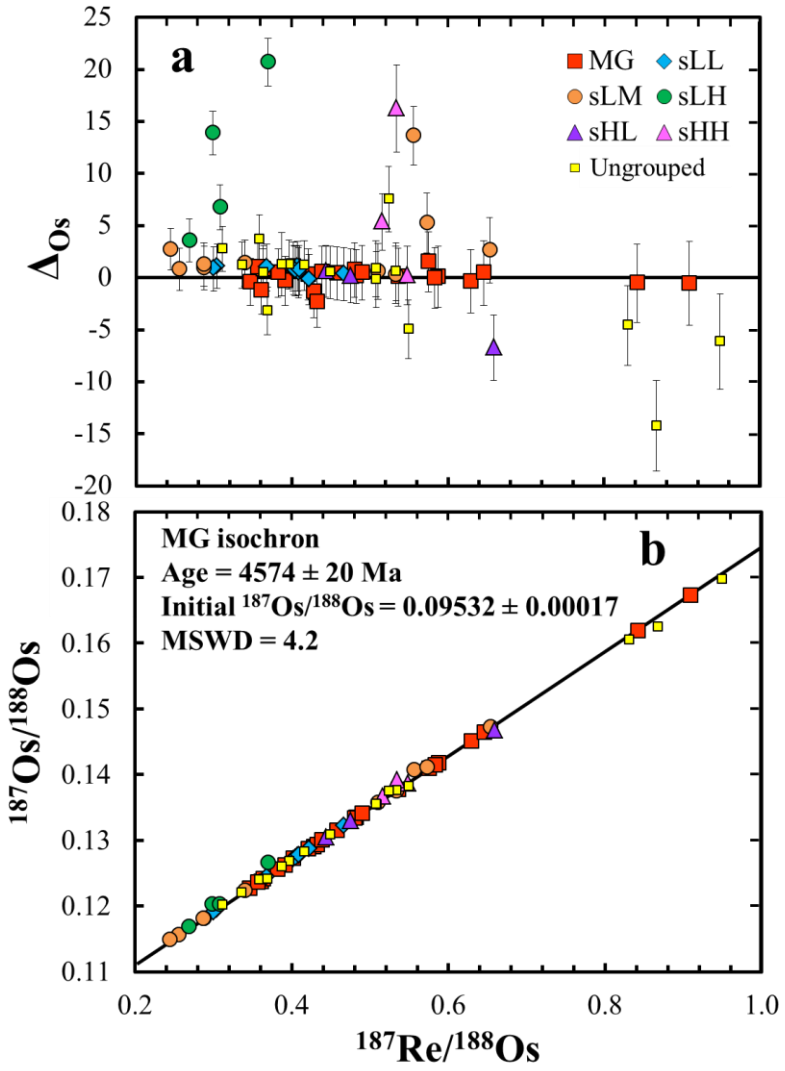

Fig. 2.2. (a) $^{187}Re/^{188}Os$ vs Δ_{Os} (parts in 10,000 deviations from the MG Re-Os isochron, calculated using the slope and initial $^{187}Os/^{188}Os$ of the MG isochron – see Table 1 for details). (b) $^{187}Re/^{188}Os$ vs. $^{187}Os/^{188}Os$ plot for the IAB complex, with the MG isochron for reference. The MG Re-Os system defines a primordial isochron, which most other IAB meteorites fall on or near. The sLM, sLH, sHL, and sHH subgroups are characterized by containing some irons which plot 5-20 Δ_{Os} units off the MG isochron. Duplicates are included in the calculation of the isochron. MSWD (mean square weighted deviation) is a measure of scatter about the regression.

Table 2.2. ^{187}Re-^{187}Os isochron slopes and initial $^{187}Os/^{188}Os$ ratios for each IAB subgroup and the IAB complex as a whole, including ungrouped IAB irons.

Group	n[a]	Age (Myr)	$^{187}Os/^{188}Os_i$	MSWD
MG	23	4574 ± 20	0.09532 ± 0.00017	4.2
sLL	10	4552 ± 23	0.09554 ± 0.00016	0.80
sLM	9	4640 ± 100	0.09513 ± 0.00068	60
sLH	4	5500 ± 2400	0.091 ± 0.013	134
sHL	3	4379 ± 35	0.09696 ± 0.00032	1.2
sHH	3	4000 ± 11000	0.10 ± 0.11	69
IAB complex	70	4533 ± 37	0.09576 ± 0.00029	55

[a]n is the number of samples, including duplicate analyses

2.5.2 HSE data for bulk samples

Highly siderophile element concentration data for bulk samples are also presented in **Table 2.1**. A detailed comparison of the data presented here with literature data is provided in the supplementary materials (**Table A2.3**). Generally, our new HSE data are within ± 20% of values reported by Goldberg et al. (1951), Smales et al. (1967), Crocket (1972), Pernicka and Wasson (1987), Hirata and Masuda (1992), Hoashi et al. (1993), Choi et al. (1995), Shen et al. (1996), Horan et al. (1998), and Wasson and Kallemeyn (2002). Some HSE data for certain samples differ by > 30% from literature values. These are the MG samples Sarepta (Re and Ir) and Cranbourne (Re, Os, Ir, Ru, Pt, and Pd); sLL sample Toluca (Ru); sLM samples Persimmon Creek (Re), Anoka (Pt), Mungindi (Re and Pd), Carlton (Pd), and Lamesa (Pd); sLH samples Freda (Re and Ir) and Dayton (Pd); sHH sample Mount Magnet (Os and Ir); and ungrouped sample Woodbine (Pt). Rhenium data reported here are systematically lower than those reported by Wasson and Kallemeyn (2002), but no other HSE have systematic offsets from the literature data.

Fourteen of the IAB complex iron meteorites were processed multiple times to assess sample heterogeneity and/or analytical reproducibility. Duplicate analyses, denoted in **Table 2.1**, yielded variable concentrations, with most duplicates having percentage differences of < 3 %, but ranging up to ~10-20%. The HSE ratios of duplicates also varied, ranging from < 3% to 23% (**Table A2.4**). Typically, duplicate analyses that were characterized by large variability in absolute HSE abundances were also characterized by HSE ratios that were variable.

We attribute the elemental and isotopic heterogeneities in bulk samples to primarily reflect chemical heterogeneity at the sample sizes processed. The heterogeneities observed most likely reflect variable distributions of kamacite and taenite in different pieces, as most of the HSE are fractionated between the two metal phases (e.g., Hirata and Nesbitt, 1997). The differences highlight the difficulty by which comparatively small pieces of a IAB meteorite can be precisely characterized by a single "bulk" composition. Nevertheless, the scale of the sample heterogeneity is not sufficient to influence the conclusions drawn below that are based on large differences in absolute and relative HSE abundances within and between subgroups.

Overall, HSE abundances in samples from the IAB complex range over as much as three orders of magnitude (**Fig. 2.3**), although concentrations within subgroups span no more than two. Palladium abundances vary less than the other HSE, both between and within subgroups, having a range of < 50% in each of the subgroups. The chondrite-normalized HSE patterns, plotted from left to right in order of decreasing 50% condensation temperatures, are characterized by similar features within a given subgroup that are not shared between all subgroups (**Fig. 2.3**). Unlike in magmatic iron groups,

HSE patterns for some meteorites cross in most of the subgroups. Also, most subgroups have HSE concentrations that are fractionated relative to chondritic abundances. The exception is the sLL subgroup, which has suprachondritic absolute HSE abundances that are in approximately chondritic relative abundances.

The HSE patterns of some subgroups resemble the patterns of some magmatic iron meteorite groups. Of note, the MG patterns share similarities with the IVA group, whereas the sHL and sHH subgroups have HSE patterns that are broadly similar to late-crystallized IIAB and IIIAB iron meteorites (**Fig. 2.3** – Pernicka and Wasson, 1987; Hoashi et al., 1993; Cook et al., 2004; McCoy et al. 2011). By contrast, the sLM and sLH subgroups have distinctive HSE patterns, compared to known magmatic irons. These subgroups are characterized by absolute Re, Os, Ir, Ru and Pt abundances that range from broadly chondritic to significantly subchondritic, but in roughly chondritic relative proportions. Palladium is considerably enriched, relative to chondrites and the other HSE in the sLM and sLH.

The ungrouped samples are characterized by HSE patterns that are highly variable. This is expected, as these samples do not belong to any one subgroup (Fig. 2.4). Some ungrouped members of the IAB complex share similarities in HSE patterns with certain IAB subgroups. Of note, the HSE pattern of Caddo County is similar to the sLL subgroup, and the pattern of Pitts is similar to the sLM subgroup.

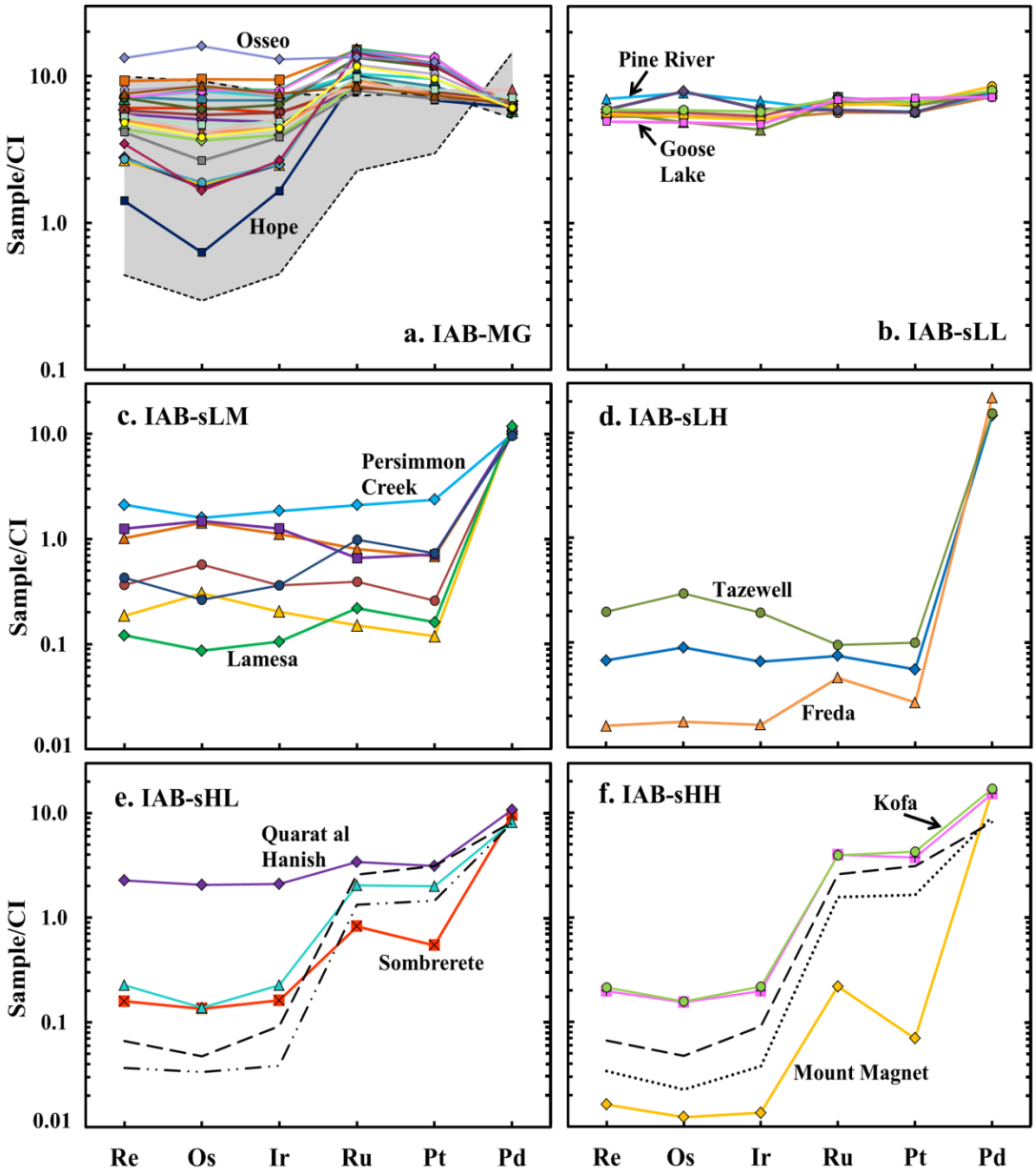

Fig. 2.3. CI chondrite-normalized HSE abundances for each of the IAB complex subgroups. Abundances are normalized to those of Orgueil (Horan et al., 2003). The HSE are plotted from left to right in order of decreasing 50% condensation temperature (Lodders, 2003). The HSE were determined by isotope dilution methods as described in text. Note the different scale in (a-b), relative to (c-f). The grey field in (a) represents the range of the IVA magmatic iron meteorite group, for reference (McCoy et al., 2011). The dashed and dotted lines represent Jamestown and Fuzzy Creek, respectively. Two unclassified samples, Osseo and Sardis, plot within the MG field, or along trend, on all HSE variation diagrams (**Fig. 2.5**). These samples likely belong to the MG, and so are plotted in (a) with blue diamond and yellow circle symbols. In (e-f), the IIIAB magmatic iron meteorites Grant (dashed lines), Thurlow (dash-dotted line), and Chupaderos (dotted line) are shown for comparison.

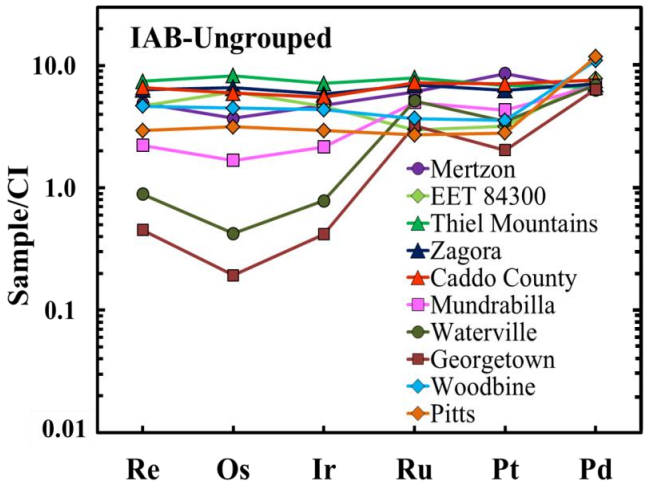

Fig. 2.4. CI chondrite-normalized HSE abundances for the IAB ungrouped iron meteorites. Some ungrouped IAB irons have HSE patterns which share similarities with those of a particular subgroup, as described in the text.

2.6 Discussion

2.6.1 Re-Os isotopic system

Because most of the IAB samples plot on or near a primordial isochron (**Fig. 2.2**), the ^{187}Re-^{187}Os isotope systematics require that the IAB complex was, in large part, a closed system to the movement of siderophile elements after the first several 10's of Ma after solar system formation, and therefore, that their HSE abundances reflect those at the time of crystallization. Conversely, the samples that do not plot within uncertainties of the MG isochron have absolute and relative HSE abundances that may reflect later-stage processes, either on the parent body, or as a result of terrestrial alteration. Late-stage parent body processes, which likely occurred greater than ~ 40 Myr after the crystallization of the non-isochronous samples, could be related to thermal or shock metamorphism due to impacts, though shock effects in IAB iron meteorites are minor (Benedix et al., 2000). Alternatively, if a late impactor was volatile-rich, aqueous

alteration could also modify the Re/Os. A few samples studied here showed evidence of terrestrial weathering as extensive rust, including Ballinger and Morasko (MG); Deport and Shrewsbury (sLL); Persimmon Creek (sLM); TIL 91275, Mertzon, and Woodbine (ungrouped). Of these, none are resolvable from the MG isochron, suggesting that the presence of rust is not indicative of non-isochronous behavior.

The non-isochronous samples are largely confined to the sLM, sLH, sHL, and sHH subgroups. This suggests that alteration on the parent body or Earth was either more pronounced in these samples, because of their generally lower Re and Os abundances, relative to the MG, or that the meteorites from these subgroups were subject to more intense alteration than those in other subgroups. Implicit in the second scenario is the assumption that the alteration was localized, or that the sLM, sLH, sHL, and sHH subgroups were spatially separated from the other subgroups, perhaps in different portions of a single parent body, or on distinct parent bodies. Nevertheless, HSE mobility in the complex was evidently limited because none of the samples plot more than 2% off of the MG isochron. Therefore, the conclusions drawn below are likely unaffected by the minor open-system behavior.

2.6.2 Classification within the IAB complex

The IAB complex is classified as such due to an observed continuum in taxonomically useful elements. In general, magmatic and silicate-bearing iron meteorite groups have been classified based on Ga, Ge, Ni, Au, and Ir abundances (e.g., Goldberg et al., 1951; Lovering et al., 1957; Wasson, 1967; Wasson, 1969). The concentrations of Ga, Ge, and Ni are not strongly affected by crystallization processes and have proven to be important in distinguishing among magmatic iron meteorite groups that underwent

extensive crystal-liquid fractionation processes (Goldberg et al., 1951; Lovering et al., 1957). Conversely, the IAB complex is characterized by a much larger range in Ni than any magmatic iron group, and is accompanied by nearly as great a range in Ir and Os concentrations as in the most highly fractionated magmatic groups (**Fig. 2.1**). Further, the IAB complex is characterized by siderophile element concentrations that define broad clouds of data on x-y plots, in comparison to the more sharply defined trends characteristic of the magmatic groups. In contrast to the complex as a whole, the IAB subgroups have considerably more restricted ranges in, e.g., Ni and Os. The new HSE data provide no cause for change in the conclusion of Wasson and Kallemeyn (2002) that the collective members of the IAB complex cannot be related by a simple crystal-liquid fractionation process. Thus, if the subgroups are all from the same parent body, it must be concluded that the subgroups crystallized from distinct melts, presumably in different locations.

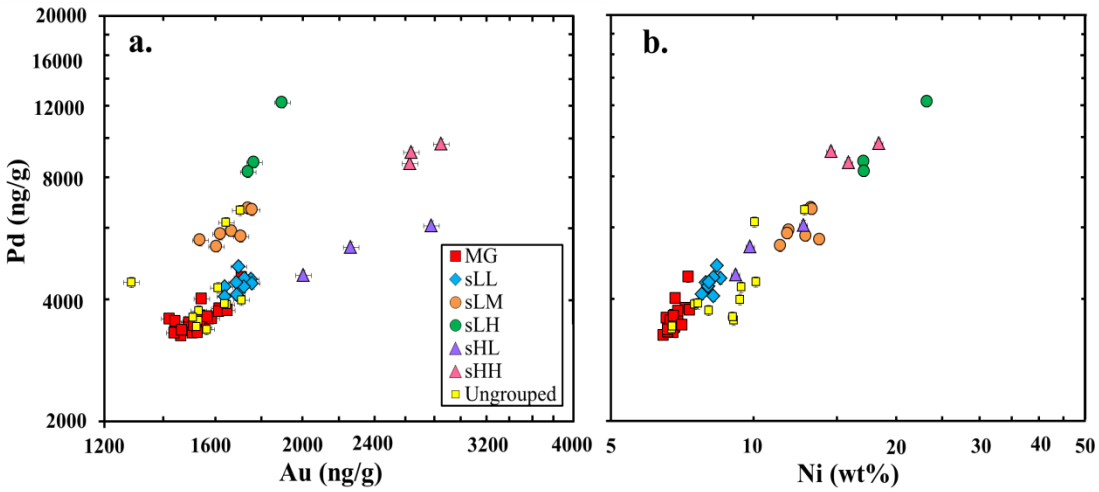

Fig. 2.5. (a) Au vs. Pd Concentrations for the IAB subgroups and ungrouped IAB irons. (b) Ni vs. Pd abundances. Pd abundances are from this study, whereas Au and Ni data are instrumental neutron activation analysis data from Wasson and Kallemeyn (2002). The subgroups of Wasson and Kallameyn (2002) can be distinguished on the basis of Pd vs. Au abundances and, to a lesser extent, Pd vs. Ni. In (b) Pd and Ni are correlated, demonstrating that the Pd vs. Au plot provides similar resolution between the subgroups as the Ni vs. Au plot from Wasson and Kallemeyn (2002).

Wasson and Kallemeyn (2002) based their division of the IAB complex into subgroups on the clustering of data when plotting Au versus other siderophile elements. The extended database for HSE here offers the opportunity to re-examine the subgroups using elements with somewhat different volatilities and crystal-liquid fractionation behaviors. The new high precision Pd data are particularly useful for this because, compared to Au, Pd has a nearly ~300 K higher 50% condensation temperature (at 10^{-4} bar), yet is only slightly less incompatible in solid metal-liquid metal systems. Thus, Pd can be strongly modified relative to Au by processes that can lead to the formation of metals, but should behave similarly to Au, once a liquid-solid metal system is established.

For the MG and each of the subgroups, Pd is well correlated with both the Ni and Au concentrations reported by Wasson and Kallemeyn (2002) (**Fig. 2.5**), strengthening the case that the chemical basis of the subgroup divisions is robust. In order to differentiate the subgroups that show overlap in the classification of Wasson and Kallemeyn (2002) (MG and sLL), or that are characterized by similar HSE patterns (sLM and sLH; sHL and sHH), each of the subgroups are shown on a plot of Au vs. Pd (**Fig. 2.5**). In Au and Pd compositional space, the sLL subgroup is characterized by some overlap with the MG, but this overlap is reduced on a plot of Ni vs. Pd.

The new HSE data can be used to reassess some of the classifications of Wasson and Kallemeyn (2002) for particular meteorites (**Figs. 2.3-2.5**). For example, Osseo and Sardis, which they termed "unclassified", are included in the IAB complex, but are neither classified as ungrouped nor do they belonging to a specific subgroup; however, both of these samples plot within the MG fields on our new HSE variation diagrams. In

Wasson (2011), Osseo is referred to as a MG iron. Therefore, we will assume both meteorites are MG irons.

Morasko and the chemically similar irons Seeläsgen, Burgavli, and Sarepta have Pd abundances within the range of the MG, and these irons were classified as belonging to the MG by Wasson and Kallemeyn (2002). Conversely, Pilski et al. (2013) recommended that Morasko and chemically similar irons be considered distinct, anomalous members of the MG, based on their low Ir concentrations. However, Ir is strongly incompatible in metallic systems with appreciable S, and splitting vs. lumping in this case could lead to an incomplete picture of the crystallization of the MG. Therefore, we continue to assume that irons with similar Pd, but low Ir are members of the MG, as discussed below. Additionally, Morasko and Seeläsgen are likely paired (Kracher et al., 1980; Pilski et al. 2013), and the similarity of the new HSE data for both meteorites further supports a Morasko-Seeläsgen link.

Three ungrouped IAB irons, Caddo County, Zagora, and TIL 91725 (**Fig. 2.4**), which fall into the "Udei Station grouplet" defined by Wasson and Kallemeyn (2002), have similar HSE patterns and abundances to the sLL subgroup and plot within or very near sLL fields on Pd vs. other HSE plots. Wasson and Kallemeyn (2002) suggested that the Udei Station grouplet is closely related to the sLL subgroup and the new HSE data are consistent with this although Ni abundances reported by Wasson and Kallemeyn (2002) are ~15 % higher in Caddo County and Zagora than the average Ni concentration of the sLL subgroup.

Pitts and Woodbine (Pitts grouplet) have higher total HSE abundances than the sLM subgroup and do not lie on some of the linear arrays defined by the sLM subgroup

on HSE plots (**Fig. 2.5**). However, the sLM subgroup and Pitts and Woodbine share the characteristic of enriched Pd relative to the other HSE, which is suggestive of a similar, but likely not common, heritage. In the sLH subgroup, the considerably higher Pd abundance in Freda suggests that it is not related to Tazewell and Dayton.

The small number of samples available for analyses in the sHL and sHH subgroups, coupled with the scatter in the sHL and sHH fields (**Fig. 2.5**), make it difficult to assess relations within these groups (Wasson, 2011). However, Sombrerete, tentatively assigned to the sHL subgroup by Wasson and Kallemeyn (2002), contains silicate with distinct $\Delta^{17}O$, compared with the small range of $\Delta^{17}O$ values in other IAB complex meteorites (Clayton and Mayeda, 1996). Further, Sombrerete is unusually P-rich, and its silicate inclusions are fractionated with respect to their major and trace lithophile element abundances, relative to the commonly chondritic silicates in other IAB irons (Ruzicka et al. 2006). Ruzicka et al. (2006) considered Sombrerete to be an ungrouped iron, not related to the IAB complex, and the HSE data are consistent with this interpretation. Quarat al Hanish and Chebankol have Pd, Ni, Au, and Ga abundances that bracket those of Sombrerete, so if Sombrerete is unrelated to the other sHL iron meteorites, Quarat al Hanish and Chebankol have little in common with one another. In the sHH subgroup, two of the three irons we analyzed have nearly identical HSE patterns, whereas the third, Mount Magnet, has a much more fractionated pattern. It is, therefore, possible that several sHL and sHH irons represent different parental melts.

2.6.3 Crystal-liquid fractionation within the IAB main group

Despite the great chemical diversity within the complex, individual IAB subgroups are characterized by more modest, yet in some subgroups significant, ranges in

siderophile element concentrations. A major question about the IAB complex is then whether or not meteorites within a subgroup can be related to one another by crystal-liquid fractionation processes or some other process, such as mixing. Using the new HSE data for meteorites from each of the subgroups, we re-examine the potential for equilibrium and fractional crystallization, as well as crystal-liquid mixing to have produced the chemical variability observed in the individual subgroups.

Solid metal-liquid metal fractionation, such as fractional crystallization, can produce large chemical variations among the HSE, as observed in magmatic iron meteorites (**Fig. 2.1**). The generation of robust crystal-liquid fractionation models requires knowledge of the partitioning behaviors of the HSE in metallic systems. These behaviors are highly dependent on the initial composition of the melt, particularly with respect to the concentrations of the light elements S, P, and C. The light elements normally behave incompatibly, and so become increasingly enriched in the liquid phase as metallic iron systems evolve. As the concentrations of these elements increase in metallic systems, the general tendency for most of the HSE is to partition more readily into the solid phase (e.g., Willis and Goldstein, 1982; Jones and Drake, 1983; Jones and Malvin, 1990). When the light element contents are taken into account, crystallization of a metallic melt will fractionate the HSE between solid and liquid metal in predictable and systematic ways. Rhenium, Os, Ir, and Ru normally behave compatibly, Pt can behave either compatibly or incompatibly, and Pd and Au typically behave incompatibly (e.g., Chabot and Jones, 2003).

For the modeling conducted here, the solid metal-liquid metal D values were calculated using a “parameterization method” that uses empirical parameters derived

from experimental partitioning data (supplementary material; Jones and Malvin, 1990; Chabot and Jones, 2003; Chabot et al., 2014). In brief, the parameterization depends on the mole fractions of S, P, and C (X_S, X_P, and X_C); an "Fe domains" variable, which constitutes the availability of light element-free domains into which siderophile elements prefer to partition; and β, which is the slope of the fit to experimental data for a given element on a plot of the natural log of D vs. the natural log of Fe domains. Because the IAB complex is characterized by comparatively high C contents, the parameterization method and modelling were modified to account for C (see Appendix section 4). The main input variables used to calculate D values are, therefore, the initial abundances of S, P, and C. The initial abundances of these light elements were chosen based on a combination of the literature estimates of their concentrations derived from modal mineralogy, and the concentrations which generated D values that can best account for the range of HSE concentrations in the individual subgroups.

As the largest and most chemically complex IAB group, the MG is considered first. Previous estimates of initial S contents in IAB melts are comparatively high, and are based mainly on modal observations pertaining to MG irons, with concentrations ranging from < 9.7 wt. % S, to just below the eutectic composition of the FeNi-FeS system (~31 wt. % S) (Kracher, 1985; McCoy et al., 1993; Wasson and Kallemeyn, 2002). Wasson and Kallemeyn (2002) also estimated P contents to be roughly 0.2 times those of S, based on modal abundance estimates of P and S from high-S MG meteorites. Carbon was estimated to be ~ 0.2 wt. % (e.g., Moore et al., 1969; Buchwald, 1975; Wasson and Kallemeyn, 2002).

2.6.3.1 Crystal segregation modelling of the MG

Wasson and Kallemeyn (2002) proposed a model for the formation of the MG IAB irons based on crystal segregation (CS) to account for most of the chemical variations observed in the suite. Their model begins with impact induced melting of a megaregolith on a porous chondritic parent body to produce a metallic liquid with broadly chondritic relative abundances of siderophile elements. This step is followed by partial equilibrium crystallization of that liquid. The model then assumes the metal crystals are separated from the melt, and the crystals and liquid subsequently re-mixed in varying proportions. The proposed two-component mixing scenario can account for the linear trends defined by siderophile element plots for the MG, such as Au vs. Ni and Au vs. Ga. In the CS model, the liquid metal is assumed to crystallize sufficiently quickly to prevent the separation of metal and silicates that were presumably derived largely from the target, accounting for the presence of silicates in some MG irons. It is also assumed that chemical equilibrium is maintained between the crystals and metallic liquid as crystallization proceeds.

Table 2.3. Initial parameters of the light element contents of metallic melts used in the crystallization models for the MG and sLM subgroups.

IP[a]	S wt. %	P wt. %	C wt. %
MG_{CS}	5.0	1.0	0.2
$MG_{CS\text{-}FC}$	10	2.0	0.05
sLM_{CS}	14	2.8	0.2

[a]Subscripts refer to the model, where CS=crystal segregation and CS-FC=crystal segregation-fractional crystallization in this and subsequent tables.

To re-examine the Wasson and Kallemeyn (2002) model with the new HSE data, we apply the equilibrium crystallization equation (1) to calculate the concentration of a given element in the liquid (C_L) and solid (C_S; where $C_S = D \cdot C_L$) using the initial bulk concentration of the system (C_0), the fraction of crystallized solid (F), and D values where:

$$C_0 = F \cdot D \cdot C_L + (1 - F)C_L \qquad (2.1)$$

Wasson and Kallemeyn (2002) calculated the solid and liquid endmember compositions by assuming 35% crystallization (F = 0.35) before the separation of metal crystals and metallic liquid, and choosing D values that would correspond to the range of abundances observed in the MG. These authors assumed a D_{Ir} of 3.0. To be consistent, we also assumed 35% crystallization. For our CS model, initial S, P, and C contents were iteratively chosen by applying the parameterization of Chabot and Jones (2003) and Chabot et al. (2014) so that D_{Ir} was also 3.0 (IP- MG_{CS}; **Table 2.3**). The parameterization was then used to calculate the corresponding D values for the other HSE (**Table 2.4**). As in Wasson and Kallemeyn (2002), the concentrations of the HSE in the initial system were chosen to be the average of the concentrations present in the MG, excluding low Ir members of the MG. By combining the estimated initial concentrations with the appropriate values for D, and assuming 35% crystallization, equation 1 was used to calculate HSE concentrations in the liquid and solid endmembers (**Table 2.5**). Two-component mixing calculations were then used to generate the mixing line with compositions incorporating 0% to 80% of the solid fraction. The silicates do not have any compositional effect on the model because of their considerably lower HSE concentrations relative to the metal phases.

The CS model works well to describe the linear trends defined by Re vs. Os, Ir, and Pd (**Fig. 2.6**). However, because plots of Re vs. Ru and Pt do not produce linear trends ($r^2 < 0.1$), the CS model alone cannot reproduce the data (**Fig. 2.6**). The scatter in Ru and Pt persists when Au data from Wasson and Kallemeyn (2002) are plotted vs. Ru and Pt, so the scatter is not a result of plotting these elements versus the compatible element Re, rather than the incompatible element Au.

An additional problem with the CS model is that, at least using similar D values as Wasson and Kallemeyn (2002), it cannot account for MG meteorites with low Re, Os, and Ir concentrations (e.g., Hope, Morasko, Sarepta, and Burgavli). Wasson and Kallemeyn (2002) and Pilski et al. (2013) suggested that the iron meteorites with low Re and Ir may have crystallized as a result of local, volumetrically minor fractional crystallization. Choi et al. (1995) also suggested that minor fractional crystallization and mixing contributed to the scatter observed in some trace element distributions in the IAB complex. Consequently, in the next section we assess the effects of late-stage fractional crystallization on this system.

Table 2.4. D values calculated as described in text and supplemental material for trace element modeling using the initial parameters in Table 3.

	IP-MG_{CS}	IP-$MG_{CS\text{-}FC}$ (i)	IP-$MG_{CS\text{-}FC}$ (50)	IP-sLM_{CS}
Ir	3.02	7.37	298	26.5
Re	2.89	6.82	194	19.7
Os	3.46	8.92	413	32.5
Ru	1.75	2.97	28.6	6.13
Pt	1.81	3.96	104	12.6
Pd	0.63	0.691	1.23	0.887

Subscripts refer to the model for which these D values were used. The degrees of fractional crystallization are given in parentheses, where i denotes the initial D values for a given set of initial parameters, and 50 refers to the D values after 50% fractional crystallization. The modelling is not conducted beyond 50% fractional crystallization because, after that point, D values for some HSE grow exponentially to values that are not physically meaningful.

Table 2.5. Initial compositions for trace element modeling of the MG, sLM, and sLL subgroups. Concentrations are ng/g. The solid and liquid endmember concentrations are calculated after 35%, 15%, and 25% crystallization for the MG_{CS} and $MG_{CS\text{-}FC}$, and sLM_{CS} models, respectively. The HSE abundances of the initial melts for each subgroup are taken as the mean of the HSE abundances as described in text.

	Re	Os	Ir	Ru	Pt	Pd
MG_{CS}						
MG mean (high Ir)	256	3032	2948	7012	8113	3612
Solid endmember	446	5636	5214	9719	11450	2611
Liquid endmember	154	1630	1728	5555	6316	4151
$MG_{CS\text{-}FC}$						
MG mean (low Pt)	226	2520	2514	6113	7086	3684
Solid endmember	821	10270	9471	14010	19420	2671
Liquid endmember	121	1152	1286	4719	4910	3863
sLM_{CS}						
sLM mean	30	374	341	492	616	5945
Solid endmember	104	1371	1227	1321	1992	5424
Liquid endmember	5	42	46	216	157	6118
sLL mean	220	2701	2446	4244	5433	4362

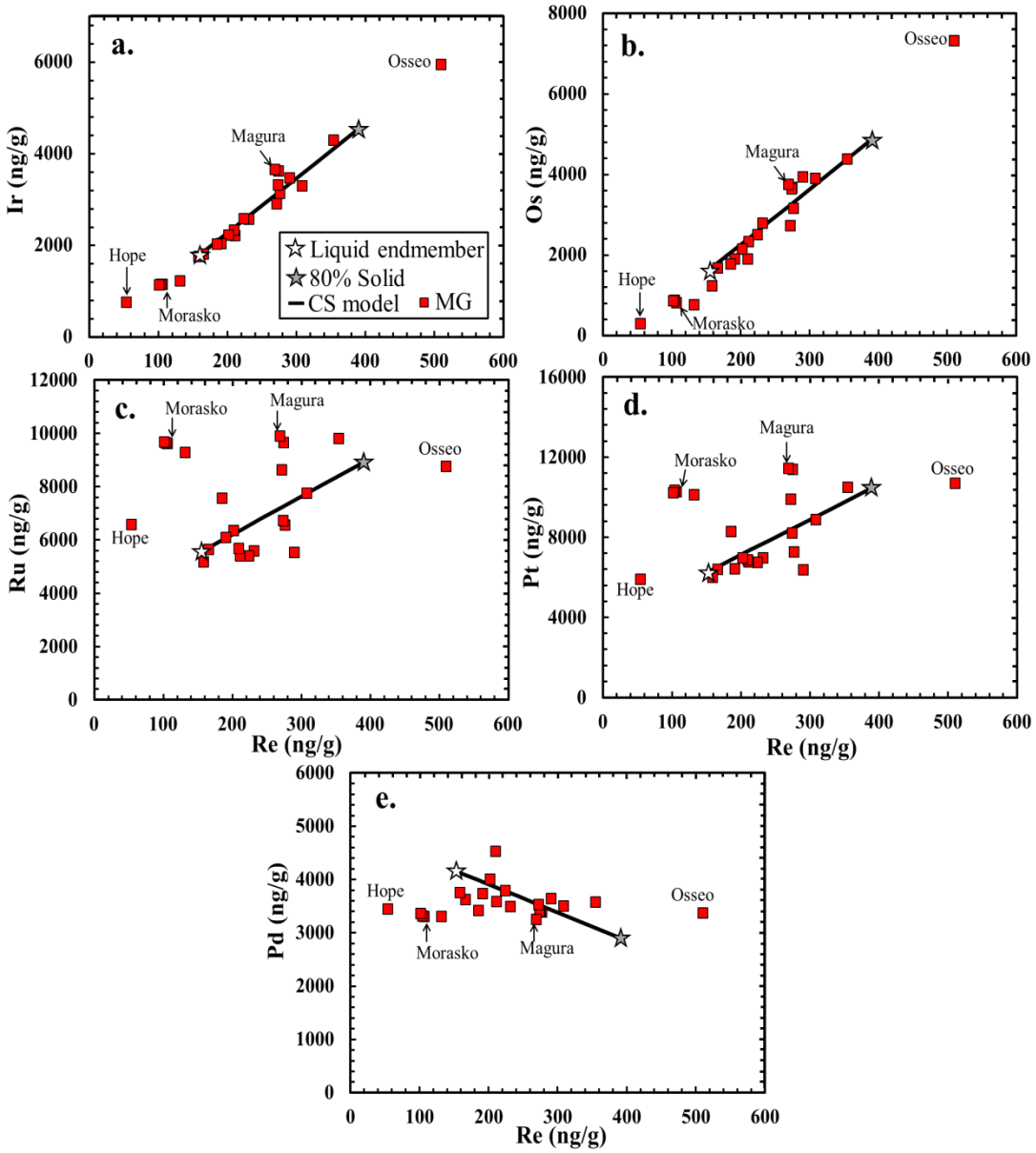

Fig. 2.6. Crystal segregation model of Wasson and Kallemeyn (2002) applied to MG meteorites for (a) Re vs. Ir, (b) Re vs. Os, (c) Re vs. Ru, (d) Re vs. Pt, and (e) Re vs. Pd. In (a, b, and e), the CS model is in general agreement with the observed data, but it cannot account for low Re-Ir-Os samples. In (c-d) the scatter in the Re vs. Ru and Pt plots and the low Re samples cannot be accounted for with the CS model. Wasson and Kellemeyn (2002) suggested the low Re, Os, Ir, samples may be accounted for by minor fractional crystallization (FC – Section 2.6.3.2). The grey star represents a mixture of 80% solid endmember, 20% liquid endmember.

2.6.3.2 Crystal segregation-fractional crystallization hybridized model

The presence of silicate inclusions in many of the MG members has been cited to argue against fractional crystallization (Wasson et al., 1980; Wasson and Kallemeyn, 2002). This argument has been made because fractional crystallization may operate over long periods of time, during which newly formed Fe-Ni crystals are likely physically and chemically removed from the liquid. At the same time, the liquid will be continuously homogenized. Lower density silicates are highly buoyant and, therefore, likely cannot remain entrained in metal on the longer time scales necessary for homogenizing and mixing the melt (e.g., Tomkins et al. 2013).

Although silicates are common in the MG irons with high total HSE abundances, silicates are rare or absent in most of the more chemically fractionated members of the MG (silicate occurrences are noted in **Tables 2.1** and in more detail in **Table A2.2**). For this reason, and because the HSE patterns for the more fractionated members of the MG are broadly similar to patterns produced by extensive fractional crystallization in some magmatic iron groups (**Fig. 2.3a**), an additional stage of fractional crystallization is assessed as a means of generating the chemical variations in the MG that cannot be accounted for by the CS model alone (e.g., the low Re-Os-Ir abundance samples). This is termed the "CS-FC model".

Several variables in the CS model were modified for our CS-FC model. The degree of crystallization before the solids and liquids were separated was set at 0.15, rather than the 0.35 used for the CS model. This was done so that the CS portion of the new model, which used higher D values, would lead to the production of a range of HSE concentrations that included Osseo, but was similar to the lower range achieved by the

Wasson and Kallemeyn (2002) model. For the same reason, our CS-FC model only involves mixtures incorporating 0% to 60% of the solid endmember, as compared to 0-80% solid in the CS model. Another important difference between the CS model and the CS-FC model is that the initial bulk composition of the CS-FC model was taken as the mean of the MG, with the exception of both the low Ir samples and the high Pt samples (**Table 2.5**). This was done because, on plots of Re vs. Pt and Ru, the low Pt and Ru samples define a generally linear correlation with Re. Therefore, by using the lower-Pt mean, the CS model can be fit to the samples that form a linear feature within the scatter.

To model fractional crystallization subsequent to CS, the liquid endmember composition generated by the modified CS model was used as the initial liquid composition, from which the evolving solid and liquid compositions produced by fractional crystallization were calculated. A number of studies have successfully modeled the effects of fractional crystallization on siderophile element abundances to account for the compositional ranges observed in the major magmatic iron meteorite groups (Wasson, 1999; Wasson and Richardson, 2001; Wasson et al., 2007; Walker et al., 2008; McCoy et al., 2011). The fractional crystallization modeling conducted here generally follows the approach that Walker et al. (2008) and McCoy et al. (2011) used to model the IVB and IVA magmatic iron meteorite systems, respectively. Although the interpretation that the IVA group was fractionally crystallized has been called into question by Albarède et al. (2013), the fractional crystallization model of McCoy et al. (2011) can well account for many of the siderophile element variations in the IVA group. As opposed to the equilibrium crystallization in the CS model, the fractional crystallization portion of the

model must account for the systematic way with which D values for the HSE change with the concentration of the incompatible S, P, and C in the crystallizing liquid.

A modified fractional crystallization model is applied, using constant D_S of 0.005, to iteratively calculate X_S, X_P, and X_C, as well as the corresponding D values and β_{SPC} for each of the HSE. The β_{SPC} represents the combined β values for S, P, and C, and collectively accounts for the effects of these elements. The concentrations of the HSE in the evolving liquid are calculated for each 0.1% step of crystallization (n) using the equilibrium crystallization equation (1) above. By iteratively changing F; the light element abundances and, thus, the D values; and by equating C_0 with the C_L at each prior step (n-1), we account for the fractional nature of the crystallization, such that:

$$C_{Ln} = C_{Ln-1}/(F_{n-1} + 1\text{-}F_{n-1}D_n) \qquad (2.2)$$

The solid composition is calculated by $C_{Sn} = C_{Ln}D_n$ at each step.

Several combinations of initial S, P, and C abundances were trialed in an attempt to find the set of D values that generates models that best fit the observed HSE trends. In light of the constraints from the literature outlined above, our preferred model assumes initial S, P, and C contents of 10, 2, and 0.05 wt. %, respectively (IP-$MG_{CS\text{-}FC}$; **Table 2.3**). The corresponding initial D values for the HSE are reported in **Table 2.4**.

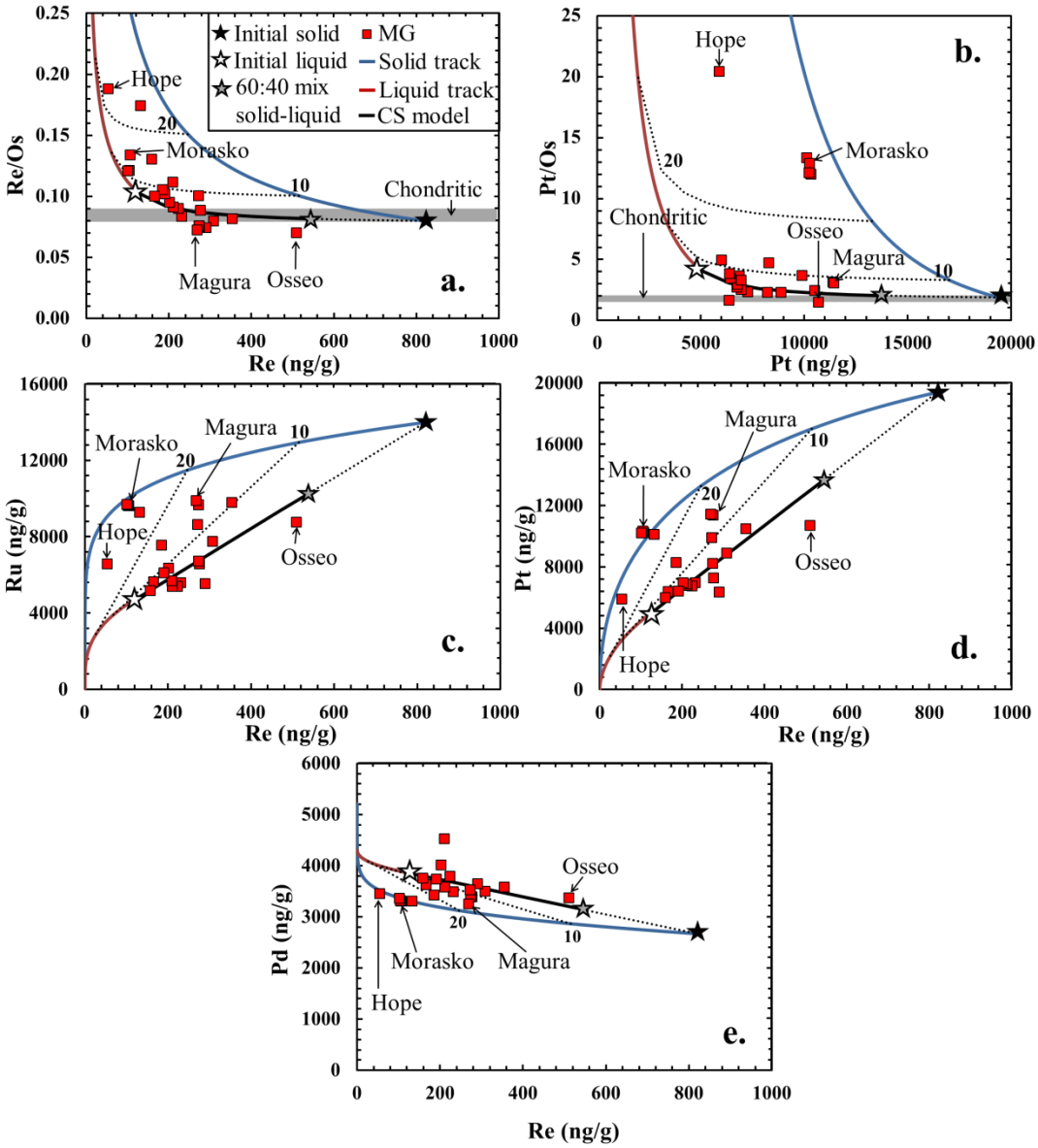

Fig. 2.7. CS-FC model applied to MG iron meteorites using parameterized D values to calculate (a) Re vs. Re/Os, (b) Pt vs. Pt/Os, (c) Re vs. Ru, (d) Re vs. Pt, and (e) Re vs. Pd. The thick black line represents the CS model and the red and blue lines correspond to the evolving solid and liquid compositions generated by the FC model. The dotted lines represent mixtures of coexisting solids and liquids at 0%, 10%, and 20% fractional crystallization. The white star corresponds to the initial liquid composition, which is the composition of the liquid endmember generated by the CS portion of the model. The black star corresponds to the initial solid composition. The grey star represents a mixture of 60 % solid and 40% liquid. All or most IAB-MG iron meteorites plot on or between the solid and liquid evolution tracks, or near the CS mixing line in (a-e). The error bars for Pd, Ru, and Pt are approximately the size of the symbols.

In general, iron meteorites that form by fractional crystallization can sample a solid that was in equilibrium with its associated liquid, a liquid composition trapped within earlier formed solids, or a mixture of the two (Wasson, 1999). Fractionally crystallized iron meteorites, therefore, tend to plot along a solid track that traces the chemical evolution of precipitating solids, a liquid track that traces the chemical evolution of the liquid, or along mixing lines between the two (Cook et al., 2004; Wasson et al., 2007; Walker et al., 2008).

The results of the preferred CS-FC model are shown in plots of Re or Pt vs. other HSE, or HSE ratios (**Fig. 2.7**), and in plots of Au vs. other HSE and moderately siderophile elements reported by Wasson and Kallemeyn (2002), in the supplementary materials. Rhenium/Os and Pt/Os ratios are useful to plot because it is assumed that the metals examined were ultimately derived from a body with a bulk chondritic composition. Thus, it is presumed that the initial metallic melts also had Re/Os and Pt/Os within the range of bulk chondrites. This range is well established through present day $^{187}Os/^{188}Os$ and $^{186}Os/^{188}Os$ of bulk chondrites (Walker et al., 2002). Hope is the most fractionated sample in the MG and is denoted in **Figure 2.7**, along with Osseo, the least fractionated. We also label the data for Morasko and Magura, two moderately fractionated samples, in each plot. Because the CS model is a mixing model, samples that do not plot between the solid and liquid tracks but near the CS mixing line (thick black line in **Fig. 2.7**), are considered to be accounted for by the CS portion of the CS-FC model. In the Re vs. Re/Os plot (**Fig. 2.7a**), all MG samples plot between the solid and liquid tracks, or near the CS mixing line. On Pt vs. Pt/Os and Re vs. Ru, Pt, and Pd plots, most MG samples plot either on or near the solid track, between the solid and liquid

tracks, or near the CS mixing line. In Re vs. Re/Os and Pt vs. Pt/Os compositional space (**Fig. 2.7a-b)**, the Re/Os and Pt/Os of the liquid endmember from the CS model are slightly higher than chondritic. However, because the initial melt in the CS model is the bulk composition of the MG, the condition of chondritic Re/Os can be met. The Pt/Os of the MG average remains slightly suprachondritic (**Table 2.5**). Therefore, the CS-FC model provides good fits for the observed HSE variations in the MG that cannot be accounted for with the CS model alone.

The observation that the hybrid CS-FC model is in good agreement with most of the observed data for the MG is not without caveats. First, we note that the initial S, P, and C contents provide non-unique solutions. Different sets of initial parameters can provide reasonable fits to the data, if the initial compositions and degrees of crystallization are adjusted accordingly. Second, the fits are imperfect for Re vs. Pt, given that several irons plot near the solid and liquid tracks, but resolvably outside of their bounds. This may be due to the use of inaccurate D values, scatter in the Pt abundances caused by some process other than fractional crystallization, inaccurate classification of some irons, or a combination thereof. Third, the degree of fractional crystallization at which certain meteorites are modeled to have crystallized (i.e., their position relative to the solid and liquid tracks and mixing lines) is not always consistent when calculated using different element pairs (e.g., Magura, Morasko). This can be attributed to significant scatter in the relative HSE abundances in the MG, as evidenced by the disordered nature of the HSE patterns in the MG, in which crossing of the HSE patterns is common. Finally, if as discussed above, the Morasko cluster of irons (Morasko/Seeläsgen, Burgavli, and Sarepta) is distinct from the MG (e.g., Pilski et al.,

2013), the low end of the compositional range of the MG can more easily be accounted for by CS alone. However, the CS-FC model, including the initial HSE and light element abundances of the CS portion of the model, are still required to account for the meteorites with high HSE abundances (e.g., Osseo, Magura, and Cranbourne).

We conclude that the compositional range of the MG, the abundant silicate inclusions, and evidence for mixing can be best accounted for by the combined CS-FC model. The importance of the CS model in the crystallization of the MG is in general agreement with that of Wasson and Kallemeyn (2002), but the additional fractional crystallization of some portion of the liquid endmember can better account for the lower Re, Os, and Ir concentrations, as well as the scatter in plots of Re vs. Ru and Pt. The involvement of fractional crystallization is also in agreement with the observation that the more fractionated HSE patterns for some MG samples share similarities with those of some magmatic IVA iron meteorites.

2.6.3.3 The physical scenario for the CS-FC model

The scenario we envision for the CS-FC process to form the MG is as follows: an initial metallic melt, produced either by impact-melting (e.g., Wasson and Kallemeyn, 2002) or during the partial differentiation of an internally heated body (e.g., Benedix et al., 2000), crystallized at equilibrium until ~15% solidification was achieved. At this point, the crystals and liquid were separated by a process, such as filter pressing (Kracher, 1985; Ruzicka et al., 2006), defining the liquid and solid endmember compositions. These endmember components were then re-mixed in varying proportions, re-equilibrated, and the liquid metal crystallized. Re-mixing of the endmember

components could be facilitated either by additional impacts or by density-driven overturn of the melt pool(s). The range of the resulting compositions is represented by the iron meteorites that fall on the initial two-component mixing lines (e.g., Landes), and is consistent with mixed compositions of up to 60% solid (thick black line in **Fig. 2.7**). We speculate that as much as 40% of the remaining liquid endmember was available for subsequent fractional crystallization. Our preferred model suggests that ~30% fractional crystallization of the remaining liquid can account for the samples with lower Ir abundances, and the scatter in plots of Re vs. Ru and Pt (4 to 8 of 23 MG iron meteorites studied here).

The stage at which the shift from equilibrium to fractional crystallization occurs is when some of the liquid endmember is no longer successfully mixed with the rest of the system. This could result from the downward migration of the liquid in the parent body to depths where it was hotter, before mixing of the liquid and solid metal and silicates could occur, or before crystallization could freeze-in silicates. In either case, the largely unmixed liquid endmember portion would have few or no entrained silicates and Fe-Ni crystals. Therefore, the fractionally crystallized samples (i.e., those with low Ir and/or high Pt and Ru) would be expected to contain fewer silicates, unless they were subsequently mixed-in by additional impacts. This is consistent with our survey of silicate occurrences in the MG (e.g., Buchwald, 1975; **Table A2.2**).

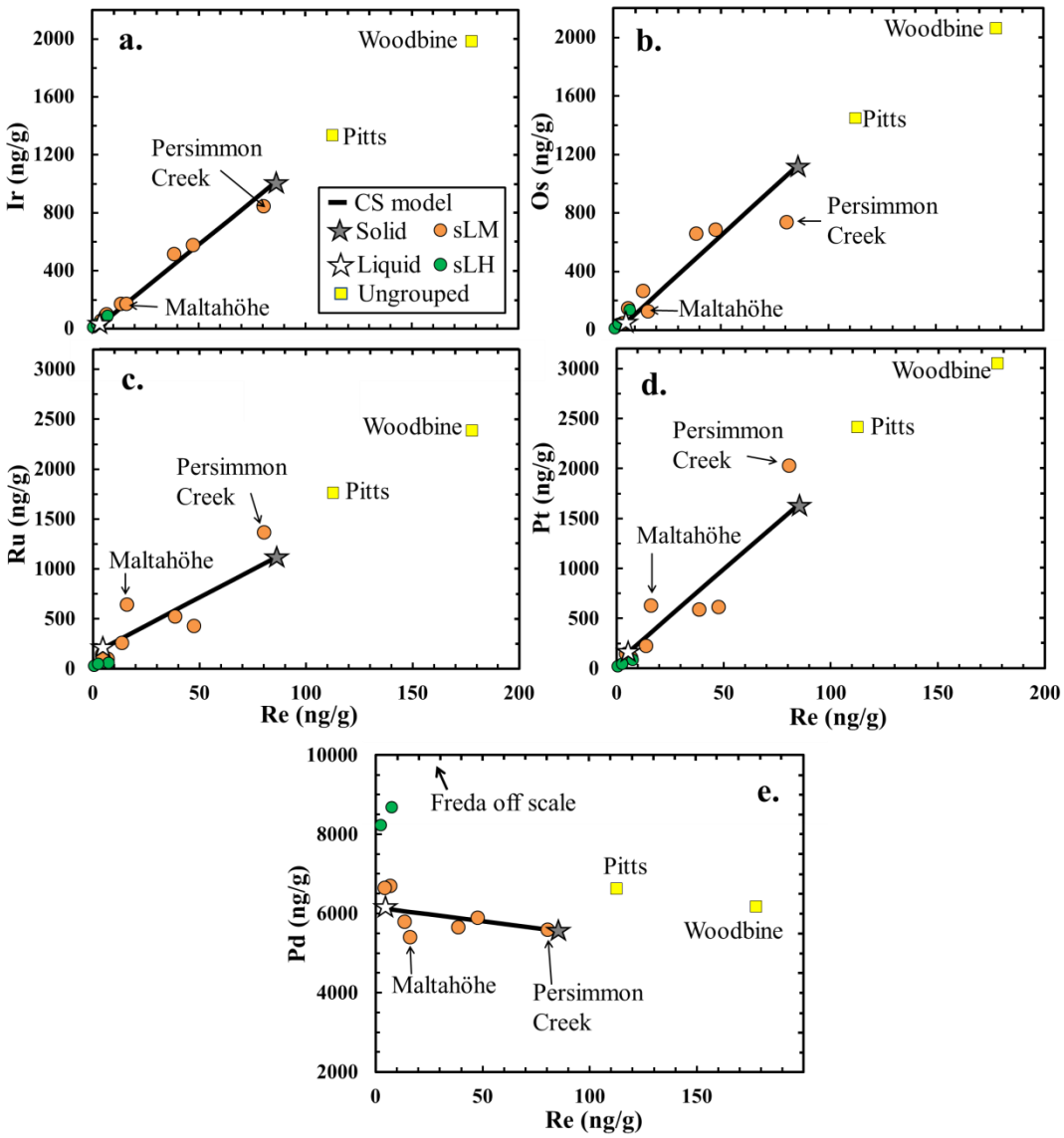

Fig. 2.8. Crystal segregation model applied to the sLM subgroup, using D values consistent with IP-sLM (**Table 4**). The CS model reproduces the ranges and slopes of Re vs. HSE. The grey star corresponds to the 80% solid, 20% liquid composition. The sLH irons and Pitts and Woodbine are plotted because the analagous HSE patterns to those of the sLM subgroup suggest that they formed in a similar manner to the sLM subgroup.

2.6.4 Trace element modeling of the subgroups

The sLM subgroup is characterized by a moderate range in HSE compositions and broadly linear trace element trends on plots of Re vs. HSE, with r^2 values > 0.7 for all but Re vs. Pd (**Fig. 2.8**). When the CS model is applied to the sLM subgroup, the ranges of HSE concentrations and the slopes of the Re vs. HSE are generally reproduced using F = 0.25 and D values consistent with 14 wt. % S, 2.8 wt. % P, and 0.2 wt. % C (IP-sLM$_{CS}$ – **Table 2.3**). The average HSE concentrations of the sLM subgroup are used as the initial composition of the melt. If Pitts and Woodbine are included in the sLM subgroup, lower F and higher total light element contents are required to account for these samples (e.g., F = 0.12; 22 wt. % S, 1 wt. % P, and 0.2 wt. % C). The HSE patterns of the sLM subgroup are unlike those expected from fractional crystallization, and the lack of systematic variation in the relative abundances of Re, Os, and Ir indicates that the chemical diversity in the sLM subgroup was not a result of fractional crystallization. The CS model alone can best account for the range of HSE compositions in the sLM subgroup. The similarity in the HSE patterns between the sLM and sLH subgroups suggests that the sLH subgroup also crystallized by CS.

The relative abundances of HSE in the sLL subgroup are generally chondritic, with a narrow range in absolute HSE abundances (**Fig. 2.3**). The presence of silicate inclusions in most sLL iron meteorites (**Table A2.2**) argues against fractional crystallization, and the limited range in HSE concentrations of the sLL subgroup makes it difficult to assess the applicability of the CS model (**Fig. A2.7**). Qualitatively, the HSE patterns and absolute abundances are similar to those of H chondrite metal fractions (Horan et al., 2009). Therefore, the sLL subgroup most likely represents metal that was

batch melted and extracted from a chondritic precursor, and subsequently crystallized without significant crystal-liquid fractionation.

As noted earlier, it is questionable whether the nominal sHL and sHH subgroups constitute genetically significant groups, but the HSE patterns share some similarities with those of the later crystallized IIAB and IIIAB iron meteorites, suggesting that some of them may have resulted from fractional crystallization. If it is assumed that the irons in the individual subgroups are related, the Re-Os, Pt-Os, and Pd element systems show a larger range of compositions than can be explained by fractional crystallization with the initial light element parameters examined here for either subgroup (**Fig. A2.8**). Therefore, if these irons crystallized by fractional crystallization, as is plausible based on their highly fractionated HSE patterns, two or fewer meteorites from each subgroup are related. Further, silicates are present in the anomalous Sombrerete and in the substantially fractionated Mount Magnet, which may preclude an interpretation of fractional crystallization. Ruzicka et al. (2006) argued for a complex partial melting scenario to account for the unusual characteristics of Sombrerete, which may be applicable to those irons with similar HSE patterns. Though not useful for determining crystallization mechanisms in these subgroups, the modeling here provides additional evidence that the iron meteorites within the sHL and sHH subgroups may not have crystallized from the same parental melt.

2.6.5 Initial melt compositions in the IAB complex

The HSE compositions of the initial melts calculated from the CS-FC model for the MG, the CS model for the sLM subgroup, and the average HSE concentrations for the

sLL subgroup are shown in Fig. 9 and provided in **Table 2.5**. The relative abundances of the MG initial melt are most similar to the LL chondrite Chainpur (**Fig. 2.9**). This implies a chondritic precursor, which is in agreement with previous work (e.g., Benedix et al. 2000; Wasson and Kallemeyn, 2002). Due to the minor fractionation in the sLL subgroup, it can be assumed that HSE abundances in the initial melt of this subgroup were also chondritic.

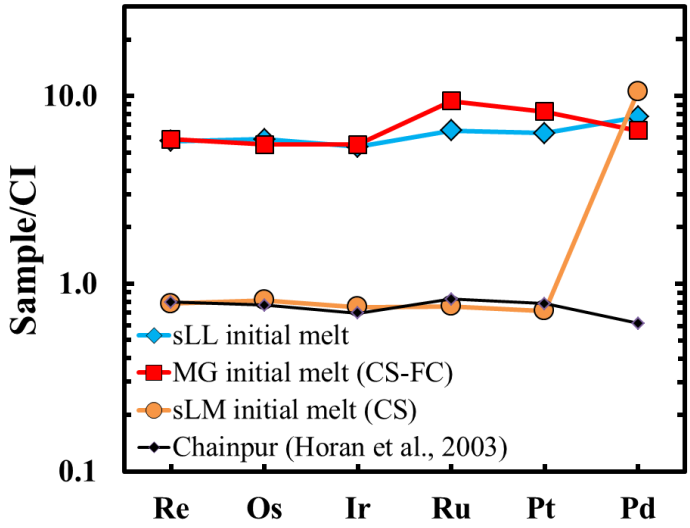

Fig. 2.9. Initial melt compositions of the MG, sLM, and sLL subgroups. The initial melt of the MG is the average HSE concentrations of MG samples, excluding low Ir and high Pt samples, as calculated for the CS-FC model. The sLM initial melt is the average HSE concentrations of all sLM samples, as calculated for the CS model. The sLL initial melt is also taken as the average of the HSE concentrations. The MG and sLL initial melts have broadly chondritic relative HSE abundances, and the MG initial melt is similar to the LL chondrite Chainpur (Horan et al., 2003). The sLM subgroup is enriched in Pd, relative to the chondritic abundances of the other HSE shown here. The HSE abundances of the calculated initial melts are given in **Table 2.5**.

The initial melt composition of the sLM subgroup has both absolute and relative abundances of Re, Os, Ir, Ru, and Pt that are similar to bulk chondrites, but is strongly enriched in Pd. Similar to Pd, the Au abundances reported by Wasson and Kallemeyn (2002) are also enriched. The initial melt of the analogous sLH subgroup was likely

similar. Therefore, if the sLM and sLH subgroups crystallized *via* the CS model, the precursor materials were subjected to some prior nebular or parent body processing to either raise the Pd and Au concentrations, or lower the other HSE concentrations. Because Pd and Au are more volatile than the other HSE, the characteristic HSE patterns in the initial sLM and sLH melts most likely resulted from a volatility-driven processes. The precursor material for these groups may have been a late-stage condensate, which would result in relative and absolute refractory element abundances that were broadly chondritic, but higher abundances of the more volatile Pd and Au. Complementary HSE patterns, in which Pd is depleted in comparison to the chondritic relative abundances of the more refractory HSE, have been observed in early nebular condensates, such as Ca-Al rich inclusions (CAIs) (Archer et al., 2014). Although we do not expect that the sLM and sLH precursor materials and CAIs were condensed from the same materials, the complementary patterns indicate that volatility-driven processes were important in their formation.

2.6.6 Formation of the IAB complex

One unresolved question relating to the IAB complex is what larger scale processes can account for the smaller scale crystallization processes that were modeled above. The mechanisms that were required to generate each of the subgroups, including the heat sources and the nature of the mixing processes, are discussed here.

The spectrum of MG metal compositions can be accounted for by crystal segregation, coupled with fractional crystallization, wherein mixing processes were important. Three important characteristics of MG irons, in the order of shortest to longest

timescales required to generate them are: 1) retention of silicates which, in the MG, are largely confined to the least fractionated irons, 2) evidence for fractional crystallization, and 3) slow sub-solidus metallographic cooling rates (e.g., Herpfer et al., 1994; Goldstein et al., 2013).

These conditions can potentially be met in a scenario that is similar to the one proposed by Benedix et al. (2000) for the IAB complex as a whole. In such a model, the MG metal partially melted and segregated due to internal heating, and the metal slowly crystallized by fractional crystallization in a core or large, sinking, or pooled diapirs. Over a short time period, at least one impact could have re-melted metal, mixed silicates, and allowed for swift crystallization of some portion of the metal; the products of which were finally reburied to cool slowly sub-solidus. However, for models requiring dominantly internal heating, such as the Benedix et al. (2000) and Kracher (1985) models, fractionally crystallized metal is expected to be more volumetrically significant than is observed for the MG. Further, more fractionated HSE patterns than are observed in the MG would also be expected to result from fractional crystallization of a S-rich core, as proposed by Kracher (1985). Because irons which may have resulted from more extensive fractional crystallization (some ungrouped, sHL, or sHH irons) are not from the same parental melt as the MG, these cannot be invoked to represent a missing fractionally crystallized reservoir. Moreover, evidence from the short-lived radiogenic Hf-W system suggests that the metal-silicate segregation age of the MG meteorite Campo del Cielo was ~5 Ma after the formation of CAIs (Schulz et al., 2012; calculated using the CAI initial $^{182}W/^{183}W$ from Kruijer et al., 2014b). This metal-silicate segregation age is

younger than those of most magmatic iron meteorite groups and is beyond the limit of the ~ 4 Ma effective lifetime of ^{26}Al heating (e.g., Kruijer et al. 2014a).

Our preferred model for the formation of the MG invokes a dominantly external heat source, where initial melting of metal and mixing of silicates was coincident due to an impact event, followed by the processes discussed in section 5.3.3, including partial equilibrium crystallization, filter-pressing enabled separation of liquid and solid, and impact-induced or density-driven mixing of solid and liquid metal and silicates. Finally, fractional crystallization of the remaining, but volumetrically minor, portion of the liquid occurred after it descended into the warmer interior. We envision that the reduced viscosity of the descending melt, due to the lack of suspended solids and higher temperatures, would slow solidification and would allow for fractional crystallization to occur.

The first irons to crystallize must have done so quickly to prevent the separation of metal and silicate, and the paucity of silicate inclusions in the fractionated MG irons indicates that the metallic liquid was separated from silicate material as crystallization progressed. The evidence for fractional crystallization and the relatively uniform, slow sub-solidus cooling rates suggest that the MG meteorites crystallized at greater depth within the parent body and/or were reburied. Therefore, the preferred MG formation model is best explained by impact heating because a dominant external heat source allows events to take place in order of short to long timescale, as would be expected in a relatively simple heating and cooling profile. Further, impact heating provides a mechanism for mixing silicates, liquid metal, and solid metal, and for subsequent reburial.

The presence of silicates and the slow metallographic cooling rates in the sLM and sLL subgroups, along with the observation that CS model can account for the HSE variations in the sLM subgroup and the limited fractionation in the sLL subgroup, indicate that mixing and burial processes were important. For the reasons outlined above for the MG, impact heating is also considered the most likely source of melting for both the sLM and sLL subgroups. We note, however, that the CS-FC model of the MG and the CS model of the sLM subgroup are applicable regardless of the original source of the melt.

Although impact heating is the preferred mechanism by which to generate the initial MG, sLM, and sLL melts, some degree of internal heating is likely. The size of the IAB parent body or bodies is not well constrained, but diameter estimates range from tens to hundreds of kilometers (e.g., Kracher, 1985; Rasmussen, 1989; Benedix et al., 2000). If the IAB parent body(ies) was large enough for heat retention to be effective, ^{26}Al and other short-lived radionuclides could contribute to internal heating, though perhaps not to melting temperatures. Studies of winonaites and silicate inclusions in IAB meteorites indicate that these meteorites experienced heating corresponding to a minimum of grade 6 metamorphism in chondrites (Takeda et al., 2000; Benedix et al., 2000). Because this evidence is from both winonaites and IAB irons, this heating was likely on a large to global scale. Keil et al. (1997) and Davison (2013), however, concluded that impact heating is not efficient on global scales. For example, for a 100 km diameter, 20% porous body, Davison et al. (2013) concluded using Monte-Carlo simulations that heating resulting from all the impacts that occurred over a 100 Ma period can raise the global average temperature of a body by a maximum of only ~ 35 K without disrupting the

body. If a disruptive event occurred, the globally averaged temperature increase can be up to 1000 K. The more likely low velocity, oblique impacts expected for planetary bodies early in solar system history probably resulted in smaller global temperature increases. These authors did not account for heating from ^{26}Al and assumed an initial temperature of 300 K. The size and porosity used by Davison (2013) are likely applicable to the size and initial porosity of the IAB parent body(ies), as 20% porosity is intermediate between the porosity of chondritic meteorites and that estimated for most asteroids (Britt et al., 2002).

It, therefore, seems unavoidable that internal heating played some role, if only to warm the parent body to metamorphic temperatures such that impact heating on local scales was more efficient. Moreover, impacts on porous chondritic bodies are also conducive to producing significant volumes of melt, especially locally (e.g., Davison et al., 2010). Thus, if impact heating was the primary heat source, as suggested by the HSE abundances and crystallization modeling discussed above, the MG, sLL, and sLM subgroups originated in locally impact-heated portions of a ≥ 20% porous, large (> 100 km diameter) parent body(ies) where metamorphic temperatures were reached and retained by internal heating from ^{26}Al. Alternately, these subgroups may have originated from a disruptive impact or impacts, in which impact-heating is more efficient.

2.6.7 Diversity among IAB complex subgroups

Potential sources for the variability of IAB complex subgroups are considered here. The similarity of the sLL and MG silicates (e.g., Benedix et al., 2000), and the absolute abundances of many major and trace elements, implies that these meteorites formed by

similar processes from similar starting materials. Variable degrees of impact melting could lead to distinct initial compositions (Choi et al., 1995; Wasson and Kallemeyn, 2002). We postulate that the volume of melt associated with the MG was larger than the sLL subgroup, so that the larger volume of MG melt took longer to cool, and could migrate and fractionally crystallize, whereas the sLL melt simply froze in place. The new results, however, provide no information regarding whether or not the MG and sLL subgroup were generated on the same parent body.

Similarly to the sLL subgroup and MG, the sLM and sLH subgroups may have originated in multiple impact-generated melt pools. In the case of these subgroups, it is likely they formed on one or more parent bodies which were not shared with the MG. This is because the initial sLM and sLH melts were likely non-chondritic (**Fig. 2.9**), and the light element abundances were potentially higher than in the MG.

The siderophile element evidence and modeling outlined above is most consistent with the formation of most IAB subgroups in separate impact-generated melts, in agreement with Wasson et al. (1980), Wasson and Kallemeyn (2002), and Tomkins et al. (2013). Evidence for different parental melts for the IAB complex subgroups has several implications for the possibility that the IAB complex was sourced from multiple parent bodies. Because the IAB subgroups are so diverse in terms of their relative and absolute siderophile element abundances, and may have crystallized in distinct light element regimes, it is unlikely that all IAB complex subgroups originated on the same asteroid-sized parent body.

This possibility can be tested using isotopic genetic tracers (e.g., O, Mo, Ru – Clayton and Mayeda, 1996; Dauphas et al., 2002a; Greenwood et al., 2006; Franchi,

2008; Chen et al., 2010; Burkhardt et al., 2011; Fischer-Gödde et al., 2015). Isotopic data in these and other genetically useful isotope systems are limited to one or two meteorites for most IAB subgroups excluding the MG, sLL subgroup and ungrouped IAB irons. For example, Carlton (sLM) and Dayton (sLH) have a similar Mo isotopic composition and $\Delta^{17}O$, respectively, to other IAB irons (Clayton and Mayeda, 1996; Burkhardt et al., 2011). Sombrerete and Magnesia (sHL), respectively, have a distinct $\Delta^{17}O$ and Mo isotopic composition from other IAB irons (Clayton and Mayeda, 1996; Dauphas et al., 2002a). Thus, it is likely that some sHL subgroup irons are genetically unrelated to the MG, whereas the existing isotopic data for sLL, sLM and sLH meteorites are permissive, but not confirmation, of a common parent body with the MG. No genetic isotope data have been published for sHH subgroup irons.

2.7 Conclusions

Multiple formational modes are represented in the IAB complex. Moreover, the models used to constrain the formational processes require different initial compositions and variable light element contents to account for the observed HSE ranges of each subgroup. Broadly, this conclusion points to a diversity of compositions and crystallization processes active on a single parent body or a number of similar parent bodies. The HSE abundances reported here, particularly Pd abundances, support the division of the complex into the subgroups suggested by Wasson and Kallemeyn (2002). The variations in the relative and absolute abundances of HSE among the subgroups are consistent with the interpretation that the subgroups originated in different parental melts. Therefore, for future studies to draw conclusions about the IAB complex, IAB meteorites

should be considered in the context of their subgroup rather than with the complex as a whole.

The Re-Os isotopic systematics of the complex indicate that the HSE abundances of most IAB irons reflect those at the time of crystallization, although minor open system behavior, which likely occurred ≥ 40 Ma after crystallization, is evident in the sLM, sLH, sHL, and sHH subgroups. The conclusion that the IAB subgroups originated in separate parental melts in different locations is supported by the observation that only some subgroups show open system behavior.

The MG of the complex reflects metal that was crystallized by crystal segregation, coupled with fractional crystallization. The initial light element abundances of the system were probably relatively high, with the best-fit crystallization models based on the assumption of ~ 12 wt. % total S, P, and C. The preferred scenario for the formation of the MG is that impact-generated melting initially produced metallic melt, into which silicates were mixed. The melt cooled and mixed quickly at first, freezing silicates in place, but some portion of the melt migrated to warmer depths in the body, where the melt entered a fractional crystallization regime. The scarcity of observed silicates in the more chemically evolved MG irons is consistent with this interpretation.

The most likely formation scenario for the sLL subgroup is an impact-generated melt origin, similar to that of the MG, but the minimally fractionated HSE patterns point to important differences between the volume of the melt, the nature of the impact, or a combination thereof. The relative abundances of the HSE calculated for the initial melts of both the MG and sLL subgroup are roughly chondritic. This suggests that their parent

body or bodies had chondritic bulk compositions with limited nebular or planetary processing of their precursor materials prior to metal-silicate segregation.

In the sLM subgroup, the distinctive HSE patterns and the broadly linear distributions of the relative HSE abundances suggest that it represents irons crystallized by crystal segregation. The sLM subgroup may have crystallized from a system with total initial light element contents significantly higher than those of the MG, between ~17-23 wt. %. The sHL subgroup probably formed in a similar manner to the sLM subgroup, based on the comparable HSE patterns. An impact origin is also considered likely in these subgroups; however, the non-chondritic HSE pattern of the initial melt and the higher initial light element abundances of the sLM system indicate that the precursor materials were unrelated to the MG. The enriched Pd and Au relative to Re, Os, Ir, Ru, and Pt abundances in the sLM initial melt suggest that the sLM precursor materials may represent late-stage condensates. The irons in the sHL and sHH subgroups may have been fractionally crystallized and, in the case of the sHL subgroup, formed on a separate parent body from the MG.

Appendix for Chapter 2

1. Samples

The list of meteorites studied here, along with U.S. national museum numbers (USNM #) and the subgroup designated by Wasson and Kallemeyn (2002) is given in **Table A2.1**. The occurrence of observed silicate inclusions in the IAB complex is tabulated in **Table A2.2**.

2. Isotope dilution data discussion

Rhenium data are within ± 20% of those reported by Wasson and Kallemeyn (2002) and Pernicka and Wasson (1987), with the exception of 11 out of 58 samples (**Table A2.3**). About half of the samples are within ± 10%. For Ir, the data are typically within ± 10% of those reported by Wasson and Kallemeyn (2002), with 11 out of 58 samples lying outside the 10% range. Most Pt concentrations are within ± 20% of previously reported data for 37 samples (Wasson and Kallemeyn, 2002; Pernicka and Wasson, 1987; Hoashi et al., 1993) with 12 samples of the 37 outside that range. Osmium, Ru, and Pd data are also generally in agreement with literature data. Out of 18 samples with previously reported data for Os, 12 are within ± 10% of the literature data (Crocket, 1972; Pernicka and Wasson, 1987; Hirata and Masuda, 1992; Shen et al. 1996). For Ru, 10 out of 16 samples are within ± 20% of previously reported data (Pernicka and Wasson, 1987; Hoashi et al., 1993). Palladium abundances are within ± 20% for 13 of 19 samples with previously published data (Goldberg et al., 1951; Smales et al., 1967; Hoashi et al., 1993).

The largest offsets with respect to the Re and Ir concentrations are for Sarepta. The concentrations determined here are lower by ~ 120%, compared with data reported by Wasson and Kallemeyn (2002). Other large offsets are for Anoka, with a Pt concentration ~ 140% lower than that reported by Wasson and Kallemeyn (2002), and Mount Magnet, with an Os concentration ~140% lower than that reported by Crocket (1972).

The maximum percentage difference for duplicates from their average value is 12.8, 8.8, 9.9, 22.8, 12.8, and 14.1 % for Re, Os, Ir, Ru, Pt, and Pd, respectively. The maximum percent differences of the HSE/Ir ratios are 13.1, 7.1, 23.2, 14.1, and 17.6 % for Re/Ir, Os/Ir, Ru/Ir, Pt/Ir, and Pd/Ir (**Table A2.4**). Duplicates of Shrewsbury were not well reproduced with respect to Ru, and it was hypothesized that one or both of the analyses were affected by an isobaric interference as measured using the ICP-MS. To test for this, the Ru cuts for each Shrewsbury sample were re-measured by N-TIMS, which utilized a different ionization process unlikely to reproduce isobaric interferences for the same masses. The N-TIMS results, however, were identical within uncertainty to those from the ICP-MS, so the differences are attributed to real differences between the sample aliquots. The differences between duplicates are attributed in part to variable inclusion of silicate material, and to mm-cm scale sample heterogeneity, as discussed in the main text.

3. Classification of IAB complex iron meteorites

An additional discrimination diagram for the IAB subgroups using a plot of Pd vs. Ru is given in **Fig. A2.1**. The plot of Pd vs. Ru discriminates the MG and sLL subgroup particularly well. Further, this plot indicates that combining the Pd data reported here and

Au and Ni data from separate pieces of the meteorites that was obtained using different techniques (i.e., isotope dilution vs. instrumental neutron activation analysis – Wasson and Kallemeyn, 2002) to evaluate the classification within the IAB complex, as was done in the main text, does not introduce any significant scatter or bias which would make the subgroups more difficult to distinguish.

4. Calculation of D values

We employed a method to calculate D values based on experimental partitioning data and the parameterization method of Jones and Malvin (1990), Chabot and Jones (2003), and Chabot et al. (2014). The fractional crystallization model we employed utilizes the systematic way with which solid metal-liquid metal partition coefficients (D) change with the concentration of incompatible light elements (e.g., S, P, and C) in the crystallizing liquid. From Chabot and Jones (2003), D values are calculated by

$$\frac{1}{D} = \frac{[\text{Fe domains}]^{\beta}}{D_0} \tag{A2.1}$$

where "Fe domains" is a variable constituting the availability of light element-free domains into which siderophile elements prefer to partition. In the Fe-Ni-S-P-C system, Fe domains can be expressed as:

$$\text{Fe domains} = \frac{1-2X_S-4X_P-4X_C}{1-X_S-3X_P-3X_C} \tag{A2.2}$$

where X_i is the mole fraction of each element, and the constants are based on the expected speciations for S, P, and C in the system (e.g., FeS, Fe_3P, and Fe_3C). In equation 1, D_0 is D in the endmember, light element-free system, and β is the slope of the fit to experimental data on a plot of the natural log of Fe domains vs. the natural log of D. The initial versions of the model only took into account S and P contents, due to the paucity of experimental Fe-Ni-C data. However, Chabot et al., (2006) found that parameterization in the Fe-Ni-C system is different from that in the Fe-Ni-S and Fe-Ni-P systems.

In IAB complex iron meteorites, the presence of cohenite suspended in the metal, and graphite and cohenite associated with troilite nodules, suggests C was present in the initial metallic melt or melts (Buchwald, 1975; Wasson and Kallemeyn, 2002). Wasson and Kallemeyn (2002) suggested the initial IAB melt or melts may have had ≥ 0.2 wt. % C, based on estimates of C contents from Moore et al. (1969), Lewis and Moore (1971), and Buchwald (1975). Therefore, incorporating the effects of C on trace element partitioning is critical for this group, and the fractional crystallization model had to be modified to take C into account.

In order to modify the model for C, the weighted average of β_S, β_P, β_C, which are constants specific to each trace element in the individual Fe-Ni-S, Fe-Ni-P, and Fe-Ni-C systems, was calculated using the relative proportions of the light elements, where,

$$\beta_{SPC} = \left[\frac{2X_S}{2X_S+4X_P+4X_C}\right]\beta_S + \left[\frac{4X_P}{2X_S+4X_P+4X_C}\right]\beta_P + \left[\frac{4X_C}{2X_S+4X_P+4X_C}\right]\beta_C \qquad \text{(A2.3)}$$

and X_S, X_P, and X_C are the mole fractions of S, P, and C (Jones and Malvin, 1990; Chabot and Jones 2003; Chabot et al., 2014). β_{SPC} is then substituted for β in equation 1. Further, β_{SPC} must be calculated iteratively for the evolving composition of the crystallizing melt. D_0 and β_S, β_P, and β_C values for each element were taken from Chabot et al. (2014).

One complexity of the Fe-S-P system is that D(P) increases with both increasing S and P in the melt (Chabot and Jones, 2003). Likewise, the D(C) may change with increasing S and P, leading to an increase or decrease of C in the melt. Currently, however, there are no experimental data specifically addressing the partitioning behavior of C in the Fe-S-C and Fe-S-P-C systems. Nevertheless, by using a series of phase diagrams from the Fe-C (Okamoto, 1992) and Fe-C-S systems (Ohtani and Nishizawa, 1986), we can roughly estimate D_0, β_C, and β_S for C, similar to what was done for Cu and Ru in Chabot et al. (2006).

First, to determine D_0 and β_C for C, D values are calculated from C abundances in co-existing solid and liquid from the Fe-C binary phase diagram (Okamoto, 1992). These D values vs. Fe domains give D_0 and β_C as the intercept and slope of the line (0.37 ± 0.10 and -0.83 ± 0.51, respectively) (**Fig. A2.2a**). Using this parameterization, the relevant portion of a calculated Fe-C phase diagram can be generated as a check (**Fig. A2.2b**). To determine β_S, vertical sections at different S contents (0.01 - 0.06 wt. %S) of the ternary Fe-S-C phase diagram from Ohtani and Nishizawa (1986) are used to obtain average D values from each vertical section. These average D values plotted vs. Fe domains give an imprecise β_S of $\sim 59 \pm 28$. The uncertainty for this parameter is likely even larger than stated due to the limited range of S concentrations available to be used in the calculation.

Fortunately, the model is not very sensitive to this parameter. Average D values were used, as opposed to the slope of D vs. Fe domains in each vertical section, in order to isolate the influence of S on the system.

To summarize the estimates generated using these phase diagrams, the partitioning of C is dependent on its own concentration in the melt and on that of S. Carbon behaves incompatibly (D_0 ~ 0.4), but as C contents increase in the melt, C becomes slightly more compatible, so that D(C) increases as crystallization progresses. With S, C still behaves incompatibly, and as C and S contents increase in the melt, C becomes more incompatible, so that D(C) decreases as crystallization progresses. In most iron meteorite systems, C will not be present without S, so the minor effect of its own abundance on its partitioning can likely be neglected, and C can be thought of as an incompatible element, which only becomes more incompatible as crystallization proceeds. Here, both the effects of C and S on the partitioning of C are taken into account. We have not assessed the effects of P on the partitioning of C, or of C on the partitioning of P, due to the paucity of experimental data in the Fe-P-C system. We have, therefore, assumed that S exerts the largest influence on the partitioning of both.

Synthesizing the effects of C, S, and P, **Figure A2.3** shows the HSE patterns that would be expected to result from fractional crystallization of an Fe-Ni liquid with initially chondritic relative HSE abundances in both high and low S and C regimes, as well as an intermediate S, C, and P regime for reference.

An alternative method for estimating D values for some of the HSE utilizes the slopes of linear correlations of Ir vs. HSE on log-log plots. The D values for the HSE are calculated relative to the D values of Ir, which are parameterized using the methods of

Jones and Malvin (1990) and Chabot and Jones (2003). This method was used by Walker et al. (2008) and McCoy et al. (2011) for modeling of the IVB and IVA iron meteorite groups. The slope-based D values yielded better fits to the observed data for the IVB and IVA iron meteorites than those obtained using parameterization methods (Walker et al., 2008; McCoy et al., 2011). In the MG, however, the slope-based method is only viable for Re and Os (supplementary materials). The other HSE do not correlate with Ir, either due to limited variation relative to Ir (Pd), or because of considerable scatter along the trends (Ru, Pt) (**Fig. A2.4, Table A2.5**). Therefore, only parameterized D values are used in the calculations in the main text. **Table A2.5** also shows the regressions for the sLL and sLM subgroups.

5. Additional trace element models of the IAB subgroups

Because most of the HSE modeled for the crystal segregation-fractional crystallization model (CS-FC) are incompatible, we also show the results of the model relative to Au, which behaves incompatibly in plots of Au vs. HSE (**Fig. A2.5**) and Au vs. Ni, Ga, As, and W (**Fig. A2.6**), where Au, Ni, Ga, As, and W data are from Wasson and Kallemeyn (2002). The fit of the CS-FC model is more variable for these elements, where several MG irons are not accounted for by the model on the plot of Au vs. Re, but all are accounted for on the plot of Au vs. Ru, As, and W. This is potentially due to the use of inappropriate D values for Au. When higher C contents (0.2-0.5 wt. %) are used, the range in Au abundances is better accounted for. However, because we constrained the model using the HSE, and because the fits for Re vs. Pt and Pd were worse with higher C,

the fit for Au is expected to be sub-optimal. Even so, the CS-FC model accounts for the variations in the majority of the elements considered here for the MG.

The CS model was applied to the sLL subgroup in and attempt to account for its modest HSE variations (**Fig. A2.7**). The sLL average HSE compositions were used as the initial melt composition, 35% crystallization was used for F, and D values corresponding to 2 wt. % S, 0.4 wt. % P, and 0.2 wt. % C were applied. However, the limited range in the HSE makes it difficult to assess the utility of this model for the sLL subgroup as discussed in the main text.

The fractional crystallization modelling of the sHL subgroup is shown on plots of Re vs. HSE, with the sHH and sLM subgroups for reference (**Fig. A2.8**). The D values used correspond to 13 wt. % S, 1.8 wt. % P, and 0.15 wt. % C. For these models, no combination of light element concentrations and initial HSE abundances could account for the full range of HSE abundances in either the sHL or sHH subgroups. Primarily, the abundances of Pt and Pd could not both be accounted for in either the sHL or sHH subgroup, and neither could the Re and Os abundances of Mount Magnet in the sHH subgroup. Further, these models require a non-chondritic Re/Os (**Fig. A2.8a**) for the HSE concentrations of the initial melt, and that Pd was enriched relative to the other HSE.

Table. A2.1. List of samples with USNM# where available.

Meteorite	USNM #	Group	Meteorite	USNM #	Group
Allan Hills A77283		MG	Maltahöhe	6482	sLM
Allan Hills A80104		sHH	Mertzon	1435	Un
Anoka	6930	sLM	Morasko	6915	MG
Bahjoi	1807	sLL	Mount Magnet	1746	sHH
Balfour Downs	3202	sLL	Mundrabilla		Un
Ballinger	824	MG	Mungindi	2944	sLM
Bischtube	2666	sLL	New Leipzig	1210	MG
Bogou	2245	MG	Odessa	639	MG
Burgavli	1879	MG	Osseo	925	Unc
Caddo County	6381	Un	Persimmon Creek	318	sLM
Campo del Cielo	5615	MG	Pine River	1421	sLL
Canyon Diablo		MG	Pitts	1378	Un
Carlton	2708	sLM	Quarat al Hanish	6176	sHL
Chebankol	1731	sHL	Sardis	1381	Unc
Comanche	2246	sLL	Sarepta	455	MG
Cranbourne	537	MG	Seeläsgen	3061, 2206	MG
Dayton	1592	sLH	Seligman	1761	MG
Deport	2267	sLL	Seymour	4518	MG
Edmonton (KY)	1413	sLM	Shrewsbury	422	sLL
Elephant Moraine 84300		Un	Smithville	3373	MG
Freda	1342	sLH	Sombrerete	5870	sHL
Georgetown		Un	Tazewell	3089	sLH
Goose Lake	1332	sLL	Theil Mountains 91725		Un
Hope	3477	MG	Toluca	460	sLL
Jenkins	3201	MG	Waterville		Un
Kofa	7009	sHH	Woodbine	2169	Un
Lamesa	6250	sLM	Yenberrie	607	MG
Landes	5663	MG	Youndegin	1752	MG
Magura	2893	MG	Zagora		Un

Table A2.2. Silicate occurrences in the IAB complex irons studied here and MG irons studied by Wasson and Kallemeyn (2002). Observations of silicates and other minerals, excluding troilite, recorded in Buchwald (1975), Benedix et al. (2000), McCoy et al., 1993), and Ruzicka et al. (2006) are given in the columns labeled "Minerals". Nickel data and additional Re and Ir data are from Wasson and Kallemeyn (2002). Samples are organized in order of decreasing Ir abundances. Samples in bold in the MG are those examined here. Bolded minerals are assemblages that include at least one observation of silicate.

Sample	Minerals[a]	Ni†	Re	Ir	Sample	Minerals[a]	Ni†	Re	Ir
IAB main group					**IAB main group (cont.)**				
Zapaliname	-	6.71	182	5900	**Canyon Diablo[a]**	**Co,H,Cg,G,S**	**6.93**	**232**	**2560**
Hasparos	-	6.61	506	5590	ALHA76002	-	6.8	287	2560
Wolsey	-	6.62	447	4860	Idaho	-	7.23	262	2540
Duel Hill 1973	Co	6.70	391	4320	Burkett	Co,G	6.96	267	2480
Landes	**S [ACS]**	**6.55**	**355**	**4293**	Jenny's Creek	Co,G,Gc	6.88	272	2410
Yardea	Co, G	7.02	369	4210	**ALHA 77283**	Co	**7.28**	**210**	**2327**
Soledade	-	6.78	393	3900	Mount Ayliff	Co,G	7.35	262	2240
Lueders	**S [ACS]**	7.02	297	3880	**Youndegin**	**H,G,Gc,Co,S**	**6.83**	**202**	**2217**
Magura	**Co,G,Gc,S**	**6.44**	**269**	**3648**	PGPA77006	-	7.24	224	2210
Cranbourne	Co,G	**6.82**	**275**	**3614**	**Jenkins**	**Co,G,S**	**6.92**	**212**	**2207**
Pecora Escarpment 91003	-	7.08	271	3610	Vaalbult	**Co,S**	6.83	281	2140
Yenberrie	co	**6.82**	**291**	**3463**	Pittsburg	Co	6.54	234	2120
Uruacu	-	6.43	327	3360	NWA 854 (Ziz)	-	6.75	210	2070
Campo del Cielo	**H,Co,G,S [ACS]**	**6.68**	**274**	**3308**	Bolivia	Cg	6.7	226	2060
Seligman	Co,G,Gc	**6.67**	**309**	**3293**	Bohumilitz	Cg,G	7.28	218	2040
Ballinger	Cg	**6.78**	**280**	**3137**	**Smithville**	**H,Co,G,Gc,S**	**6.92**	**191**	**2028**
Copiapo	**H,G,S [ACS]**	7.29	287	3050	**Sardis**	Co ,G	**6.73**	**186**	**2023**
Kaalijarv	Co	7.55	246	3040	Rifle	-	7.05	211	1940
Oscuro Mountain	G(Co)	6.89	283	2970	Rosario	Co	7.06	191	1900
Gladstone (iron)	**H,Co,G,S**	6.56	321	2950	Wichita County	**Cg,G,S**	6.79	210	1900
Black Mountain	**S**	6.42	338	2920	Gahanna	-	6.93	232	1870
New Leipzig	none	**6.68**	**272**	**2904**	**Seymour**	H,Co,G	**6.78**	**167**	**1807**
Lexington County	G,Gc,Co	6.84	293	2860	Nantan	-	6.88	168	1790
Linwood	**Gc,S [ACS]**	6.71	301	2850	Fairfield, OH	-	6.72	161	1790
Coolac	**Co,G,S**	6.99	295	2840	**Bogou**	**H,Co,G,S (assoc. w/ troilite)**	**7.33**	**159**	**1747**
Silver Crown	none	7.16	289	2810	Deelfontein	Co,G	7.03	150	1560
Cosby's Creek	Co,G	6.47	344	2720	Jaralito	-	6.66	166	1500
Chuckwalla	-	6.59	243	2720	Casey County	Co	6.97	155	1350
Pooposo	none	7	246	2680	**Burgavali**	G	**6.64**	**132**	**1217**
Ocotillo	**S [ACS, NCS]**	7.09	256	2610	**Seelasgen**	Co,G	**6.59**	**104**	**1143**
Ozren	**S**	7.09	204	2590	**Morasko**	Co	**6.76**	**107**	**1141**
Dungannon	(Co),G	6.95	242	2580	**Sarepta**	Co	**6.59**	**101**	**1131**
Odessa	**H,G ,Gc,Co,S [RGR]**	**7.19**	**224**	**2572**	**Hope**	**Co,G,S (rare)**	**7.06**	**54**	**753**
Itapuranga	-	6.52	242	2570	La Serena	-	7.62	<70	550
MG continued					Zaffra	G	7.31	<30	62

(continued)

Table A2.2. cont.

Sample	Minerals[a]	Ni†	Re	Ir	Sample	Minerals[a]	Ni†	Re	Ir
IAB sLL					**IAB sHL**				
Pine River	**G,S [ACS]**	8.04	268.1	3085	Quarat al Hanish	-	12.75	86.75	957.6
Shrewsbury	**G,Gc,S,Cg**	8.53	226.5	2729	Chebankol	none	9.17	8.632	102.9
Comanche	**G,S**	8.24	226.4	2614	Sombrerete	**S**	9.84	6.099	73.80
Bahjoi	**H,Co,G,S**	7.94	220.2	2429	**IAB sHH**				
Toluca	**H,Co,G,S [RGR]**	8.02	215.9	1962	Kofa	none	18.39	8.218	99.22
Deport	H,Co,C,G	8.05	215.8	2429	ALHA 80104	-	15.86	7.584	90.42
Balfour Downs	**Cg,G,S**	8.38	212.0	2302	Mount Magnet	**S**	14.57	0.6252	6.176
Bischtübe	**H,Co,G,S**	7.78	201.6	2326	**IAB ungrouped**				
Goose Lake	**H,Co,G,S**	8.24	188.2	2139	TIL 91725	**S [ACS]**	8.04	285.3	3244
IAB sLM					Caddo County	**S, [ACS, NCS]**	9.42	254.0	2515
Persimmon Creek	**G, S [SR, ACS]**	13.79	80.73	840.2	Zagora	**S [SR, ACS]**	9.36	243.0	2655
Mungindi	H	11.86	47.86	570.3	Mertzon	**S**	9.08	188.0	2160
Edmonton (KY)	H	12.90	38.86	508.4	EET 84300	**S [ACS]**	10.11	183.4	2161
Maltahöhe	**S (McCoy et al. 1993)**	11.40	16.42	165.0	Woodbine	**Co, G, S [SR, ACS]**	10.05	177.9	1984
Anoka	C	11.80	13.84	167.9	Pitts	**Co, G, S [SR]**	12.81	117.9	1244
Carlton	**H, S (McCoy et al. 1993)**	13.23	7.113	92.49	Mundrabilla	**G [SR]**	7.50	81.62	998.0
Lamesa	-	13.28	4.582	48.14	Waterville	G	7.63	34.86	366.8
IAB sLH					Georgetown	**S**	9.03	17.33	190.4
Tazewell	Co,H	17.06	7.512	87.84	**IAB unclassified-MG**				
Dayton	**G?, S (McCoy et al. 1993)**	17.10	2.594	31.37	Osseo	Co, G	6.71	510.3	5934
Freda	Co,H,G	23.21	0.6164	7.500	Sardis	Co, G	6.73	185.3	2022

[a] Abbreviations for the types of minerals are the same as in Buchwald (1975). In brackets are the descriptions of the silicates from Benedix et al. (2000). From Buchwald (1975): C = carbides, Co = cohenite, Cg = carbide under decomposition to graphite, H = haxonite, G =graphite, Gc =graphite with distinct cliftonitic development, and S =silicates. From Benedix et al. (2000): ACS = angular, chondritic silicates; NCS = nonchondritic silicates; SR = sulfide-rich; RGR = rounded, graphite-rich; and PB = phosphate bearing. None indicates that no minerals (excluding troilite) were observed. The dash indicates that no observational data were available.

Table A2.3. Comparison of HSE data obtained by isotope dilution with literature data.

Sample	Re	Re (literature)	Os	Os (literature)	Ir	Ir (literature)	Ru	Ru (literature)	Pt	Pt (literature)	Pd	Pd (literature)
IAB main group												
Landes	354.8	349[a], 320[d], 349.4[k]	4368	4210[k]	4293	4330[a], 4260[d]	9805		10500	12500[a]	3581	
Seligman	308.7	327[a], 330[d], 296.7[m]	3891	3726[m]	3293	3290[a], 3300[d]	7754		8886	7200[a], 7200[d]	3502	
Yenberrie	290.6	319[a], 320[d], 303.6[m]	3926	4075[m]	3463	3500[a], 3500[d]	5536		6359	5700[a], 5700[d]	3647	
Ballinger average	277.0	320[a], 240[d]	3145		3124	3200[a], 2210[d]	6561		7266	6400[a], 7200[d]	3392	
Cranbourne	275.0	168[a], 185[b], 180[d]	3670	1830[b], 1770[l]	3614	1730[a], 1700[d], 1430[l]	9662	5800[b], 3770c	11380	4600[b], 5040[c]	3398	6970[c], 4800[e]
Campo del Cielo	274.1	370[a], 320[d]	3632	3800[f], 4620[l]	3308	3550[a], 3190[d], 3900[f], 3150[l]	6725	5120[c], 8100[f]	8213	7600[a], 6700[d], 8640[c], 9700[f]	3403	3330[c]
New Leipzig	272.4	281[a], 280[d], 269.9[m]	2723	2715[m]	2904	2950[a], 2830[d]	8626		9898		3527	
Magura	269.2	327[a], 360[d], 278.8[m]	3743	3813[m]	3648	3650[a], 3600[d]	9892		11430		3254	
Canyon Diablo	231.7	253[a], 198[b], 250[d], 209.7[j], 243.7[k]	2780	2200[b], 2100[f], 1982[j], 2513[k]	2560	2420[a], 2180[b], 2320[d], 2000[f]	5579	5700[b], 5240[c], 5200[f], 5400[h]	6959	6100[a], 5800[b], 6200[c], 6200[d], 8000[f]	3494	4400[c], 3600[e], 3980[g]
Odessa	224.3	242[a], 245[b], 240[d], 231.5[j], 239.8[k]	2501	2520[b], 2428[j], 2373[k], 1830[l]	2572	2380[a], 2440[b], 2400[d], 1600[l]	5392	4700[b], 4290[c], 4900[h]	6749	5800[a], 5500[b], 5670[c], 6200[d]	3795	4210[c], 4150[g]
Jenkins	211.6	247[a], 250[d]	2327		2207	2160[a], 2160[d]	5403		6772		3585	
ALHA 77283	210.2	226[a], 260[d]	1891		2327	2160[a], 2040[d]	5687		6867	7000[a]	4526	
Youndegin	202.4	217[a], 220[d]	2134	1800[f]	2217	2150[a], 1900[f], 2150[d]	6354	4710[c], 6100[f]	6960	5400[a], 6860[c], 11500[f], 5400[d]	4010	3240[c], 3900[e]
Smithville	191.4	198[a], 230[d]	1884		2028	1880[a], 1900[d]	6096		6422	5700[a], 5700[d]	3734	
Seymour	166.5	194[a], 190[d]	1673		1807	1740[a], 1670[d]	5636		6383		3627	
Bogou	158.9	194[a], 200[d]	1219		1747	1720[a], 1720[d]	5178		5999	4800[a]	3754	
Burgavali	132.1	162[a], 170[d]	759.2		1217	1190[a], 1180[d]	9283		10120		3305	
Morasko	106.8	124[a], 90[d]	799.0		1141	1110[a], 1100[d]	9612		10260		3306	
Seelasgen	104.3	108[a], 110[d], 106.0[m]	863.4	875.9[m]	1143	1140[a], 1150[d]	9643		10340		3314	3400[e]
Sarepta average	102.0	421[a], 420[d]	847.2		1134	4380[a], 4010[d]	9684		10230		3360	
Hope	54.26	70[a], 50[d]	288.9		753.1	750[a], 750[d]	6584		5893		3449	
IAB sLL (low Au, low Ni) subgroup												
Pine River	268.1	305[a], 280[d]	3515		3085	3060[a], 3050[d]	3812		4925	5000[a], 5000[d]	4286	
Shrewsbury average	226.5	260[a], 260[d], 235.0[m]	3615	3699[m]	2723	2770[a], 2770[d]	3819		4868		4476	
Comanche	226.4	227[a], 230[d]	2698		2614	2820[a], 2690[d]	4577		5738	6100[a], 6100[d]	4499	
Bahjoi	220.2	290[a], 300[d]	2598		2429	2540[a], 2500[d]	4659		5739	5600[a], 5800[d]	4370	
Toluca	215.9	250[a], 270[d]	2232		1962	2470[a], 2390[d], 2220[l]	4351	2960[c]	5426	5700[a], 4840[c], 6100[d]	4283	5560[c], 3000[e]
Deport	215.8	263[a], 260[d]	2587		2429	2370[a], 2370[d]	4633		5613		4389	4450[g]
Balfour Downs	212.0	242[a], 222[b], 240[d]	2422	2890[b]	2302	2170[a], 2000[b], 2150[d]	4148	3920[b]	5613	5500[a],4700[b]	4809	
Bischtube average	203.2	210[a], 210[d], 211.9[j]	2428	2536[j]	2332	2300[a], 2310[d]	3688		4880	5700[a], 5700[d]	4094	4100[e]
Goose Lake	188.2	210[a], 220[d]	2217		2139	2150[a], 2130[d]	4509		6094	5900[a], 6000[d]	4056	3340[g]
IAB sLM (low Au, medium Ni) subgroup												
Persimmon Creek	80.7	112[a], 82[b]	730.6	800[b]	840.2	852[a], 840[b]	1360	1440[b]	2026	1900[b]	5585	
Mungindi	47.86	76[a], 43[b], 80[d]	678.4	710[b], 490[l]	570.3	583[a], 560[b], 550[d], 540[l]	426.2	350[b], 360[c]	610.7	1400[a], 500[b], 380[c], 1500[d]	5881	12200[c]
Edmonton (KY) av.	38.8	38[b]	650.6	670[b]	505.2	457[a], 480[b], 500[d]	519.0	530[b]	585.6	700[b]	5708	5970[g]
Maltahohe	16.42	< 50[a]	121.4		165.0	170[a], 180[d]	641.0		626.2	1900[a], 1900[d]	5390	
Anoka average	13.84	< 30[a]	260.2		165.0	172[a], 160[d]	254.7		222.8	1200[a]	5784	
Carlton	7.113	6.6[b], 14[i]	140.0	129[b], 260[f], 100[i]	92.49	82[a], 83[b], 80[d], 46[f], 100[i], 80[l]	97.70	103[b], 100[c], 190[f], 230[i]	101.9	350[b], 100[c]	6689	15200[c], 6700[e], 6520[g]
Lamesa average	4.6	< 30[a]	39.78	530[l]	48.00	45[a], 40[d], 40[l]	142.7	110[c]	138.8	110[c]	6636	14400[c]

Table A2.3. (cont.)

Sample	Re	Re (literature)	Os	Os (literature)	Ir	Ir (literature)	Ru	Ru (literature)	Pt	Pt (literature)	Pd	Pd (literature)
IAB sLH (low Au, high Ni) subgroup												
Tazewell	7.512	8.1[b]	134.7	149[b]	87.84	100[a], 100[b], 90[d]	62.04	80[b]	85.93	70[b]	8687	7730[g]
Dayton average	2.6	2.5[b]	41.82	47[b]	30.03	30[a], 28[b], 30[d], 20[l]	48.67	45[b], 70[c]	47.70	1400[a], 100[b], 70[c]	8228	16400[c]
Freda	0.6164	0.99[b]	8.043	8.0[b]	7.500	15[a], 12[b], 20[d]	30.00	30[b]	23.02	<250[b]	12210	
IAB sHL (high Au, low Ni) subgroup												
Quarat al Hanish	86.75	100[a]	943.4		957.6	856[a]	2214		2671		6066	
Chebankol	8.632	< 60[a]	63.31		102.9	90[a]	1328		1711		4578	
Sombrerete	6.099	< 100[a]	61.87		73.80	80[a]	537.6		468.2		5369	
IAB sHH (high Au, high Ni) subgroup												
Kofa	8.218	< 20[a]	72.38		99.22	100[a]	2554		3671		9650	
ALHA 80104	7.584	< 30[a]	70.94		90.42	83[a]	2597		3225	4200[a]	8641	
Mount Magnet	0.6252	< 60[a]	5.650	31[f]	6.176	15[a], 17[f]	142.6	170[f]	59.90	3000[f]	9212	9300[e]
IAB ungrouped												
Theil Mountains	285.3	245[a], 250[d]	3784		3244	3670[a], 3670[d]	5151		5934	6200[a], 6200[d]	3743	
Caddo County	254.0	287[a], 320[d]	2728		2515	2530[a], 2550[d]	4696		6058	6400[a], 7500[d]	4267	
Zagora[a,b]	243.0	267[a], 280[d]	3026		2655	2830[a], 2740[d]	4520		5413	6300[a], 6600[d]	3981	
Mertzon	188.0	180[a]	1701		2160	2200[a]	3959		7395		3540	
EET84300[a,b]	180.1	163[a]	2804		2123	1830[a]	1936		2731	3000[a]	4402	
Woodbine	177.9	209[a], 177[b], 210[d]	2062	2250[b], 2010[l]	1984	1980[a], 1400[b], 1970[d], 1680[l]	2389	2490[b], 2280[c]	3053	5300[a], 1900[b], 2490[c]	6181	7720[c]
Pitts	112.6	95[a], 110[d]	1449		1336	1220[a], 1220[d]	1765		2414	1800[a], 3100[d]	6625	
Mundrabilla[a,b]	85.5	91[a], 84[b], 90[d]	768.7	710[b]	984.8	906[a], 910[d], 810[l]	3237	3160[b], 2880[c]	3726	3600[b], 4200[c]	3877	4560[c]
Waterville[a,b]	34.1	37[a]	194.6		357.6	372[a], 350[d]	3336		2995	3100[a]	3891	
Georgetown[a,b]	17.33	< 20[a]	88.47		190.4	238[a], 250[d]	2105		1750	3000[a], 3600[d]	3601	
IAB unclassified												
Osseo	510.3	610[a], 530[d], 518.6[m]	7313	7337[m]	5934	6040[a], 5850[d]	8769		10690		3368	
Sardis	185.5	250[a], 270[d], 198.2[m]	1763	1806[m]	2023	2020[a], 2010[d]	7567		8291		3422	

[a]Wasson and Kallemeyn (2002), [b]Pernicka and Wasson (1987), [c]Hoashi et al. (1993), [d]Choi et al. (1995), [e]Smales et al. (1967), [f]Crocket (1972), [g]Goldberg et al. (1951), [h]Hermann et al. (1971), [i]Seitner et al. (1971), [j]Shen et al. (1996), [k]Hirata and Masuda (1992), [l]Ryan et al. (1990), [m]Horan et al. (1998)

Table A2.4. Percent differences of HSE abundances and ratios for duplicates

Sample	Re	Re/Ir	Os	Os/Ir	Ir	Ru	Ru/Ir	Pt	Pt/Ir	Pd	Pd/Ir	$^{187}Re/^{188}Os$	$^{187}Os/^{188}Os$
Ballinger	2.1	1.3	0.5	0.4	0.8	6.7	5.9	2.4	3.2	0.6	0.2	1.6	0.3
Sarepta	2.6	2.2	0.5	0.1	0.4	6.4	6.1	0.8	0.4	4.3	3.9	2.1	0.6
Shrewsbury	0.01	0.5	1.5	1.9	0.4	22.8	23.2	1.2	1.6	2.8	2.4	1.4	0.3
Bischtübe	1.6	1.1	0.3	0.7	0.5	7.3	6.8	0.4	0.1	7.9	7.5	1.8	1.0
Persimmon Creek	12.8	11.5	8.4	7.1	1.3	3.5	2.2	5.4	4.2	7.4	6.2	4.4	1.3
Edmonton (KY)	0.3	1.0	0.1	1.1	1.3	1.1	0.2	0.4	0.8	2.1	0.9	0.2	0.0
Anoka	1.5	5.0	0.2	3.7	3.5	1.2	2.3	1.5	2.0	2.1	5.6		
Lamesa	2.6	3.2	0.3	0.3	0.6	0.1	0.7	0.3	0.9	0.1	0.5	3.0	0.4
Dayton	0.1	8.8	3.1	5.8	9.0	1.9	7.1	4.0	4.9	0.8	8.1	3.0	0.0
EET 84300	3.7	0.1	2.5	1.1	3.6	6.2	2.6	2.7	0.9	14.0	10.4	1.3	0.3
Pitts[a]	3.2	13.1	4.0	5.9	9.9	0.6	9.3	4.2	14.1	7.8	17.6	7.2	2.1
Mundrabilla	9.1	11.8	4.4	7.1	2.7	0.3	3.0	5.3	2.6	2.5	0.2	4.7	0.6
Waterville	4.5	0.7	8.8	3.7	5.1	3.5	8.6	12.8	7.7	0.9	6.0	4.3	1.2
Sardis	0.2	0.1	0.3	0.2	0.1	0.6	0.7	0.05	0.1	0.1	0.2	0.1	0.1

[a] % differences for Pitts were determined for just two of the triplicate analyses

Table A2.5. Linear regressions and uncertainties of log-log plots of HSE vs. Ir for which the MSWD was < 10. Linear regressions were calculated using the average of duplicate analyses.

	Slope	2σ	MSWD
MG			
Re	1.00	0.094	4.7
Os	1.53	0.13	4.2
Pd	0.025	0.074	3.5
sLL			
Re	0.72	0.44	2.9
Os	1.35	0.36	1.5
Ru	-0.72	0.88	6.7
Pt	-0.40	0.50	3.0
Pd	0.13	0.39	2.2
sLM			
Pd	-0.054	0.067	2.4

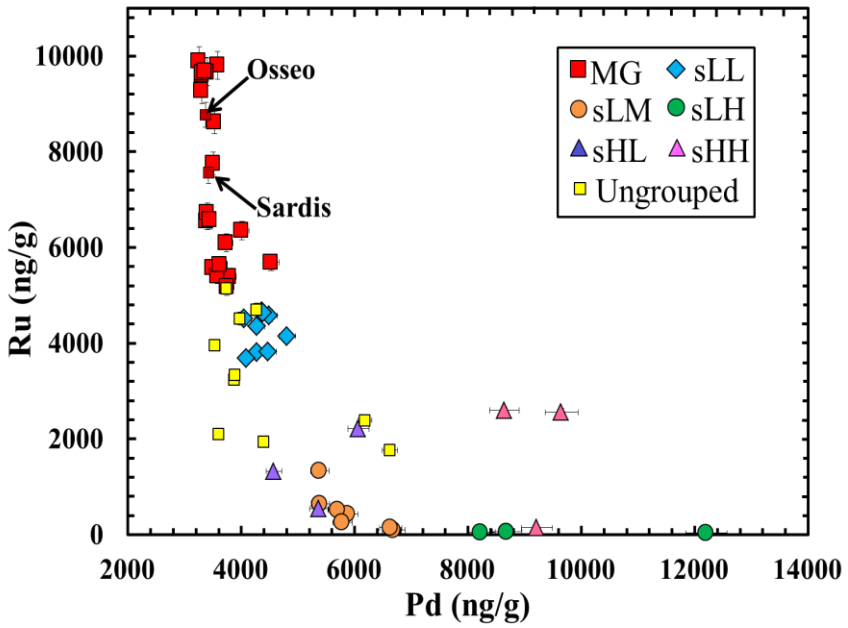

Fig. A2.1. Palladium vs. Ru concentrations for the IAB subgroups and ungrouped IAB irons. The MG and sLL subgroups can be distinguished on the basis of Pd vs. Ru abundances. The subgroups characterized by similar HSE patterns are also chemically distinguished, largely by differing Pd abundances, such that the sLM and sLH subgroups are distinct from one another, and the sHL and sHH subgroups are also distinguished.

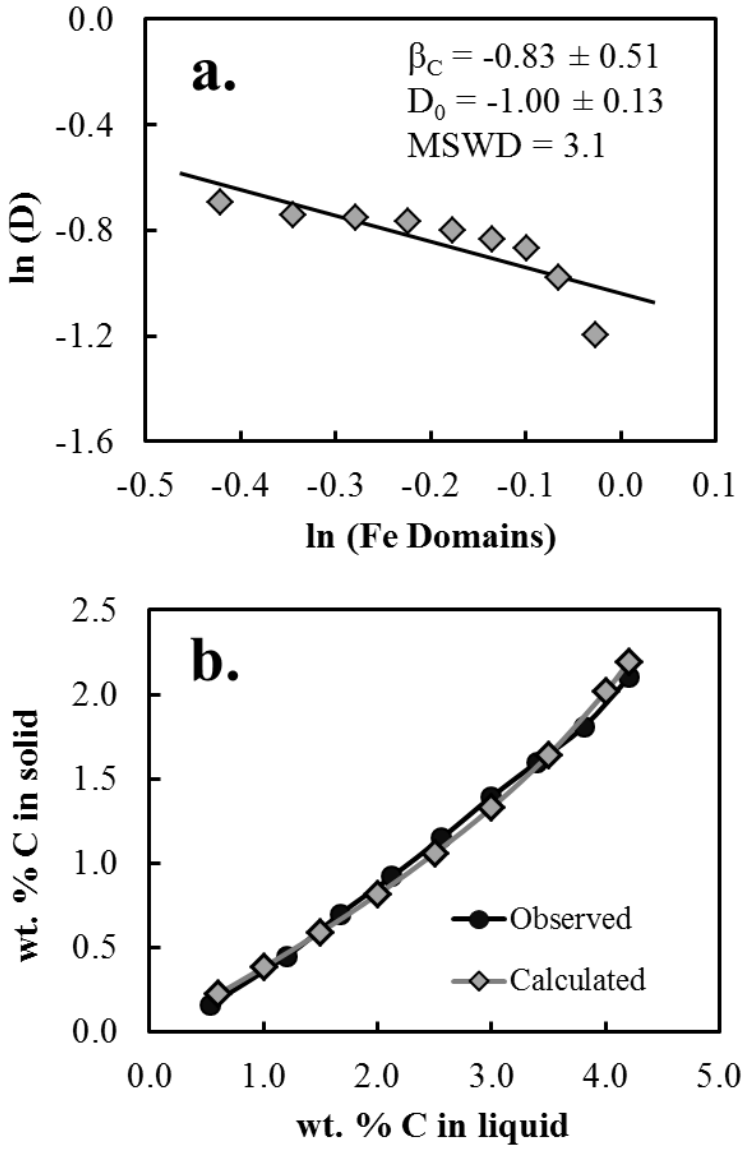

Fig. A2.2. a) Carbon parameterization in Fe-C system. D values were calculated using co-existing solid and liquid C contents from Okamoto (1992), where D is the concentration of C in the solid divided by that in the liquid. The same approach was used for the Fe-S-C system using average D values from each vertical section at different S contents. MSWD (mean square weighted deviation) is a measure of scatter about the regression. b) Wt. % C in solid vs. wt. % C in liquid observed from Okamoto (1992) and calculated using the parameterization in (a).

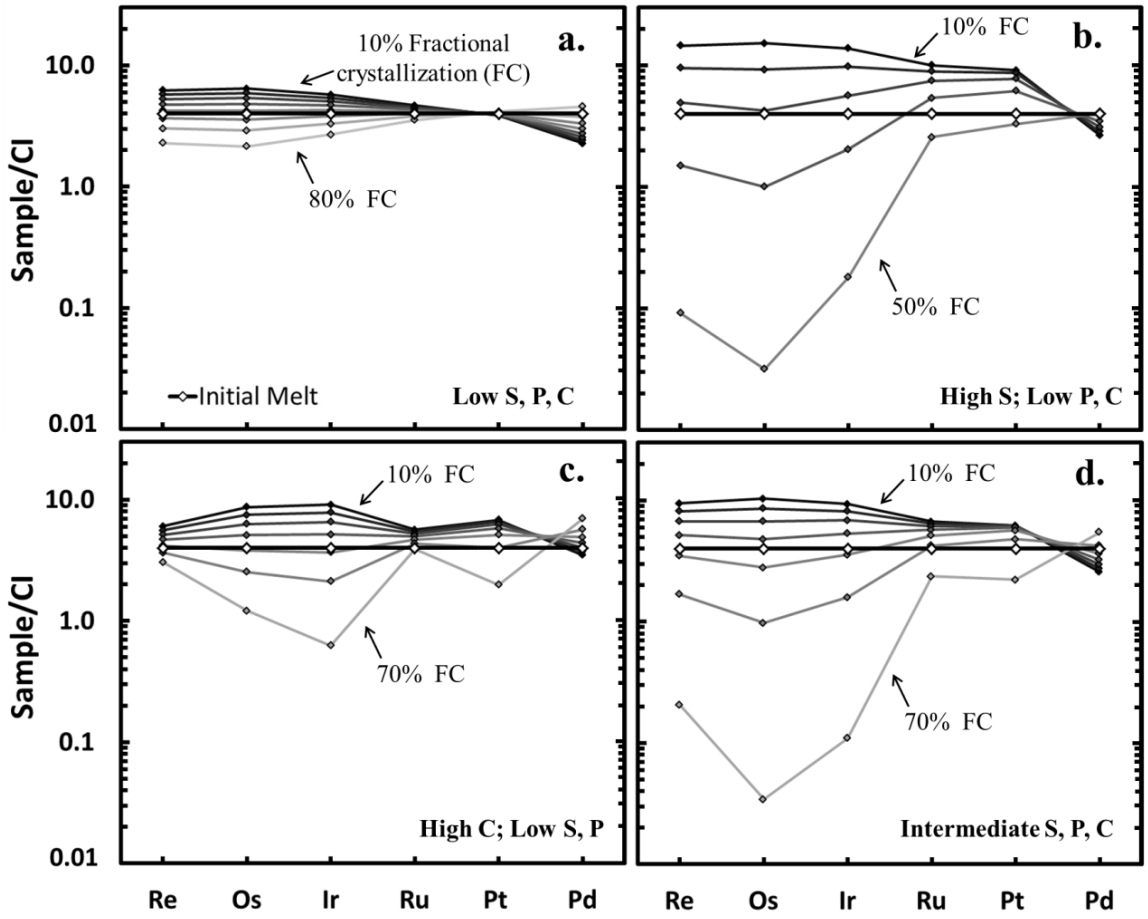

Fig. A2.3. Chondrite-normalized fractional crystallization trends for HSE for different S, P, and C contents in an initial melt of a superchondritic composition (4× CI chondrite Orgueil – Horan et al., 2003). D values are from Chabot et al. (2014). The initial concentrations of S, P, and C are as follows: a) S = 0.1 wt. %, P = 0.01 wt. %, and C = 0.01 wt. %.; b) S = 10 wt. %, P = 0.01 wt. %, and C = 0.01 wt. %.; c) S = 0.1 wt. %, P = 0.01 wt. %, and C = 2 wt. %.; d) S = 5 wt. %, P = 0.2 wt. %, and C = 0.15 wt. %.

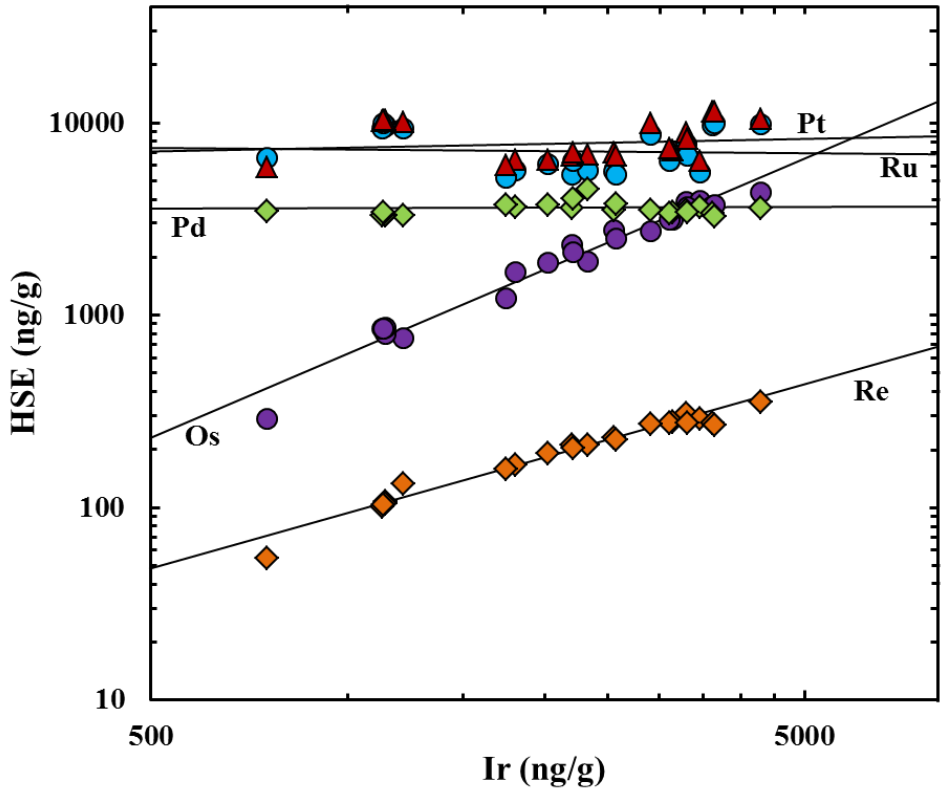

Fig. A2.4. Logarithmic plots of HSE vs. Ir abundances of the MG. Rhenium and Os have well-correlated, positive slopes with Ir. Platinum (red triangles) and Ru (blue circles) exhibit scatter about the regression with Ir, whereas Pd has a relatively uniform distribution. Osseo and Sardis are not shown and are not included in the calculations of the MG slopes.

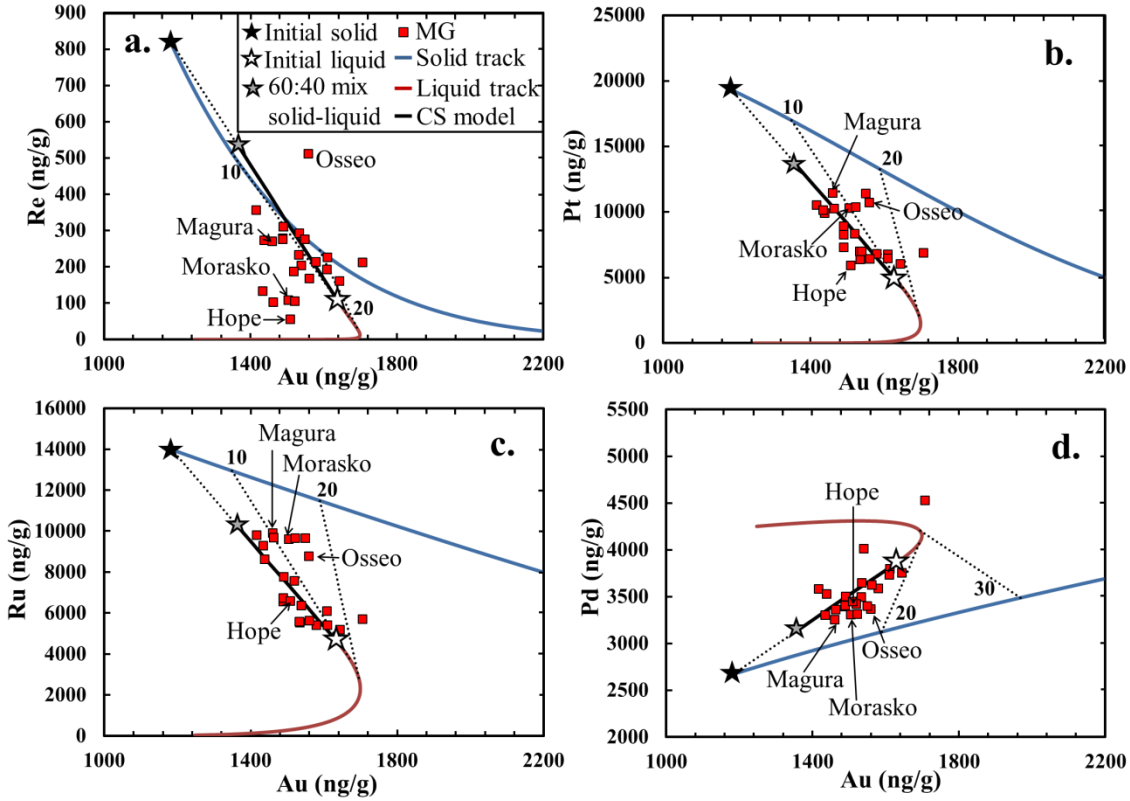

Fig. A2.5. The CS-FC model using parameterized D values to calculate a) Au vs. Re, b) Au vs. Pt, c) Au vs. Ru, d) Au vs. Pd. Au data are from Wasson and Kallemeyn (2002). The thick black line represents the CS model and the red and blue lines correspond to the evolving solid and liquid compositions generated by the FC model. The dotted lines represent mixtures of coexisting solids and liquids at 0%, 10%, and 20% or 30% fractional crystallization. The white star corresponds to the initial liquid composition, which is the composition of the liquid endmember generated by the CS portion of the model. The black star corresponds to the initial solid composition. The grey star represents a mixture of 60 % solid and 40% liquid. Many IAB-MG iron meteorites do not plot on or between the solid and liquid evolution tracks, or near the CS mixing line in (a). In (b-d) the fit of the model is better than in (a). Error bars for Au are slightly larger than the symbols (~ 2%) and are not plotted for clarity.

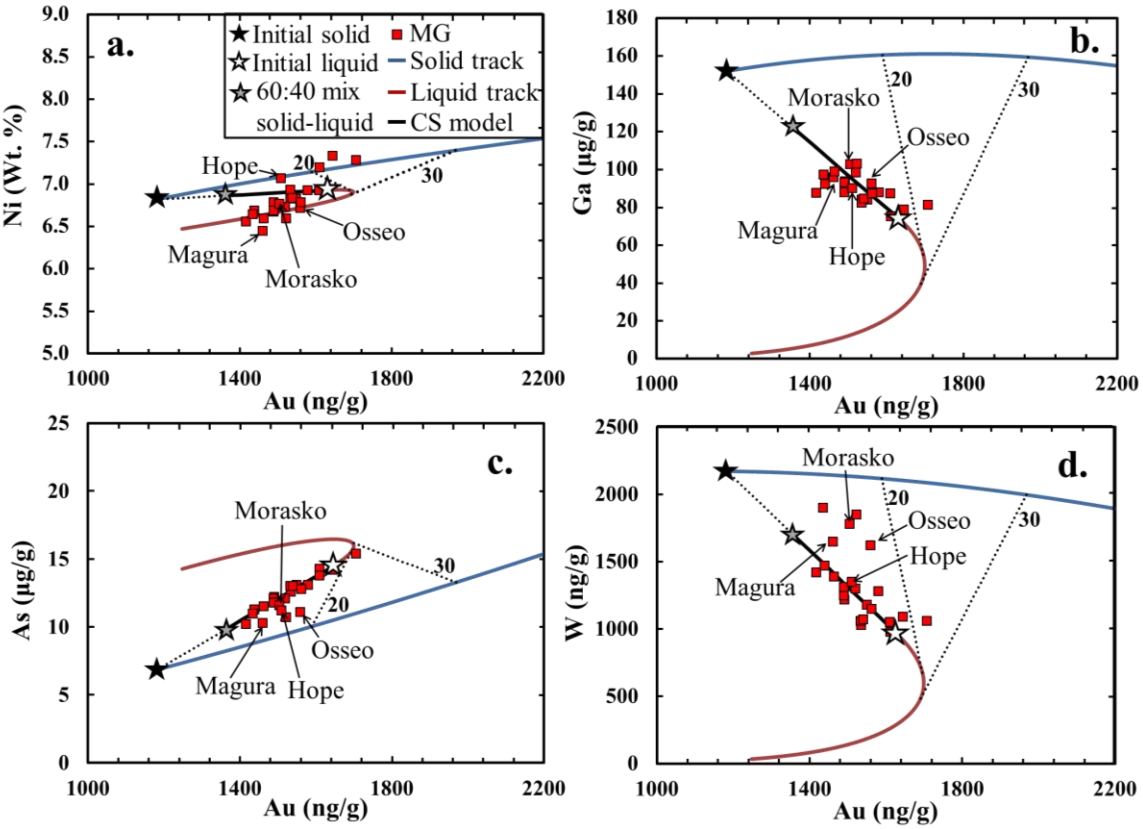

Fig. A2.6. The CS-FC model using parameterized D values to calculate a) Au vs. Ni, b) Au vs. Ga, c) Au vs. As, d) Au vs. W. All data are from Wasson and Kallemeyn (2002). Error bars are not shown for clarity, but are ~2%. The CS-FC model generally reproduces the variations in these elements.

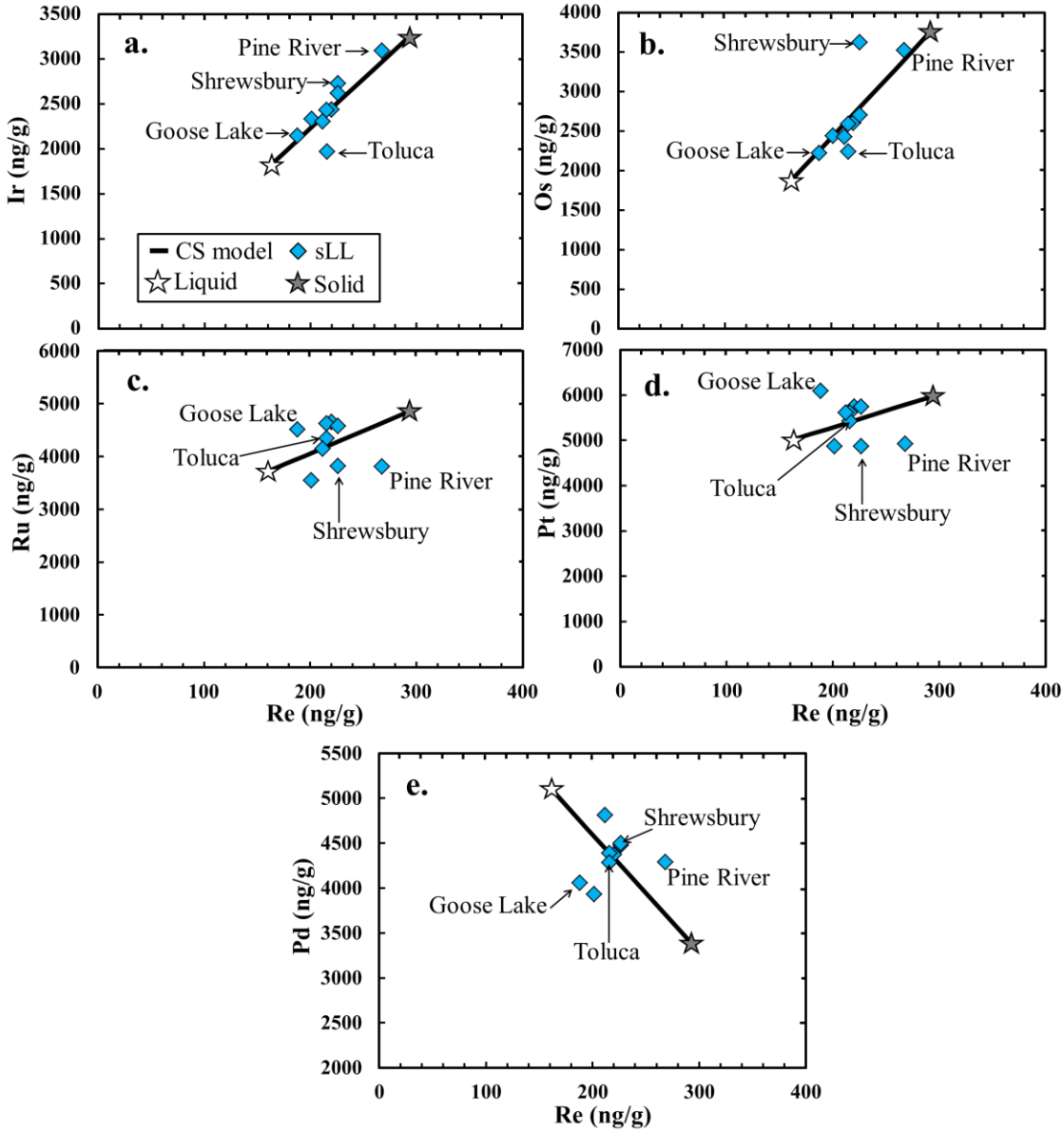

Fig. A2.7. The CS model applied to the sLL subgroup using D values consistent with 2 wt. % S, 0.4 wt. % P, and 0.2 wt. % C for a) Re vs. Re/Os, b) Re vs. Pt/Os, c) Re vs. Ru, d) Re vs. Pt, and e) Re vs. Pd. The white star corresponds to the liquid endmember and the grey star corresponds to a mixture incorporating 80% of the solid endmember.

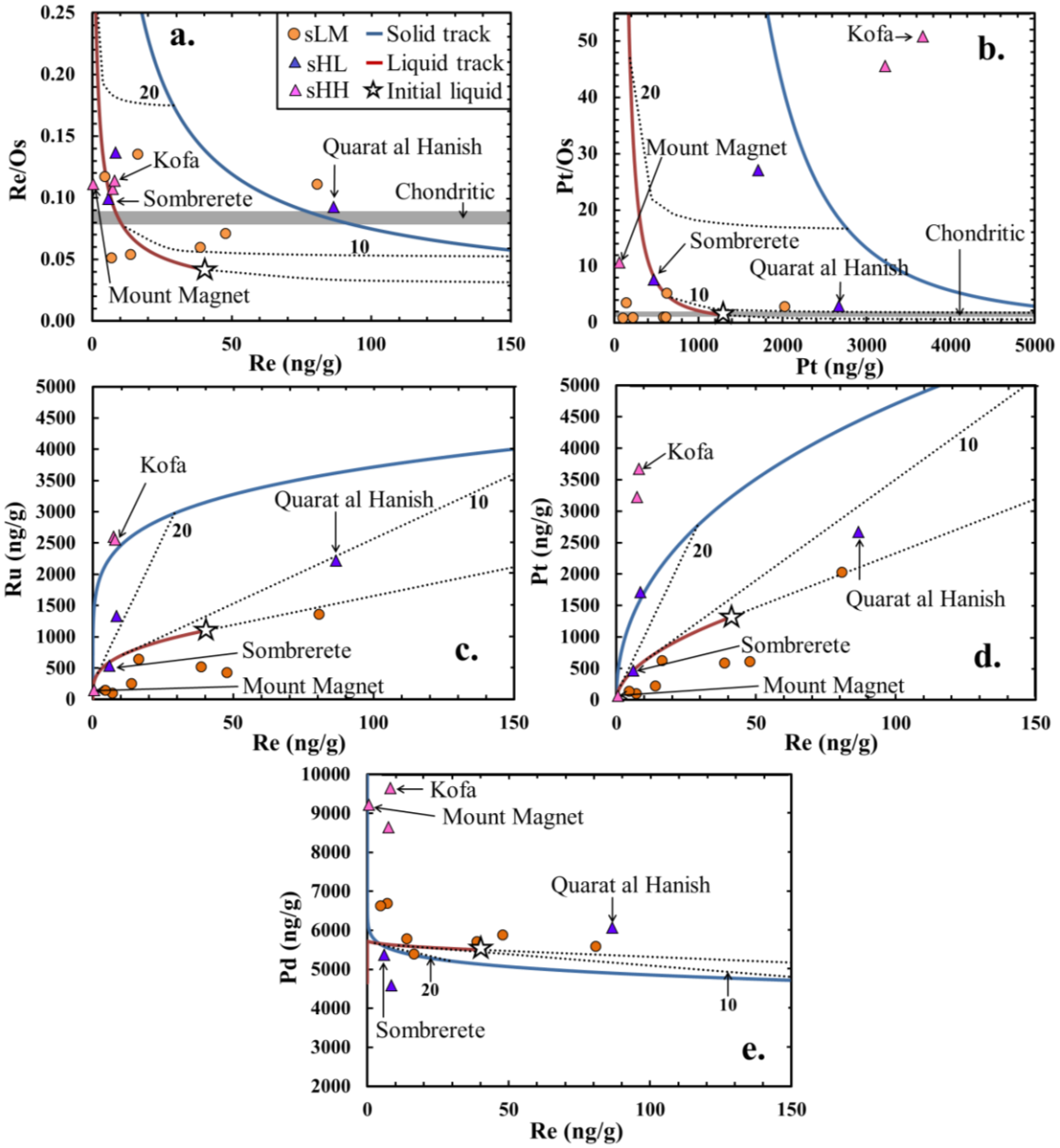

Fig. A2.8. The fractional crystallization model applied to the sHL subgroup for a) Re vs. Re/Os, b) Re vs. Pt/Os, c) Re vs. Ru, d) Re vs. Pt, and e) Re vs. Pd. The D values used for this model are consistent with 13 wt. % S, 1.8 wt. % P, and 0.15 wt. % C. The sHH subgroup and sLM subgroups are shown for reference. The model reproduces the HSE variations in the sLH subgroup for all plots but Re vs. Re/Os and Re vs. Pd.

Chapter 3: Micro-scale chemical characterization of IAB complex iron meteorites

3.1 Abstract

In situ siderophile trace element data for IAB iron meteorites obtained by laser ablation inductively coupled plasma mass spectrometry techniques are reported. Large chemical variations in several siderophile elements are observed between kamacite and taenite on the mm-cm scale, consistent with previous studies. This indicates that certain siderophile elements partition preferentially into kamacite or taenite and that the diffusion of those elements was effective on the timescale of kamacite and taenite exsolution.

By combining data from multiple line traces across kamacite and taenite grains, bulk concentrations are determined. Trace element concentration variations are observed within and between the IAB complex main group and subgroups. The majority of the siderophile elements, including Ni, Rh, Au, Ga, and Ge, are characterized by large ranges among the subgroups, and restricted ranges within the subgroups. In addition to previous data for Ni, Au, Ga, Ge, and Pd abundances as taxonomically useful elements for distinguishing the IAB subgroups, the new Rh data can also be used as a diagnostic tool. Most subgroups in the IAB complex are volatile-rich, having Ga and Ge abundances that are higher than those in the magmatic IVA and IVB iron meteorite groups, but generally similar to the IIAB and IIIAB iron meteorite groups, which is consistent with previous studies. The relative abundances of redox-sensitive siderophile elements indicate that most IAB precursors were comparatively reduced, in agreement with prior studies. The

relative and absolute abundances of volatile siderophile elements suggest that condensation/volatilization processes were important in the sLM, sLH, sHH, and sHL subgroups.

3.2 Introduction

Siderophile elements are characterized by their geochemical affinity to partition into metal over silicate phases. These elements have a wide range of condensation temperatures, redox behaviors, and partitioning behaviors. In iron meteorites, siderophile elements have been useful geochronometers and geothermometers, and have been used to classify groups of meteorites and to examine metal-silicate segregation and crystallization mechanisms.

Most iron meteorites contain both kamacite (low Ni FeNi alloy) and taenite (high Ni FeNi alloy), which form Widmanstätten patterns. This pattern was created in iron meteorites by the sub-solidus exsolution of kamacite and taenite during slow cooling (e.g., Goldstein and Ogilvie, 1965; Yang et al., 1996). During cooling and exsolution of the phases, several elements of interest (e.g., Ni, Au, Pd) partition *via* diffusion more readily into either kamacite or taenite (e.g., Rasmussen et al., 1988; Hirata and Nesbitt, 1997). However, relatively few studies have considered partitioning of elements between phases, and those studies examined a limited number of iron meteorites (e.g., Rasmussen et al., 1988; Hirata and Nesbitt, 1997; Hsu et al., 2000). Therefore, the variability of partitioning behaviors among different types of iron meteorites under different conditions is unknown. For example, variations in temperature, pressure, composition, and cooling

rate may affect the partitioning behavior of siderophile elements during exsolution of kamacite and taenite. Further, determinations of the concentrations of elements which preferentially partition into kamacite or taenite may be affected by variable distributions of the phases, such that an analysis of a sample may not be representative of the bulk, if the sample that was analyzed was smaller than some minimum size. To what extent, if any, the partitioning of certain elements between kamacite and taenite affects their bulk analyses is unknown, and is investigated here using *in situ* analyses of IAB complex iron meteorites.

Prior trace element abundance data, obtained using analytical techniques that utilized bulk meteorite samples, have revealed chemical heterogeneity among IAB complex iron meteorites (Wasson and Kallemeyn, 2002; Worsham et al., 2016a – **Tables A2.3-A2.4**). However, an open question regarding the chemical heterogeneity is whether it is related to mineralogy (i.e., the distribution of kamacite and taenite), or whether it is due to disequilibrium processes. The *in situ* measurement of IAB samples provides the opportunity to investigate micro-scale variations among trace element distributions, and may give insight into the nature and scale of the chemical heterogeneity in IAB meteorites.

The variations in major and trace siderophile element abundances within and between the subgroups of the IAB iron meteorite complex are unlike those of magmatic iron meteorite groups (Scott, 1972; Kelly and Larimer, 1977; Wasson et al., 1980; Pernicka and Wasson, 1987). Previously published major and trace siderophile element data indicate that subgroups within the IAB complex cannot be related to one another by crystal-liquid fractionation processes, and therefore, likely originated in separate parental

melts (e.g., Wasson and Kallemeyn, 2002; Worsham et al., 2016a). The relations between IAB complex subgroups were also investigated by Worsham et al. (2016a) using highly siderophile element (HSE) abundances. However, the HSE are characterized by a relatively narrow range in volatilities, so they have somewhat limited utility in evaluating nebular processes that preceded accretion of the parent body(ies). It is, therefore, also useful to examine a larger suite of siderophile elements *in situ* to address questions relating to the nature of the parent body(ies) sampled by IAB complex meteorites.

The abundances of comparatively redox-sensitive and volatile siderophile elements in different IAB complex subgroups are of particular interest, because they may give further insight into the nebular conditions and/or precursor materials of the different subgroups. For example, Au and Pd have the lowest 50% condensation temperatures of the HSE (Lodders, 2003). The abundances of Pd and Au are enriched relative to the other HSE in the sLM and sLH subgroups, suggesting that the precursor materials of these subgroups may have been late-stage condensates (Worsham et al., 2016a). However, the limited range of volatilities among the HSE make it difficult to evaluate the extent of possible volatile enrichment. In order to further investigate potential volatile enrichment in the IAB complex, a wide range of siderophile element abundances in IAB meteorites from each subgroup were determined by *in situ* laser ablation inductively coupled plasma mass spectrometry (LA-ICP-MS).

3.3 Laser ablation methods

Trace and major siderophile elements, including monoisotopic Rh and Au, which cannot be measured by isotope dilution, were measured *in situ* in small pieces of the metal phase of each IAB meteorite using a *UP213* laser ablation system (*New Wave Research*) with a photon wavelength of 213 nm coupled to a *Thermo Finnegan Element 2* ICP-MS. For these analyses, sample pieces adjacent to those used for HSE isotope dilution analyses (Worsham et al., 2016a) were polished with 220, 400, and finally 600 grit carborundum paper. They were then sonicated in ethanol and etched with 0.8 M HNO_3 so that taenite and kamacite could be discriminated. The system and operating methods for the *in situ* analysis of iron meteorites are detailed by Walker et al. (2008) and McCoy et al. (2011). In this study, the laser sampling was conducted for at least four randomly oriented line traces using a 55 µm beam, flashed at a frequency of 10 Hz at 49-51% power. Before laser sampling, the sample was cleaned with the laser at 40% power while the sample was moved at 50 µm/s. For data collection, the sample was moved horizontally at a rate of 10 to 20 µm/s, producing lines between 80 and 160 µm long. Five line traces were done for most samples. Data were collected on mass stations corresponding to ^{51}V, ^{53}Cr, ^{55}Mn, ^{57}Fe, ^{59}Co, ^{61}Ni, ^{63}Cu, ^{69}Ga, ^{71}Ga, ^{73}Ge, ^{74}Ge, ^{75}As, ^{95}Mo, ^{97}Mo, ^{99}Ru, ^{101}Ru, ^{103}Rh, ^{105}Pd, ^{108}Pd, ^{182}W, ^{183}W, ^{185}Re, ^{188}Os, ^{189}Os, ^{191}Ir, ^{193}Ir, ^{194}Pt, ^{195}Pt and ^{197}Au. Two line traces on two iron meteorites, Hoba and North Chile, were measured as standards under the same conditions as samples every 12 analyses of line traces on samples.

Laser ablation data were processed using LAMTRACE software (Achterbergh et al., 2001). LAMTRACE was used to calculate element concentrations using background-

subtracted count rates of samples and standards, known concentrations in the standards, and a known concentration of one element in the samples. Previous studies from our group applying *in situ* laser ablation techniques for the analysis of iron meteorites used Pt as an internal standard to calculate the element concentrations (Walker et al., 2008; McCoy et al., 2011). However, Pt concentrations in some IAB subgroups are too low to be used as the internal standard.

To process all the data in an internally consistent way, we used Ni (input as ^{61}Ni) as the internal standard, despite some difficulty in accounting for Ni heterogeneity due to variable proportions of kamacite and taenite. In an attempt to circumvent the issue of Ni heterogeneity, the Ni values used as the internal standard were obtained using a two-step procedure (Campbell et al., 2002; Humayun et al., 2010). First, Ni concentrations from bulk analyses of IAB irons taken from Wasson and Kallemeyn (2002) were used as an initial input into LAMTRACE as the internal standard. Major element outputs for Fe and Co, along with Ni concentrations from Wasson and Kallemeyn (2002), were then normalized to make up 100 wt. % of the sample. The normalized Ni concentration was then used as the internal standard to calculate the other major and trace element abundances. Therefore, if a given laser track led to the ablation of a disproportionate amount of taenite relative to the bulk sample, the normalized Ni would be more appropriate to calculate the rest of the element abundances, rather than using a bulk Ni concentration. The uncertainties for each sample are reported as the standard deviation of multiple line traces, and are typically on the order of ± 5-10% (1σ). Average concentrations of elements for which multiple isotopes were determined are reported.

3.4 Results

In situ laser ablation data are presented in **Table 3.1**. Some samples are characterized by large variations in Cr, Co, Ga, Ge, As, Cu, Mo, Ru, Pd, and Au about their average concentrations due to their preference for taenite or kamacite. Low count rates for some elements in low-abundance samples also contributed to the variance (e.g., W, Re, Os, Ir, and Pt).

Accessory phases containing Cr and Mo were present in many samples, as evidenced by sporadic, major increases in signal intensity for these elements during line trace analyses, which contributed to the variance in Mo and Cr concentrations. These phases were likely phosphides, based on the high concentrations of Mo and Cr measured in phosphides found in Odessa and Canyon Diablo (Hermann et al., 1971). For Mo, the concentrations measured during affected line traces were excluded from the average, if two or more lines did not appear to be affected. For Cr, the line traces that were affected by accessory phases were the only lines that yielded Cr concentrations above background in many cases. Additionally, the Cr and Mo heterogeneities were not always correlated with one another. For these reasons, lines that were discarded for calculating average Mo concentrations were not discarded for Cr concentrations. Therefore, Cr concentrations are significantly more uncertain than other element concentrations and should be considered upper limits. The Mo and Cr accessory phases were estimated to be on the order of 100 μm across, based on the duration of Cr and Mo signal deviations and the rate at which the sample was moved.

Table 3.1. Mean compositions of IAB iron meteorites determined by *in situ* LA-ICP-MS data. The data are reported in µg/g unless otherwise noted. The Ni concentrations are the averages of the normalized internal standard values described in the text. Numbers in italics are estimates. *Samples for which two sets of line trace analyses were conducted.

MG	Landes	Seligman*	Yenberrie	Ballinger	Cranbourne*	Campo del Cielo	New Leipzig	Magura	Odessa*	Jenkins
V	—	*0.01*	0.03 ± 0.01	*0.21*	*0.02*	*0.03*	0.07 ± 0.05	—	0.05 ± 0.03	—
Cr	—	—	30 ± 10	20 ± 20	—	—	80 ± 50	50 ± 20	—	40 ± 30
Mn	*3.2*	—	—	*1.5*	—	—	—	—	—	—
Fe %	93.2 ± 0.2	93.1 ± 0.5	93.4 ± 0.2	93.3 ± 0.1	92.6 ± 0.3	93.2 ± 0.2	92.5 ± 0.8	93.5 ± 0.2	90.2 ± 2	92.8 ± 0.7
Co	4690 ± 80	4800 ± 200	4820 ± 80	4890 ± 60	5160 ± 80	4800 ± 60	4600 ± 400	4900 ± 100	5300 ± 600	4800 ± 300
Ni %	6.3 ± 0.2	6.2 ± 0.5	6.2 ± 0.2	6.2 ± 0.1	6.7 ± 0.3	6.3 ± 0.2	6.7 ± 0.7	6.0 ± 0.2	9 ± 2	6.7 ± 0.7
Cu	310 ± 30	130 ± 10	104 ± 5	118 ± 6	130 ± 10	109 ± 5	140 ± 20	105 ± 5	160 ± 50	120 ± 30
Ga	93 ± 2	102 ± 2	84 ± 1	89 ± 2	115 ± 2	95 ± 6	94 ± 2	95 ± 1	94 ± 5	89 ± 6
Ge	453 ± 6	464 ± 7	346 ± 5	394 ± 7	584 ± 6	420 ± 30	443 ± 6	486 ± 8	320 ± 10	380 ± 10
As	11.0 ± 0.2	14.3 ± 0.7	14.2 ± 0.8	12.2 ± 0.3	13.2 ± 0.6	12.2 ± 1	12.4 ± 0.6	11.0 ± 0.3	18 ± 2	13.4 ± 0.3
Mo	8.3 ± 0.2	6.4 ± 0.4	7 ± 1	8.0 ± 0.9	3.6 ± 0.3	8.4 ± 0.1	8.4 ± 0.4	9.3 ± 0.9	3.4 ± 0.3	8 ± 1
Ru	9.0 ± 0.5	8 ± 1	5.8 ± 0.6	6.8 ± 0.2	11.3 ± 0.3	7.1 ± 0.5	9.1 ± 0.8	9.6 ± 0.3	5.8 ± 0.4	6.5 ± 0.8
Rh	1.68 ± 0.03	1.63 ± 0.05	1.45 ± 0.05	1.44 ± 0.06	2.02 ± 0.09	1.46 ± 0.07	1.6 ± 0.1	1.77 ± 0.06	1.40 ± 0.07	1.5 ± 0.1
Pd	3.3 ± 0.1	3.9 ± 0.2	3.9 ± 0.2	3.0 ± 0.2	4.2 ± 0.3	3.0 ± 0.1	3.8 ± 0.3	3.4 ± 0.1	6.0 ± 0.6	3.7 ± 0.4
W	1.55 ± 0.09	1.27 ± 0.05	1.2 ± 0.1	1.17 ± 0.08	1.25 ± 0.07	1.22 ± 0.06	1.57 ± 0.08	1.66 ± 0.07	0.59 ± 0.04	1.09 ± 0.07
Re	0.36 ± 0.02	0.34 ± 0.02	0.36 ± 0.04	0.26 ± 0.02	0.33 ± 0.03	0.29 ± 0.04	0.25 ± 0.05	0.27 ± 0.02	0.25 ± 0.03	0.24 ± 0.02
Os	4.4 ± 0.1	4.0 ± 0.1	4.5 ± 0.2	3.1 ± 0.2	4.2 ± 0.1	4.0 ± 0.2	2.8 ± 0.2	3.7 ± 0.1	2.6 ± 0.2	2.4 ± 0.1
Ir	4.44 ± 0.07	3.34 ± 0.06	4.10 ± 0.09	3.1 ± 0.2	4.2 ± 0.2	3.7 ± 0.2	3.1 ± 0.1	3.81 ± 0.06	2.9 ± 0.1	2.39 ± 0.09
Pt	11.0 ± 0.1	9.5 ± 0.2	7.4 ± 0.3	7.4 ± 0.3	13.9 ± 0.6	9.5 ± 0.5	10.2 ± 0.4	12.4 ± 0.1	8.1 ± 0.4	7.3 ± 0.2
Au	1.48 ± 0.05	1.8 ± 0.1	1.75 ± 0.07	1.46 ± 0.08	2.1 ± 0.2	1.56 ± 0.09	1.7 ± 0.3	1.42 ± 0.02	2.4 ± 0.3	1.6 ± 0.2

(continued)

Table 3.1. (continued)

MG	ALHA 77283	Youndegin	Smithville	Seymour*	Bogou	Burgavali	Morasko	Seeläsgen	Sarepta	Hope
V	*0.1*	*0.009*	*0.1*	*0.04*	*1.3*	0.05 ± 0.03	—	*0.1*	*0.1*	—
Cr	—	16 ± 5	—	—	21 ± 17	40 ± 30	13 ± 2	19 ± 7	27 ± 6	15 ± 1
Mn	*1.6*	—	*0.8*	—	—	—	—	—	—	—
Fe %	92.5 ± 0.9	93.0 ± 0.8	92.3 ± 0.7	92.4 ± 0.5	92.2 ± 1	93.4 ± 0.3	93.3 ± 0.3	93.6 ± 0.3	93.5 ± 0.3	93.0 ± 0.1
Co	5500 ± 200	4900 ± 200	5200 ± 500	5400 ± 200	4700 ± 300	4700 ± 100	4890 ± 90	4800 ± 100	4700 ± 200	4790 ± 50
Ni %	7.0 ± 0.9	6.5 ± 0.8	7.2 ± 0.7	7.1 ± 0.5	7.3 ± 1	6.2 ± 0.3	6.2 ± 0.3	6.0 ± 0.3	6.1 ± 0.3	6.5 ± 0.1
Cu	130 ± 30	125 ± 2	140 ± 30	110 ± 20	170 ± 50	121 ± 7	134 ± 7	127 ± 6	108 ± 8	124 ± 2
Ga	92 ± 4	84 ± 1	98 ± 6	102 ± 3	85 ± 7	97 ± 2	100 ± 1	97 ± 2	93 ± 3	91 ± 2
Ge	347 ± 4	367 ± 5	400 ± 10	419 ± 7	309 ± 6	495 ± 8	529 ± 2	507 ± 6	500 ± 10	431 ± 6
As	19 ± 1	14.1 ± 0.4	14.2 ± 0.7	18 ± 1	14.4 ± 0.5	10.6 ± 0.3	12.5 ± 0.4	11.4 ± 0.5	11.2 ± 0.8	12.9 ± 0.5
Mo	2.3 ± 0.3	4.9 ± 0.3	3.2 ± 0.3	2.6 ± 0.2	7 ± 1	9.4 ± 0.9	7.0 ± 0.4	8.3 ± 0.2	8.9 ± 0.7	8 ± 1
Ru	5.8 ± 0.9	6.1 ± 0.5	7.0 ± 0.9	6.8 ± 0.4	6 ± 1	10.0 ± 0.4	10.3 ± 0.2	9.4 ± 0.3	10.3 ± 0.3	6.4 ± 0.2
Rh	1.42 ± 0.08	1.46 ± 0.06	1.60 ± 0.09	1.72 ± 0.04	1.22 ± 0.09	1.82 ± 0.07	1.85 ± 0.05	1.74 ± 0.04	1.9 ± 0.1	1.54 ± 0.05
Pd	4.1 ± 0.5	4.0 ± 0.3	3.8 ± 0.4	5.2 ± 0.2	3.6 ± 0.4	3.2 ± 0.1	3.4 ± 0.2	3.2 ± 0.2	4.0 ± 0.2	3.24 ± 0.08
W	0.62 ± 0.03	1.06 ± 0.09	0.76 ± 0.04	0.67 ± 0.04	0.86 ± 0.08	1.5 ± 0.3	1.7 ± 0.1	1.8 ± 0.1	2.0 ± 0.1	1.21 ± 0.06
Re	0.23 ± 0.03	0.22 ± 0.06	0.21 ± 0.03	0.19 ± 0.02	0.16 ± 0.01	0.14 ± 0.03	0.12 ± 0.02	0.10 ± 0.02	0.13 ± 0.04	0.056 ± 0.008
Os	2.1 ± 0.1	2.2 ± 0.2	2.0 ± 0.1	1.7 ± 0.1	1.2 ± 0.1	0.8 ± 0.1	0.87 ± 0.06	0.92 ± 0.04	0.94 ± 0.06	0.29 ± 0.03
Ir	2.6 ± 0.1	2.4 ± 0.1	2.27 ± 0.09	1.94 ± 0.06	1.8 ± 0.1	1.36 ± 0.09	1.26 ± 0.04	1.27 ± 0.03	1.25 ± 0.07	0.80 ± 0.01
Pt	8.3 ± 0.2	7.4 ± 0.4	7.3 ± 0.3	7.6 ± 0.2	6.2 ± 0.4	11.1 ± 0.4	11.8 ± 0.2	11.9 ± 0.3	12.0 ± 0.6	6.4 ± 0.1
Au	2.0 ± 0.2	1.64 ± 0.09	1.7 ± 0.1	2.2 ± 0.2	1.6 ± 0.2	1.5 ± 0.1	1.53 ± 0.07	1.58 ± 0.08	1.7 ± 0.2	1.62 ± 0.03

(continued)

Table 3.1. (continued)

sLL	Shrewsbury	Comanche	Bahjoi*	Toluca	Deport*	Balfour Downs	Bischtübe	Goose Lake
V	*0.08*	*0.5*	*0.06*	0.8 ± 0.3	*0.04*	—	0.07 ± 0.02	—
Cr	—	50 ± 60	18 ± 7	12 ± 3	*16.4*	30 ± 20	*69.9*	16 ± 5
Mn	—	*1.1*	—	1.4 ± 0.4	—	—	—	*1.3*
Fe%	92.4 ± 0.6	92 ± 2	92 ± 1	91 ± 1	90 ± 2	91 ± 1	92.6 ± 0.4	92.6 ± 0.4
Co	5400 ± 100	4900 ± 400	5200 ± 300	4900 ± 500	4800 ± 500	5000 ± 400	5300 ± 100	5300 ± 100
Ni%	7.0 ± 0.6	8 ± 2	7 ± 1	8 ± 1	9 ± 2	8 ± 2	6.8 ± 0.4	6.9 ± 0.4
Cu	130 ± 20	180 ± 90	110 ± 60	180 ± 50	170 ± 80	140 ± 40	61 ± 9	120 ± 10
Ga	53 ± 2	76 ± 9	70 ± 6	68 ± 6	71 ± 5	63 ± 5	68 ± 3	71 ± 3
Ge	193 ± 3	264 ± 7	285 ± 7	235 ± 9	270 ± 10	210 ± 6	247 ± 4	300 ± 10
As	16.4 ± 0.9	17.0 ± 0.8	17 ± 1	16 ± 1	16 ± 2	18 ± 1	20 ± 2	19 ± 2
Mo	6.0 ± 0.3	7 ± 2	5.5 ± 0.9	6.4 ± 0.6	6.7 ± 0.7	7.3 ± 0.6	6 ± 1	6.0 ± 0.7
Ru	3.0 ± 0.4	4.7 ± 0.9	4.9 ± 0.6	4.7 ± 0.8	5.0 ± 0.6	4.6 ± 0.7	3.9 ± 0.6	4.5 ± 0.5
Rh	0.87 ± 0.08	1.12 ± 0.07	1.08 ± 0.06	1.04 ± 0.07	1.05 ± 0.06	0.97 ± 0.08	1.0 ± 0.1	1.09 ± 0.07
Pd	4.4 ± 0.4	5 ± 1	4.6 ± 0.5	4.4 ± 0.6	5.7 ± 0.9	5.0 ± 0.5	4.1 ± 0.5	3.6 ± 0.2
W	0.52 ± 0.09	0.83 ± 0.03	0.74 ± 0.06	0.76 ± 0.07	0.76 ± 0.07	0.59 ± 0.05	0.70 ± 0.06	0.82 ± 0.04
Re	0.23 ± 0.02	0.25 ± 0.02	0.26 ± 0.03	0.22 ± 0.03	0.23 ± 0.02	0.21 ± 0.02	0.23 ± 0.05	0.19 ± 0.02
Os	3.7 ± 0.2	2.9 ± 0.1	2.9 ± 0.2	2.2 ± 0.1	2.7 ± 0.1	2.5 ± 0.1	2.5 ± 0.2	2.4 ± 0.1
Ir	2.9 ± 0.1	2.94 ± 0.07	2.71 ± 0.08	2.1 ± 0.1	2.62 ± 0.09	2.49 ± 0.04	2.5 ± 0.1	2.42 ± 0.08
Pt	5.3 ± 0.2	6.9 ± 0.2	6.4 ± 0.1	6.0 ± 0.3	6.0 ± 0.2	6.3 ± 0.2	5.5 ± 0.3	6.8 ± 0.2
Au	1.7 ± 0.2	2.0 ± 0.4	1.9 ± 0.3	1.9 ± 0.3	2.3 ± 0.4	1.9 ± 0.3	1.5 ± 0.2	1.7 ± 0.1

(continued)

Table 3.1. (continued)

sLM	Persimmon Creek	Mungindi*	Edmonton (KY)	Maltahöhe	Anoka	Carlton*	Lamesa
V	*0.1*	*0.06*	—	*0.02*	1.0 ± 0.9	*0.02*	—
Cr	—	—	—	—	*9.1*	—	—
Mn	—	—	*1.6*	—	2.4 ± 0.5	—	—
Fe%	84 ± 1	85 ± 1	87 ± 2	89 ± 2	88 ± 2	85 ± 1	87 ± 1
Co	5400 ± 300	5300 ± 200	5600 ± 500	5200 ± 700	5700 ± 500	5700 ± 300	6000 ± 300
Ni%	15 ± 1	14 ± 1	12 ± 2	11 ± 2	11 ± 2	14 ± 1	13 ± 1
Cu	374 ± 40	230 ± 30	400 ± 100	170 ± 60	180 ± 60	220 ± 40	270 ± 40
Ga	38 ± 5	23 ± 1	25 ± 4	27 ± 2	19 ± 1	12.3 ± 0.5	12.8 ± 0.7
Ge	90 ± 10	30 ± 1	38 ± 4	49 ± 3	22.1 ± 0.8	9.5 ± 0.4	11.6 ± 0.4
As	16 ± 3	19 ± 4	21 ± 6	23 ± 4	23 ± 3	28 ± 2	28 ± 2
Mo	4.6 ± 0.7	3.9 ± 0.3	3.9 ± 0.3	4.3 ± 0.5	3.8 ± 0.4	3.2 ± 0.3	3.0 ± 0.2
Ru	1.9 ± 0.3	0.81 ± 0.09	0.8 ± 0.1	0.87 ± 0.05	0.64 ± 0.08	0.41 ± 0.07	0.57 ± 0.03
Rh	0.50 ± 0.05	0.28 ± 0.02	0.33 ± 0.02	0.38 ± 0.02	0.25 ± 0.02	0.15 ± 0.01	0.16 ± 0.01
Pd	6.9 ± 0.5	7.8 ± 0.4	5.5 ± 0.9	6.2 ± 0.9	5.7 ± 0.9	7.6 ± 0.5	5.8 ± 0.3
W	0.3 ± 0.1	0.07 ± 0.02	0.10 ± 0.02	0.13 ± 0.05	0.09 ± 0.02	0.020 ± 0.006	0.032 ± 0.007
Re	0.10 ± 0.02	0.06 ± 0.02	0.035 ± 0.008	0.01 ± 0.01	0.016 ± 0.008	0.008 ± 0.003	0.005 ± 0.003
Os	0.9 ± 0.1	0.72 ± 0.07	0.56 ± 0.07	0.11 ± 0.03	0.26 ± 0.02	0.15 ± 0.02	0.039 ± 0.009
Ir	1.1 ± 0.1	0.59 ± 0.02	0.48 ± 0.04	0.18 ± 0.03	0.18 ± 0.01	0.10 ± 0.01	0.048 ± 0.007
Pt	2.4 ± 0.3	0.68 ± 0.05	0.53 ± 0.04	0.68 ± 0.08	0.25 ± 0.02	0.12 ± 0.01	0.15 ± 0.02
Au	1.8 ± 0.3	2.1 ± 0.2	1.6 ± 0.3	1.8 ± 0.2	1.7 ± 0.2	2.0 ± 0.2	1.7 ± 0.1

(continued)

Table 3.1. (continued)

	sLH			sHL			sHH		
	Tazewell	Dayton	Freda	Quarat al Hanish*	Chebankol	Sombrerete	Kofa	ALHA 80104	Mount Magnet*
V	0.8 ± 0.5	—	*0.6*	*0.01*	0.03 ± 0.03	0.7 ± 0.4	*0.02*	—	*0.08*
Cr	—	—	—	—	—	—	—	—	—
Mn	3.3 ± 0.8	—	—	—	—	*1.4*	—	—	—
Fe%	82.1 ± 0.9	80.6 ± 0.9	76.2 ± 0.2	87 ± 1	92.4 ± 0.2	86.4 ± 0.6	79.4 ± 0.9	81.7 ± 0.9	80.8 ± 0.9
Co	6090 ± 80	5900 ± 200	6490 ± 40	5700 ± 200	5900 ± 200	4990 ± 70	7000 ± 300	6800 ± 100	5600 ± 200
Ni%	17.3 ± 0.9	19 ± 1	23.1 ± 0.2	13 ± 1	7.0 ± 0.2	13.1 ± 0.6	20 ± 1	17.6 ± 0.9	18.6 ± 0.9
Cu	360 ± 20	440 ± 20	631 ± 4	190 ± 30	70 ± 10	310 ± 30	380 ± 40	320 ± 30	230 ± 20
Ga	5.0 ± 0.2	5.4 ± 0.3	2.14 ± 0.07	19 ± 1	21.3 ± 0.5	24 ± 1	5.3 ± 0.3	6.9 ± 0.3	10.0 ± 0.3
Ge	5.2 ± 0.3	4.3 ± 0.2	3.28 ± 0.08	34 ± 1	55 ± 2	13.9 ± 0.4	11.1 ± 0.3	10.9 ± 0.3	7.8 ± 0.1
As	28 ± 2	26 ± 3	34 ± 1	33 ± 2	19 ± 2	21 ± 2	28 ± 2	28 ± 1	24 ± 1
Mo	2.6 ± 0.2	2.5 ± 0.1	1.8 ± 0.3	6.1 ± 0.5	5.8 ± 0.5	13.0 ± 0.4	3.9 ± 0.3	3.7 ± 0.4	4.6 ± 0.2
Ru	0.71 ± 0.07	0.57 ± 0.03	0.78 ± 0.07	2.5 ± 0.3	1.4 ± 0.1	1.07 ± 0.08	2.9 ± 0.3	3.1 ± 0.2	0.4 ± 0.1
Rh	0.080 ± 0.004	0.075 ± 0.003	0.063 ± 0.007	0.64 ± 0.05	0.93 ± 0.07	0.82 ± 0.07	0.63 ± 0.02	0.75 ± 0.03	0.23 ± 0.01
Pd	9.0 ± 0.2	8.3 ± 0.3	12.2 ± 0.6	6.6 ± 0.4	4.3 ± 0.4	8.6 ± 0.7	10.0 ± 0.5	8.9 ± 0.5	11.7 ± 0.4
W	0.015 ± 0.008	0.016 ± 0.006	0.009 ± 0.004	0.28 ± 0.07	0.20 ± 0.06	3.1 ± 0.2	0.29 ± 0.05	0.36 ± 0.03	0.05 ± 0.01
Re	0.005 ± 0.003	0.003 ± 0.003	0.003 ± 0.004	0.12 ± 0.52	0.014 ± 0.006	0.009 ± 0.005	0.009 ± 0.007	0.006 ± 0.002	0.0046 ± 0.0007
Os	0.17 ± 0.03	0.05 ± 0.01	0.013 ± 0.006	1.1 ± 0.1	0.06 ± 0.03	0.08 ± 0.02	0.05 ± 0.03	0.08 ± 0.01	0.016 ± 0.007
Ir	0.104 ± 0.007	0.035 ± 0.006	0.008 ± 0.004	1.13 ± 0.08	0.1 ± 0.02	0.078 ± 0.009	0.10 ± 0.03	0.091 ± 0.007	0.011 ± 0.002
Pt	0.10 ± 0.01	0.07 ± 0.02	0.03 ± 0.02	3.2 ± 0.3	1.8 ± 0.1	0.58 ± 0.05	3.8 ± 0.2	3.6 ± 0.2	0.08 ± 0.02
Au	2.0 ± 0.2	2.0 ± 0.1	1.88 ± 0.06	3.4 ± 0.6	2.0 ± 0.1	3.2 ± 0.4	3.0 ± 0.2	3.0 ± 0.3	3.6 ± 0.1

(continued)

Table 3.1. (continued)

Un	Theil Mountains	Caddo County	Mertzon	Woodbine	Pitts	Osseo	Sardis
V	*0.04*	*0.05*	*0.05*	0.020 ± 0.009	0.03 ± 0.02	0.02 ± 0.01	—
Cr	—	*8.5*	*4.0*	—	—	30 ± 20	17 ± 3
Mn	—	—	—	—	—	—	—
Fe%	92.6 ± 0.9	91 ± 1	91 ± 2	87 ± 4	86.7 ± 0.8	93 ± 1	92.8 ± 0.7
Co	4900 ± 300	5200 ± 200	4200 ± 300	5400 ± 2000	5600 ± 200	4850 ± 90	4810 ± 70
Ni%	7 ± 1	8 ± 1	9 ± 2	12 ± 5	12.8 ± 0.8	5.9 ± 0.2	6.8 ± 0.7
Cu	160 ± 40	290 ± 70	700 ± 200	200 ± 100	350 ± 30	134 ± 7	143 ± 8
Ga	78 ± 5	73 ± 3	76 ± 3	50 ± 8	37 ± 2	95.8 ± 0.6	91 ± 2
Ge	320 ± 10	297 ± 4	342 ± 8	150 ± 20	99 ± 7	480 ± 3	420 ± 10
As	14.6 ± 0.8	19 ± 1	14 ± 1	22 ± 5	19 ± 5	11.9 ± 0.7	11.3 ± 0.7
Mo	6.6 ± 0.4	6.8 ± 0.4	4.4 ± 0.4	2.7 ± 0.7	3.8 ± 0.3	7.6 ± 0.8	8.3 ± 0.5
Ru	5.6 ± 0.7	5.0 ± 0.3	5.9 ± 0.8	3.3 ± 0.5	1.9 ± 0.2	8.6 ± 0.4	8.1 ± 0.4
Rh	1.4 ± 0.1	1.32 ± 0.09	1.2 ± 0.1	0.81 ± 0.08	0.54 ± 0.03	1.53 ± 0.08	1.62 ± 0.08
Pd	4.5 ± 0.5	4.8 ± 0.6	4.6 ± 0.5	7 ± 2	6.6 ± 0.2	3.1 ± 0.2	4.5 ± 0.5
W	0.81 ± 0.05	0.9 ± 0.1	0.9 ± 0.1	0.28 ± 0.05	0.33 ± 0.04	1.34 ± 0.08	1.5 ± 0.2
Re	0.32 ± 0.08	0.29 ± 0.02	0.21 ± 0.01	0.21 ± 0.04	0.10 ± 0.02	0.55 ± 0.08	0.20 ± 0.06
Os	4.7 ± 0.4	3.0 ± 0.2	1.8 ± 0.2	2.5 ± 0.2	1.4 ± 0.2	7.0 ± 0.2	1.9 ± 0.2
Ir	4.1 ± 0.2	2.9 ± 0.2	2.2 ± 0.1	2.6 ± 0.3	1.32 ± 0.06	5.8 ± 0.2	2.2 ± 0.1
Pt	8.1 ± 0.6	7.0 ± 0.4	7.6 ± 0.2	4.1 ± 0.5	2.8 ± 0.2	10.5 ± 0.2	8.9 ± 0.3
Au	2.0 ± 0.3	2.1 ± 0.2	2.1 ± 0.2	2.4 ± 0.7	1.73 ± 0.06	1.45 ± 0.08	1.79 ± 0.06

The HSE data obtained by isotope dilution and laser ablation are in agreement with one another for some samples, but not others (Worsham et al., 2016a; **Table 2**). Typically, the *in situ* trace element concentrations are higher than concentrations obtained *via* isotope dilution, where 27% of *in situ* Os concentrations to 58% of *in situ* Ru concentrations are > 10% higher than isotope dilution concentrations (averaging 4 to 12% higher *in situ* HSE concentrations) (**Table A3.1**). Furthermore, some of the *in situ* concentrations reported here are typically > 10% higher than bulk analyses reported by Wasson and Kallemeyn (2002) for some elements, ranging from 31% of Ga concentrations to 54% of Au concentrations. (**Table A3.2** and **Fig. A3.1)**.

Bulk samples were used for isotope dilution here and by Wasson and Kallemeyn (2002) for neutron activation analysis (INAA). The use of bulk samples of some meteorites containing silicates or sulfides may have diluted the concentrations of siderophile elements, which dominantly reside in the metal phase. The generally better agreement of the *in situ* Ga data, as compared to Au, with that of Wasson and Kallemeyn (2002) is consistent with the discrepancy potentially being due, at least in part, to the direct measurement of metal vs. the measurement of bulk samples because Ga is less siderophile. Therefore, Ga could be diluted less by the presence of nonmetal phases in the bulk samples. Alternatively, the offsets between *in situ* trace element data, isotope dilution data, and literature data may be due to the choice of the internal standard. Because all the laser ablation data were obtained the same way, relative abundances between samples and variations between subgroups were likely only marginally affected by systematic variations potentially induced by the calculations. This possibility is discussed below.

Other discrepancies between the abundances determined using different methods may have resulted from variable proportions of kamacite and taenite in the samples, or insufficient sampling of the true proportions of the two phases (Hirata and Nesbitt, 1997; Hsu et al. 2000). Finally, sample heterogeneity on the mm - cm scale may contribute to some of the differences. The large offsets in the sLM, sLH, sHL, and sHH subgroups in Ru (~ 30-190%) are interpreted to reflect either an isobaric interference sampled during the laser ablation analysis of these samples, or an unknown analytical issue resulting from the lower concentrations of Ru in these samples. Rhodium concentrations are typically lower or higher (~20-85% difference) than those reported by Ryan et al. (1990), with 4 out of 7 samples having significantly lower abundances. Only the Rh concentration of Woodbine is in good agreement with Ryan et al. (1990). Rhodium abundances reported here can be used to distinguish the IAB subgroups (**Fig. 3.1**), despite disagreement with Rh data of Ryan et al. (1990).

Ten of the 18 samples for which the new Au data deviated from those of Wasson and Kallemeyn (2002) by 13-39 % were analyzed a second time, using line traces parallel to the initial line traces. These ten samples were chosen because it was suspected that lower instrumental sensitivity during these analyses (and several others) was the cause of the discrepancy. However, the averages of the two sets of line traces were within uncertainty of one another for all elements except Cu. The reason for the Cu discrepancy is unknown. Therefore, where two sets of line traces were made, the average of the two sets is reported for all elements but Cu, for which we report the data from the first set of line traces. Uncertainties of these samples are reported as 1σ of each set of line traces, propagated through the calculation of the average.

CI chondrite-normalized concentrations of siderophile elements are plotted from left to right, in order of decreasing 50% condensation temperatures (**Fig. 3.2**). Not shown in the plot are major depletions in redox-sensitive V, Cr, and Mn in the MG and each of the subgroups, as have been observed in some magmatic groups (Walker et al., 2008; McCoy et al., 2011). Other redox-sensitive elements, such as Fe, are depleted relative to the chondrite-normalized abundances of Co and Pd in the MG and subgroups. Copper is depleted in the MG and the sLL subgroup, and minor relative Cu depletions are present in a few sLM and sHL meteorites (i.e., Persimmon Creek, Maltahöhe, Mungindi, and Anoka (sLM), and Chebankol (sHL)). Tungsten and Mo, which are both moderately siderophile and redox-sensitive, generally show enrichments, relative to Os and Ir in the MG and subgroups, though the enrichments are small in the sLL subgroup. Only five MG samples show depletions in Mo, relative to chondrite-normalized Ir concentrations. Three sLM and one sLH IAB irons show depletions or chondritic abundances of W relative to Os and Ir. Similar to the HSE abundances determined by isotope dilution for bulk samples (Worsham et al., 2016a), the chondrite-normalized siderophile element patterns for meteorites within each of the subgroups are broadly similar, yet crossing patterns are common.

3.5 Discussion

3.5.1 Heterogeneity in IAB complex iron meteorites

The large uncertainties in the bulk *in situ* laser ablation data for some elements, relative to the uncertainties of bulk isotope dilution or INAA data, are not related to an

analytical issue, such as insufficient counts. Rather, heterogeneity across line traces, observed as an increase or decrease in the signal of some elements during transit across a kamacite/taenite phase boundary, indicates that the large uncertainties are a result of the variable distributions of kamacite and taenite (e.g., Ni, Pd, Au). Therefore, the abundances of several elements that partition into kamacite or taenite preferentially are variable on the mm-cm scale. This heterogeneity is reflected on a larger scale in the variable HSE data obtained for duplicates of some samples by bulk isotope dilution methods, and by the variability in reported concentrations of HSE in the literature (**Tables A2.3** and **A2.4**). For example, duplicates of Shrewsbury, one of which was only ~ 30 mg, exhibit comparatively large differences in the measured Ru abundance (Worsham et al., 2016a). While most bulk isotope dilution and INAA concentration data are likely not significantly biased due to the use of small samples, care should be taken to use larger sample sizes of coarse octahedrites where possible.

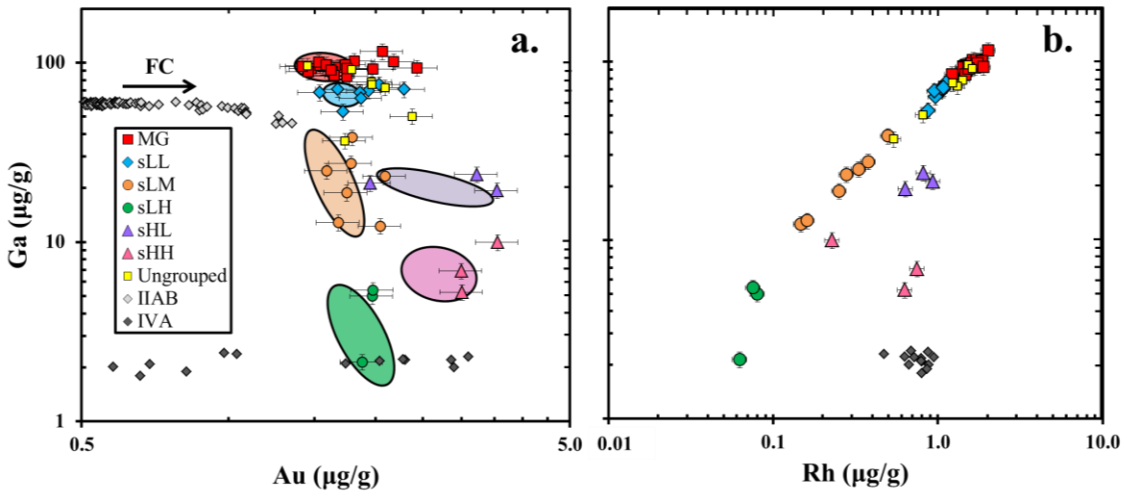

Fig. 3.1. *In situ* Ga vs. Au (a) and Ga vs. Rh (b) concentrations for IAB complex iron meteorites. Fields are adapted from Wasson and Kallemeyn (2002), with Ga vs. Au *in situ* data overlaying. In (b) the plot of Ga vs. Rh distinguishes the subgroups well. Magmatic groups IIAB and IVA are shown for comparison. Fractional crystallization (FC) produces solids with increasing Au concentrations as crystallization progresses, whereas crystallization processes produce little change in Ga and Rh concentrations. IIAB data are from Wasson et al. (2007) and IVA data are from McCoy et al. (2011).

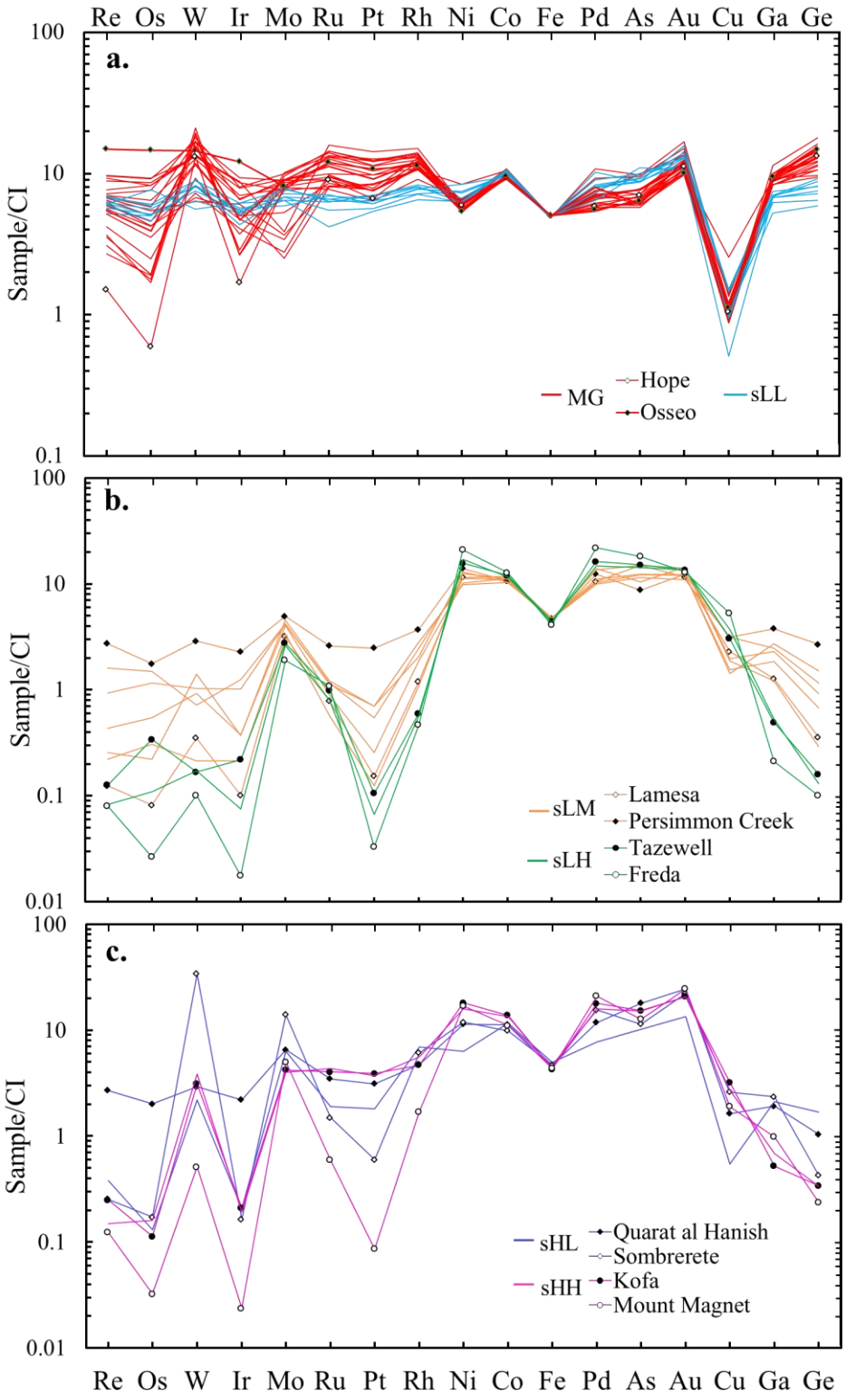

Fig. 3.2. *In situ* laser ablation concentrations normalized to the CI chondrite Orgueil (Anders and Grevesse, 1989). a) MG and sLL IAB iron meteorites, b) sLM and sLH IAB irons, and c) sHL and sHH IAB irons. The uncertainties are on the order of ~5-10% (1σ), and are excluded from the figure for clarity.

In addition to mm-cm scale heterogeneity, much of the *in situ* data for most elements measured here have higher concentrations relative to isotope dilution and literature data. The reason for this is unknown, but may be related to the internal normalization method used. If the line traces over-sampled taenite or kamacite, the internal normalization using Ni abundances may have failed to account for the partitioning tendencies of elements that do not behave similarly to Ni. This would result in a systematic bias in elements that partition into taenite more strongly than Ni (e.g., Cu and Au, in some cases) and in elements that partition into kamacite (e.g., Co) (Rasmussen et al., 1988; McDonough et al. 1999). If this is the case, it would be expected that for meteorites where taenite was oversampled, the *in situ* data would be systematically low for Co, and systematically high for Cu and Au. The opposite may be true for meteorites where kamacite was oversampled.

In comparison to the INAA data reported by Wasson and Kallemeyn (2002), the Au data are consistent with taenite being oversampled in most meteorites; however, the Cu data are typically low, and the Co data are high relative to INAA data (**Fig. A3.1**). Copper and W are the only elements that are systematically low in comparison to INAA data. For Cu, this may be because Cu is hosted in troilite in some instances (Sutton et al., 1987). *In situ* analyses would, therefore, record lower Cu concentrations than bulk analyses that incorporated troilite, which is present in many IAB meteorites. This effect could potentially mask the tendency of Cu to go into taenite more readily than Ni. However, W and Ni partition into taenite in a roughly equivalent manner (Rasmussen et al., 1988). As no dependence on partitioning is clear in the data, it is unlikely that the

internal normalization method is the source of the offsets from INAA data in more than a few IAB irons (**Fig. A3.1**).

Distributions of elements between kamacite and taenite have been measured in few iron meteorites, so the consistency of the partitioning behaviors under different chemical and physical conditions is not well constrained (e.g., Rasmussen et al., 1988; Hirata and Nesbitt, 1997; McDonough et al., 1999; Hsu et al., 2000). Therefore, although the cause of the offsets in the majority of irons examined here remains unknown, *in situ* abundance data for elements that have no strong preference for taenite or kamacite are sufficiently precise to examine differences between the subgroups. Moreover, interpretations drawn below from the large variations within and between subgroups are likely not affected by the degree of uncertainty caused by sample heterogeneity or potential analytical bias discussed above.

3.5.2 Redox sensitive element abundances in IAB subgroups

Depletions in the chondrite-normalized Fe concentrations in the IVB and IVA iron meteorite groups may represent oxidative loss of Fe (Campbell and Humayun, 2005; McCoy et al., 2011). In some instances, the depletions of redox-sensitive siderophile elements may be controlled by the decreased siderophile behavior of moderately siderophile elements, which are more likely to form oxides and partition into the silicate under oxidizing conditions. Therefore, the IVB metals, for example, were likely depleted in V, Cr, Mn, Fe, W, and potentially Ga during oxidation of the metal prior to crystallization of the cores, possibly during metal-silicate segregation (Campbell and Humayun, 2005; Walker et al., 2008). The IVB parent body may have had an oxygen

fugacity of ~ 1 log unit below the iron-wüstite buffer (IW) (Campbell and Humayun, 2005). By contrast, the precursor materials of IAB iron meteorites were likely reduced, with an oxygen fugacity intermediate between ordinary and enstatite chondrites (2.3-3.2 log units below IW – Benedix et al., 2005).

In some cases, enrichments in W and Mo may be due to their more compatible behavior during crystal-liquid fractionation, relative to the HSE (Chabot et al., 2014). However, this is not likely the case in the sLL, sLM, and sLH subgroups, because crystal-liquid fractionation did not strongly fractionate the HSE relative to one another in these subgroups (Worsham et al., 2016a). Therefore, the reduced nature of the materials during metal-silicate segregation may account for the variable enrichments in Mo and W in some IAB subgroups. Moreover, the lack of consistent Mo and W enrichments in the MG and some subgroups indicate that metals and silicates may not have equilibrated prior to metal-silicate segregation.

Depletions in Fe and Cu (and V, Cr, and Mn) are evident in the MG and sLL subgroup, despite the comparatively reduced precursor materials. With the exception of Cu in most cases, the other IAB subgroups are also depleted in Fe, V, Cr, and Mn. This likely indicates that conditions were sufficiently oxidizing to lessen the siderophile behavior of these elements. The MG and sLL metals may have segregated under more oxidizing conditions than the other subgroups, given the large depletion in Cu. Alternately, Cu may have been preferentially hosted in troilite in these meteorites. Copper preferentially partitions into troilite relative to metal when Ni contents in the metal are < 10 wt. % (Sutton et al., 1987). The MG and sLL irons, and some sLM and sLH irons have Ni contents approximately ≤ 10 wt. %, and these are the only subgroups

which show Cu depletions. The IAB subgroups and irons with higher Ni contents do not exhibit Cu depletions. Therefore, the latter interpretation that Cu is hosted in troilite in the MG and sLL subgroup irons, and in some sLM and sLH irons, is favored. Consequently, the oxidation states of most IAB subgroups were likely similar, considering the shared features of relative enrichments in Mo and W, and depletions in Fe, V, Cr, and Mn.

3.5.3. Volatile siderophile element abundances in IAB subgroups

A shared feature of the sLM, sLH, sHL, and sHH subgroups is a "hump" in the chondrite-normalized siderophile element patterns between Pt and Ge (**Fig. 3.2**). The relative abundances of elements from Pt to Ge, plotted in order of the 50 % condensation temperatures, increase to a maximum of generally chondritic relative abundances between Ni and Au. By contrast, the siderophile elements of the MG and sLL are in roughly chondritic relative abundances. The enrichment of elements between Rh and Cu likely reflects a primary feature of the precursor materials, rather than a crystallization process. This is because the sLM, sLH, sHL, and sHH subgroups crystallized by different processes (Worsham et al., 2016a). Further, Worsham et al. (2016a) reported that the calculated initial metallic melt compositions of the sLM and sLH subgroups had distinctive chondrite-normalized HSE patterns, compared to other iron meteorite groups, in which Pd was enriched relative to Re, Os, Ir, Ru, and Pt. Consistent with this, the *in situ* data reported here show that the HSE Rh and Au, along with other elements between Rh and Cu, are also enriched. The modeling of the sHL and sHH subgroups also indicated that their initial melts were enriched in Pd (Worsham et al., 2016a). Because the

HSE are not expected to be strongly fractionated from one another during metal-silicate segregation, it is likely that the "hump" feature is related to a nebular process(es).

In some fractionally crystallized magmatic iron meteorite groups, variations in siderophile element abundances appear to be related to their comparative volatilities (Walker et al., 2008; McCoy et al., 2011). For example, the IVB iron meteorite group is strongly depleted in volatile siderophile elements such as Au, Cu, Ga, and Ge, suggesting that the precursor materials of the IVB parent body were subject to high temperature evaporation and/or condensation-driven nebular processing (Campbell and Humayun, 2005; Walker et al., 2008). Likewise, the abundances of volatile siderophile elements in the individual IAB subgroups suggest that volatility-driven nebular processing may have resulted in some of the observed differences in the subgroups.

The enrichment of the elements between Rh and Cu, relative to the surrounding elements, may be accounted for if the precursors incorporated a larger proportion of material that condensed over a temperature range of ~1390-1037 K, corresponding to the 50% condensation temperatures of Rh and Cu (Lodders, 2003). This is consistent with the interpretation that the precursor materials of the sLM, sLH, sHL, and sHH subgroups were late-stage condensates from the solar nebula (Worsham et al., 2016a). Alternately, Cu, Ga, and Ge may have also been condensed in chondritic relative proportions over a temperature range of ~1390-885 K, and later evaporation processes may have depleted these elements, relative to the elements with condensation temperatures that were intermediate between Ni and Au. The present data do not recommend one temperature range of condensation over the other. Further work is needed to determine if late-stage condensation alone may account for the distribution of volatile siderophile elements, or if

more complex multi-stage condensation/evaporation events are required. Finally, this interpretation of the "hump" feature may be inconsistent with the interpretation of Worsham et al. (2016a) that the sLM subgroup was S-rich. This is because S is more volatile than Ge and would, therefore, be depleted in materials condensed above ~900 K. As the abundance of S is not well constrained by the modeling results of Worsham et al. (2016a), the results of the modeling and the interpretation that the precursor materials are late-stage condensates are still applicable.

3.6 Conclusions

The *in situ* measurement of trace element abundances in the IAB complex highlights the nature of the chemical heterogeneity in IAB meteorites. The variable distributions of kamacite and taenite result in mm-cm scale heterogeneity in a range of trace elements. Despite the relatively large uncertainties resulting from chemical heterogeneity, orders-of-magnitude variations of the siderophile elements within and between subgroups indicate that Mo and W are enriched in some IAB irons, most likely due to comparatively reducing conditions during metal-silicate segregation, although oxidative loss of Fe, V, Cr, and Mn is still evident.

The sLM, sLH, sHL, and sHH subgroups exhibit siderophile element abundances that were strongly influenced by volatility-controlled processes. By contrast, the relative siderophile element abundances in the MG and the sLL subgroup show no strong volatility controls. The enrichment of elements in the order of decreasing 50% condensation temperatures from Rh to Cu, relative to elements with higher and lower

condensation temperatures indicates that the sLM, sLH, sHH, and sHL parent body or bodies formed from materials which condensed in a narrow temperature range from ~1390-1030 K. If the enrichment of elements between Rh and Cu in the sLM, sLH, sHL, and sHH subgroups was caused by late-stage condensation, it implies that these subgroups formed in a comparatively cool portion of the solar nebula, or at a later time, relative to the MG and sLL subgroup.

Appendix for Chapter 3.

In situ trace element data are compared to isotope dilution HSE data and literature data from Wasson and Kallemeyn (2002) in **Tables A3.1** and **A3.2**. The concentrations determined by *in situ* laser ablation techniques are typically slightly higher than both isotope dilution abundances and those reported by Wasson and Kallemeyn (2002) (**Fig. A3.1**). This difference may be related to the nature of the *in situ* measurement vs. bulk sample measurement, or it may be an effect of the calculation method. For instance, most of the Au data are within uncertainty of those of Wasson and Kallemeyn (2002), but several are 15-40 % higher (e.g., Odessa, Seymour).

Table A3.1. Comparison of HSE data determined by isotope dilution (ID) and *in situ* laser ablation (LA)

Sample	Re (ID)	Re (LA)	Os (ID)	Os (LA)	Ir (ID)	Ir (LA)	Ru (ID)	Ru (LA)	Pt (ID)	Pt (LA)	Pd (ID)	Pd (LA)
IAB main group												
Landes	0.3548	0.36 ± 0.02	4.368	4.4 ± 0.1	4.293	4.44 ± 0.07	9.805	9.0 ± 0.5	10.50	11.0 ± 0.1	3.581	3.3 ± 0.1
Seligman	0.3087	0.34 ± 0.02	3.891	4.0 ± 0.1	3.293	3.34 ± 0.06	7.754	8 ± 1	8.886	9.5 ± 0.2	3.502	3.9 ± 0.2
Yenberrie	0.2906	0.36 ± 0.04	3.926	4.5 ± 0.2	3.463	4.10 ± 0.09	5.536	5.8 ± 0.6	6.359	7.4 ± 0.3	3.647	3.9 ± 0.2
Ballinger average	0.2770	0.26 ± 0.02	3.145	3.1 ± 0.2	3.124	3.1 ± 0.2	6.561	6.8 ± 0.2	7.266	7.4 ± 0.3	3.392	3.0 ± 0.2
Cranbourne	0.2750	0.33 ± 0.03	3.670	4.2 ± 0.1	3.614	4.2 ± 0.2	9.662	11.3 ± 0.3	11.38	13.9 ± 0.6	3.398	4.2 ± 0.3
Campo del Cielo	0.2741	0.29 ± 0.04	3.632	4.0 ± 0.2	3.308	3.7 ± 0.2	6.725	7.1 ± 0.5	8.213	9.5 ± 0.5	3.403	3.0 ± 0.1
New Leipzig	0.2724	0.25 ± 0.05	2.723	2.8 ± 0.2	2.904	3.1 ± 0.1	8.626	9.1 ± 0.8	9.898	10.2 ± 0.4	3.527	3.8 ± 0.3
Magura	0.2692	0.27 ± 0.02	3.743	3.7 ± 0.1	3.648	3.81 ± 0.06	9.892	9.6 ± 0.3	11.43	12.4 ± 0.1	3.254	3.4 ± 0.1
Odessa	0.2243	0.25 ± 0.03	2.501	2.6 ± 0.2	2.572	2.9 ± 0.1	5.392	5.8 ± 0.4	6.749	8.1 ± 0.4	3.795	6.0 ± 0.6
Jenkins	0.2116	0.24 ± 0.02	2.327	2.4 ± 0.1	2.207	2.39 ± 0.09	5.403	6.5 ± 0.8	6.772	7.3 ± 0.2	3.585	3.7 ± 0.4
ALHA 77283	0.2102	0.23 ± 0.03	1.891	2.1 ± 0.1	2.327	2.6 ± 0.1	5.687	5.8 ± 0.9	6.867	8.3 ± 0.2	4.526	4.1 ± 0.5
Youndegin	0.2024	0.22 ± 0.06	2.134	2.2 ± 0.2	2.217	2.4 ± 0.1	6.354	6.1 ± 0.5	6.960	7.4 ± 0.4	4.010	4.0 ± 0.3
Smithville	0.1914	0.21 ± 0.03	1.884	2.0 ± 0.1	2.028	2.27 ± 0.09	6.096	7.0 ± 0.9	6.422	7.3 ± 0.3	3.734	3.8 ± 0.4
Seymour	0.1665	0.19 ± 0.02	1.673	1.7 ± 0.1	1.807	1.94 ± 0.06	5.636	6.8 ± 0.4	6.383	7.6 ± 0.2	3.627	5.2 ± 0.2
Bogou	0.1589	0.16 ± 0.01	1.219	1.2 ± 0.1	1.747	1.8 ± 0.1	5.178	6 ± 1	5.999	6.2 ± 0.4	3.754	3.6 ± 0.4
Burgavali	0.1321	0.14 ± 0.03	0.7592	0.8 ± 0.1	1.217	1.36 ± 0.09	9.283	10.0 ± 0.4	10.12	11.1 ± 0.4	3.305	3.2 ± 0.1
Morasko	0.1068	0.12 ± 0.02	0.7990	0.87 ± 0.06	1.141	1.26 ± 0.04	9.612	10.3 ± 0.2	10.26	11.8 ± 0.2	3.306	3.4 ± 0.2
Seelasgen	0.1043	0.10 ± 0.02	0.8634	0.92 ± 0.04	1.143	1.27 ± 0.03	9.643	9.4 ± 0.3	10.34	11.9 ± 0.3	3.314	3.2 ± 0.2
Sarepta average	0.1020	0.13 ± 0.04	0.8472	0.94 ± 0.06	1.134	1.25 ± 0.07	9.684	10.3 ± 0.3	10.23	12.0 ± 0.6	3.360	4.0 ± 0.2
Hope	0.05426	0.056 ± 0.008	0.2889	0.29 ± 0.03	0.7531	0.80 ± 0.01	6.584	6.4 ± 0.2	5.893	6.4 ± 0.1	3.449	3.24 ± 0.08
IAB sLL (low Au, low Ni) subgroup												
Shrewsbury average	0.2265	0.23 ± 0.02	3.615	3.7 ± 0.2	2.723	2.9 ± 0.1	3.819	3.0 ± 0.4	4.868	5.3 ± 0.2	4.476	4.4 ± 0.4
Comanche	0.2264	0.25 ± 0.02	2.698	2.9 ± 0.1	2.614	2.94 ± 0.07	4.577	4.7 ± 0.9	5.738	6.9 ± 0.2	4.499	5 ± 1
Bahjoi	0.2202	0.26 ± 0.03	2.598	2.9 ± 0.2	2.429	2.71 ± 0.08	4.659	4.9 ± 0.6	5.739	6.4 ± 0.1	4.370	4.6 ± 0.5
Toluca	0.2159	0.22 ± 0.03	2.232	2.2 ± 0.1	1.962	2.1 ± 0.1	4.351	4.7 ± 0.8	5.426	6.0 ± 0.3	4.283	4.4 ± 0.6
Deport	0.2158	0.23 ± 0.02	2.587	2.7 ± 0.1	2.429	2.62 ± 0.09	4.633	5.0 ± 0.6	5.613	6.0 ± 0.2	4.389	5.7 ± 0.9
Balfour Downs	0.2120	0.21 ± 0.02	2.422	2.5 ± 0.1	2.302	2.49 ± 0.04	4.148	4.6 ± 0.7	5.613	6.3 ± 0.2	4.809	5.0 ± 0.5
Bischtube average	0.2032	0.23 ± 0.05	2.428	2.5 ± 0.2	2.332	2.5 ± 0.1	3.688	3.9 ± 0.6	4.880	5.5 ± 0.3	4.094	4.1 ± 0.5
Goose Lake	0.1882	0.19 ± 0.02	2.217	2.4 ± 0.1	2.139	2.42 ± 0.08	4.509	4.5 ± 0.5	6.094	6.8 ± 0.2	4.056	3.6 ± 0.2
IAB sLM (low Au, medium Ni) subgroup												
Persimmon Creek	0.08073	0.10 ± 0.02	0.7306	0.9 ± 0.1	0.8402	1.1 ± 0.1	1.360	1.9 ± 0.3	2.026	2.4 ± 0.3	5.585	6.9 ± 0.5
Mungindi	0.04786	0.06 ± 0.02	0.6784	0.72 ± 0.07	0.5703	0.59 ± 0.02	0.4262	0.81 ± 0.09	0.6107	0.68 ± 0.05	5.881	7.8 ± 0.4
Edmonton (KY) average	0.03880	0.035 ± 0.008	0.6506	0.56 ± 0.07	0.5052	0.48 ± 0.04	0.5190	0.8 ± 0.1	0.5856	0.53 ± 0.04	5.708	5.5 ± 0.9
Maltahohe	0.01642	0.01 ± 0.01	0.1214	0.11 ± 0.03	0.1650	0.18 ± 0.03	0.6410	0.87 ± 0.05	0.6262	0.68 ± 0.08	5.390	6.2± 0.9
Anoka average	0.01384	0.016 ± 0.008	0.2602	0.26 ± 0.02	0.1650	0.18 ± 0.01	0.2547	0.64 ± 0.08	0.2228	0.25 ± 0.02	5.784	5.7 ± 0.9
Carlton	0.007113	0.008 ± 0.003	0.1400	0.15 ± 0.02	0.09249	0.10 ± 0.01	0.09770	0.41 ± 0.07	0.1019	0.12 ± 0.01	6.689	7.6 ± 0.5
Lamesa average	0.004644	0.005 ± 0.003	0.03978	0.039 ± 0.009	0.04800	0.048 ± 0.007	0.1427	0.57 ± 0.03	0.1388	0.15 ± 0.02	6.636	5.8 ± 0.3

Table A3.1. (cont.)

Sample	Re (ID)	Re (LA)	Os (ID)	Os (LA)	Ir (ID)	Ir (LA)	Ru (ID)	Ru (LA)	Pt (ID)	Pt (LA)	Pd (ID)	Pd (LA)
IAB sLH (low Au, high Ni) subgroup												
Tazewell	0.007512	0.005 ± 0.003	0.1347	0.17 ± 0.03	0.08784	0.104 ± 0.007	0.06204	0.71 ± 0.07	0.08593	0.10 ± 0.01	8.687	9.0 ± 0.2
Dayton average	0.002592	0.003 ± 0.003	0.04182	0.05 ± 0.01	0.03003	0.035 ± 0.006	0.04867	0.57 ± 0.03	0.04770	0.07 ± 0.02	8.228	8.3 ± 0.3
Freda	0.0006164	0.003 ± 0.004	0.008043	0.013 ± 0.006	0.007500	0.008 ± 0.004	0.03000	0.78 ± 0.07	0.02302	0.03 ± 0.02	12.21	12.2 ± 0.6
IAB sHL (high Au, low Ni) subgroup												
Quarat al Hanish	0.08675	0.12 ± 0.52	0.9434	1.1 ± 0.1	0.9576	1.13 ± 0.08	2.214	2.5 ± 0.3	2.671	3.2 ± 0.3	6.066	6.6 ± 0.4
Chebankol	0.008632	0.014 ± 0.006	0.06331	0.06 ± 0.03	0.1029	0.1 ± 0.02	1.328	1.4 ± 0.1	1.711	1.8 ± 0.1	4.578	4.3 ± 0.4
Sombrerete	0.006099	0.009 ± 0.005	0.06187	0.08 ± 0.02	0.07380	0.078 ± 0.009	0.5376	1.07 ± 0.08	0.4682	0.58 ± 0.05	5.369	8.6 ± 0.7
IAB sHH (high Au, high Ni) subgroup												
Kofa	0.008218	0.009 ± 0.007	0.07238	0.05 ± 0.03	0.09922	0.10 ± 0.03	2.554	2.9 ± 0.3	3.671	3.8 ± 0.2	9.650	10.0 ± 0.5
ALHA 80104	0.007584	0.006 ± 0.002	0.07094	0.08 ± 0.01	0.09042	0.091 ± 0.007	2.597	3.1 ± 0.2	3.225	3.6 ± 0.2	8.641	8.9 ± 0.5
Mount Magnet	0.0006252	0.0046 ± 0.0007	0.05650	0.016 ± 0.007	0.006176	0.011 ± 0.002	0.1426	0.4 ± 0.1	0.05990	0.08 ± 0.02	9.212	11.7 ± 0.4
IAB ungrouped												
Theil Mountains	0.2853	0.32 ± 0.08	3.784	4.7 ± 0.4	6.731	4.1 ± 0.2	5.151	5.6 ± 0.7	5.934	8.1 ± 0.6	3.743	4.5 ± 0.5
Caddo County	0.2540	0.29 ± 0.02	2.728	3.0 ± 0.2	2.515	2.9 ± 0.2	4.696	5.0 ± 0.3	6.058	7.0 ± 0.4	4.267	4.8 ± 0.6
Mertzon	0.1880	0.21 ± 0.01	1.701	1.8 ± 0.2	2.160	2.2 ± 0.1	3.959	5.9 ± 0.8	7.443	7.6 ± 0.2	3.541	4.6 ± 0.5
Woodbine	0.1779	0.21 ± 0.04	2.062	2.5 ± 0.2	3.113	2.6 ± 0.3	2.389	3.3 ± 0.5	3.053	4.1 ± 0.5	6.181	7 ± 2
Pitts	0.1126	0.10 ± 0.02	1.449	1.4 ± 0.2	1.336	1.32 ± 0.06	1.765	1.9 ± 0.2	2.414	2.8 ± 0.2	6.625	6.6 ± 0.2
IAB unclassified												
Osseo	0.5103	0.55 ± 0.08	7.313	7.0 ± 0.2	5.934	5.8 ± 0.2	8.770	8.6 ± 0.4	10.66	10.5 ± 0.2	3.368	3.1 ± 0.2
Sardis	0.1855	0.20 ± 0.06	1.763	1.9 ± 0.2	2.023	2.2 ± 0.1	7.567	8.1 ± 0.4	8.291	8.9 ± 0.3	3.422	4.5 ± 0.5

Table A3.2. Concentrations of major and trace elements determined by *in situ* laser ablation (LA) techniques compared to literature concentrations from Wasson and Kallemeyn (2002). Data are reported in µg/g, except for Ni (wt. %). The Ni(LA*) concentrations are the averages of the normalized internal standard values described in the main text.

Sample	Co (LA)	Co (Lit.)	Ni (LA*)	Ni (Lit.)	Cu (LA)	Cu (Lit.)	Ga (LA)	Ga (Lit.)	Ge (LA)	Ge (Lit.)	As (LA)	As (Lit.)	W (LA)	W (Lit.)	Au (LA)	Au (Lit.)
IAB main group																
Landes	4690 ± 80	4510	6.3 ± 0.2	6.55	310 ± 30	317	93 ± 2	87.5	453 ± 6	414	11.0 ± 0.2	10.2	1.55 ± 0.09	1.42	1.48 ± 0.05	1.417
Seligman	4800 ± 200	4590	6.2 ± 0.5	6.67	130 ± 10	162	102 ± 2	93.5	464 ± 7	423	14.3 ± 0.7	12.2	1.27 ± 0.05	1.22	1.8 ± 0.1	1.491
Yenberrie	4820 ± 80	4720	6.2 ± 0.2	6.82	104 ± 5	159	84 ± 1	84.0	346 ± 5	319	14.2 ± 0.8	12.6	1.2 ± 0.1	1.03	1.75 ± 0.07	1.535
Ballinger average	4890 ± 60	4610	6.2 ± 0.1	6.78	118 ± 6	148	89 ± 2	87.8	394 ± 7	341	12.2 ± 0.3	12.1	1.17 ± 0.08	1.25	1.46 ± 0.08	1.490
Cranbourne	5160 ± 80	4600	6.7 ± 0.3	6.82	130 ± 10	139	115 ± 2	83.8	584 ± 6	372	13.2 ± 0.6	13.1	1.25 ± 0.07	1.18	2.1 ± 0.2	1.550
Campo del Cielo	4800 ± 60	4580	6.3 ± 0.2	6.68	109 ± 5	140	95 ± 6	93.0	420 ± 30	394	12.2 ± 1	11.8	1.22 ± 0.06	1.31	1.56 ± 0.09	1.490
New Leipzig	4600 ± 400	4650	6.7 ± 0.7	6.68	140 ± 20	149	94 ± 2	92.2	443 ± 6	445	12.4 ± 0.6	11.3	1.57 ± 0.08	1.47	1.7 ± 0.3	1.439
Magura	4900 ± 100	4620	6.0 ± 0.2	6.44	105 ± 5	136	95 ± 1	95.6	486 ± 8	483	11.0 ± 0.3	10.3	1.66 ± 0.07	1.65	1.42 ± 0.02	1.461
Odessa	5300 ± 600	4720	9 ± 2	7.19	160 ± 50	129	94 ± 5	75.0	320 ± 10	279	18 ± 2	14.3	0.59 ± 0.04	0.98	2.4 ± 0.3	1.611
Jenkins	4800 ± 300	4550	6.7 ± 0.7	6.92	120 ± 30	151	89 ± 6	87.7	380 ± 10	353	13.4 ± 0.3	13.1	1.09 ± 0.07	1.28	1.09 ± 0.07	1.580
ALHA 77283	5500 ± 200	4870	7.0 ± 0.9	7.28	130 ± 30	145	92 ± 4	81.1	347 ± 4	320	19 ± 1	15.4	0.62 ± 0.03	1.06	2.0 ± 0.2	1.707
Youndegin	4900 ± 200	4700	6.5 ± 0.8	6.83	125 ± 2	145	84 ± 1	84.5	367 ± 5	330	14.1 ± 0.4	13.0	1.06 ± 0.09	1.07	1.64 ± 0.09	1.540
Smithville	5200 ± 500	4650	7.2 ± 0.7	6.92	140 ± 30	160	98 ± 6	87.1	400 ± 10	363	14.2 ± 0.7	13.8	0.76 ± 0.04	1.05	1.7 ± 0.1	1.610
Seymour	5400 ± 200	4680	7.1 ± 0.5	6.78	110 ± 20	159	102 ± 3	87.2	419 ± 7	381	18 ± 1	12.8	0.67 ± 0.04	1.15	2.2 ± 0.2	1.562
Bogou	4700 ± 300	4670	7.3 ± 1	7.33	170 ± 50	163	85 ± 7	78.5	309 ± 6	301	14.4 ± 0.5	14.2	0.86 ± 0.08	1.09	1.6 ± 0.2	1.645
Burgavali	4700 ± 100	4450	6.2 ± 0.3	6.64	121 ± 7	168	97 ± 2	97.1	495 ± 8	519	10.6 ± 0.3	11.0	1.5 ± 0.3	1.90	1.5 ± 0.1	1.435
Morasko	4890 ± 90	4530	6.2 ± 0.3	6.76	134 ± 7	154	100 ± 1	102.7	529 ± 2	500	12.5 ± 0.4	11.6	1.7 ± 0.1	1.78	1.53 ± 0.07	1.505
Seelasgen	4800 ± 100	4540	6.0 ± 0.3	6.59	127 ± 6	159	97 ± 2	102.8	507 ± 6	493	11.4 ± 0.5	10.7	1.8 ± 0.1	1.85	1.58 ± 0.08	1.523
Sarepta average	4700 ± 200	4650	6.1 ± 0.3	6.59	108 ± 8	149	93 ± 3	98.8	500 ± 10	456	11.2 ± 0.8	11.5	2.0 ± 0.1	1.39	1.7 ± 0.2	1.464
Hope	4790 ± 50	4600	6.5 ± 0.1	7.06	124 ± 2	148	91 ± 2	89.9	431 ± 6	402	12.9 ± 0.5	11.2	1.21 ± 0.06	1.35	1.62 ± 0.03	1.510
IAB sLL (low Au, low Ni) subgroup																
Shrewsbury average	5400 ± 100	4880	7.0 ± 0.6	8.53	130 ± 20	217	53 ± 2	62.6	193 ± 3	196	16.4 ± 0.9	17.3	0.52 ± 0.09	0.610	1.7 ± 0.2	1.750
Comanche	4900 ± 400	4990	8 ± 2	8.24	180 ± 90	176	76 ± 9	76.3	264 ± 7	270	17.0 ± 0.8	17.0	0.83 ± 0.03	0.890	2.0 ± 0.4	1.720
Bahjoi	5200 ± 300	4830	7 ± 1	7.94	110 ± 60	146	70 ± 6	69.7	285 ± 7	273	17 ± 1	17.1	0.74 ± 0.06	0.960	1.9 ± 0.3	1.754
Toluca	4900 ± 500	4900	8 ± 1	8.02	180 ± 50	170	68 ± 6	68.9	235 ± 9	245	16 ± 1	16.5	0.76 ± 0.07	0.830	1.9 ± 0.3	1.718
Deport	4800 ± 500	4730	9 ± 2	8.05	170 ± 80	177	71 ± 5	64.8	270 ± 10	255	16 ± 2	17.2	0.76 ± 0.07	1.120	2.3 ± 0.4	1.685
Balfour Downs	5000 ± 400	4870	8 ± 2	8.38	140 ± 40	161	63 ± 5	58.6	210 ± 6	194	18 ± 1	16.6	0.59 ± 0.05	1.140	1.9 ± 0.3	1.695
Bischtube average	5300 ± 100	4920	6.8 ± 0.4	7.78	61 ± 9	136	68 ± 3	67.9	247 ± 4	238	20 ± 2	16.9	0.70 ± 0.06	0.680	1.5 ± 0.2	1.687
Goose Lake	5300 ± 100	4860	6.9 ± 0.4	8.24	120 ± 10	172	71 ± 3	69.4	300 ± 10	305	19 ± 2	16.4	0.82 ± 0.04	1.070	1.7 ± 0.1	1.636
IAB sLM (low Au, medium Ni) subgroup																
Persimmon Creek	5400 ± 300	5480	15 ± 1	13.79	374 ± 40	382	38 ± 5	33.2	90 ± 10	78.3	16 ± 3	15.8	0.3 ± 0.1	0.230	1.8 ± 0.3	1.535
Mungindi	5300 ± 200	5500	14 ± 1	11.86	230 ± 30	248	23 ± 1	18.8	30 ± 1	22.2	19 ± 4	22.4	0.07 ± 0.02		2.1 ± 0.2	1.665
Edmonton (KY) av.	5600 ± 500	5480	12 ± 2	12.90	400 ± 100	404	25 ± 4	24.2	38 ± 4	34.3	21 ± 6	21.3	0.10 ± 0.02	0.290	1.6 ± 0.3	1.705
Maltahohe	5200 ± 700	5260	11 ± 2	11.40	170 ± 60	163	27 ± 2	24.0	49 ± 3	38.5	23 ± 4	19.2	0.13 ± 0.05	0.200	1.8 ± 0.2	1.600
Anoka average	5700 ± 500	5560	11 ± 2	11.80	180 ± 60	197	19 ± 1	17.8	22.1 ± 0.8	15.7	23 ± 3	21.4	0.09 ± 0.02	0.110	1.7 ± 0.2	1.617
Carlton	5700 ± 300	5670	14 ± 1	13.23	220 ± 40	260	12.3 ± 0.5	11.9	9.5 ± 0.4	8.59	28 ± 2	23.5	0.020 ± 0.006	<0.2	2.0 ± 0.2	1.737
Lamesa average	6000 ± 300	5600	13 ± 1	13.28	270 ± 40	323	12.8 ± 0.7	13.1	11.6 ± 0.4	11.9	28 ± 2	24.2	0.032 ± 0.007	<0.1	1.7 ± 0.1	1.754

Table A3.2. (cont.)

Sample	Co (LA)	Co (Lit.)	Ni (LA*)	Ni (Lit.)	Cu (LA)	Cu (Lit.)	Ga (LA)	Ga (Lit.)	Ge (LA)	Ge (Lit.)	As (LA)	As (Lit.)	W (LA)	W (Lit.)	Au (LA)	Au (Lit.)
IAB sLH (low Au, high Ni) subgroup																
Tazewell	6090 ± 80	5890	17.3 ± 0.9	17.06	360 ± 20	391	5.0 ± 0.2	4.75	5.2 ± 0.3	3.78	28 ± 2	26.6	0.015 ± 0.008	<0.10	2.0 ± 0.2	1.763
Dayton average	5900 ± 200	5920	19 ± 1	17.10	440 ± 20	435	5.4 ± 0.3	4.85	4.3 ± 0.2	3.41	26 ± 3	25.2	0.016 ± 0.006	<0.2	2.0 ± 0.1	1.736
Freda	6490 ± 40	6290	23.1 ± 0.2	23.21	631 ± 4	672	2.14 ± 0.07	2.12	3.28 ± 0.08	2.24	34 ± 1	30.1	0.009 ± 0.004		1.88 ± 0.06	1.895
IAB sHL (high Au, low Ni) subgroup																
Quarat al Hanish	5700 ± 200	5510	13 ± 1	12.75	190 ± 30	212	19 ± 1	16.7	34 ± 1	29.7	33 ± 2	26.7	0.28 ± 0.07	0.270	3.4 ± 0.6	2.78
Chebankol	5900 ± 200	5160	7.0 ± 0.2	9.17	70 ± 10	108	21.3 ± 0.5	22.8	55 ± 2	52.5	19 ± 2	18.4	0.20 ± 0.06	0.300	2.0 ± 0.1	2.00
Sombrerete	4990 ± 70	5070	13.1 ± 0.6	9.84	310 ± 30	247	24 ± 1	19.9	13.9 ± 0.4	11.3	21 ± 2	21.1	3.1 ± 0.2	2.040	3.2 ± 0.4	2.26
IAB sHH (high Au, high Ni) subgroup																
Kofa	7000 ± 300	6940	20 ± 1	18.39	380 ± 40	465	5.3 ± 0.3	4.79	11.1 ± 0.3	8.61	28 ± 2	28.4	0.29 ± 0.05	0.34	3.0 ± 0.2	2.85
ALHA 80104	6800 ± 100	6800	17.6 ± 0.9	15.86	320 ± 30	298	6.9 ± 0.3	5.87	10.9 ± 0.3	10.3	28 ± 1	26.3	0.36 ± 0.03	0.37	3.0 ± 0.3	2.63
Mount Magnet	5600 ± 200	6050	18.6 ± 0.9	14.57	230 ± 20	195	10.0 ± 0.3	7.67	7.8 ± 0.1	5.26	24 ± 1	24.7	0.05 ± 0.01	<0.4	3.6 ± 0.1	2.64
IAB ungrouped																
Theil Mountains	4900 ± 300	4700	7 ± 1	8.04	160 ± 40	174	78 ± 5	73.6	320 ± 10	234	14.6 ± 0.8	12.7	0.81 ± 0.05	1.02	2.0 ± 0.3	1.529
Caddo County	5200 ± 200	4900	8 ± 1	9.42	290 ± 70	352	73 ± 3	68.4	297 ± 4	273	19 ± 1	14.5	0.9 ± 0.1	1.05	2.1 ± 0.2	1.607
Mertzon	4200 ± 300	3970	9 ± 2	9.08	700 ± 200	653	76 ± 3	65.5	342 ± 8	293	14 ± 1	12.7	0.9 ± 0.1	0.96	2.1 ± 0.2	1.528
Woodbine	5400 ± 2000	5420	12 ± 5	10.05	200 ± 100	167	50 ± 8	35.8	150 ± 20	114	22 ± 5	17.8	0.28 ± 0.05	0.6	2.4 ± 0.7	1.640
Pitts	5600 ± 200	5600	12.8 ± 0.8	12.81	350 ± 30	376	37 ± 2	34.5	99 ± 7	95.6	19 ± 5	20.2	0.33 ± 0.04	0.33	1.73 ± 0.06	1.700
IAB unclassified																
Osseo	4850 ± 90	4610	5.9 ± 0.2	6.71	134 ± 7	161	95.8 ± 0.6	92.4	480 ± 3	463	11.9 ± 0.7	11.1	1.34 ± 0.08	1.62	1.45 ± 0.08	1.560
Sardis	4810 ± 70	4610	6.8 ± 0.7	6.73	143 ± 8	138	91 ± 2	98.1	420 ± 10	472	11.3 ± 0.7	12.1	1.5 ± 0.2	1.30	1.79 ± 0.06	1.520

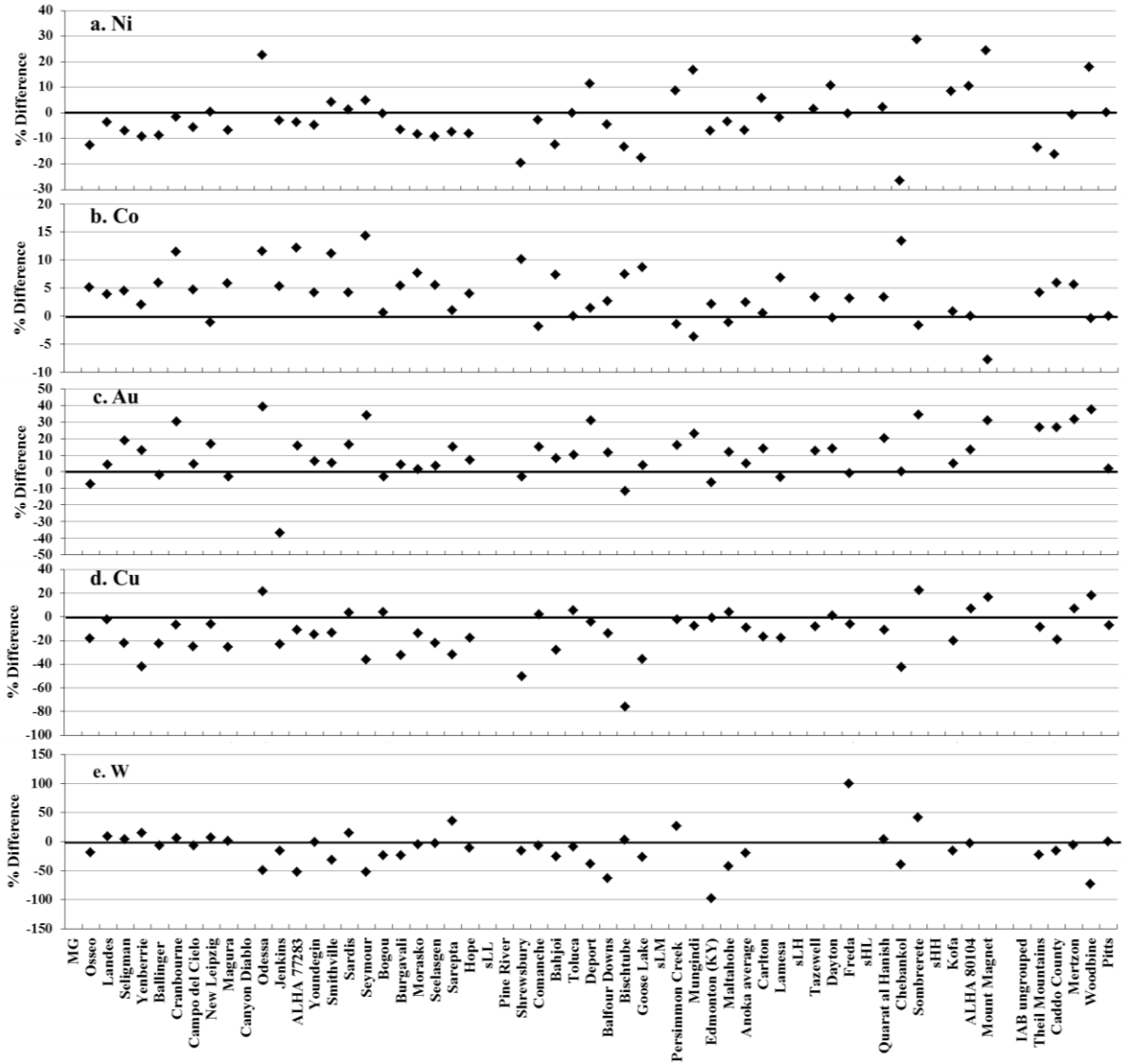

Fig. A3.1. Percent differences for *in situ* data vs. INAA data from Wasson and Kallemeyn (2002) for Ni (a), Co (b), Au (c), Cu (d), and W (e). In (a) samples which plot significantly above the line may have oversampled taenite, and samples that plot below the line may have oversampled kamacite (see main section 3.5.1 for details). Copper and W data reported here are systematically low relative to the INAA data, whereas Co and Au are systematically high.

Chapter 4: High-precision molybdenum isotope analysis by negative thermal ionization mass spectrometry

4.1 Abstract

Procedures for the separation, purification, and high-precision analysis of mass-independent isotopic variations in molybdenum (Mo) using negative thermal ionization mass spectrometry are reported. Separation and purification of Mo from silicate and metal matrices is achieved using a two-stage anion exchange chromatographic procedure. Molybdenum is ionized as the MoO_3^- species using a double filament assembly. The MoO_3^- ion beams are collected using Faraday cup detectors equipped with a mixed array of amplifiers utilizing 10^{11} and 10^{12} Ω resistors, which allows for *in situ* measurement and correction of O isobars. The long-term external reproducibility of $^{97}Mo/^{96}Mo$, the most precisely measured Mo isotope ratio, is ± 5.4 ppm (2SD), based on the repeated analyses of the *Alfa Aesar Specpure*® Mo plasma standard and using $^{98}Mo/^{96}Mo$ for fractionation correction. The long-term external reproducibilities of $^{92}Mo/^{96}Mo$, $^{94}Mo/^{96}Mo$, $^{95}Mo/^{96}Mo$, and $^{100}Mo/^{96}Mo$ are ± 107, 37, 23, and 32 ppm (2SD), respectively. With this precision, smaller differences in Mo isotopic compositions can be resolved than have been previously possible.

4.2 Introduction

The molybdenum (Mo) isotopic system is uniquely suited to address current issues in cosmochemistry from the origin of isotopic heterogeneity in the solar nebula to the diversity of planetary bodies. Though the cosmochemical applications for Mo

isotopes are the primary focus of this study, the application of mass-dependent Mo isotope effects as indicators of paleoredox conditions has been the focus of most Mo isotope studies in geochemistry (e.g., Barling et al., 2001; Siebert et al., 2003; Anbar et al., 2001). In cosmochemistry, "mass-independent" nucleosynthetic Mo isotope anomalies have been observed in a variety of cosmochemical materials, including at the bulk meteorite scale. These anomalies have been used primarily to evaluate the extent of mixing and/or thermal processing in the solar nebula, and to test genetic relations amongst solar system materials (e.g., Dauphas et al., 2002a; Yin et al., 2002; Becker and Walker, 2003; Burkhardt et al., 2011). The use of Mo as a genetic tracing tool is important for the elucidation of nebular and planetary processes, including the characterization of the nebular feeding zones of planetary bodies. By merging groups or incorporating ungrouped or anomalous meteorites into existing groups, the accretionary histories and evolution of meteorite parent bodies can be further developed. As a corollary, by demonstrating that certain solar system objects are unrelated, the parent bodies' evolutionary histories can be clarified.

Molybdenum has been previously analyzed by thermal ionization mass spectrometry in both positive (P-TIMS – e.g., Lu and Masuda, 1992; Turnlund et al., 1993; Wieser and De Laeter, 2000, 2009) and negative mode (N-TIMS – Giussani et al., 1995; Yin et al., 2002; Becker and Walker, 2003; Nagai and Yokoyama, 2016a). Molybdenum isotopes in cosmochemical and terrestrial materials have also been measured by multi-collector inductively coupled plasma mass spectrometry (MC-ICP-MS) (e.g., Lee and Halliday, 1995; Dauphas et al., 2001; Dauphas et al. 2002a; Burkhardt et al., 2011; Burkhardt et al., 2014). The current state-of-the-art precision (2SD) of the

measured $^{97}Mo/^{96}Mo$ isotope ratio is ± 13 ppm by N-TIMS (Nagai and Yokoyama, 2016a) and ± 21 ppm by MC-ICP-MS (Burkhardt et al., 2011). Although the method of Nagai and Yokoyama (2016a) produces high precision Mo isotope ratios, 1000 ng - 4000 ng of Mo were used in their study. This requires large sample masses of up to 4 g for some chondritic meteorites. Due to the valuable nature of cosmochemical materials, it is desirable to use as little material as possible.

In an effort to increase the resolving power of the Mo isotopic system when ≤ 1000 ng of Mo are available, we developed procedures for the separation, purification, and high-precision analysis of Mo using a *Thermo-Fisher Triton Plus* N-TIMS at the University of Maryland. Using N-TIMS has the advantage of more stable signal intensities and lower likelihood of isobaric interferences, as opposed to P-TIMS and MC-ICP-MS. In addition, the sensitivity of N-TIMS is typically higher than that of P-TIMS for elements that form negative ions or oxyanions, such as Mo (Heumann et al., 1995; Wieser et al., 2007). The method, however, requires correction for interferences from oxides containing the heavier oxygen isotopes (e.g., Heumann et al., 1995). One recent advance in the application of N-TIMS is the *in situ* measurement of certain oxygen isobars, which can account for variability in the oxygen isotopic composition during analysis (Liu et al., 1998; Luguet et al., 2008; Aggarwal et al., 2009; Chatterjee and Lassiter, 2015; Chu et al., 2015; Bermingham et al., 2016b; Nagai and Yokoyama, 2016a; Trinquier et al., 2016). This study incorporates the use of 10^{12} Ω resistors to measure and correct for oxygen isobars.

The methods presented here are primarily applicable to the measurement of mass-independent nucleosynthetic effects, but may also be adapted to double-spike methods for

the determination of mass dependent stable isotope effects. To demonstrate the utility of these procedures, the Mo isotopic compositions of standards, a gravimetrically prepared spike-standard mixture, the iron meteorites Toluca and Skookum, and the chondrite Allegan are reported.

4.3 Sample preparation

Iron meteorite samples were cut into 0.3 to 2 g pieces using a water-cooled Leco "Vari-cut" saw with a 12.7 cm diamond wafering blade. All iron meteorite pieces were mechanically abraded with different pieces of carborundum paper for each sample, and sonicated in ethanol three times to remove any adhering rust, fusion crust, or saw blade contamination. All acids used for digestion and ion exchange chromatography were sub-boiling distilled with a quartz still (HCl and HNO_3) or a *Savillex Teflon*® still (HF) in-house. High purity water used for dilutions and cleaning was produced using a *Milli-Q* water purification system (deionized to a resistivity of 18.2 MΩ·cm). Iron meteorite samples were digested using 30-40 ml of 8M HCl in *Savillex Teflon*® beakers which were heated at 130-140 °C on a hotplate for at least 48 hours. The chondrite sample (Allegan) was powdered in an agate mortar and pestle, and digested in 30 ml of a concentrated HF/HNO_3 mixture in 5:1 proportions. The Allegan solution was evaporated to a sludge, 5 ml of concentrated HNO_3 was added to dilute the remaining HF, and then 5 ml of concentrated HCl was added and evaporated twice to dissolve fluorides that are insoluble in HNO_3. Chondrite and iron meteorite samples were dried to a sludge, and 3 ml of concentrated HNO_3:HCl in 2:1 proportions was added to the samples and heated at 100 °C overnight or 115 °C for at least an hour in an effort to drive Mo to its highest

oxidation state (MoVI). This step was used in an attempt to mitigate loss of Mo during ion exchange due to the presence of multiple valences of Mo on the column. The acid phase was evaporated to a sludge, at which point 6M HCl was added and dried to sludge twice to remove traces of HNO_3. Then 1M HF was added and dried to sludge twice, and finally the samples were taken into the 1M HF loading solution. At this point, some Mo was likely reduced to a lower oxidation state, but the successive additions of HCl and HF were necessary to ensure that the loading solution was the correct molarity of HF, with minimal traces of HCl and HNO_3.

The separation and purification of Mo from natural samples utilized a two-stage anion exchange chromatography method adapted from Pietruszka et al. (2006), Scheiderich et al. (2010), and Nagai and Yokoyama (2014) (**Table 4.1**). *Eichrom* AG 1X8 200-400 mesh resin was pre-cleaned using reagent grade 1M HCl and 6M HCl, followed by quartz-distilled 6M HCl and 1M HCl, added in succession with *Milli-Q* water between stages of cleaning. The primary column generally follows the same procedure as the primary column of Nagai and Yokoyama (2014). Disposable *Biorad Poly-Prep* columns with 2 ml resin bed volume capacity were loaded with 1.4 ml of resin, which was further cleaned using the procedures outlined in **Table 4.1**. Samples were loaded in 1 ml of 1M HF for each column, with 1 column per ~100 mg of iron meteorite and 300 mg of chondrite. Major elements were eluted in an additional 3 ml of 1M HF; Zr, Ru, Ti, and Hf were eluted in 6 ml of 9M HCl-0.05M HF; W was eluted in 12 ml of 9M HCl-1M HF; and Mo was collected in 10 ml of 6M HNO_3-3M HF. Before the addition of 6M HNO_3-3M HF, 1.5 ml of Milli-Q H_2O was added to the column to prevent the formation of *aqua regia* in the column.

Table 4.1. The anion exchange chromatographic procedures for the separation and purification of Mo. The secondary column was repeated one time to improve sample purity.

Acid	Volume per column (ml)	Step
Primary column - 1-8 *Biorad* columns filled with 1.4 ml AG 1-X8 200-400 mesh		
6M HCl	10	Cleaning
Milli-Q H_2O	10	Cleaning
6M HNO_3 – 3M HF	10	Cleaning
Milli-Q H_2O	5	Cleaning
1M HF	3	Equilibration
1M HF	1	Load sample
1M HF	3	Rinse (Fe, matrix)
9M HCl – 0.05M HF	3 + 3	Rinse (Ru, Zr, Ti, Hf)
9M HCl – 1M HF	3 + 3 + 3 + 3	Rinse (W, Re)
Milli-Q H_2O	1.5	Remove HCl
6M HNO_3 – 3M HF	10	Collect Mo
Secondary column - 1 *Teflon*® column filled with ~ 0.3 ml AG 1-X8 200-400 mesh		
0.01 M HCl	4	Cleaning
1M HCl	8	Cleaning
6M HCl	4	Cleaning
6M HCl	0.5	Load sample
6M HCl	4	Rinse remaining matrix
0.01M HCl – 0.1M HF	1	Rinse remaining matrix
0.01M HCl	3	Rinse remaining matrix
1M HCl	12.5	Collect Mo

The secondary column was a small version of the anion column described by Pietruszka et al. (2006), and was used to further purify the Mo. The columns used for this study were made with *Teflon*® heat-shrink tubing and were fitted with *Teflon*® frits. The resin bed for these columns had dimensions of 0.4 x 2.4 cm. The secondary column was filled to the base of the reservoir with *Eichrom* AG 1X8 200-400 mesh resin (~300 μl).

The resin bed was then cleaned using 0.01M HCl, 1M HCl, and 6M HCl. Prior to loading, samples were dissolved in 2:1 HNO_3:HCl and heated overnight or for one hour, as was done prior to the primary column. Again, 6M HCl was added and dried to remove traces of HNO_3 twice, and then the sample was taken up into 0.5 ml of 6M HCl to be loaded onto the column. Four ml of 6M HCl was added to the column to elute remaining impurities, such as Fe, Ni, and Co, followed by 1 ml of 0.01M HCl-0.1M HF to remove remaining Fe, followed by 3 ml of 0.01M HCl. Molybdenum was then collected in 12.5 ml of 1 M HCl (**Table 4.1**). This column, including the oxidation stage with 2:1 HNO_3:HCl, was repeated once to improve sample purity. Molybdenum purity and yield was monitored qualitatively using a *Thermo-Fisher Element 2* single-collector ICP-MS prior to loading onto filaments. Occasional above-background signals on masses corresponding to Na, Al, V, Mn, Zn, and Sn were observed; some of which may have been generated by gas species from the plasma. The largest and most variable signals were observed for ^{23}Na and ^{27}Al, and the ratios of these signals to the corresponding ^{98}Mo signals were typically 0.02-2 ($^{23}Na/^{98}Mo$) and 0.2-1 ($^{27}Al/^{98}Mo$). Other species typically had signal ratios, relative to ^{98}Mo, significantly less than ~ 0.2. The occurrences of these non-analyte species were not correlated with poor ionization of Mo.

Three total analytical blanks were determined for these procedures. Each blank used either one, three, or four primary columns, and resulted in blanks of 0.92, 1.3, and 2.8 ng of Mo, respectively. The total analytical blank using one primary column is, therefore, estimated to be ~ 0.9 ± 0.3 ng (2SD). These blanks were sufficiently low to be negligible for the quantities of Mo used for the analyses reported.

The total yield for the chemistry described above was ~ 50 - 65%. It is possible that the sub-optimal recovery of Mo resulted in mass-dependent fractionation of the Mo isotopes. However, the Mo isotopic compositions reported here were fractionation corrected for mass-dependent isotope effects that occurred naturally and/or that resulted from the column chemistry. Although Rizo et al. (2016) showed that fractionation correction of mass-dependently fractionated materials can result in apparent mass-independent anomalies in W isotopes, the agreement of the Mo data reported here with those of previous studies, as discussed below, indicate that fractionation that occurred during the column chemistry was effectively corrected for.

Loss of Mo primarily occurred in the primary column in the loading stage where some Mo was eluted with the Fe. Because the yield for the secondary column was typically 80-100%, and matrix was largely absent at this stage, it is likely that the matrix was the complicating factor in the primary column. The breakthrough of Mo in the primary column was mitigated by loading in 1M HF, as opposed to the 0.4M HCl-0.5M HF loading solution used by Nagai and Yokoyama (2014). The partition coefficient between the resin and the acid phase (K_d) for Mo is relatively low in 0.4M HCl-0.5M HF compared to 1M HF (K_d = 45 in 0.4M HCl-0.5M HF vs. K_d = 573 in 1M HF - Nagai and Yokoyama 2014). These authors chose not to use 1M HF due to the high K_d values they measured for Zr and Hf, but we observed that these elements were efficiently separated from Mo in the primary and secondary columns. Although Fe does not occupy anion exchange sites in 1M HF, overloading the column may reduce the tendency of Mo to stick to the resin when Fe is present. The sample sizes loaded onto each primary column were small in order to minimize the effect of Fe on the behavior of Mo on the column.

Alternatively, the presence of redox-sensitive Fe or other major elements may change the valence of Mo, resulting in the persistence of mixed valence states in the primary column. One way to mitigate this possible effect is to load the column using H_2O_2 or another oxidizing agent to better control the oxidation state of Mo (and Fe) (e.g., Bandi et al., 1961), but this is yet to be incorporated into methods described here.

After the completion of the chromatographic procedures, the purified sample was taken into solution in 2:1 concentrated HNO_3:HCl and dried to remove resin-derived organics. This step was repeated seven times for each sample. Following the last addition of 2:1 HNO_3:HCl, concentrated HCl was added and dried three times to remove traces of HNO_3. Samples were then dissolved in 6M HCl to load onto filaments.

4.4 Mass spectrometry

4.4.1 Sample loading procedure

Samples and standards were loaded onto outgassed Re filaments. The 99.99% pure Re ribbon used for this study was 0.76 mm wide and 0.030 mm thick and was purchased from the *H. Cross Company*. Rhenium filaments were outgassed at 4.2 A for 40 minutes at least 24 hours before loading. A double filament assembly was found to increase signal intensity and duration of the ionization of Mo, compared to single filaments, in agreement with Turnlund et al. (1993) and Giussani et al. (1995). Further, we found that the double filament assembly provided better control of the ionization of Mo than was achieved with single filaments. The ionization of Mo on single filaments typically would reach a point where the growth of the signal and temperature became exponential without increasing the current applied to the filament. Soon after, both the

signal and temperature would reach a maximum and then the signal would decrease precipitously. The use of an ionization filament and evaporation filament prevented the exponential growth by providing a non-direct heat source, which dramatically improved signal duration and stability. Further, Mo isotopes ionized on single filaments were often fractionated more quickly and more intensely than Mo that was ionized using a double filament assembly. This phenomenon was reflected by the absolute range in the fractionation factor, β, in the exponential law which was used for fractionation correction as discussed below. Over the course of a given analysis, β had an absolute range up to ~ 0.5 for single filament analyses, but a range of < 0.3 for most double filament analyses, which also had run times that were ~ 3.5 times longer in duration.

About 400-1000 ng Mo for samples and 1000 ng Mo for standards were loaded onto the evaporation filament in two ~0.5 µl aliquots, and dried at 0.6 A. Before the first aliquot was dry, the second was added so that distinct reservoirs of Mo did not form. The avoidance of distinct reservoirs was found to improve the ionization of Mo on single filaments in the early stages of the development of these procedures. For samples, once the deposit was dried, the current was increased slowly from 0 to ~2 A until a faint red glow was observed or until the sample transitioned from cloudy white to a colorless or bronze-colored deposit with a black rim. This was done to remove any remaining organics not eliminated by successive additions of 2:1 HNO_3:HCl prior to loading. Care was taken not to heat the filament beyond a dull glow because otherwise the sample can burn off. Ten micrograms of 5 µg/µl $La(NO_3)_3$ in 1M HNO_3 were then added as an electron emitter to reduce the work function of Re and promote the ionization of MoO_3^- (e.g., Heumann et al., 1995; Becker and Walker, 2003). The $La(NO_3)_3$ activator was dried

at 0.6 A, but because the solution does not dry completely, the current was then increased from 0 to ~2 A until the solution was observed to boil to dryness. Ten micrograms of $La(NO_3)_3$ was also added to the ionization filament, using the same drying procedure.

As this loading procedure was developed, variables such as the type of loading solution, the type and amount of activator, the filament assembly, and the placement of activator on the ionization and/or evaporation filaments were systematically varied in order to optimize the ionization of Mo to facilitate stable, long lasting signals. It was found that loading Mo in a chloride form in HCl led to better ionization than when Mo was loaded in HBr or in HNO_3. In agreement with Nagai and Yokoyama (2016a), the optimal activator was found to be $La(NO_3)_3$, although we also trialed $Ba(OH)_2$, $Ca(NO_3)_2$, and a mixture of La and Gd. Nagai and Yokoyama (2016a) also found that a ratio of 5:1 La:Mo was most effective. The results of the initial work with single filaments in this study are consistent with this conclusion, though the optimal ratio of La:Mo for double filaments appears to be higher. Initially, 1ug of Mo was loaded onto the evaporation filament and 5ug of $La(NO_3)_3$ was loaded only onto the ionization filament, but it was found that adding an additional 5ug of $La(NO_3)_3$ on top of the sample or standard improved ionization. However, when this was done, the problem of exponential growth and subsequent rapid decrease of the Mo signals that was observed with single filaments persisted. When the amount of $La(NO_3)_3$ was doubled on both the ionization and evaporation filaments, the temperature of the filaments and the ionization of Mo were better controlled, and, thus, more stable and long-lived.

The loading blank using this loading procedure was ~1 ng. It was suspected that the Mo was primarily sourced from the Re ribbon, as Mo was not observed in the

$La(NO_3)_3$ activator when it was examined by ICP-MS. Because Mo was not eliminated by outgassing, and Mo and Re are chemically similar, Mo may be bound in the structure of the Re ribbon. The effect of the loading blank on the measured isotope ratios was examined using different size loads of the gravimetrically prepared spike-standard mixture (400-1000 ng), and was observed to be negligible.

4.4.2 Instrumental setup and measurement routine

A *Thermo-Fisher Triton Plus* solid source mass spectrometer was used to measure the Mo isotopic compositions of samples and standards. The instrument was equipped with nine Faraday cups, seven of which were used to measure Mo isotopes. A gain calibration of the Faraday cup detectors was performed each day. Liquid nitrogen was added to a cryopump each day to maintain a stable working vacuum. Using a variable leak valve, high-purity oxygen was bled into the source can in an attempt to promote the formation and ionization of MoO_3^-. The O_2 partial pressure was ~1.73×10^{-7} mbar above the baseline pressure with liquid nitrogen, such that the total pressure in the source can was typically 2.0 - 2.4 x 10^{-7} mbar. Using single filaments, standards were also analyzed with no O_2 bled into the source, and with total pressures up to 4 x 10^{-7} mbar. With double filaments, total pressures up to 7.4 x 10^{-7} mbar were tested. This testing did not definitively show that Mo ionization correlates with the amount of O_2 that is used. For their single filament method, Nagai and Yokoyama (2016a) observed that best results were obtained without bleeding O_2 into the source.

The heating protocol for the filaments was consistent for all standards and samples. Because of the close proximity of the two filaments, the ionization and

evaporation filaments were initially slowly heated to avoid warping the Re ribbon. The ionization filament was heated first at 50 mA/min to 1000 mA, then at 20 mA/min to 1700 mA, and then at 10 mA/min to 1930 mA, in order to gently warm the evaporation filament. When the ionization filament reached 1700 mA, the evaporation filament was heated at 30 mA/min to 500 mA, then at 20 mA/min. Both filaments were continuously heated, with the rate gradually being decreased during the heating procedure until the ionization and evaporation filaments were heated at 0.1 mA/min and 0.1-0.2 mA/min, respectively. Once the ionization filament reached ~1930 mA and the evaporation filament reached ~ 630 mA, a mV-level signal was typically registered on the Faraday cups. During the warm-up of samples and standards, the intensity of the signal usually went through periods during which it decreased substantially until the evaporation filament reached 1200-1500 mA. The peak shapes during this period were also usually asymmetrical, likely due to overlapping peaks from ribbon-derived Mo that was not equilibrated with the sample or standard. After the evaporation filament heating current surpassed 1200-1500 mA and the intensity of the signal on $^{98}Mo^{16}O_3^-$ (m/z ~146) reached 400 mV, the peak shape typically became symmetrical for samples and standards. Once the signal intensity reached 800 mV to 1000 mV on $^{98}Mo^{16}O_3^-$, the analyses were started. This signal intensity typically required currents of 1650-1800 mA and 2080-2150 mA applied to the evaporation filament and ionization filament, respectively. At the beginning of the analyses of samples, the signal often decreased for the duration of ~ 50-100 ratios, but would then stabilize or begin to grow. During a single analysis, lasting ~13 h, the typical signal intensity for $^{98}Mo^{16}O_3^-$ ranged between 1000 mV and 1600 mV.

Molybdenum was measured as $^{x}MoO_3^-$ in a static single-line measurement routine. Seven Faraday cup detectors, which were electronically connected to amplifiers equipped with 10^{11} Ω resistors, were used to collect the $^{x}MoO_3^-$ beams, with $^{96}Mo^{16}O_3^-$ in the center cup (m/z ~ 144 – **Table 4.2**). An additional Faraday cup (H4) was electronically connected to an amplifier equipped with a 10^{12} Ω resistor. This detector was used to collect the $^{100}Mo^{18}O^{16}O_2$ beam, which was used for the *in-situ* oxide correction. Later in the development of the analytical method, the L3 cup and a 10^{12} Ω resistor were used to collect the $^{92}Mo^{17}O^{16}O_2$ beam, as discussed below. The amplifiers equipped with 10^{11} Ω resistors were electronically rotated to remove amplifier bias using the virtual amplifier capability of the *Triton*.

Although Zr tends to form positive ions (e.g., Sahoo and Masuda, 1997), and Ru, which forms negative trioxides, does not ionize on Re filaments at the running temperature of Mo (Bermingham et al., 2016b), potential minor isobaric interferences from Zr and Ru were monitored by scanning the low and high masses surrounding the mass range of $^{x}MoO_3^-$ (140-148) using the electron multiplier. No interferences were observed corresponding to Zr or Ru. Further, no unaccounted-for signals (those not associated with MoO_2^- and MoO_4^-) were observed to be greater than ~ 10-200 cps, excluding a ~1000 cps peak at mass 155 that we attribute to LaO^-. Therefore, no corrections for isobaric interferences from species in the MoO_3 mass range were applied, excluding oxide corrections.

Table 4.2. Faraday cup configuration for Mo analyses. The resistors equipped to the amplifiers for each cup and the trioxide interferences are also shown.

	L4	L3[c]	L2	L1	C	H1	H2	H3	H4
Resistor (Ω)[a]	10^{11}	10^{12}	10^{11}	10^{11}	10^{11}	10^{11}	10^{11}	10^{11}	10^{12}
Species	$^{92}Mo^{16}O_3$	$^{92}Mo^{17}O^{16}O_2$	$^{94}Mo^{16}O_3$	$^{95}Mo^{16}O_3$	$^{96}Mo^{16}O_3$	$^{97}Mo^{16}O_3$	$^{98}Mo^{16}O_3$	$^{100}Mo^{16}O_3$	$^{100}Mo^{18}O^{16}O_2$
Interfering Trioxide[b]			$^{92}Mo^{50}O_3$	$^{92}Mo^{51}O_3$ $^{94}Mo^{49}O_3$	$^{92}Mo^{52}O_3$ $^{94}Mo^{50}O_3$ $^{95}Mo^{49}O_3$	$^{94}Mo^{51}O_3$ $^{95}Mo^{50}O_3$ $^{96}Mo^{49}O_3$	$^{94}Mo^{52}O_3$ $^{95}Mo^{51}O_3$ $^{96}Mo^{50}O_3$ $^{97}Mo^{49}O_3$	$^{96}Mo^{52}O_3$ $^{97}Mo^{51}O_3$ $^{98}Mo^{50}O_3$	$^{98}Mo^{52}O_3$

[a]Only amplifiers equipped with 10^{11} Ω resistors were rotated during analyses to remove amplifier bias.
[b]Trioxide masses are the total mass of the O_3. For instance, $^{92}Mo^{50}O_3$ is composed of both $^{92}Mo^{18}O^{16}O_2$ and $^{92}Mo^{17}O_2{}^{16}O$.
[c]L3 was used to measure $^{92}Mo^{17}O^{16}O_2$ from standard 35 onward, but was not used to calculate $^{17}O/^{16}O$ due to the lower internal precision, relative to the $^{18}O/^{16}O$ measurement.

Table 4.3. Molybdenum isotopic compositions of repeated analyses of the *Alfa Aesar Specpure*® Mo plasma standard using the *in situ line by line* oxide correction and fractionation correction using the molecular trioxide mass and $^{98}Mo/^{96}Mo$. Measured, not fractionation corrected $^{18}O/^{16}O$ ratios, averaged over the course of each analysis, are also shown. The 2SE is given in ppm.

Std	92/96	±	94/96	±	95/96	±	97/96	±	100/96	±	$^{18}O/^{16}O$
1	0.883168	9.5	0.552441	5.9	0.953191	4.5	0.573952	4.2	0.581460	6.6	0.002067
2	0.883225	9.3	0.552453	6.8	0.953205	3.9	0.573950	3.4	0.581472	5.8	0.002072
3	0.883106	6.6	0.552430	4.4	0.953188	2.9	0.573955	2.2	0.581446	3.7	0.002063
4	0.883189	20	0.552443	8.1	0.953197	5.0	0.573953	3.6	0.581465	8.4	0.002074
5	0.883174	8.2	0.552441	4.7	0.953198	3.9	0.573954	3.0	0.581452	4.5	0.002060
6	0.883169	6.3	0.552441	3.9	0.953193	3.0	0.573950	2.3	0.581459	3.5	0.002068
7	0.883211	6.8	0.552450	3.7	0.953206	3.3	0.573951	2.7	0.581468	4.6	0.002066
8	0.883176	11	0.552443	5.0	0.953196	3.3	0.573953	2.6	0.581457	4.8	0.002060
9	0.883189	18	0.552447	8.5	0.953201	5.5	0.573952	3.9	0.581462	8.1	0.002055
10	0.883195	5.6	0.552449	3.3	0.953203	2.8	0.573954	2.2	0.581460	3.4	0.002054
11	0.883135	8.9	0.552437	4.5	0.953195	2.9	0.573953	2.1	0.581450	3.9	0.002058
12	0.883148	8.7	0.552438	5.3	0.953192	3.7	0.573953	2.6	0.581456	4.6	0.002084
13	0.883129	12	0.552434	7.8	0.953185	4.9	0.573953	3.7	0.581455	6.8	0.002089
14	0.883113	7.6	0.552432	5.3	0.953188	3.7	0.573953	2.9	0.581451	4.8	0.002071
15	0.883262	8.9	0.552461	5.4	0.953206	3.9	0.573949	3.5	0.581481	5.0	0.002044
16	0.883197	7.6	0.552448	5.1	0.953198	3.6	0.573952	5.4	0.581473	5.0	0.002062
17	0.883164	10	0.552440	6.5	0.953191	3.9	0.573953	3.8	0.581468	5.8	0.002078
18	0.883180	6.7	0.552443	4.8	0.953190	3.2	0.573952	2.7	0.581469	4.1	0.002064
19	0.883238	9.9	0.552455	5.5	0.953203	4.1	0.573952	2.8	0.581478	5.8	0.002069
20	0.883211	8.7	0.552449	6.4	0.953192	4.7	0.573948	3.3	0.581479	5.9	0.002052
21	0.883186	12	0.552438	7.6	0.953191	6.3	0.573951	5.0	0.581476	7.5	0.002056
22	0.883189	6.9	0.552443	4.8	0.953194	3.6	0.573949	3.1	0.581471	4.3	0.002072
23	0.883194	9.5	0.552441	6.4	0.953191	4.1	0.573950	3.4	0.581476	5.5	0.002053
24	0.883135	7.6	0.552432	5.1	0.953186	3.5	0.573954	3.1	0.581465	5.1	0.002055
25	0.883182	12	0.552444	9.4	0.953186	5.8	0.573952	5.5	0.581479	9.5	0.002058
26	0.883154	5.0	0.552435	3.9	0.953186	2.5	0.573952	2.4	0.581471	3.2	0.002062
27	0.883189	7.5	0.552446	4.1	0.953197	4.1	0.573954	3.7	0.581475	5.2	0.002043
28	0.883138	9.8	0.552434	5.4	0.953188	4.2	0.573952	3.0	0.581465	5.1	0.002056
29	0.883140	6.4	0.552436	3.6	0.953187	3.8	0.573953	2.9	0.581465	4.5	0.002057
30	0.883108	7.0	0.552427	4.1	0.953177	3.1	0.573952	2.4	0.581459	4.2	0.002067
31	0.883093	8.0	0.552424	4.4	0.953175	2.9	0.573954	2.5	0.581460	4.3	0.002064
32	0.883149	8.3	0.552438	5.7	0.953185	4.3	0.573953	3.1	0.581468	5.1	0.002047
33	0.883218	9.9	0.552450	7.4	0.953200	4.5	0.573951	3.9	0.581473	6.4	0.002041
34	0.883100	6.7	0.552428	4.9	0.953176	3.3	0.573954	2.5	0.581461	4.2	0.002059
35	0.883112	5.0	0.552430	3.4	0.953182	2.4	0.573953	1.9	0.581454	3.1	0.002055
36	0.883074	4.7	0.552420	3.3	0.953172	2.4	0.573954	1.8	0.581454	3.1	0.002055
37	0.883200	5.4	0.552444	3.8	0.953189	2.8	0.573951	2.2	0.581475	3.3	0.002056
38	0.883158	5.5	0.552437	3.6	0.953183	2.5	0.573953	2.0	0.581469	3.1	0.002059
39	0.883170	4.9	0.552439	3.8	0.953184	2.5	0.573953	2.0	0.581468	3.4	0.002054
40	0.883155	5.1	0.552437	3.3	0.953184	2.3	0.573952	1.8	0.581465	3.1	0.002053
41	0.883066	5.1	0.552418	3.5	0.953169	2.5	0.573953	2.0	0.581453	3.2	0.002061
42	0.883089	5.8	0.552422	3.8	0.953167	2.5	0.573952	1.8	0.581462	3.3	0.002058
43	0.883090	5.9	0.552424	4.0	0.953170	2.8	0.573951	2.5	0.581452	3.7	0.002056
44	0.883102	5.6	0.552424	4.0	0.953170	2.9	0.573951	2.2	0.581458	3.8	0.002060
45	0.883055	6.6	0.552413	4.6	0.953163	3.5	0.573951	2.9	0.581451	4.4	0.002059
46	0.883172	7.4	0.552437	5.6	0.953181	3.6	0.573950	2.7	0.581475	4.9	0.002049
47	0.883194	5.3	0.552442	3.6	0.953186	2.8	0.573950	2.2	0.581480	3.2	0.002042
48	0.883138	7.1	0.552432	4.6	0.953174	3.2	0.573950	2.3	0.581469	4.0	0.002055
Avg	**0.883157**		**0.552438**		**0.953188**		**0.573952**		**0.581465**		**0.002060**
2SD	**107**		**37**		**23**		**5.4**		**32**		**0.96%**

The procedures for incorporating the use of 10^{12} Ω resistors into the measurement routine were adapted from Koornneef et al. (2013), Liu and Pearson (2014), and Trinquier et al. (2016). Baseline measurement times of 1200 s, with a 30 s settling time, and idle times of 15 s were used. Due to the longer settling time of the 10^{12} Ω resistor, compared to 10^{11} Ω resistors, and the lower signal intensity of the $^{100}Mo^{18}O^{16}O_2$ species (2-4 mV), the optimal time over which the isotope ratio measurements were initially integrated was 67.109 s. Much of the data for the standards and samples were, therefore, collected using two 67.109s integrations such that the isotope ratio measurements were integrated over a total of 134.218 s. It was subsequently determined, however, that this integration time was unnecessarily long, so it was halved and the number or ratios was doubled from standard 35 onward (**Table 4.3**). No difference in the measured ratios was evident with the long vs. short integration times, but the internal statistics improved slightly with the shorter integration times. Measurements were taken in 50 blocks with 10 cycles/block for a total of 500 ratios. Baselines were measured every 10 blocks and the pilot mass $^{96}Mo^{16}O_3$ was centered and automatically focused every 2 blocks.

4.4.3 Fractionation correction

The isotope ratios were oxide corrected, as described below, and then fractionation corrected for natural and instrumental mass-dependent fractionation using the exponential law (Russell et al., 1978). Instrumental mass-dependent fractionation in thermal ionization is largely due to the preferential evaporation of the lighter isotopes. Traditionally, the normalizing ratio of $^{98}Mo/^{96}Mo$ has been used (Dauphas et al., 2002a; Burkhardt et al., 2011), where $^{98}Mo/^{96}Mo \equiv 1.453171$ (Lu and Masuda, 1994). The

exponential law is commonly used to correct a given isotope ratio $\left(R_y^x\right)$ by normalizing to a second ratio $\left(R_y^w\right)$ of two stable and non-radiogenic isotopes (Russell et al., 1978), where:

$$R_{wy}^{xy} = \left(R_y^x \times M_y^x\right)^{-\beta} \quad (4.1)$$

and R_{wy}^{xy} is the fractionation corrected ratio, R_y^x is the oxide-corrected, measured ratio, M_y^x is the isotope mass ratio of the isotopes being fractionation corrected, and β is the fractionation factor:

$$\beta = \frac{ln\left(R_y^w / R_{y\ Accepted}^w\right)}{ln(M_y^w)} \quad (4.2)$$

where R_y^w is the measured, oxide-corrected ratio, $R_{y\ Accepted}^w$ is the accepted value (^{98}Mo/^{96}Mo = 1.453171), and M_y^w is the mass ratio of the isotopes used for normalization. Because Mo is measured as a trioxide, the molecular mass ratios were used in addition to the isotope mass ratios (e.g., 140/144 vs. 92/96). These results are compared below (**Table 4.4**). The molecular mass was required to fractionation correct the $^{100}Mo^{18}O^{16}O_2$ species because it has no corresponding isotope mass, as ^{100}Mo is the heaviest Mo isotope.

Table 4.4. Comparison of the various data reduction methods. The best external precision (2SD) is obtained for the $^{97}Mo/^{96}Mo$ ratio using the *line by line* oxide correction and the molecular mass fractionation correction.

Fractionation correction	Oxygen correction	External Precision (ppm)				
		$^{92}Mo/^{96}Mo$	$^{94}Mo/^{96}Mo$	$^{95}Mo/^{96}Mo$	$^{97}Mo/^{96}Mo$	$^{100}Mo/^{96}Mo$
Isotope mass	Nier	175	73	45	67	90
	Measured single value	169	50	34	16	42
	Line by line	166	56	30	6.7	45
	Line by line (FC)	158	76	21	20	76
Molecular mass	Nier	117	63	40	66	87
	Measured single value	110	31	28	15	35
	Line by line	107	37	23	5.4	32
	Line by line (FC)	100	54	17	23	55

4.4.4 Oxide corrections

Because Mo was measured as a trioxide, the intensity measured for each $^{x}MoO_3^-$, except the lowest mass $^{92}MoO_3^-$, must be corrected for isobaric interferences from the heavier oxygen isotope trioxides of lower mass Mo isotopes (**Table 4.2**). For example, $^{94}Mo^{16}O_3^-$ at mass 142 must be corrected for the interference caused by $^{92}Mo^{18}O^{16}O_2^-$ at mass 142. Other oxide species which generate significant interferences are $Mo^{17}O\ ^{16}O_2^-$, $Mo^{17}O_2{}^{16}O^-$, $Mo^{18}O_2{}^{16}O^-$, $Mo^{18}O\ ^{17}O\ ^{16}O^-$, $Mo^{17}O_3^-$, and $Mo^{17}O_2{}^{18}O^-$. Additional species ($Mo^{17}O^{18}O_2^-$ and $Mo^{18}O_3^-$) were also formed, but in such low abundance that they do not generate significant interferences (Yin, 1995). The relative abundances of the oxide species were calculated as in Creaser et al. (1991) and Harper and Jacobsen (1996) using the isotopic composition of oxygen.

Oxide corrections commonly have been applied using a single oxygen isotopic composition, such as that from Nier (1950) ($^{17}O/^{16}O$ = 0.0003749 and $^{18}O/^{16}O$ =

0.0020439), for every sample or standard. However, systematic variations in the isotope ratios from standard to standard are likely due to variability in the oxygen isotopic composition, as has been the case for other measurements of Mo by N-TIMS (Nagai and Yokoyama, 2016a) and for measurements of Os, B, W, and Ru by N-TIMS (e.g., Liu et al. 1998; Luguet et al. 2008; Aggarwal et al., 2009; Touboul and Walker, 2012; Bermingham et al., 2016b; Trinquier et al., 2016). Therefore, 10^{12} Ω resistors were installed in order to measure $^{100}Mo^{18}O^{16}O_2$, and later $^{92}Mo^{17}O^{16}O_2$, from which the oxygen isotope composition can be calculated. The 10^{12} Ω resistor reduces the signal to noise ratio and is most advantageous for signals between ~5 and 20 mV (e.g., Koornneef et al., 2013), which is on the order of the typical signal intensity for $^{100}Mo^{18}O^{16}O_2$ (2 - 4 mV). The ratio of the intensities of $^{100}Mo^{18}O^{16}O_2$ /$^{100}Mo^{16}O_3$ divided by 3 gives the $^{18}O/^{16}O$ ratio. By dividing by 3, the different permutations that ^{18}O can be configured in a trioxide are accounted for (Yin, 1995).

The methods for measuring oxygen *in situ* were adapted from Liu et al. (1998) and Luguet et al. (2008). In agreement with Liu et al. (1998) and Luguet et al. (2008), the $^{18}O/^{16}O$ and $^{17}O/^{16}O$ ratios were observed to increase over the course of a run, and the average $^{18}O^{16}O$ and $^{17}O/^{16}O$ ratio was found to vary from standard to standard (**Table 4.3**) and sample to sample. Because of the changing oxygen isotope ratio within analyses, the oxide correction was done for each cycle (referred to as *line by line* oxide correction). Data were also corrected using the oxygen isotopic composition of Nier (1950) (*Nier* oxide correction), the measured oxygen isotopic composition averaged over the entire run (*measured single value* oxide correction), and the line by line oxygen correction with "fractionation corrected" $^{100}Mo^{18}O^{16}O_2$ (*line by line (FC)* oxide correction).

For the *measured single value, line by line, and line by line (FC)* oxide corrections, the data reduction required two-iterations (Luguet et al., 2008). The first was to correct the measured $^{100}Mo^{18}O^{16}O_2^-$ intensity for the interference from $^{98}Mo^{18}O_2{}^{16}O^-$ using the oxygen isotopic composition of Nier (1950), termed the first-order oxide correction. The second iteration used the average oxide-corrected $^{100}Mo^{18}O^{16}O_2$ intensity for the *measured single value* oxide correction, or the oxide-corrected $^{100}Mo^{18}O^{16}O_2$ intensities for each line for the *line by line* oxide correction to calculate the $^{18}O/^{16}O$ ratio(s). For *the line by line (FC)* oxide correction, the oxide-corrected $^{100}Mo^{18}O^{16}O_2$ was fractionation corrected as described above.

The $^{17}O/^{16}O$ was calculated from the $^{18}O/^{16}O$ ratio using the slope of the terrestrial fractionation line (TFL). The $^{17}O/^{16}O$ was also measured *in situ* from standard 35 onward. However, the signal intensity for the $^{92}Mo^{17}O^{16}O_2$ species was at the limit of the effective range of the $10^{12}\Omega$ resistor (< 2 mV), and the internal precision of these measurements was not as precise as the measurement of $^{18}O/^{16}O$. A $10^{13}\Omega$ resistor, with a lower effective range (~0.3-20 mV – Koornneef et al., 2014), may be advantageously employed to measure this species, but this has not yet been tested. Only negligible differences in the external reproducibility of the 14 standards were observed when the oxide correction was done using the calculated vs. measured $^{17}O/^{16}O$, although the absolute values of the Mo isotope ratios were different (**Table 4.5**). To be consistent and to characterize the long-term external reproducibility, only Mo isotope data that was oxide corrected using the calculated $^{17}O/^{16}O$ is reported here.

Table 4.5. Molybdenum isotopic compositions of standards 35-48, where the oxide corrections were done using the measured $^{17}O/^{16}O$, as opposed to the $^{17}O/^{16}O$ calculated using the TFL. Also shown are the measured $^{17}O/^{16}O$ and $^{18}O/^{16}O$, averaged over the course of the analysis and not fractionation corrected.

Std	92/96	±	94/96	±	95/96	±	97/96	±	100/96	±	$^{17}O/^{16}O$	$^{18}O/^{16}O$
Measured $^{17}O/^{16}O$												
35	0.883175	5.1	0.552459	3.4	0.953203	2.4	0.573932	1.9	0.581451	3.1	0.0003872	0.002055
36	0.883136	4.7	0.552448	3.3	0.953193	2.4	0.573934	1.8	0.581451	3.1	0.0003871	0.002055
37	0.883262	5.4	0.552472	3.8	0.953210	2.8	0.573930	2.2	0.581472	3.3	0.0003870	0.002056
38	0.883219	5.6	0.552465	3.7	0.953203	2.5	0.573932	2.0	0.581466	3.1	0.0003872	0.002059
39	0.883231	4.9	0.552467	3.8	0.953205	2.5	0.573933	2.0	0.581465	3.4	0.0003869	0.002054
40	0.883218	5.1	0.552466	3.3	0.953205	2.3	0.573932	1.8	0.581462	3.1	0.0003869	0.002053
41	0.883128	5.1	0.552446	3.5	0.953190	2.5	0.573933	2.0	0.581450	3.2	0.0003876	0.002061
42	0.883152	5.9	0.552450	3.8	0.953188	2.5	0.573931	1.8	0.581459	3.3	0.0003875	0.002058
43	0.883151	5.9	0.552452	4.0	0.953191	2.8	0.573930	2.5	0.581449	3.7	0.0003872	0.002056
44	0.883163	5.6	0.552452	4.0	0.953190	2.8	0.573930	2.3	0.581455	3.8	0.0003875	0.002060
45	0.883117	6.6	0.552441	4.6	0.953184	3.4	0.573930	2.8	0.581448	4.4	0.0003875	0.002059
46	0.883233	7.5	0.552465	5.6	0.953201	3.7	0.573930	2.7	0.581471	4.9	0.0003865	0.002049
47	0.883256	5.3	0.552470	3.6	0.953207	2.8	0.573929	2.3	0.581476	3.2	0.0003858	0.002042
48	0.883201	7.2	0.552461	4.6	0.953195	3.2	0.573929	2.3	0.581466	4.0	0.0003874	0.002055
Avg.	**0.883189**		**0.552458**		**0.953198**		**0.573931**		**0.581460**		**0.0003871**	**0.002055**
2SD	**110**		**36**		**17**		**5.2**		**33**		**0.25%**	**0.49%**
TFL calculated $^{17}O/^{16}O$												
Avg.	**0.883127**		**0.552430**		**0.953177**		**0.573952**		**0.581463**			
2SD	**111**		**36**		**18**		**5.2**		**33**			

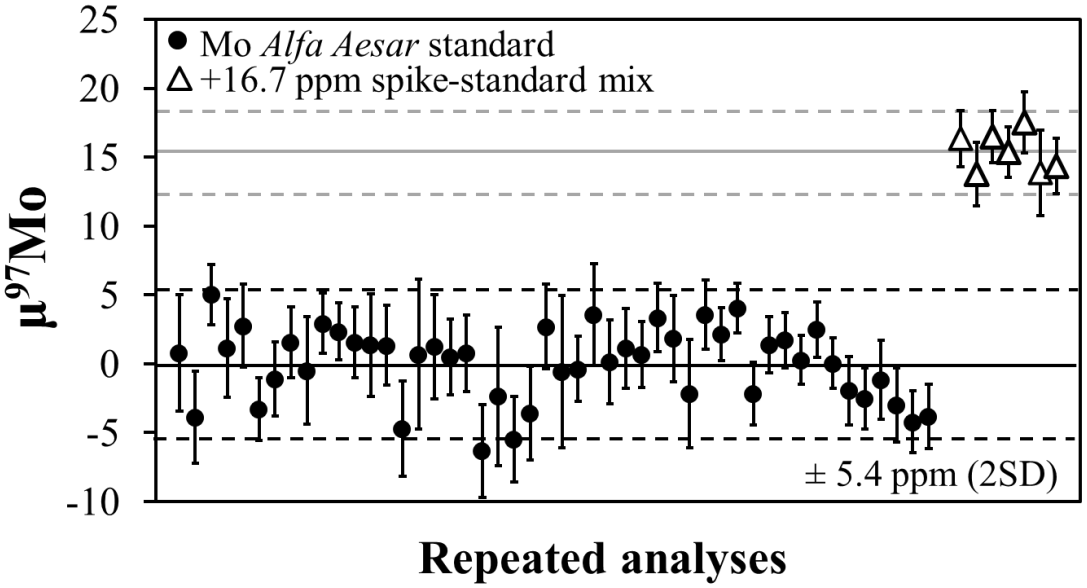

Fig. 4.1. The μ^{97}Mo for repeated analyses of the *Alfa Aesar* Mo plasma standard and the gravimetrically prepared spike-standard mixture. The collection period was 13 months. Data were reduced using *in situ* $^{18}O/^{16}O$ measurements and the *line by line* oxide correction. Data were fractionation corrected with $^{98}Mo/^{96}Mo$ = 1.453171 (Lu and Masuda, 1994) and using the molecular mass instead of the isotope mass as described in text. Dotted lines represent two standard deviations of the analyses (2SD). For standards, 2SD = ± 5.4 ppm and for spike standard mixes, 2SD = ± 2.9 ppm. The spike-standard mixture was gravimetrically predicted to have a μ^{97}Mo value of + 16.7 ppm. This compares favorably with the measured ratio of μ^{97}Mo = + 15.4 ± 2.9. Error bars for the individual analyses are the internal standard error of the mean (2SE).

4.5 Results and discussion

The standard data for all Mo isotopes using the preferred data reduction method is shown in **Table 4.3** and **Figure 4.1**. The external reproducibilities of the standards for the $^{97}Mo/^{96}Mo$ measurement, which is the Mo isotope ratio that is measured to the best statistical precision, using the various oxide and fractionation correction methods are compared in **Table 4.4**. The magnitudes of the oxide interferences for each Mo isotope are presented in **Table 4.6**. The results for spike-standard mixtures and samples are

reported in μ notation (**Tables 4.7** and **4.8**), which gives the deviation of $^{x}Mo/^{96}Mo$ of a sample relative to the average $^{x}Mo/^{96}Mo$ of the repeated analyses of the *Alfa Aesar* Mo plasma standard over a given period of time, in parts per million. For example, for $\mu^{97}Mo$:

$$\mu^{97}Mo_{sample} = \left[\frac{\left(Mo\frac{97}{96}\right)_{sample}}{\left(Mo\frac{97}{96}\right)_{standard}} - 1\right] \times 10^{6} \qquad (4.3)$$

The best external reproducibility (2SD) for all oxide (except *Nier*, as described below) and fractionation correction methods (molecular vs. isotope mass) was obtained for ^{97}Mo because it is bracketed by the normalizing isotope ratio.

4.5.1 Oxide corrections comparison and molecular vs. isotopic fractionation correction

The average $^{18}O/^{16}O$ measured for standards was 0.002060 ± 0.000020 (2SD, n = 48), which is within uncertainty of the ratio reported by Nagai and Yokoyama (2016a) (0.002064 ± 0.000005, n = 21). The long-term external reproducibility of $^{97}Mo/^{96}Mo$ using the *Nier*, *measured single value*, *line by line*, *and line by line (FC)* oxide corrections and the molecular mass fractionation correction were ± 66 ppm, 15 ppm, 5.4 ppm, and 23 ppm, respectively (**Table 4.4**). For the *Nier* oxide correction, ^{95}Mo had the best precision of the Mo isotopes (40 ppm). This effect is likely because the $^{95}MoO_3^-$ beam has the smallest oxide interference compared to the other Mo isotope beams, especially $^{97}MoO_3^-$ and $^{100}MoO_3^-$ (**Table 4.6**). Therefore, the difference between the Nier (1950) and measured oxygen isotopic compositions was magnified with the *Nier* oxide correction on $^{97}MoO_3^-$, compared to $^{95}MoO_3^-$. All oxide corrections using the *in situ*

measured oxygen isotopic composition resulted in improved precision relative to the *Nier* oxide correction, demonstrating that the variability of the oxygen isotopic composition between analyses adversely affects precision. Further, better precision for $^{97}Mo/^{96}Mo$ resulted from using the *line by line* correction vs. the *measured single value* correction, which demonstrates that the variability of the oxygen isotopic composition within a single analysis also affects external precision. The *line by line (FC)* correction exhibits worse external reproducibility for most Mo isotopes, including $^{97}Mo/^{96}Mo$, relative to the non-fractionation corrected *line by line* method. This is likely because the fractionation correction using the $^{100}Mo^{18}O^{16}O_2$ species does not sufficiently account for oxygen isotope fractionation that originates in the tank from which O_2 is bled into the source can, or during formation of the trioxide (Luguet et al., 2008). Therefore, the preferred oxide correction method is the *line by line* correction.

The fractionation correction of Mo using the isotope mass, as opposed to the molecular mass, gives a long-term external reproducibility of 6.7 ppm for $^{97}Mo/^{96}Mo$. The reason for the difference between the two methods is unclear; however, the discrepancy may indicate that Mo forms the molecular trioxide before evaporation on the filament fractionates Mo. Thus, using the molecular mass for fractionation correction provides a more accurate correction.

The best external reproducibility for $^{97}Mo/^{96}Mo$ was obtained using the *line by line* oxide correction and the fractionation correction using the molecular mass. Using these correction methods, the long-term external reproducibility (2SD) over 13 months of periodic measurement campaigns (**Fig. 4.1** and **Table 4.3**, n = 48) was ± 107 ppm for ^{92}Mo, 37 ppm for ^{94}Mo, 23 ppm for ^{95}Mo, 5.4 ppm for ^{97}Mo, and 32 ppm for ^{100}Mo. The

short-term external reproducibility for one ~2 week period (n = 8) was ± 112, 37, 17, 3.7, and 28 ppm for ^{92}Mo, ^{94}Mo, ^{95}Mo, ^{97}Mo, and ^{100}Mo, respectively. The internal precision (2SE) was typically < 4 ppm for ^{97}Mo. The findings that a *line by line* oxide correction and fractionation correction using the molecular mass produce the most precise measurements of the Mo isotope ratios is in agreement with Nagai and Yokoyama (2016a), who used a single filament assembly and measured both $^{17}O/^{16}O$ and $^{18}O/^{16}O$ from the $^{100}Mo^{17}O^{16}O_2$ and $^{100}Mo^{18}O^{16}O_2$ species using 10^{11} Ω resistors. However, the external reproducibility of $^{97}Mo/^{96}Mo$ reported in this study is improved by a factor of ~2.4 relative to Nagai and Yokoyama (2016a), the precision of $^{100}Mo/^{96}Mo$ is roughly equivalent to slightly better on the short term, and the other isotope ratios are less precise (by a factor of ~2.3 at most).

The methods reported here produce more or equivalently precise ratios for the heavy Mo isotopes and less precise ratios for the lighter Mo isotopes, relative to Nagai and Yokoyama (2016a). The reason for this is unknown, but may be related to the differences in fractionation of Mo on single vs. double filaments and/or to the measurement vs. calculation of the oxygen isotope ratios. Nagai and Yokoyama (2016a) reported an absolute range in the fractionation factor, β, of ~0.6, similar to the range we obtained using single filaments. As noted above, the range in β over the course of an analysis is ~0.3 for double filaments. Therefore, if fractionation of Mo isotopes were the dominant cause for the difference in precision between this study and Nagai and Yokoyama (2016a), one might expect that more strongly fractionated measurements would have poorer precision on the light Mo isotopes. This is because the light Mo isotopes are evaporated more readily than the heavier isotopes and are farther in atomic

mass units from the normalizing ratio, which could cause the fractionation correction to be inadequate. However, this is not observed, likely because Mo fractionation is coupled with the effects of the fractionating oxygen isotope composition, since the trioxides evidently form before Mo is fractionated by evaporation.

The magnitude of the oxide correction is largest on ^{97}Mo and ^{100}Mo, and the contribution of ^{18}O to the total oxide interference signal becomes larger relative to ^{17}O from ^{95}Mo to ^{100}Mo (**Table 4.6**). Because this study utilized a $10^{12}\Omega$ resistor to measure the $^{100}Mo^{18}O^{16}O_2$ species, the variance of the $^{18}O/^{16}O$ ratio may be better accounted for relative to measurements using $10^{11}\Omega$ resistors (Nagai and Yokoyama, 2016a). Therefore, the oxide correction applied here for ^{97}Mo and ^{100}Mo, which is larger in magnitude than for other isotopes, may be more accurate, resulting in higher precision for these isotope ratios.

Table 4.6. The magnitude of the oxide interference corrections for each Mo isotope, given as percent relative to the oxide corrected signal intensity. Also shown are the percentages of the most abundant ^{17}O- and ^{18}O-bearing species relative to the total oxide interference signal. Other species incorporating ^{17}O and ^{18}O are minor and not taken into account for these calculations, such that the totals are generally not 100%.

	94	95	96	97	98	100
Total oxide signal (% relative to oxide corrected signal)	0.99	0.066	0.45	1.2	0.47	1.5
Total $^{17}O^{16}O_2$ signal (%)	-	99.3	23.9	16.1	9.5	-
Total $^{18}O^{16}O_2$ signal (%)	100.0	-	75.9	83.9	90.4	99.8
Total	100.0	99.3	99.7	100.0	99.9	99.8

It is possible that some of the low mass Mo isotopes (i.e., ^{95}Mo and ^{96}Mo – **Table 4.6**) are less accurately corrected, and therefore less precise, because the contribution of species incorporating ^{17}O is larger on these isotopes than on the heavier Mo isotopes. Because ^{96}Mo is affected by this, and because the data are normalized to ^{96}Mo, the effect of an inaccurate correction on ^{96}Mo may be magnified on ^{94}Mo and ^{92}Mo, which are far from the normalizing ratio in terms of atomic mass units. The low mass Mo isotopes are measured less precisely in this study when both the measured ^{17}O/^{16}O and the calculated ^{17}O/^{16}O are used for the oxide correction. This may be because of the lower internal precision of the ^{17}O/^{16}O measurements or that the canonical TFL slope is not the optimal slope by which to calculate ^{17}O/^{16}O in this system. Bermingham et al. (2016b) and Trinquier (2016) found that the oxygen isotopic compositions of RuO_3^- and U^+/UO_2^+, respectively, do not always fractionate along the canonical TFL slope (i.e., $\delta^{18}O$ vs. $\delta^{17}O$ = 0.52 or ^{18}O/^{16}O vs. ^{17}O/^{16}O = 0.0954). Instead, for RuO_3^-, which is run in negative mode like Mo, oxygen fractionation may result from mixing isotopically distinct reservoirs of oxygen from the oxygen tank and from the filament.

To test for this possibility during analysis of Mo isotopes, a ^{97}Mo-^{100}Mo double spike was measured, such that sufficiently intense signals were generated for the $^{100}Mo^{17}O^{16}O_2^-$ (2-4 mV) and $^{100}Mo^{18}O^{16}O_2^-$ species (10-20 mV) using $10^{12}\Omega$ resistors (**Fig. 4.2**). For the longer of the two analyses, the slope of ^{18}O/^{16}O vs. ^{17}O/^{16}O was 0.1128 ± 0.015 (2SD), which is marginally higher than the canonical slope of 0.0954. This indicates that mixing of two isotopically distinct reservoirs of oxygen may result in an inaccurate calculation of ^{17}O/^{16}O when using the TFL. This effect is evidently minor, however, as the standard data that was oxide corrected using the measured ^{17}O/^{16}O

produces nearly identical precision. Alternatively, the mixing effect may simply not be observed when $^{17}O/^{16}O$ is measured using $^{92}Mo^{17}O^{16}O_2^-$ when its signal intensity is < 2 mV. Because the effective range of 10^{13} Ω resistors includes signals of < 2 mV, future methods using a 10^{13} Ω resistor to measure the $^{92}Mo^{17}O^{16}O_2^-$ or $^{100}Mo^{17}O^{16}O_2^-$ species and a 10^{12} Ω or 10^{13} Ω resistor to measure the $^{100}Mo^{18}O^{16}O_2^-$ will likely be necessary to optimize the precision on all the Mo isotope ratios. It is also worth noting that the intensity of the $^{92}Mo^{17}O^{16}O_2^-$ species is higher than the $^{100}Mo^{17}O^{16}O_2^-$ species, due to the larger abundance of ^{92}Mo, and it requires no first-order oxide correction. Thus, the use of the $^{92}Mo^{17}O^{16}O_2$ species to calculate the $^{17}O/^{16}O$ ratio is advantageous.

In addition to the in-run oxygen isotopic compositions of the double spikes, the average measured oxygen isotopic composition of the standards for which $^{17}O/^{16}O$ and $^{18}O/^{16}O$ were measured is shown in **Figure 4.2** (UMD mean O). The oxygen isotopic composition of the spikes and the standards are similar to the mean oxygen isotopic composition reported by Nagai and Yokoyama (2016a). The UMD mean O is not similar to the Nier (1950) value, or the value recommended by IUPAC. This dissimilarity suggests that the use of the Nier (1950) value for the first-order correction may be inappropriate. However, when the UMD mean O is used for the first-order correction instead, the precision of each ratio and the absolute isotope ratios, excluding $^{92}Mo/^{96}Mo$ are within ~1-2 ppm of those calculated with the Nier (1950) value.

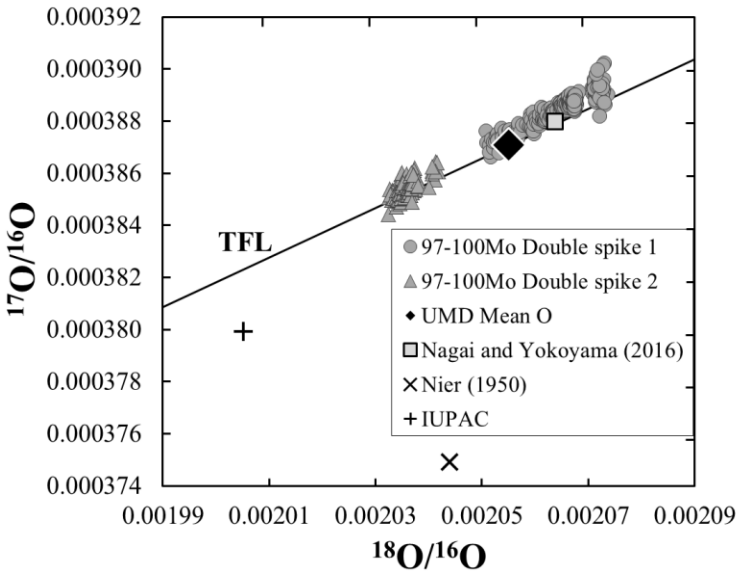

Fig. 4.2. In-run $^{18}O/^{16}O$ vs. $^{17}O/^{16}O$ measured *in situ* for two Mo double spike analyses using the $^{100}Mo^{17}O^{16}O_2$ and $^{100}Mo^{18}O^{16}O_2$ species and two $10^{12}\Omega$ resistors. The average $^{18}O/^{16}O$ and $^{17}O/^{16}O$ measured *in situ* for 14 standards, where $^{17}O/^{16}O$ was measured using the $^{92}Mo^{17}O^{16}O_2$ species and a $10^{12}\Omega$ resistor, is shown as the black diamond ($^{18}O/^{16}O$ = 0.002055 and $^{17}O/^{16}O$ = 0.0003871– **Table 4.5**). Also shown are the oxygen isotopic compositions of Nier (1950), the "best measured" value reported by IAPC (Meija et al., 2015; citing Baertschi, 1976 and Li et al., 1988), and the "Mean O" value reported by Nagai and Yokoyama (2016a). The black line represents the terrestrial fractionation line, which is forced through the UMD mean O value and is calculated using the canonical slope of 0.52.

4.5.2 Gravimetrically prepared spike-standard mixture

To test the accuracy of the methods described above, an isotopically-enriched mixture was analyzed in the same way as samples and standards using the *line by line* oxygen correction and molecular mass fractionation correction. The mixture was gravimetrically prepared using a ^{97}Mo-enriched spike (Oak Ridge National Lab) and the *Alfa Aesar* Mo plasma standard. The concentration of the ^{97}Mo-enriched spike solution was calibrated prior to preparing the mixture. Once the spike and standard were combined in the appropriate proportions, the mixture was allowed to equilibrate on a hotplate at ~120 °C overnight. The mixture was then evaporated to dryness and 2:1

HNO_3:HCl was added and dried one time. Finally, the mixture was taken into solution in 6M HCl to load onto the filaments. The predicted "anomaly" for the mixture was μ^{97}Mo = +16.7. Repeated measurements of the spike-standard mixture yielded μ^{97}Mo = +15.4 ± 2.9 (2 SD, n = 7), which is in excellent agreement with the predicted value (**Table 4.7, Fig. 4.1**). The very good reproducibility indicates that, over the short-term, differences in μ^{97}Mo < 10 ppm may be resolved.

Table 4.7. μ^{97}Mo values for the spike-standard mixes. Mixes 6 and 7 were analyzed with only 400 ng of Mo.

	μ^{97}Mo	2SE
16.7 ppm mix 1	16.4	2.0
16.7 ppm mix 2	13.8	2.3
16.7 ppm mix 3	16.5	1.9
16.7 ppm mix 4	15.4	1.8
16.7 ppm mix 5	17.5	2.2
16.7 ppm mix 6	13.9	3.1
16.7 ppm mix 7	14.3	2.0
Average	15.4	2.9 (2SD)

It was suspected that Mo derived from the Re ribbon resulted in relatively large Mo signals that interfered with Mo signals from the samples and standards. To test for this, five of the analyses of the spike-standard mixture were for loads of ~1000 ng and two of the analyses were for loads of ~ 400 ng Mo. The smaller loads showed μ^{97}Mo values within uncertainties of the larger loads, so any effect of the loading blank was not reflected in the measurements. Further, any differences in fractionation behavior caused by the different amounts of Mo on the filament were not evident. These data show that the measurement procedure and data reduction provide accurate and precise data that can be routinely used to resolve differences in μ^{97}Mo of ~10-15 ppm.

4.5.3 Natural Samples

Data for natural samples are shown in **Table 4.8** and **Figure 4.3**. One piece of Toluca and Allegan were digested and processed using the methods described above. Two other pieces of Toluca and two pieces of Skookum were processed during the development of the method using different chemical separation procedures; resulting in variable yields for some samples (see **Table 4.8** for details).

The Mo yield for the three digestions of Toluca ranged from ~15-55 %. The yield for one Toluca digestion was low (15%), potentially due to loss of Mo during the loading stage of the primary column using the 0.4M HCl-0.5M HF loading solution as described above. The yields for the two digestions of Skookum were similar at around 45%. The μ^{97}Mo values obtained for the three digestions of Toluca with variable yields are within uncertainty of one another and the *Alfa Aesar* Mo standard. The μ^{97}Mo for Toluca is not within uncertainty of the Mo isotopic composition reported by Yin et al. (2002), but is in good agreement with data reported by Dauphas et al. (2002a) and Burkhardt et al. (2011) for meteorites from the IAB group. Likewise, μ^{97}Mo for the two digestions of Skookum are in agreement with data reported for other irons belonging to the IVB group (Yin et al., 2002; Dauphas et al., 2002a; and Burkhardt et al., 2011). These data demonstrate that the analyses are not affected by variable yield or different chromatographic processing. The data for Allegan are in agreement with H5 chondrite data from Burkhardt et al. (2011). This indicates that the methods described above are applicable to metallic and silicate matrices.

Table 4.8. Molybdenum isotopic compositions of natural samples (in ppm). Different pieces of the same meteorite are numbered and different analyses of the same solution from the same piece of meteorite are numbered and lettered.

Samples[a]	μ^{92}Mo	2SD	μ^{94}Mo	2SD	μ^{95}Mo	2SD	μ^{97}Mo	2SD	μ^{100}Mo	2SD
Toluca 1	-15	111	2.6	36	-9.7	18	2.0	5	3.2	33
Toluca 2	12	90	9.1	29	-5.9	15	1.3	6	0.8	24
Toluca 3	30	92	19	29	-3.9	14	0.02	5	0.4	34
Toluca mean	9	45	10	17	-6.5	6	1.1	2	1.46	3.0
Skookum 1a	302	92	173	29	116	14	51	5	119	34
Skookum 1b	278	92	170	29	114	14	55	5	107	34
Skookum 2a	267	92	164	29	109	14	54	5	109	34
Skookum 2b	146	90	123	29	97	15	57	6	63	24
Skookum mean	248	139	157	46	109	17	54	5	100	50
Allegan	43	111	52	36	22	18	19	5.2	21	33

[a]Toluca 1 and Allegan were processed using the procedures described here. Toluca 2 and Skookum 2 were digested and processed using the same methods, with the exception that these pieces were loaded onto the primary column using 0.4M HCl-0.5M HF as the loading solution. Toluca 3 was obtained as a byproduct of the chemistry used to separate and purify W (Touboul and Walker, 2012), and was purified using the secondary anion column described here. Skookum 1 was processed using a different primary anion column that was more similar to the secondary column (Pietruszka et al., 2006).

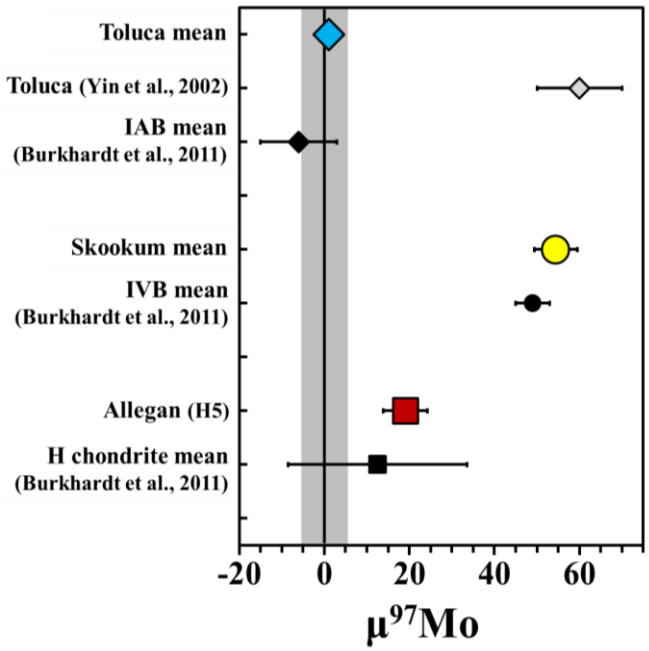

Fig. 4.3. The μ^{97}Mo for the Toluca and Skookum iron meteorites, and the Allegan chondrite, compared to some literature values. For Toluca and Skookum, uncertainties are the 2SD of the separate analyses. For Allegan, the uncertainty is the 2SD external reproducibility of the standards, represented also by the grey bar (±5.4 ppm). The μ^{97}Mo for all three samples are in good agreement with data from meteorites of the same groups (Burkhardt et al., 2011). The datum for Toluca is not within uncertainty of that of Yin et al. (2002).

4.6 Conclusions

The procedures for measuring Mo by N-TIMS using the *Thermo-Fisher Triton Plus* are shown to be accurate and precise. The use of a double filament assembly improved signal stability and duration over those achieved using single filaments. Repeated analyses of the *Alfa Aesar Specpure*® Mo plasma standard using the oxygen isotope composition measured *in situ* and a *line by line* oxide correction yields a long-term external reproducibility of 5.4 ppm for μ^{97}Mo. The repeated measurement of μ^{97}Mo that is in agreement with the predicted value of the gravimetrically prepared ^{97}Mo spike-standard mixture demonstrates the accuracy of the technique and that differences in

$\mu^{97}Mo \geq 10$ ppm can be resolved. The precision for $^{97}Mo/^{96}Mo$ was increased by a factor of ~ 3.9 compared to ICP-MS (Burkhardt et al. 2011), and by a factor of ~ 2.4 compared to other TIMS methods (Nagai and Yokoyama, 2016a). The analyses of iron meteorite and chondrite samples show that different dissolutions and chromatographic procedures do not produce analytical artifacts related to variable yields, blanks, or matrices.

Chapter 5: Molybdenum and tungsten isotope evidence for diverse genetics and chronology among IAB iron meteorite complex subgroups

5.1 Abstract

The IAB iron meteorite complex consists of a main group (MG) and five chemical subgroups. Here, mass-independent Mo and radiogenic ^{182}W isotope compositions are reported for IAB complex meteorites to evaluate the genetics and chronology, respectively, of the subgroups. Osmium isotopes are used to correct for cosmic ray exposure effects on isotopes of Mo and W. The MG, sLL, sLM, and sLH subgroups have Mo isotopic compositions that overlap, consistent with common genetic origins. The Mo isotopic compositions of the sHL and sHH subgroups are identical within uncertainty, but are distinct from the MG and other subgroups, indicating derivation from genetically distinct materials. The MG has a post calcium-aluminum inclusion (CAI) formation, 2-stage metal segregation age of 3.4 ± 0.7 Ma. The sLL and sLM subgroups formed ~ 5 Ma after CAI formation, and the sHL and sHH subgroups formed ~ 0.3-2 Ma after CAI. The new Mo-W data, coupled with chemical data, indicate that the MG and sLL subgroup formed on the same parent body in different impact-generated melts. The sLM and sLH subgroups formed via impact(s) on a parent body that was isotopically identical, but chemically distinct from the MG and sLL parent body. The sHL and sHH subgroups likely formed on a separate, internally-heated parent body or

bodies from other IAB subgroups. The IAB complex meteorites fall on a linear trend defined by $^{94}Mo/^{96}Mo$ vs. $^{95}Mo/^{96}Mo$, along with most other iron meteorite groups. Variation along this line was caused by mixing between at least two nebular components. One component is defined by an enrichment of a pure *s*-process nucleosynthetic carrier or carriers, relative to most meteorites, and the other represents a homogenized nebular component. Sombrerete, currently classified as an sHL iron, has a Mo isotopic composition that is distinct from all IAB complex meteorites analyzed here. Along with group IVB iron meteorites and some ungrouped iron meteorites, it falls on a separate line from other meteorites, which may reflect addition of an *r*-process-enriched component. The MG, sLL, sLM, and sLH subgroups are the only cosmochemical materials yet identified with Mo isotopic compositions that are identical to Earth.

5.2 Introduction

Based on chemical data, iron meteorites may sample > 50 unique planetary bodies (e.g., Goldstein et al., 2009). "Magmatic" iron meteorite groups, including IIAB, IIIAB, IVA, and IVB, likely originated in the cores of distinct, differentiated planetesimals and sample portions of the fractional crystallization sequence by which they crystallized (e.g., Lovering, 1957; Scott, 1972). "Non-magmatic" groups, including the IAB complex and the IIE group, have chemical compositions that cannot be produced by simple fractional crystallization (Scott, 1972). "Ungrouped" iron meteorites have chemical compositions that do not fit into any recognized groups.

The IAB complex iron meteorites are chemically and texturally distinct from the magmatic iron groups. The complex includes a main group (MG) and five subgroups

(sLL, sLM, sLH, sHL, and sHH). Previous studies have shown that the subgroups cannot be related to one another by crystal-liquid fractionation processes, and, therefore, likely originated in separate parental melts (e.g., Wasson and Kallemeyn, 2002; Worsham et al., 2016a). In addition, winonaites are primitive achondrites that have chemical and O isotopic compositions similar to silicate inclusions in some IAB meteorites. This has led to the suggestion that they are from the same parent body as IAB meteorites (e.g., Bild, 1977; Clayton and Mayeda, 1996).

The proposed mechanisms by which the IAB complex (and winonaites) formed are varied with respect to internal (e.g., ^{26}Al) or external (e.g., impact) heating on either a partially differentiated or undifferentiated parent body (e.g., Benedix et al., 2000; Wasson and Kallemeyn, 2002). One way to investigate the origin of the IAB complex is to employ isotopic genetic tracing and chronological tools to examine the MG and subgroups of the complex. Parent body-specific isotope anomalies have been observed at the bulk meteorite scale for a variety of elements, including O (e.g., Clayton and Mayeda, 1996), Ti (e.g., Trinquier et al., 2009), Cr (e.g., Trinquier et al., 2007), Ru (e.g., Fischer-Gödde et al., 2015), and Mo (Dauphas et al., 2002a; Burkhardt et al., 2011). With the exception of O, isotopic variability in these elements between meteorite groups has been attributed to nucleosynthetic effects, which likely originated as a result of inhomogeneous mixing and/or thermal processing of isotopically diverse presolar materials.

The isotopic variability among planetary bodies of an element like Mo makes it an ideal element with which to test whether or not meteorites could have come from the same parent body. By measuring the Mo isotopic composition of IAB meteorites from each subgroup, it can be assessed whether any of the subgroups originated on separate

parent bodies. Molybdenum is applicable here as a genetic tracer because it is a siderophile element present in high abundances in IAB meteorites. It consists of seven stable isotopes that are created by a variety of nucleosynthetic processes; the *p*-process (^{92}Mo and ^{94}Mo), the *s*-process (trace ^{94}Mo, ^{95}Mo, ^{96}Mo, ^{97}Mo ^{98}Mo), and the *r*-process (^{95}Mo, ^{97}Mo, ^{98}Mo, ^{100}Mo; Burbidge et al., 1957). It is this variety of nucleosynthetic processes represented in Mo isotopes that makes Mo an ideal tracer of the relative proportions of diverse presolar carriers in solar system materials (e.g., Dauphas et al., 2002a; Yin et al., 2002; Burkhardt et al., 2011).

The relative timing of metal-silicate segregation of the various IAB subgroups may also clarify the nature of the relations between them. The chronology of core formation on the magmatic iron meteorite parent bodies has commonly been assessed using the short-lived ^{182}Hf-^{182}W chronometer (e.g., Lee and Halliday, 1996; Kruijer et al., 2014a). Hafnium-182, which is lithophile, decays to ^{182}W, which is siderophile, through double β^- decay with a half-life of 8.9 Myr. Hafnium and W are, thus, strongly fractionated during metal-silicate segregation, with metals recording the ^{182}W composition at the time that metal-silicate equilibration ends. Model ages of metal-silicate segregation can be calculated relative to the solar system initial ^{182}W/^{184}W, recorded in Ca-Al rich inclusions (CAI), which are the earliest dated condensates from the solar nebula.

Model ages of metal-silicate segregation can give insight into whether the dominant heat source that facilitated metallic melting was internal or external. Radioactive decay of short-lived nuclides, such as ^{26}Al, was likely the dominant internal heat source by which planetesimals differentiated in the early solar system (e.g., Lee et

al., 1977). The half-life of ^{26}Al is ~0.7 Ma, so it was largely extinct by ~ 4 Ma after CAI formation. Most magmatic iron meteorite parent bodies differentiated within the first 2-3 Myr of solar system evolution, consistent with ^{26}Al heating (e.g., Kruijer et al., 2014a). By contrast, Schulz et al. (2012) reported model ages > 5 Ma for IAB irons, suggesting that impact heating may have been the source of metal segregation. A detailed assessment of the ^{182}W in IAB subgroups would, therefore, provide further opportunity to distinguish between ^{26}Al- or impact-generated IAB complex irons.

The isotopic compositions of meteorites are subject to modification by cosmic ray exposure (CRE). Both the Mo and W isotopic compositions of some iron meteorites may require corrections, depending on the duration of exposure and the neutron fluence conditions (e.g., Masarik, 1997; Markowski et al., 2006). Certain Os isotopes are typically homogenous at the bulk meteorite scale, but are affected in predictable ways by CRE, so they are used here as a neutron fluence dosimeter to monitor and correct for CRE effects (e.g., Walker et al., 2012; Wittig et al., 2013).

5.3 Samples

Most samples examined in this study were obtained from the Division of Meteorites, Department of Mineral Sciences, Smithsonian Institution, National Museum of Natural History (see **Table S1** for USNM #). Northwest Africa 725 (NWA 725) was obtained from the Lunar and Planetary Institute. For IAB complex iron meteorites, Mo, W, and Os isotope data were obtained from adjacent pieces to those used for highly siderophile element (HSE) and ^{187}Re-^{187}Os analyses (Worsham et al., 2016a). Although NWA 725 is currently classified by the Meteoritical Society as an acapulcoite, its O

isotopic composition is similar to winonaite NWA 1463 and silicates from IAB iron meteorites (Greenwood et al., 2012). Here, NWA 725 is considered as a possible genetic relation to the IAB complex irons, similar to winonaites. Magmatic iron meteorites from groups IVB, IVA, IIIAB, and IC, ungrouped iron meteorites, ordinary chondrites, and an enstatite chondrite were also analyzed for their Mo isotopic compositions to make comparisons with the IAB complex meteorites.

5.4 Analytical methods

5.4.1 Chemical separation and purification procedures

Molybdenum, W, and Os isotopic compositions were obtained using methods previously described (Cook et al., 2004; Touboul and Walker, 2012; Walker, 2012; Worsham et al., 2016b; Archer et al., 2016). Iron meteorites were cut into 0.5-2.5 g pieces for Mo and W analyses. Adjacent 0.1-0.3 g pieces were cut for Os analyses for most meteorites, except where an aliquot for Os analysis was taken from the digestion used for Mo or W analysis. Molybdenum from some of the IAB irons was obtained as a byproduct of the W chemistry (**Table A5.1**).

Samples used for Os isotopic analyses were digested in *Pyrex*® Carius tubes. Osmium was separated and purified using solvent extraction and microdistillation (Cohen and Waters, 1996; Birck et al., 1997). The Os total analytical blank was negligible for all samples, comprising < 0.1% of the total Os extracted, averaging 4 ± 2 pg (2SD; n=7). Molybdenum separation and purification was achieved using a 2-stage anion exchange chromatographic procedure (Worsham et al., 2016b). The total analytical blank ranged from 1-5 ng (2SD; n = 3) and comprised < 1% of the Mo extracted, which was negligible

for all analyses. Tungsten was separated and purified from the sample matrix using a 4-stage cation and anion chromatographic procedure (Touboul and Walker, 2012). Prior to separation, an ether extraction step was done to aid in the removal of the Fe matrix (Dodson et al., 1936). The total analytical blank for these procedures was 1 ng (n=1), which constituted a negligible contribution to the total W extracted.

5.4.2 Mass spectrometry

Osmium and W analyses were conducted using a *Thermo-Fisher Triton* thermal ionization mass spectrometer (in negative mode; N-TIMS), and Mo analyses were conducted using a *Thermo-Fisher Triton Plus* N-TIMS at the University of Maryland.

Loading procedures for Os analyses were similar to those reported by Cook et al. (2004). A static analytical routine using multiple Faraday cups was used (Walker, 2012), and data were normalized to $^{192}Os/^{188}Os = 3.08271$ (Allègre and Luck, 1980) to correct for instrumental and natural mass-fractionation. The long-term external reproducibilities of $^{189}Os/^{188}Os$ and $^{190}Os/^{188}Os$ were ± 5.6 ppm and ± 7.2 ppm (2SD), respectively, determined by repeated analyses of an Os reference material (n = 28).

Molybdenum was loaded and analyzed using a double filament assembly, as detailed in Worsham et al. (2016b). Molybdenum was measured as $^{i}MoO_3^-$ in a static single-line measurement routine using Faraday cup detectors and an *in situ* measurement of $^{18}O/^{16}O$ which was used for correction of trioxide isobars. Data were normalized to $^{98}Mo/^{96}Mo = 1.453171$ (Lu and Masuda, 1994). The long-term external reproducibility (2SD) over 13 months was ± 107 ppm for ^{92}Mo, 37 ppm for ^{94}Mo, 23 ppm for ^{95}Mo, 5.4 ppm for ^{97}Mo, and 32 ppm for ^{100}Mo (n=48).

Loading and analytical procedures for analysis of W were adapted from Touboul and Walker (2012) and Archer et al. (2016). The analytical procedures evolved during the course of this study. Approximately half of the samples were measured using the technique of Touboul and Walker (2012) (termed "method I"). These data were corrected using a second-order oxide correction to mitigate the effect of variable oxygen isotope compositions on the precision of the W analyses (Touboul and Walker, 2012; see SM). Recent developments allowed for an *in situ* oxide correction, as with Mo analyses (Archer et al., 2016). Thus, the other half of the samples were measured and corrected using the measured $^{18}O/^{16}O$ (termed "method II"). Tungsten data were fractionation-corrected using $^{186}W/^{183}W = 1.98590$ and $^{186}W/^{184}W = 0.92767$ (Volkening et al., 1991). In both cases, the $^{182}W/^{184}W$ ratio is reported. The external reproducibilities (2SD) of $^{182}W/^{184}W$ were ± 4.5 ppm (n = 30) for method I and ± 4.4 ppm (n = 31) for method II, when the data were fractionation-corrected using $^{186}W/^{183}W$.

5.5 Results

5.5.1 Cosmic ray exposure corrections

Cosmic ray exposure can modify the original isotopic composition of most elements. The CRE effects are dependent on the depth within a sample, so it is important to monitor and correct for CRE effects using the same meteorite piece, or a piece from within a few cm of samples analyzed for other isotopic compositions (Markowski et al., 2006). Osmium isotopes do not show resolvable nucleosynthetic effects on the bulk meteorite scale, so the Os isotopic compositions of bulk meteorites reflect CRE effects, as well as the ingrowth of radiogenic ^{186}Os and ^{187}Os (Walker, 2012). As a result, Os can

serve as a siderophile element CRE dosimeter (Wittig et al., 2013). Platinum-196 has similarly been used as a dosimeter (Wittig et al., 2013; Kruijer et al., 2013). Values for μ^{189}Os and μ^{190}Os, where μ notation is the deviation of the measured ratio from that of terrestrial standards, multiplied by 10^6, are typically the most useful Os isotopes for use as neutron fluence dosimeters because of their moderately high relative abundances and comparatively large neutron capture cross sections and resonance integrals (Mughabghab, 2003). Of the meteorites with Os isotopic anomalies studied here, μ^{189}Os and μ^{190}Os are correlated, in agreement with expectations for CRE modification (**Fig. A5.1**; Walker, 2012). Here, μ^{189}Os values are used for CRE corrections because ^{189}Os exhibits larger effects and is typically measured more precisely than ^{190}Os.

Osmium data are reported in **Table 5.1**. New data for several magmatic irons, also analyzed by Walker (2012), are in good agreement with that study (**Table A5.2**). Osmium isotopic compositions for most of the IAB complex are within uncertainty of terrestrial values, but some samples show negative deviations in μ^{189}Os, indicative of CRE. In the sLL subgroup, for example, the Os isotopic composition of Toluca is within uncertainty of the terrestrial standards, whereas Deport and Bischtübe show large Os isotopic anomalies (μ^{189}Os = -107 ± 5 and -28 ± 7, respectively). Deport has the most negative μ^{189}Os yet reported, indicating that it experienced the highest neutron fluence of any iron meteorite yet measured.

Table 5.1. $\mu^{189}Os$ and $\mu^{190}Os$ data for IAB complex meteorites. Osmium isotope data for other iron meteorites are reported in **Table S2**.

Sample	n[a]	$\mu^{189}Os$	2SD	$\mu^{190}Os$	2SD
MG					
Canyon Diablo[a]	1	0	7	3	5
Landes	2	-5	5	2	6
Campo del Cielo	2	4	5	1	6
Bogou	2	-7	5	-1	9
Morasko	3	-12	4	3	3
Hope	1	-20	3	-4	5
sLL					
Toluca	4	-5	6	1	3
Bischtübe	3	-28	5	16	8
Deport	3	-107	3	59	4
sLM					
Edmonton (KY)	1	-3	5	0	3
Maltahöhe	1	-37	3	18	5
Persimmon Creek	2	5	5	-9	3
sLH					
Tazewell	1	-7	5	-10	3
sHH					
ALHA 80104	1	0	5	-5	3
sHL					
Quarat al Hanish	1	0	3	-1	5
Chebankol	1	-12	3	-5	5
Sombrerete	1	-10	5	2	3

[a]n is the number of analyses. Data for Canyon Diablo are from Walker (2012). Uncertainties for samples analyzed once are 2SD of the standards run in the same analytical campaign. For 2-3 analyses, the uncertainties are either the 2SD of the standards or of the analyses, whichever is larger. Uncertainties for samples measured >3 times are the 2SE.

Molybdenum and W isotope data that are uncorrected for CRE are reported in **Tables A5.3-A5.4**. Cosmic ray exposure effects have not been previously recognized in the Mo isotopic compositions of iron meteorites. Variations in the $\mu^{i}Mo$ values among meteorites from the sLL and sLM subgroups, however, are correlated with $\mu^{189}Os$, indicating some Mo isotopes can be modified by CRE (primarily ^{95}Mo and ^{96}Mo) (**Table 5.2**, discussed in SM). The slopes of these correlations are similar to the slope observed

for group IVB magmatic iron meteorites, which exhibit known CRE effects (**Fig. 5.1a, Table 5.2**). Well defined linear trends of μ^{189}Os vs. μ^{182}W are also observed for the MG and sLL and sLM subgroups (**Table 5.3**; **Fig. 5.1b**). Notably, CRE modification of the isotopic compositions of both Mo and W only produces more negative μ^{i}Mo and μ^{182}W values.

The correlations between μ^{189}Os vs. μ^{i}Mo or μ^{182}W for related meteorites can be used to correct to pre-exposure isotopic compositions (**Fig. 5.1a-b**). For ^{182}W, the pre-exposure isotopic composition has been obtained by projecting the correlation of μ^{189}Os vs. μ^{182}W to the intercept (e.g., Wittig et al., 2013), giving one pre-exposure composition for a group of meteorites having the same metal-silicate segregation age (termed the "intercept-derived, group pre-exposure"). This method of correction is used for subgroups that generate precise correlations on plots of μ^{189}Os vs. μ^{i}Mo or μ^{182}W, determined by linear regression (using ISOPLOT – Ludwig, 2003). The precisions of the slopes and intercepts vary among meteorite subgroups due to the uncertainties of the measurements and the magnitude of the CRE effects.

For Mo isotopes, the most precise correlations were obtained for the sLL and sLM subgroups (and the IVB magmatic group). For μ^{182}W, the most precise correlations were obtained for the MG and the sLL and sLM subgroups. For these subgroups, slopes and intercepts of the regressions of μ^{189}Os vs. μ^{i}Mo are reported in **Table 5.2**, and those of μ^{189}Os vs. μ^{182}W are reported in **Table 5.3**.

Table 5.2. Linear regression results of the measured $\mu^{189}Os$ vs. $\mu^{i}Mo$ for the sLL and sLM subgroups and IVB magmatic iron meteorite group using data from **Tables 1** and **A5.2-A5.3,** calculated using ISOPLOT. The MG is not included because it does not produce well-defined correlations. The mean square weighted deviation (MSWD) is a measure of scatter about the regression.

	n	**Slope**	**±**	**Intercept**	**±**	**MSWD**
sLL	3					
92		1.12	0.63	7	44	0.91
94		0.57	0.21	10	16	0.84
95		0.50	0.064	-4.8	6.3	0.75
97		0.090	0.069	1.3	2.1	0.90
100		0.050	0.27	1.6	3.3	0.11
sLM	3					
92		1.3	2.5	-3	66	0.29
94		0.69	0.77	9	21	0.24
95		0.56	0.35	-3.9	10	0.73
97		0.18	0.15	1.9	3.4	0.64
100		0.01	0.99	-1	22	0.03
IVB	3					
92		1.38	1.60	247	76	1.2
94		0.66	0.45	155	22	2.4
95		0.73	0.19	117	10	1.5
97		0.179	0.068	57	3.4	0.01
100		-0.08	0.71	84	24	2.8
Average sLL and sLM slope						
92		1.21	0.25			
94		0.63	0.17			
95		0.53	0.09			
97		0.14	0.13			
100		0.03	0.06			

Table 5.3. Linear regressions of the measured μ^{189}Os vs. μ^{182}W for each subgroup for which > 2 samples were measured using data from **Tables 5.1** and **A5.2** and **A5.4**. The intercept gives the pre-exposure μ^{182}W for each subgroup.

	n	Slope	±	Intercept	±	MSWD
MG	4	1.67	0.76	-312	6	0.1
sLL slope	3	1.52	0.14	-297	8	1.6
sLM slope	3	1.18	0.20	-297	5	1.8
Average slope		1.46	0.50			

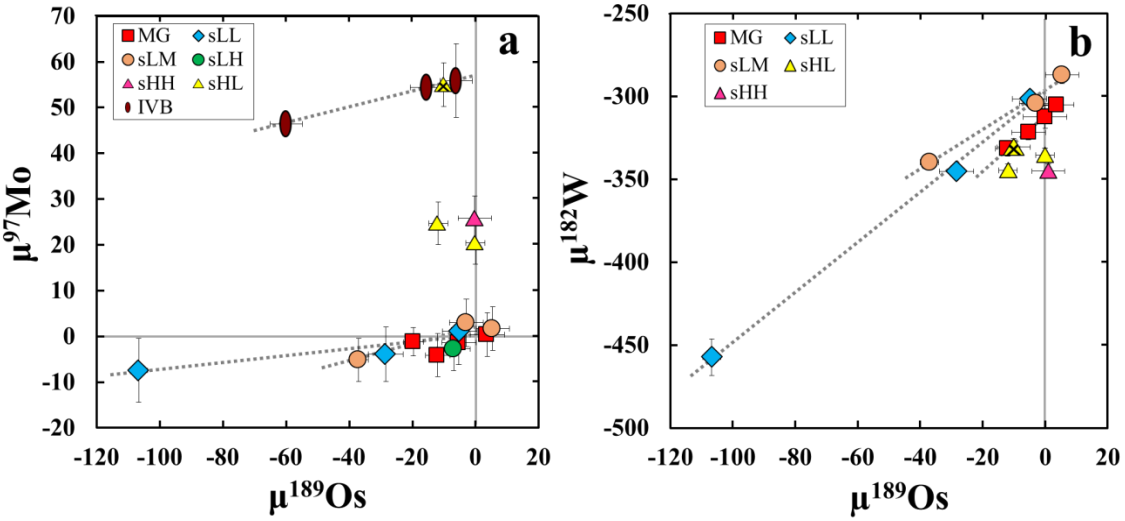

Fig. 5.1. (a) μ^{189}Os vs. μ^{97}Mo, and (b) μ^{189}Os vs. μ^{182}W used for CRE correction, using data from Tables 5.1, A5.3-A5.4. Duplicate analyses are averaged and used in the linear regressions. In (a) the linear regressions are shown for the sLL and sLM subgroups and the IVB magmatic iron meteorite group, using data from this work. In (b) regressions are shown for the MG and the sLL and sLM subgroups. Sombrerete is denoted with the crossed yellow triangle symbol. Slopes and intercepts of each regression are given in Tables 5.2-5.3. Uncertainties of the standards are not shown for clarity, but are ~ 6 ppm for μ^{189}Os and ~5 ppm for μ^{97}Mo and μ^{182}W. Error bars are the 2SD of the standards or the 2SD or 2SE of multiple analyses.

The Mo or W isotopic composition of an individual meteorite can also be corrected by projecting the μ^{i}Mo or μ^{182}W value of a sample to a μ^{189}Os of zero, using the simple linear equation and well-defined slopes of correlations between μ^{189}Os vs. μ^{i}Mo or μ^{182}W. This method of CRE correction is here termed the "slope-derived, individual pre-exposure" method, and is necessary to correct individual meteorites from each subgroup, especially in subgroups with few members.

The Mo and ^{182}W isotopic compositions of individual meteorites within the sLL and sLM subgroups (and the MG for ^{182}W) were corrected using the respective slopes of their subgroups. For Mo, other IAB and magmatic meteorites for which CRE-correction was necessary were corrected using the average of the sLL and sLM slopes. For ^{182}W, IAB meteorites for which correction was necessary were corrected using the average slope of the MG, sLL, and sLM subgroups.

Molybdenum and W data, corrected for CRE, for IAB complex meteorites are provided in **Tables 5.4-5.5**. New Mo data for magmatic and ungrouped iron meteorites and enstatite and ordinary chondrites are also provided in **Table 5.4**. The CRE correction method used for each meteorite/meteorite group is given in **Table A5.1**. Uncertainties for intercept-derived, group pre-exposure values are the uncertainties of the intercepts of the regressions calculated using ISOPLOT (95% confidence). Uncertainties for the slope-derived, individual pre-exposure values are propagated through the linear calculation of the CRE correction, combining the 2SD (number of analyses – $n \leq 3$) or 2SE ($n > 3$) uncertainties of the measurements and the uncertainties of the slopes, calculated using ISOPLOT. For individual meteorites corrected using an average slope, the 2SD of the slopes used to calculate the average was incorporated into the uncertainties of the data.

Table 5.4. The CRE-corrected Mo isotopic compositions of IAB complex iron meteorites and other meteorites.

Sample	n[a]	μ^{92}Mo	±	μ^{94}Mo	±	μ^{95}Mo	±	μ^{97}Mo	±	μ^{100}Mo	±
MG											
Landes	1	-35	92	-9	29	-12	14	-0.7	4.9	1	34
Campo del Cielo[b]	1	-28	92	0	29	-8	14	0.4	4.8	-4	34
Morasko	1	-8	71	2	21	-7	9	-2.5	5.0	-5	31
Hope	2	-12	120	5	42	-1	19	1.5	5.3	-1	34
MG mean		-21	13	0	6	-7	5	-0.3	1.7	-2	3
sLL											
Toluca	3	15	45	13	17	-4	6	1.5	2.1	1	3
Bischtübe	1	-33	92	-2	29	-11	15	-1.4	6.3	-3	24
Deport	2	10	83	11	27	-5	7	2	10	-2	28
sLL intercept		7	44	10	16	-5	6	1.3	2.1	-1	5
sLM											
Edmonton (KY)	2	-27	110	2	36	-10	17	3.5	5.3	-3	33
Maltahöhe	1	0	117	10	35	-3	16	1.5	7.3	-1	31
Persimmon Creek[b]	1	18	92	17	29	2	14	1.7	4.8	1	34
sLM intercept		-3	66	9	21	-4	10	1.9	3.4	-1	4
sLH											
Tazewell	1	-55	71	-7	21	-14	9	-1.8	4.8	-8	31
Dayton[c]	1	19	71	14	21	-1	9	-3.7	4.7	-1	31
Freda[c]	1	-58	68	-16	24	-17	16	0.3	4.7	-9	30
sLH mean		-31	88	-3	31	-11	17	-1.8	4.0	-6	9
sHH											
ALHA80104[b]	2	44	92	77	29	28	14	26	5	5	34
Kofa[c]	1	8	71	52	21	20	9	23	5	3	31
Mount Magnet[c]	1	173	68	120	24	54	16	24	5	42	30
sHH mean		75	173	83	69	34	36	24	3	16	44
sHL											
Quarat al Hanish[b]	1	88	71	95	21	37	9	20	5	30	31
Chebankol	1	166	71	124	21	53	9	26	5	40	31
sHL mean		127	111	109	42	45	22	23	8	35	14
Sombrerete	1	220	93	173	29	115	15	57	5	72	34
Primitive achondrite											
NWA 725[c]	1	155	68	120	24	52	16	30	5	63	30
Magmatic groups											
IVB intercept	9 (3)	247	76	155	22	117	10	57	3	84	33
IC	2 (1)	124	90	91	28	28	15	21	6	37	24
IVA	3 (3)	104	73	83	27	38	12	20	7	24	30
IIIAB	5 (3)	141	72	110	26	46	16	25	4	44	24
Ungrouped iron meteorites											
Chinga	2	231	148	166	46	114	15	55	4	77	56
Tishomingo	2	216	94	149	22	99	14	47	6	75	49
Dronino	1	162	90	139	28	98	15	55	6	63	24
Chondrites											
Richardton metal (H5)	1	100	92	105	29	53	14	30	5	11	34
Allegan (H5)	1	43	110	52	36	22	17	19	5	21	33
St. Sauveur (EH5)	1	103	110	59	36	25	17	11	5	42	33

[a]n is the number of analyses. For the magmatic iron meteorite groups, the number of analyses is given first, followed in parentheses by the number of iron meteorites representing the group. The uncertainties are the 2SD ($n \leq 3$) or 2SE ($n > 3$). The

uncertainties shown here for individual meteorites were propagated through the CRE correction calculation, accounting for the uncertainties of the measurements and the slopes. Due to the lack of a correlation between ^{189}Os and ^{100}Mo, ^{100}Mo is not corrected for CRE.
[b]Samples for which μ^{189}Os was > -1 were not CRE-corrected. See Appendix 5 for details.
[c]Os isotope data were not obtained for these samples, so they are not corrected for CRE.

Table 5.5. Cosmic ray exposure-corrected μ^{182}W isotopic compositions and model ages for IAB complex iron meteorites.

Sample	Method[a]	n	$\mu^{182}W_{186/183}$	±	$\mu^{182}W_{186/184}$	±	Δt_{CAI}	±
MG								
Canyon Diablo[b]	I	1	-312	7	-311	9	3.4	0.7
Landes	I	1	-313	11	-314	10	3.3	1.1
Campo del Cielo[b]	I	1	-305	5	-305	6	4.1	0.5
Morasko	II	1	-311	12	-318	10	3.5	1.3
MG intercept			-312	6			3.4	0.7
sLL								
Toluca	I	2	-294	10	-293	10	5.4	1.2
Bischtübe	II	1	-302	10	-311	11	4.5	1.2
Deport	I, II	2	-295	16	-298	17	5.3	2.0
Goose Lake[c]	I	1	-298	6	-303	8	4.9	0.8
sLL intercept			-297	8			5.0	1.0
sLM								
Edmonton (KY)	II	1	-301	7	-305	9	4.6	0.9
Maltahöhe	II	1	-296	9	-298	10	5.2	1.1
Persimmon Creek[b]	I	1	-287	5	-288	6	6.3	0.7
sLM intercept			-297	5			5.1	0.6
sHH								
ALHA80104[b]	I	1	-345	5	-345	6	0.3	0.4
Kofa[c]	II	1	-330	5	-335	7	1.6	0.5
sHL								
Quarat al Hanish[b]	II	1	-335	4	-331	7	1.1	0.4
Chebankol	II	1	-327	8	-327	9	1.9	0.8
Sombrerete	I	2	-316	10	-315	11	3.0	1.1

[a]Method I used a second-order correction to account for variable oxygen isotope compositions between analyses. Method II measured the oxygen isotopic composition *in situ* as described in text. Uncertainties are as in **Tables 5.1** and **5.4**.
[b]Samples for which μ^{189}Os was > -1 were not CRE-corrected. See SM for details.
[c]Samples for which Os isotope data were not obtained, and are, thus, not corrected for CRE. Goose Lake was not included in the calculation of the sLL intercept.

The isotopic compositions of several meteorites were not corrected for CRE using the slope-derived, individual correction method (see **Tables 5.4-5.5** and **A5.1)** because they were minimally affected by CRE (μ^{189}Os values > -1; e.g., Campo del Cielo, Persimmon Creek, ALHA 80104). Osmium data were not collected due to low Os concentrations for four samples: Dayton, Freda, Kofa, and Mount Magnet. Possible uncorrected CRE effects on these meteorites do not affect the interpretations of the Mo and W isotopic data, as discussed below. Osmium data were also not obtained for NWA 725, or bulk chondrites, because stony meteorites generally have much lower exposure ages than iron meteorites.

5.5.2 CRE-corrected Mo and W isotope results

The ^{97}Mo/^{96}Mo ratio is measured to the highest precision in this study and is minimally affected by CRE, as evidenced by the small effect observed in the μ^{97}Mo value of Deport (-7.5 ± 7; 2SD), which exhibits the largest known effect in μ^{189}Os. Because of this, the μ^{97}Mo values of the few samples for which Os data were not collected were likely minimally affected. For these reasons, μ^{97}Mo is used for genetic comparisons here.

The CRE-corrected Mo isotope data for IAB complex irons, magmatic irons, and chondrites (**Table 5.4**) are in agreement with data reported by Dauphas et al. (2002a) and Burkhardt et al. (2011) for irons and chondrites from the same groups, but the μ^{97}Mo values reported here are typically ≥ 2 times more precise. Most IAB complex iron meteorites have Mo isotopic compositions that are within uncertainty of the terrestrial Mo isotopic composition, represented by the average Mo isotopic composition of standards (**Figs. 5.2** and **A5.2**). The MG (μ^{97}Mo = -0.2 ± 1.7; 2SE), sLL (μ^{97}Mo = 1.3 ± 2.1; 2SD),

sLM (μ^{97}Mo = 1.9 ± 3.4; 2SD), and sLH (μ^{97}Mo = -1.7 ± 4.0; 2SD) samples have Mo isotopic compositions that are indistinguishable from one another. By contrast, the μ^{97}Mo values for the sHL (μ^{97}Mo = 23 ± 9; 2SD) and sHH (μ^{97}Mo = 24 ± 3; 2SD) subgroups are well resolved from the MG and other IAB subgroups. They do, however, overlap with one another, and some magmatic iron groups (e.g., IC, IVA, IIIAB). Sombrerete, which is currently characterized as an sHL iron (Wasson and Kallemeyn, 2002), has a μ^{97}Mo value of 57 ± 5 that is much higher than other IAB complex meteorites reported here. It overlaps with the μ^{97}Mo value of the magmatic IVB group and the ungrouped iron meteorites Chinga, Tishomingo, and Dronino, which were also analyzed here. NWA 725 has a μ^{97}Mo value of 30 ± 5 which overlaps with the sHL and sHH subgroup irons, but is higher than the MG. Ordinary chondrites, Richardton (H5) and Allegan (H5) have μ^{97}Mo values of 30 ± 5 and 19 ± 5, respectively, that are resolved from one another. The enstatite chondrite, Saint-Sauveur (EH5), has a Mo isotopic composition (μ^{97}Mo = 11 ± 5) that is higher than the terrestrial Mo isotopic composition.

The CRE-corrected μ^{182}W values are shown in **Fig. 5.3** and **Table 5.5**. Tungsten isotope data were not collected for sLH irons or Mount Magnet (sHH), due to their low W concentrations. For the MG, the intercept-derived, group pre-exposure μ^{182}W value is -312 ± 6. This is resolved from the group pre-exposure μ^{182}W values for the sLL (μ^{182}W = -297 ± 8) and sLM (μ^{182}W = -297 ± 5) subgroups. Sombrerete (sHL) has a slope-derived, individual pre-exposure μ^{182}W of -316 ± 10 that is within uncertainty of the MG. The other sHL and sHH samples have resolvably lower slope-derived, individual pre-exposure μ^{182}W values (μ^{182}W ~ -345 to -327), relative to the MG. ALHA 80104 and Kofa (sHH) are not within uncertainty of each other. This is not because Kofa is

uncorrected for CRE, as CRE would make $\mu^{182}W$ more negative and not more positive. The MG $\mu^{182}W$ value is within uncertainty of the IVB and IID magmatic iron groups, whereas the $\mu^{182}W$ values of sHL and sHH samples overlap with those of the IVA, IIAB, and IIIAB magmatic iron groups (Kruijer et al., 2014a) (**Fig. 5.3**).

The pre-exposure W isotopic compositions for the MG and sLL subgroup are lower (14 to 29 ppm) than the combined IAB, pre-exposure $\mu^{182}W$ value reported by Schulz et al. (2012) of -283 ± 3. The reason for the offset is unclear. Schulz et al. (2012) used the regression of CRE ages from the literature vs. ^{182}W to obtain the pre-exposure $\mu^{182}W$, combining data for both MG and sLL iron meteorites. Cosmic ray exposure ages, however, are not directly related to neutron fluence, because CRE ages are determined using cosmogenic noble gases that are produced by higher energy protons and neutrons than the thermal neutrons that modify W isotopic compositions. Further, the application of CRE ages obtained from different meteorite pieces from those analyzed for $\mu^{182}W$ likely does not account for the depth-dependence of CRE effects (e.g., Masarik 1997; Markowski et al., 2006; Qin et al., 2008a). Although Sm isotopes were measured by Schulz et al. (2012) to monitor for neutron fluence and different shielding conditions, these were not used for correction of the CRE ages or the W isotopic compositions.

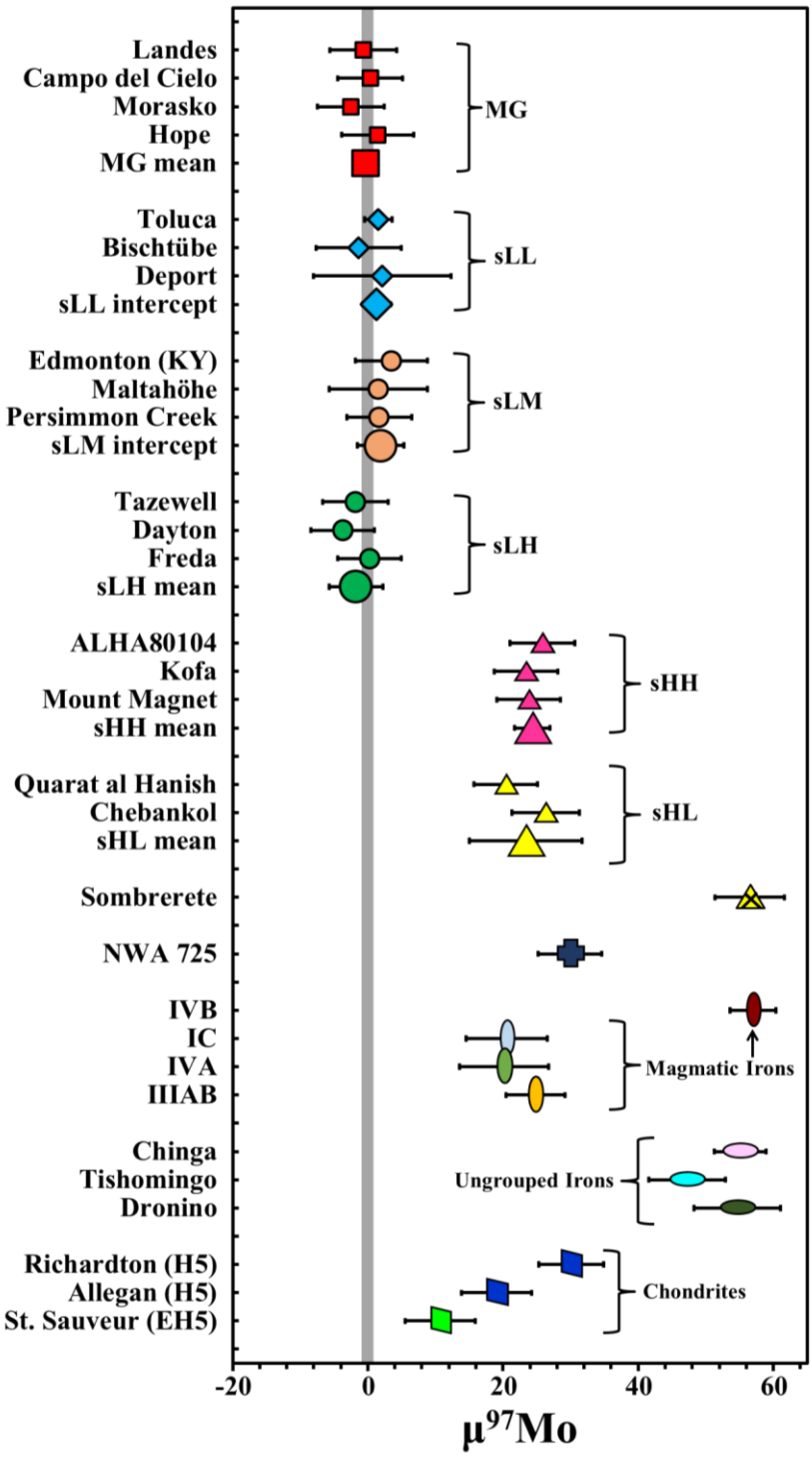

Fig. 5.2. Pre-exposure μ^{97}Mo for the IAB complex iron meteorites and NWA 725. Shown for comparison are the μ^{97}Mo values of magmatic iron meteorite groups, ungrouped iron meteorites, and chondrites from this study. The light grey bar is the 2SE of repeated analyses of terrestrial standards. Error bars for each sample here and in Fig. 5.3 are the propagated 2SD or 2SE uncertainties (see text and Table 5.4 for details).

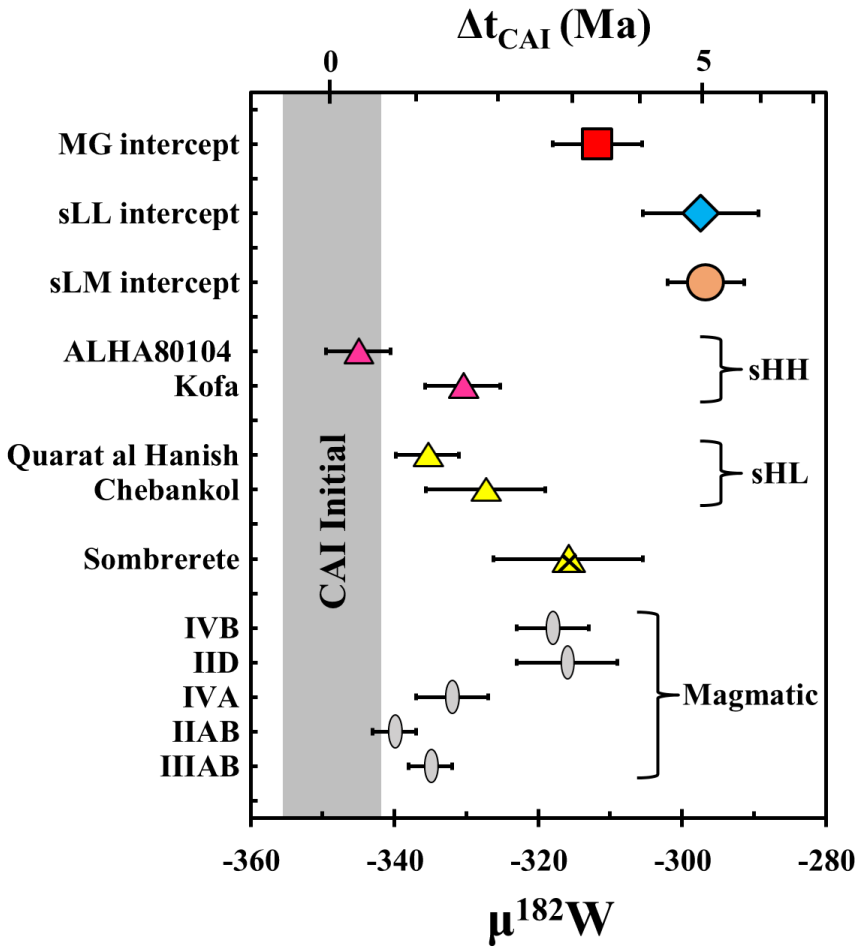

Fig. 5.3. CRE-corrected $\mu^{182}W$ for the IAB complex meteorites. For the MG and sLL and sLM subgroups, the intercept-derived, group pre-exposure $\mu^{182}W$, as determined using the linear regression of $\mu^{189}Os$ vs. $\mu^{182}W$, are shown. Other meteorites were corrected using an average MG, sLL, and sLM slope. Magmatic iron meteorite groups are shown for comparison (from Kruijer et al., 2014a). The CAI initial ^{182}W is from Kruijer et al. (2014b).

5.6 Discussion

5.6.1 IAB subgroup genetics inferred by Mo isotopes

The similarity of Mo isotopic data for the MG and the sLL, sLM, and sLH subgroups is consistent with their generation on either the same parent body, or multiple, genetically related parent bodies (**Fig. 5.2**). Formation of MG and sLL meteorites on a

single parent body is supported by the compositional and mineralogical similarities of MG and sLL metals and silicates (Wasson and Kallemeyn, 2002; Benedix et al., 2000). Despite the similarities, the MG and sLL subgroup likely crystallized from separate parental melts on the same parent body. This is because differences in Ni, Au, and Pd abundances between the MG and sLL subgroup cannot be accounted for by crystal-liquid fractionation, but could result from different degrees of partial melting (Wasson and Kallemeyn, 2002; Worsham et al., 2016a). Thus, if the parental melts of these groups were melted due to impact (e.g., Wasson and Kallemeyn, 2002), more than one impact was required to generate these compositions. Likewise, if these subgroups melted due to internal heating and partial differentiation of the parent body (e.g., Benedix et al., 2000), they must have crystallized in different metal diapirs or melt pockets.

The sLM and sLH subgroups have μ^{97}Mo values that overlap within uncertainties. These subgroups are also characterized by similar major and trace element abundances (e.g., Wasson and Kallemeyn, 2002). The similarity in isotopic and chemical compositions is consistent with their formation on the same parent body. Despite μ^{97}Mo values that overlap with the MG and sLL subgroup, however, the absolute and relative abundances of the HSE suggest that the sLM and sLH subgroups formed on a separate parent body from the MG and sLL subgroup (Worsham et al., 2016a). Therefore, at least two parent bodies are represented in the IAB complex meteorites that have a μ^{97}Mo of approximately zero.

The sHL and sHH subgroups are chemically distinguished from the other IAB complex meteorites by their high abundances of Au. They are distinguished from one another by the low and high Ni abundances in the sHL and sHH subgroups, respectively

(Wasson and Kallemeyn, 2002). These subgroups are characterized by a wide range in siderophile element compositions and relatively few members, and prior studies noted the difficulty of assigning these meteorites to genetically significant groups (e.g., Wasson and Kallemeyn, 2002). The Mo isotopic compositions of these two subgroups are distinct from the MG and other IAB subgroups, but indistinguishable from one another (with the exception of Sombrerete). This indicates that the sHL and sHH subgroups formed on at least one additional parent body from any of the low Au subgroups.

Sombrerete was tentatively assigned to the sHL subgroup by Wasson and Kallemeyn (2002) based on its siderophile element abundances, yet it has a distinct μ^{97}Mo compared to all the IAB iron meteorites studied here. This is also consistent with its distinct Δ^{17}O, unusually high P abundance, and its non-chondritic silicate inclusions, compared with other IAB complex meteorites (Clayton and Mayeda, 1996; Ruzicka et al., 2006). The Mo isotope data support the conclusion of Ruzicka et al. (2006), that Sombrerete is an ungrouped iron that is not related to the IAB complex. Henceforth, Chebankol and Quarat al Hanish are considered the only sHL meteorites studied here.

The Mo isotopic composition of NWA 725 is well resolved from that of the IAB MG, but overlaps with the high Au subgroups. This indicates that either NWA 725 is not a winonaite, or that winonaites are not related to the MG. By contrast, the data permit a genetic relation to the high Au subgroups. No Δ^{17}O data for silicates in the sHL and sHH irons currently exist to compare to NWA 725, so a genetic link between NWA 725 and the high Au subgroups cannot be further evaluated at this time.

5.6.2 IAB subgroup metal-silicate segregation chronology

Metal-silicate Hf-W segregation model ages (Δt_{CAI}) are calculated relative to a CAI initial $\mu^{182}W$ = -349 ± 7 (Kruijer et al., 2014b), assuming precursors with a chondritic $^{180}Hf/^{184}W$ = 1.29 ± 0.09, which corresponds to a present-day chondritic $\mu^{182}W$ = -190 (Kleine et al., 2004). The model age uncertainties reported here do not take into account the uncertainties associated with the CAI initial ratio or Hf/W in the precursor materials.

The intercept-derived MG $\mu^{182}W$ of -312 ± 6 corresponds to a model age of 3.4 ± 0.7 Ma after CAI formation (**Fig. 5.3**). Model ages for the sLL and sLM subgroups are 5.0 ± 1.0 and 5.1 ± 0.6 Ma, respectively. The difference in age between the MG and sLL subgroup is negligible within uncertainties. However, the ~5 Ma segregation ages of the sLL and sLM subgroups are younger than those of magmatic iron meteorite groups (e.g., Kruijer et al., 2014a) and are beyond the end of the effective lifetime of ^{26}Al. This suggests that impact-generated heating was likely the source of melting in these subgroups, if they formed on small parent bodies or near-surface on larger parent bodies.

The model age of the MG of ~3.4 Ma is nearing the end of the effective lifetime of ^{26}Al, but it overlaps with the IVB and IID magmatic iron groups, which have model ages of 2.9 ± 0.5 and 3.1 ± 0.8, respectively (Kruijer et al., 2014a). The relative timing of core formation in the magmatic iron parent bodies was evidently partly controlled by S abundance, where core formation occurred in two stages due to the lower melting temperature of FeS, relative to Fe. Therefore, bodies with higher S abundances have older segregation ages than low-S parent bodies (Kruijer et al., 2014a). As the MG likely had S abundances similar to the IIIAB group with a metal segregation age of 1.2 ± 0.3 (Kruijer

et al., 2014a; Worsham et al., 2016a), an apparent earlier metal segregation age would be expected if two-stage core formation, due to internal heating, took place. Alternately, if the MG-sLL parent body accreted relatively late, the S abundance and the segregation age may be reconciled with internal heating. Although the MG model age suggests that the MG melt could have segregated due to internal heat-induced partial differentiation, the similarity of the characteristics of the MG and sLL subgroup suggests that they formed in a similar manner, as discussed in section 5.6.3.

In contrast to the MG and the sLL and sLM subgroups, the sHL and sHH subgroups have metal segregation ages that are well within the lifetime of ^{26}Al. The model age of each meteorite is also resolved from the MG. These metal segregation ages overlap with the magmatic iron meteorite groups, and allow that the parental melts of the sHL and sHH irons originated due to internal heating and differentiation. In the case of ALHA 80104 and Kofa, the disparate ages suggest they formed in separate metal segregation events.

5.6.3 IAB complex formation informed by combined Mo-W isotope data

When the Mo and W isotope data are collectively considered, it is apparent that the IAB complex represents multiple parent bodies and metal-silicate segregation events. The MG and sLL subgroup probably formed on the same parent body, in two metal segregation events separated by ~ 0 to 3 Ma. While the MG metal segregation event may have occurred during the effective lifetime of ^{26}Al, especially on a large parent body that would have retained heat more efficiently, the sLL melt likely segregated too late for the decay of ^{26}Al to have been the heat source. The sLL subgroup has chondritic relative

abundances of the HSE, which indicates crystallization with little chemical processing (Worsham et al., 2016a). This, in addition to the relatively late segregation age, implies that the sLL subgroup was formed due to impact-generated melting.

The formation model proposed by Benedix et al. (2000) invokes partial differentiation due to internal heating of a parent body, followed by catastrophic breakup and reassembly which mixed different silicate lithologies. In this scenario, the conditions of the MG and sLL W isotopic compositions could potentially be met if partial differentiation, driven by the decay of ^{26}Al, formed the initial MG melt, and an impact into a still metal-rich megaregolith produced the sLL melt. This model is not preferred here, however, because the proposed breakup and reassembly event would likely have led to re-melting and/or mixing of the metal, in addition to mixing the silicate lithologies. This would likely have led to the equilibration of the W isotopic compositions of the metals and silicate, resetting the μ^{182}W values and/or erasing the small difference in μ^{182}W between the MG and sLL subgroup.

Our preferred formation model for the MG and sLL subgroup is the impact-generated melt model described by Wasson and Kallemeyn (2002). In this scenario, the MG melt formed via an impact into a warm, but not differentiated body. A separate impact event formed the sLL subgroup in a different location on the same parent body. The chemical differences between the MG and sLL subgroup may be the result of different degrees of partial melting, controlled by the size of the impacts that generated the melts (e.g., Wasson and Kallemeyn, 2002). The HSE abundances in the MG indicate the occurrence of crystal-liquid fractionation and mixing effects in the melt, in contrast to

the minor chemical processing of the sLL melt (Worsham et al., 2016a). This suggests that the sLL event was smaller and involved less melt than the MG event.

The sLM subgroup likely formed on a separate parent body from the MG-sLL parent body in an impact event which occurred ~ 1.7 Ma later than the impact which created the MG. The chemical and isotopic similarities of the sLM and sLH subgroups suggest that they formed on the same parent body. The distinct Ni and Pd contents of these subgroups may reflect different degrees of partial melt from impacts of different sizes, or impacts into more or less metal-rich portions of the parent body.

The Mo isotopic compositions of the sHL and sHH subgroups indicate that they formed from a different nebular reservoir than the MG or other IAB complex subgroups. The metal segregation event or events were earlier than the MG, and early enough that the decay of ^{26}Al was likely the heat source which generated the melt/melts. This suggests that the parent body or bodies were either partially or fully differentiated, which is supported by the observation that the HSE patterns of the sHL and sHH subgroups are similar to some of the late-crystallized IIAB and IIIAB magmatic iron meteorites. Worsham et al. (2016a) suggested these irons may have been produced by fractional crystallization in a manner similar to magmatic irons. The difference in the abundances of Ni in these subgroups indicates that they formed from separate parental melts (Wasson and Kallemeyn, 2002). Therefore, irons from the sHL and sHH subgroups represent either metal which melted and coalesced into separate descending metal diapirs in the same or different parent bodies, or metal which formed cores on distinct parent bodies. Fractional crystallization is plausible for either of these scenarios.

5.6.4 Mo isotopic compositions of IAB meteorites compared to other meteorites and implications for distinct nebular reservoirs

The various nebular isotopic reservoirs represented in the IAB complex and other meteorite groups may be characterized by their relative proportions of nucleosynthetic components using Mo isotopes. Generally, the Mo isotopic compositions in bulk meteorites likely reflect an *s*-process deficit, relative to the Earth, though an *r*- and *p*-process excess has been identified in type-B CAIs (Dauphas et al., 2002a; Burkhardt et al., 2011). The *r*-process excess in CAIs is characterized by depletion in ^{94}Mo, relative to the other Mo isotopes when they are normalized to ^{98}Mo/^{96}Mo. However, it has been proposed that the relative nucleosynthetic effects in ^{94}Mo are also variable at the bulk meteorite scale (Nagai and Yokoyama, 2016b).

The CRE-corrected μ^{94}Mo and μ^{95}Mo of the IAB complex and our new data for grouped and ungrouped magmatic iron meteorites are shown in **Fig. 5.4**. The IAB data form a generally linear trend constituted by two clusters. The low Au IAB MG and subgroups plot near μ^{95}Mo = 0 and are well resolved from magmatic iron groups. The high Au IAB subgroups form the second cluster around μ^{95}Mo of ~ 20-60 ppm, along with IVA, IIIAB, and IC magmatic irons. Our new data for ordinary and enstatite chondrites also plot in this cluster. Sombrerete plots in a third cluster with the IVB magmatic group, and ungrouped irons Chinga, Dronino, and Tishomingo at μ^{95}Mo values of ~ 100 ppm.

The trend defined by the IAB complex overlaps with a theoretical *s*-process deficit line, calculated here using the equations of Dauphas et al. (2004) and the stellar model of Arlandini et al. (1999). This is in agreement with Dauphas et al. (2004) and

Burkhardt et al. (2011), and it indicates that the trend reflects two-component mixing. The first component, characterized by an *s*-deficit, is potentially a homogenized nebular component (Dauphas et al., 2002b; Burkhardt et al., 2012). The second component may be "residue" left from thermal processing of the homogenized component, where volatile loss of thermally labile Mo oxides depleted in *s*-process Mo, or enriched in *r*- and *p*-process Mo, imparted a variably *s*-enriched isotopic signature, relative to bulk meteorites (Burkhardt et al., 2012).

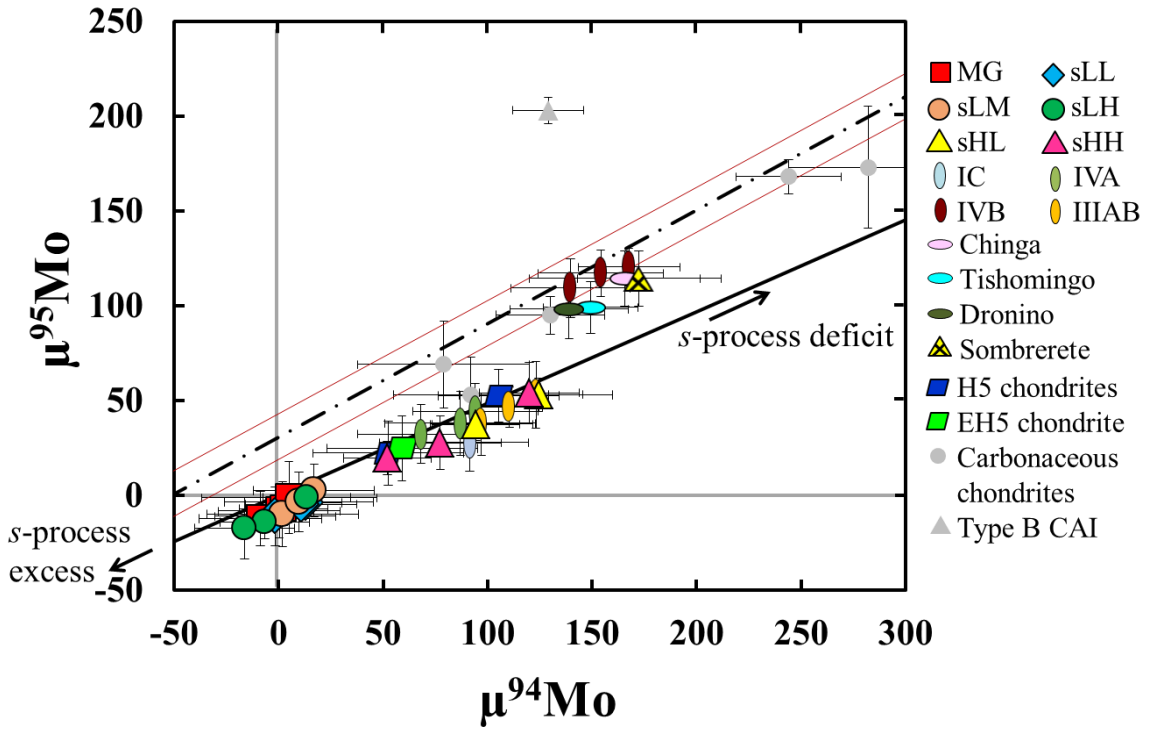

Fig. 5.4. CRE corrected μ^{94}Mo vs. μ^{95}Mo for IAB complex meteorites, magmatic iron meteorite groups, and chondrites. Carbonaceous chondrite and type B CAI data are from Burkhardt et al. (2011). The solid black line is a theoretical mixing line between a pure *s*-process deficit component and an *s*-process excess component calculated using equations from Dauphas et al. (2004) and data from Arlandini (1999). The dashed line is the linear regression through Murchison leachate data (Burkhardt et al., 2012), plotted with the error envelope (red lines). Three different nebular reservoirs are evident. Variations in the Mo isotope ratios are due to both variable depletions in the *s*-process component and deviations in the relative abundances of the *r*-process and *s*-process components.

Sombrerete and the IVB and ungrouped meteorites do not fall on this line. These meteorites fall along a line defined by leachates of the carbonaceous chondrite Murchison (Burkhardt et al., 2012; Nagai and Yokoyama, 2016b). Data for other carbonaceous chondrites also fall along this line, but type B CAIs, characterized by an *r*-and *p*-process excess (Burkhardt et al., 2011), plot well above it. Thus, the offset of these bulk iron meteorites and chondrites from the pure *s*-process deficit line indicates a smaller depletion of ^{94}Mo, relative to ^{95}Mo than is observed in type B CAIs. This is consistent with mixing with a source that has both an *s*-process deficit and an enrichment of an *r*-process component (Fischer-Gödde et al., 2016).

The three distinct populations of meteorites may reflect a variety of presolar carriers representing both *s*- and *r*-process components, and/or complex thermal processing which contributed to the isotopic signature recorded in the various meteorite groups. Variable thermal processing of mineralogically different presolar carriers may explain why the *s*-depleted (e.g., IAB) and the *s*-depleted/*r*-enriched (e.g., Sombrerete, IVB) components are distinct from one another. Alternately, the excess *r*-process component may be due to a late injection of *r*-process enriched materials from a nearby supernova (e.g., Dauphas et al., 2010). Because the *s*-depleted/*r*-enriched reservoirs are characterized by both volatile-rich carbonaceous chondrites and volatile-depleted IVB iron meteorites, late injection of *r*-process enriched material is more likely. Of note, all meteorites measured thus far which have large Mo nucleosynthetic anomalies (μ^{97}Mo $\geq$ 40) plot on the line reflecting an excess *r*-component in addition to an *s*-deficit. Thus, large nucleosynthetic anomalies in Mo are either a product or a cause of the *r*-process excess.

The Mo isotopic compositions of the MG, sLL, sLM, and sLH subgroups overlap with the terrestrial Mo isotopic composition. This makes the MG and these subgroups of the IAB complex unique among iron meteorite groups and chondrites. Although enstatite chondrites have been promoted as representative precursor materials to Earth (e.g., Javoy, 1995), they have a resolvably higher μ^{97}Mo (**Fig. 5.2**), as well as resolved Ti isotopic compositions (Zhang et al., 2012). The H5 ordinary chondrites also have well resolved Mo isotopic compositions from Earth (Burkhardt et al., 2011; this work). Therefore, the present database suggests that much of the IAB complex represents Earth's closest genetic relation, due either to location in the nebula and/or the time at which precursor materials condensed.

5.7 Conclusions

The pre-exposure Mo and W isotopic compositions are most consistent with the formation of IAB complex subgroups on at least three separate parent bodies. Moreover, at least three periods of metal-silicate segregation occurred to generate the various melts on the different parent bodies. While it is useful to think about the IAB complex in terms of similar processes, it can no longer be considered a genetically related family of meteorites.

The MG, sLL, sLM, and sLH subgroups have identical Mo isotopic compositions. The MG and sLL subgroup likely formed on the same parent body in separate metal segregation events at ~3.4 Ma and ~5.0 Ma, respectively, although the current data do not rule out simultaneous formation. The HSE evidence suggests that the sLM and sLH subgroups formed on a separate parent body from the MG. Thus, the Mo nebular

reservoir in which the MG and the sLM subgroup formed was isotopically homogenous, but chemically heterogeneous. The sLM subgroup likely formed ~ 5.1 Ma after CAI formation. The relatively late segregation ages of the MG and the sLL and sLM subgroups are near the end or outside the range of the effective lifetime of ^{26}Al, suggesting that the metallic melts by which the MG and sLL and sLM subgroups formed were generated by impact-induced melting.

The sHH and sHL subgroups have Mo isotopic compositions which overlap with each other, but are distinct from the MG. These meteorites also have relatively old metal segregation ages that are within the effective lifetime of ^{26}Al. These meteorites likely formed in the fractionally crystallized cores or large diapirs of an internally heated parent body or bodies.

Sombrerete has a Mo isotopic composition that is distinct from other IAB meteorites analyzed here, indicating that it formed on a separate parent body. Its Mo isotopic composition overlaps with that of the IVB magmatic iron meteorite group and several ungrouped iron meteorites. This cluster of meteorites exhibit depletions in ^{94}Mo, relative to ^{95}Mo, indicating that the parent bodies represented by these meteorites formed in a nebular reservoir which was characterized by both an *s*-process deficit and an enrichment in *r*-process Mo.

In contrast to enstatite chondrites, the MG and the sLL, sLM, and sLH subgroups constitute some of the only cosmochemical materials that share a Mo isotopic composition with the Earth, indicating that the parent bodies of these meteorites are the closest genetic relations to the precursor materials of the Earth.

Appendix for Chapter 5

1. *Samples*

The samples analyzed here are given in **Table A5.1**, along with their U.S. national museum numbers (USNM #), where applicable**.**

2. *Cosmic ray exposure*

A number of elements exhibit isotopic modifications as a result of CRE, including Mo and W. Osmium (and Pt) can be used as CRE dosimeters because neither shows nucleosynthetic variation at the bulk meteorite scale, but are strongly affected by CRE (e.g., Wittig et al., 2013). The methods used for CRE correction, as discussed in the main text are presented in **Table A5.1**, along with details regarding the chemistry of the Mo and Os used for isotopic analyses.

Osmium isotopic data of IAB and magmatic iron meteorites are given in **Tables 5.1** and **A5.2**, respectively. The μ^{189}Os and μ^{190}Os isotope data are correlated, consistent with modification due to CRE. These data create an array which lies along a neutron production/burnout model calculated by Walker (2012) (**Fig. A5.1**). Molybdenum isotope data are correlated with the Os isotope data, indicating that Mo is also modified by CRE. Because ^{95}Mo has the largest neutron capture cross section and resonance integral of the Mo isotopes by a wide margin (Mughabghab, 2003), the most significant nuclear reaction affecting the Mo isotopic compositions used in this study is likely: ^{95}Mo(n,γ)^{96}Mo. Molybdenum-96 is used in the normalizing ratio, so all Mo isotope ratios may potentially be modified by high neutron fluence conditions. When the Mo data were normalized to

^{96}Mo, the correlations of each Mo isotope with μ^{189}Os were used to correct for CRE effects. Tungsten isotopic compositions were also corrected for CRE (**Tables 5.4-5.5** in the main text). Measured Mo and W isotopic compositions which are not CRE-corrected are given in **Tables A5.3** and **A5.4**.

3. Molybdenum isotope data

Cosmic ray exposure-corrected Mo isotopic compositions of the IAB meteorites, primitive achondrite, chondrites, and average magmatic iron meteorite groups are reported in **Table 5.4** and **Fig. A5.2**. The CRE-corrected Mo isotopic compositions of individual magmatic iron meteorites are reported in **Table A5.5**.

The classification of Hope and Morasko as MG irons has been questioned by Pilski et al. (2013), due primarily to comparatively low Ir abundances. The consistency of the Mo isotopic compositions, however, indicates that Hope and Morasko are genetically associated with the MG. The low Ir abundances may be a result of fractional crystallization (Worsham et al., 2016a).

4. Tungsten isotope data

Both analytical methods for analysis of W used in this study required a first-order oxide correction to correct for isobaric ^{17}O- and ^{18}O-bearing trioxide interferences, before the different secondary oxide corrections could be made (Touboul and Walker, 2012; Archer et al., 2016). For the first-order oxide correction in both methods, the $^{18}O/^{16}O$ ratio measured by Archer et al. (2016) was used in place of the Nier (1950) value used by

Touboul and Walker (2012). This was done so that the data which were collected and corrected using both methods were consistent.

Nucleosynthetic anomalies in $\mu^{183}W$ in IVB iron meteorites have been observed (Qin et al., 2008b). Using the method of Touboul and Walker (2012), the $^{183}W/^{184}W$ ratio is used for the second-order correction to account for variable oxygen isotopic compositions within and between analyses, such that $\mu^{183}W$ cannot be measured using this method. The Archer et al. (2016) W analytical method allows for the *in situ* measurement of the O isotopic composition, so the $\mu^{183}W$ values can be measured precisely. The $\mu^{183}W$ results are presented in **Table A5.4**. No resolvable W nucleosynthetic effects are observed in the IAB meteorites which were analyzed using this method.

Table A5.1. List of iron meteorites studied here and USNM #. The analyses conducted for Os, Mo, and W isotopic compositions for each meteorite are marked with an "x". Also included are the methods used for CRE correction for Mo and W for each meteorite/ group, and details about the chemistry for Mo and Os.

Sample	USNM #	Os	Mo	W	Mo CRE corr.[a]	W CRE corr.	Mo from W chem.[b]	Os aliquoted/ adjacent[c]
MG								
Canyon Diablo	1530	x	-	x	-	Not corrected		adjacent
Landes	5663	x	x	x	sLL-sLM avg. slope	MG slope	yes	adjacent
Campo del Cielo	5615	x	x	x	Not corrected	Not corrected	yes	adjacent
Morasko	6915	x	x	x	sLL-sLM avg. slope	MG slope	no	both
Hope	3477	x	x	-	sLL-sLM avg. slope	-	no	aliquot
Bogou	2245	x	-	-	-	-		adjacent
MG mean/intercept					Mean of individuals	MG intercept		
sLL								
Toluca	460	x	x	x	sLL slope	sLL slope	1 of 3	both
Bischtübe	2666	x	x	x	sLL slope	sLL slope	no	aliquot
Deport	2267	x	x	x	sLL slope	sLL slope	1 of 2	both
Goose Lake	1332	-	-	x	-	Not corrected		-
sLL intercept					sLL intercept	sLL intercept		
sLM								
Edmonton (KY)	1413	x	x	x	sLM slope	sLM slope	no	aliquot
Maltahöhe	6482	x	x	x	sLM slope	sLM slope	no	aliquot
Persimmon Creek	318	x	x	x	Not corrected	Not corrected	yes	adjacent
sLM intercept					sLM intercept	sLM intercept		
sLH								
Tazewell	3089	x	x	-	sLL-sLM avg. slope	-	no	adjacent
Dayton	1592	-	x	-	Not corrected	-	no	-
Freda	1342	-	x	-	Not corrected	-	no	-
sLH mean					Mean of individuals			
sHH								
ALHA80104		x	x	x	Not corrected	Not corrected	yes	adjacent
Kofa	7009	-	x	x	Not corrected	Not corrected	no	aliquot
Mount Magnet	1746	-	x	-	Not corrected	-	no	-
sHH mean					Mean of individuals	Not reported (n < 3)		
sHL								
Quarat al Hanish	6176	x	x	x	Not corrected	Not corrected	no	aliquot
Chebankol	1731	x	x	x	sLL-sLM avg. slope	MG-sLL-sLM avg. slope	no	aliquot
sHL mean					Mean of individuals	Not reported (n < 3)		
Sombrerete	5870	x	x	x	sLL-sLM avg. slope	MG-sLL-sLM avg. slope	yes	adjacent
Primitive achondrite								
NWA 725		-	x	-	Not corrected	-	no	-

continued

Table A5.1. Continued.

Sample		Os	Mo	W	Mo CRE corr.[a]	W CRE corr.	Mo from W chemistry[b]	Os aliquoted/ adjacent[c]
Magmatic groups								
IVB								
Skookum	536	x	x	-	IVB slope	-	no	aliquot
Hoba	6506	x	x	-	IVB slope	-	no	aliquot
Tlacotepec	872	x	x	-	IVB slope	-	no	aliquot
IVB mean					IVB intercept			
IC								
Bendego		-	x	-	Not corrected	-	no	-
IVA								
Maria Elena	1221	x	x	-	sLL-sLM avg. slope	-	no	aliquot
Yanhuitlan	459	x	x	-	sLL-sLM avg. slope	-	no	aliquot
Charlotte	577	x	x	-	Not corrected	-	no	aliquot
IVA mean								
IIIAB								
Tamarugal	6680	x	x	-	sLL-sLM avg. slope	-	no	aliquot
Trenton	2173	x	x	-	sLL-sLM avg. slope	-	no	aliquot
Casas Grandes	369	x	x	-	sLL-sLM avg. slope	-	no	aliquot
IIIAB mean								
Ungrouped iron meteorites		x						
Chinga	3451	x	x	-	sLL-sLM avg. slope	-	no	aliquot
Tishomingo	5862	x	x	-	sLL-sLM avg. slope	-	no	aliquot
Dronino	7203	x	x	-	sLL-sLM avg. slope	-	no	aliquot
Chondrites								
Richardton metal (H5)		-	x	-	Not corrected	-	no	-
Allegan (H5)	217	-	x	-	Not corrected	-	no	-
St. Sauveur (EH5)	7213	-	x	-	Not corrected	-	no	-

[a]For individual meteorites corrected using the slope-based, individual pre-exposure method, the slope used to calculate the pre-exposure value is given. Subgroups corrected using the intercept-derived, pre-exposure group method are denoted by "sLL intercept", for example. Subgroups or groups not corrected in this way are denoted by "MG mean of individuals", for example.

[b]Some Mo used for isotopic analyses was obtained as a byproduct of the W chemistry. These are labeled with "yes", or the number of analyses using Mo from the W chemistry conducted out of the total number of analyses.

[c]Osmium isotope data were obtained from either adjacent iron meteorite pieces to those used for Mo and W analyses, from aliquots from the digestion used for Mo or W analyses, or from both.

Table A5.2. $\mu^{189}Os$ and $\mu^{190}Os$ values for some magmatic iron meteorites. The $\mu^{189}Os$ data were used to correct the Mo isotopic compositions measured in these iron meteorites (**Table A5.3**).

Sample	n	$\mu^{189}Os$	2SD	$\mu^{190}Os$	2SD
Magmatic iron meteorites					
IVB					
Skookum	1	-16	5	6	6
Hoba	1	-6	5	2	6
Tlacotepec	1	-60	5	37	6
IVA					
Maria Elena	1	-39	5	10	6
Yanhuitlan[a]	2	-22	12	10	13
Charlotte	1	3	7	2	14
IIIAB					
Tamarugal[a]	1	-16	12	11	12
Trenton	1	-17	5	12	5
Casas Grandes	1	-34	5	13	5
Ungrouped iron meteorites					
Chinga	1	-5	5	-2	6
Tishomingo	1	-12	5	4	6
Dronino	1	-16	5	8	6

[a]Data are from Walker (2012).

Table A5.3. Molybdenum isotopic compositions for IAB complex iron meteorites and other meteorites. Data are uncorrected for CRE effects.

Sample	n[a]	μ^{92}Mo	±	μ^{94}Mo	±	μ^{95}Mo	±	μ^{97}Mo	±	μ^{100}Mo	±
MG											
Landes	1	-41	92	-12	29	-15	14	-1.4	4.8	1	34
Campo del Cielo	1	-28	92	0	29	-8	14	0.4	4.8	-4	34
Morasko	1	-22	71	-5	21	-14	9	-4.1	4.7	-5	31
Hope	2	-36	120	-7	42	-12	19	-1.2	3.1	-1	34
MG mean		-32	8	-6	5	-12	3	-1.6	1.9	-2	3
sLL											
Toluca	3	9	45	10	17	-6	6	1.1	2.0	1	3
Bischtübe	1	-65	90	-18	28	-25	15	-3.9	6.0	-3	24
Deport	2	-110	49	-50	14	-58	2	-7.5	7.0	-2	28
sLL mean		-55	120	-19	60	-30	52	-3.4	8.6	-1	5
sLM											
Edmonton (KY)	2	-31	110	0	36	-12	17	3.0	5.2	-3	33
Maltahöhe	1	-48	71	-16	21	-24	9	-5.1	4.7	-1	31
Persimmon Creek	1	18	92	17	29	2	14	1.7	4.8	1	34
sLM mean		-20	68	0	33	-11	27	-0.2	8.7	-1	4
sLH											
Tazewell	1	-64	71	-11	21	-18	9	-2.8	4.7	-8	31
Dayton	1	19	71	14	21	-1.1	9	-3.7	4.7	-1	31
Freda	1	-58	68	-16	24	-17	16	0.3	4.7	-9	30
sLH mean		-34	93	-5	32	-12	19	-2.1	4.2	-6	9
sHH											
ALHA80104	2	44	92	77	29	28	14	26	5	4.6	34
Kofa	1	8	71	52	21	20	8.6	23	5	2.7	31
Mount Magnet	1	173	68	120	24	54	16	24	5	42	30
sHH mean		75	173	83	69	34	36	24	3	16	44
sHL											
Quarat al Hanish	1	88	71	95	21	37	8.6	20	5	30	31
Chebankol	1	152	71	117	21	47	8.6	25	5	40	31
sHL mean		120	90	106	32	42	13	23	6	35	14
Sombrerete	1	206	92	166	29	109	14	55	5	72	34
Primitive achondrite											
NWA 725	1	155	68	120	24	52	16	30	5	63	30
IVB											
Skookum	4	248	70	157	23	109	8.6	54	3	100	25
Hoba	2	186	117	136	28	105	15	56	8	67	30
Tlacotepec	3	162	50	115	13	73	2.9	46	2	85	30
IVB mean		199	89	136	43	96	39	52	10	84	33
IC											
Bendego	1	124	90	91	28	28	15	21	6	37	24
IVA											
Maria Elena	1	62	92	69	29	24	14	14	5	11	34
Yanhuitlan	1	38	92	54	29	21	14	21	5	20	34
Charlotte	1	137	110	87	36	38	17	17	5	40	33
IVA mean		79	103	70	33	27	19	17	7	24	30
IIIAB											
Tamarugal	3	114	31	100	14	38	8	22	11	33	16
Trenton	1	90	68	87	24	29	16	21	5	43	30
Casas Grandes	1	140	110	102	36	35	17	23	5	57	33
IIIAB mean		115	49	96	17	34	9.4	22	2	44	24
Ungrouped iron meteorites											
Chinga	2	226	148	163	46	112	14	54	4	77	56
Tishomingo	2	201	93	141	22	93	13	46	5	75	49
Dronino	1	142	90	129	28	89	15	52	6	63	24
Chondrites											
Richardton metal (H5)	1	100	92	105	29	53	14	30	5	11	34
Allegan (H5)	1	43	110	52	36	22	17	19	5	21	33
St. Sauveur (EH5)	1	103	110	59	36	25	17	11	5	42	33

Table A5.4. Tungsten isotopic compositions for IAB complex iron meteorites. Data are uncorrected for CRE effects.

Sample	Method	n	$\mu^{182}W_{186/183}$	±	$\mu^{182}W_{186/184}$	±	$\mu^{183}W$	±	Δt_{CAI}	±
MG										
Canyon Diablo	I	1	-312	7	-311	9			3.4	0.7
Landes	I	1	-322	5	-322	6			2.4	0.4
Campo del Cielo	I	1	-305	5	-305	6			4.2	0.5
Morasko	II	1	-332	4	-335	6	-7	7	1.5	0.3
MG intercept			-312	6					3.4	0.7
sLL										
Toluca	I	2	-302	5	-301	6			4.6	0.5
Bischtübe	II	1	-345	4	-355	6	-14	7	0.3	0.3
Deport	I, II	2	-457	11	-460	6	-9	7	-6.7	0.5
Goose Lake	I	1	-298	6	-303	8			4.9	0.8
sLL intercept			-298	8					4.9	0.9
sLM										
Edmonton (KY)	II	1	-304	4	-308	6	-6	7	4.3	0.4
Maltahöhe	II	1	-340	4	-342	6	-4	7	0.8	0.3
Persimmon Creek	I	1	-287	5	-288	6			6.3	0.7
sLM intercept			-297	5					5.1	0.6
sHH										
ALHA80104	I	1	-345	5	-345	6			0.3	0.4
Kofa	II	1	-330	5	-335	7	-8	7	1.6	0.5
sHL										
Quarat al Hanish	II	1	-335	4	-331	7	2	7	1.2	0.4
Chebankol	II	1	-345	4	-344	6	2	7	0.4	0.3
Sombrerete	I	2	-331	5	-330	6			1.6	0.4

Table A5.5. CRE-corrected Mo isotopic compositions of magmatic iron meteorite groups

Sample	n[a]	μ^{92}Mo	±	μ^{94}Mo	±	μ^{95}Mo	±	μ^{97}Mo	±	μ^{100}Mo	±
IVB											
Skookum	4	270	74	168	24	120	10	57	3	100	25
Hoba	2	195	117	140	28	109	15	57	8	67	30
Tlacotepec	3	245	109	154	30	117	12	57	4	85	30
IC											
Bendego	1	124	90	91	28	28	15	21	6	37	24
IVA											
Maria Elena	1	109	93	94	30	44	15	19	7	11	34
Yanhuitlan	1	65	93	68	30	32	15	24	6	20	34
Charlotte	1	137	110	87	36	38	17	17	5	40	33
IIIAB											
Tamarugal	3	133	35	110	16	46	11	24	11	33	16
Trenton	1	110	68	97	24	37	16	23	5	43	30
Casas Grandes	1	181	111	123	37	53	17	27	7	57	33

[a]n is the number of analyses. Uncertainties are the 2SD of the standards or analyses ($n \leq 3$) or 2SE ($n > 3$).

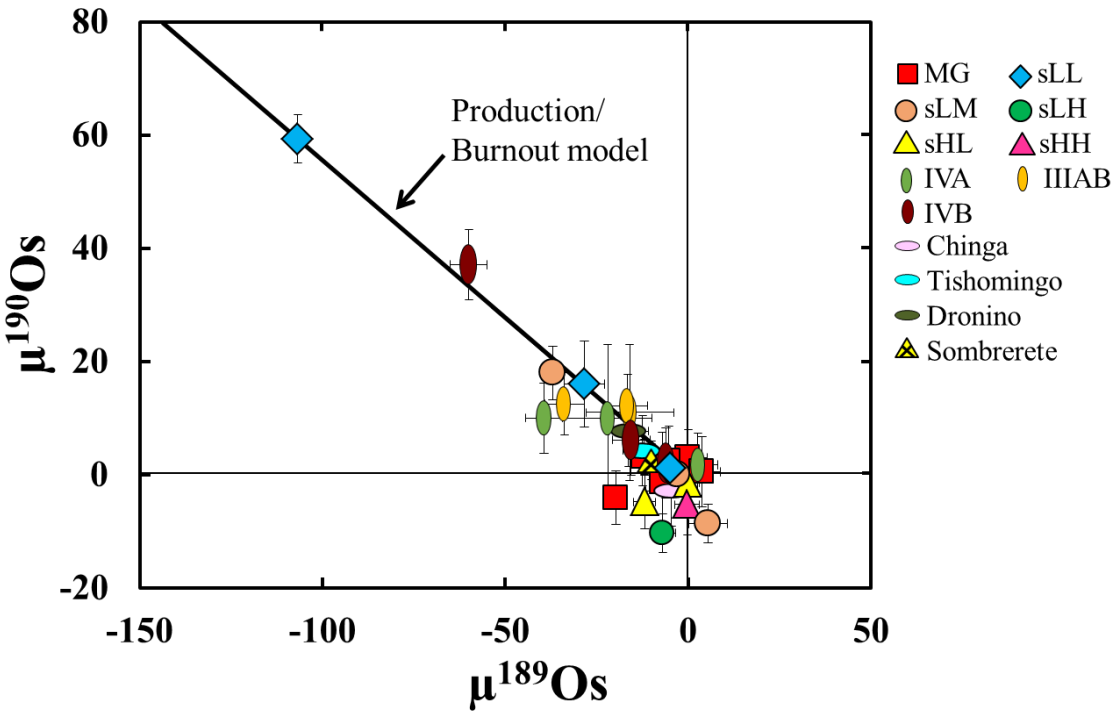

Fig. A5.1. $\mu^{189}Os$ vs. $\mu^{190}Os$ for IAB, magmatic, and ungrouped iron meteorites. Osmium isotope production/burnout, due to neutron capture on isotopes of Os, Re, Ir, and W, was calculated by Walker (2012), and is shown for reference.

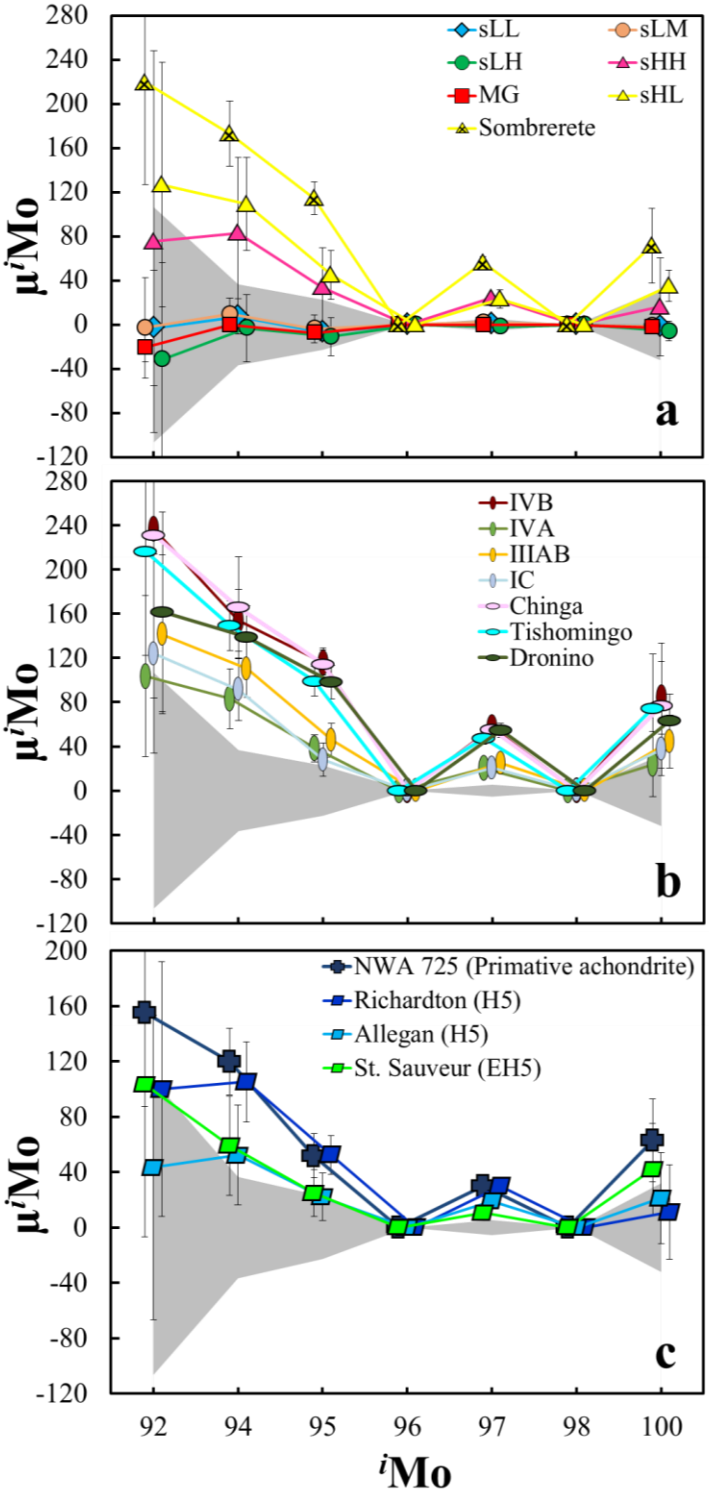

Fig. A5.2. μ^{i}Mo for (a) IAB complex iron meteorites, (b) Magmatic iron meteorite groups and ungrouped irons, and (c) H5 ordinary and enstatite chondrites and primitive achondrite NWA 725. Note the change of scale in (c).

Chapter 6: Conclusions and future directions

6.1 Summary of research conclusions

Nebular and planetary diversity in the early solar system may be examined through detailed study of the chemical and isotopic characteristics of certain types of meteorites, such as the IAB complex of iron meteorites. These meteorites provide an opportunity to examine whether or not a suite of chemically and texturally linked iron meteorites formed from the same genetic pool at the same time. Determining why IAB meteorites are so distinct from most other iron meteorites groups may also provide new insights into nebular and accretionary processes.

The absolute and relative HSE abundances of meteorites within the complex indicate that the IAB subgroups formed from a minimum of five separate parental melts, and that most subgroups crystallized by complex crystal liquid fractionation and mixing processes. Volatile siderophile element concentrations in IAB irons indicate that most of the subgroups formed from precursor materials that were late-stage condensates, or that experienced nebular processing. Nucleosynthetic Mo isotope evidence indicates that at least three parent bodies are sampled by the IAB complex MG and subgroups. Tungsten-182 data, used to obtain relative metal-silicate segregation model ages, indicates that at least four metal segregation events occurred on the various IAB complex parent bodies.

Collectively, the siderophile element concentrations and Mo and W isotopic data indicate that the MG and other low Au sLL, sLM, and sLH subgroups likely formed in separate impact generated melt pools, in agreement with the impact-melt formation

model of the IAB complex (Wasson and Kallemeyn, 2002). These subgroups formed from the same nebular Mo isotopic reservoir, likely on two separate parent bodies. By contrast, the sHL and sHH subgroups probably formed due to partial or complete differentiation on two separate internally heated parent bodies derived from a different isotopic reservoir compared to the MG and low Au subgroups. The various IAB complex parent bodies and preferred formation scenarios are shown in **Figure 6.1**.

In terms of nebular and planetary diversity, the IAB complex is comprised of groups which formed on the same parent body at similar times (i.e., MG and sLL); groups which formed at similar times on different parent bodies (i.e., sLL and sLM; MG and Sombrerete); and groups which formed both in different locations and at different times (e.g., sHH and sLM). Although the siderophile element abundances of the sLM, sLH, sHL, and sHH subgroups likely reflect condensation/evaporation processes (Chapter 3), these processes were not restricted to a single nebular region, given the different Mo isotopic compositions of the sLM, sLH and sHL, sHH subgroups. Importantly, the low Au subgroups of the IAB complex represent the closest known match to the precursor materials of the Earth.

The characteristics which distinguish some IAB complex iron meteorites from magmatic iron meteorite groups, including the relative abundances of trace elements such as Ni and Os, and the presence of silicates in some IAB irons, likely originated as a result to their formation on undifferentiated parent bodies where impacting and mixing processes were important. This, in addition to the genetic difference between some IAB irons and magmatic groups, implies that these IAB parent bodies and magmatic parent bodies formed in a different location and/or time in the protoplanetary disk.

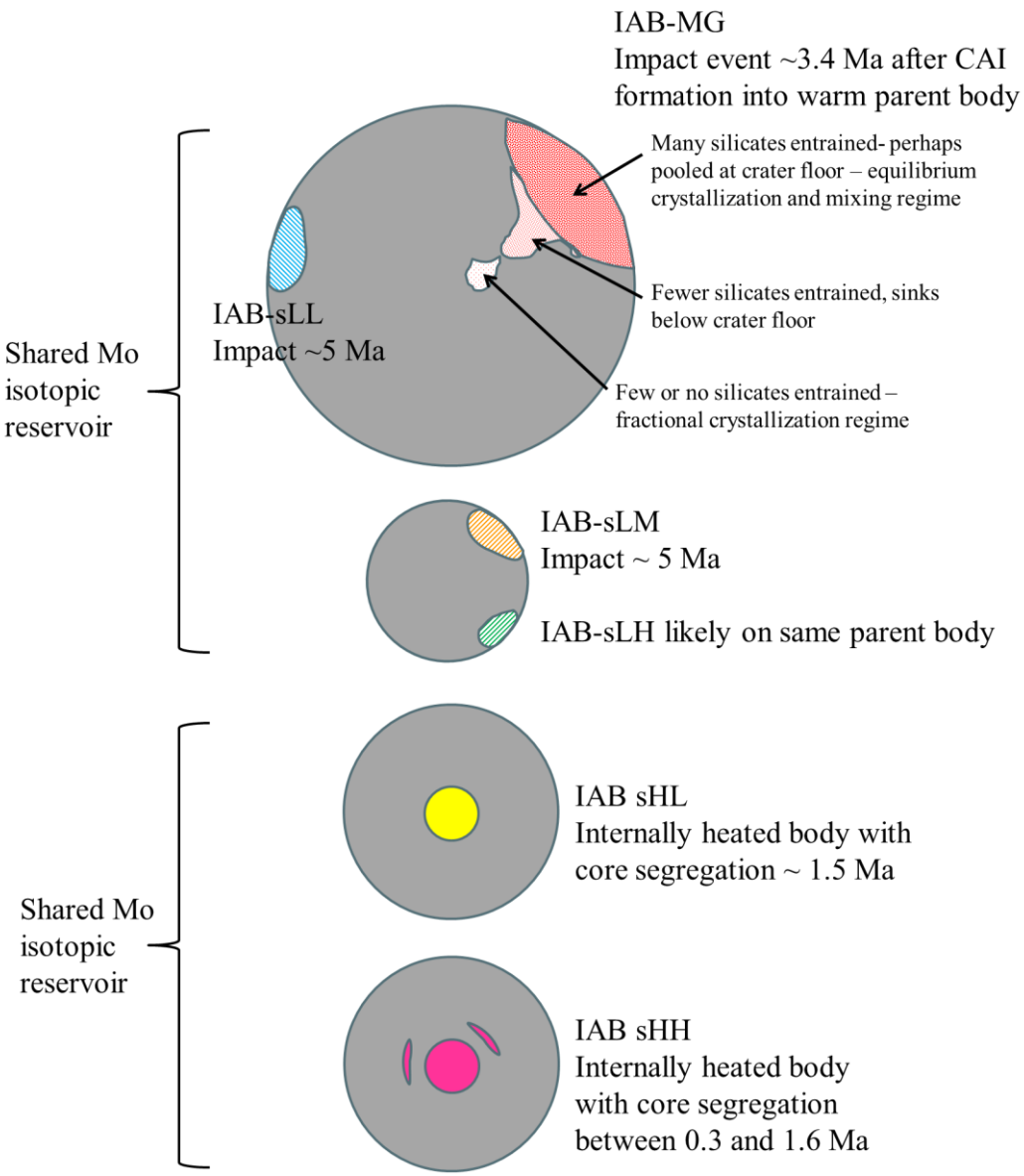

Fig. 6.1 Idealized parent bodies and preferred formation scenarios for the IAB complex subgroups. Parent bodies are not to scale.

6.2 Outstanding issues

For reasons discussed in Chapters 2 and 5, the formation scenarios favored here for the MG and the sLL, sLM, and sLH low Au subgroups invoke local impact-generated melting on undifferentiated parent bodies (e.g., Wasson and Kallemeyn, 2002), rather

than melting from internal heating, followed by disruptive impacts on partially differentiated parent bodies (e.g., Benedix et al., 2000). However, several questions remain regarding the nature of the IAB complex parent bodies and the formation of the IAB iron meteorites. Primarily, the efficiency of impact-melting and the impact energy required to generate appropriate volumes of melt must be evaluated in order to better understand the formation of the IAB subgroups. Important parameters, such as the relative sizes of the target parent body and impactor, porosity of the target, and impact velocity and angle control the volume of melt produced and whether or not the target body is disrupted. This is because these parameters dictate the distribution of impact energy into the body; specifically, how the energy of the impact is converted into heat and kinetic energy (e.g., Asphaug et al., 2015). If the type of impact(s) which created the MG and the low Au subgroups can be constrained, impacting processes and their role in generating certain types of cosmochemical materials in the early solar system may be better understood.

The presence of features consistent with low degrees of shock is characteristic of some IAB irons (Benedix et al, 2000), which places important constraints on the types of impacts that can have generated IAB melts. For example, it is unclear whether the volume of MG material (potentially on the order of 3-6 km^3 – Wasson and Kallemeyn, 2002) is consistent with the volumes of melt expected from local impact-heating at low shock pressures. Therefore, in addition to non-disruptive impacts favored here and by Wasson and Kallemeyn (2002), larger disruptive impacts (Benedix et al., 2000), or hit-and-run collisions must also be considered. Low-velocity hit-and-run collisions are expected to create substantial melt and little shock (Asphaug et al., 2006). This scenario

has been invoked to account for cooling rate differences in magmatic iron meteorite groups, such as the IVA group (Yang et al., 2007; Asphaug, 2010), and may be applicable to the IAB complex, given that the lack of shock features in IAB complex silicates is consistent with this type of collision (Goldstein et al., 2013). However, the requirement of uniform insulation shortly after crystallization, as evidenced by the slow sub-solidus cooling rates in IAB irons, may be difficult to meet by a glancing impact. Though cooling rate measurements in IAB irons have been observed to be tightly clustered around 10-20 K/Myr, few measurements currently exist (Goldstein et al., 2013). The observation of a wider range of cooling rates in future measurements of IAB irons could provide support for a hit-and-run or catastrophic breakup and reassembly origin. Further calculations of the volume of the IAB complex melts, in comparison to the volume of melt that can be generated locally or globally by different types of impact into warm vs. cold bodies at the time IAB metal segregated, are required to test such hypotheses.

6.3 Future Directions

The type of study presented here, where data for multiple isotope systems are paired with major and trace element concentrations, can be applied to any group of cosmochemical materials. Ungrouped iron meteorites may sample ≥ 50 unique parent bodies, so it is important to determine if the variety of ungrouped iron meteorites will extend the sample size of nebular reservoirs represented by iron meteorites.

Some important groups of meteorites for which isotopic and elemental evidence would be useful are the groups H, L, and LL ordinary chondrites, which constitute the largest population of meteorites. Oxygen isotopes suggest that each of these meteorite groups sample one parent body, or more than one closely related parent bodies (Clayton et al., 1991). Molybdenum data for Richardton and Allegan (both H5), suggest that at least two parent bodies may be sampled by the H chondrites. A systematic study of the Mo isotopic compositions of H, L, and LL chondrites may shed light on how many parent bodies are represented by the most common type of meteorite.

It would be also informative to investigate the primitive achondrites in this way. The winonaites, acapulcoites, lodranites, brachinites, and ureilites are small groups that have been the focus of relatively few studies each. These meteorites are intermediate between chondrites and differentiated meteorites, in terms of the degree to which their parent bodies were heated. They therefore represent an opportunity to study the nebular connection between undifferentiated and differentiated parent bodies. Further, the ureilites may have originated on an isotopically heterogeneous parent body (Goderis et al., 2015), and may be important for understanding how planetary processes can modify nucleosynthetic isotopic signatures.

Coupling Mo isotopes with other isotopic systems that show nucleosynthetic effects will also provide insight into the origin of nucleosynthetic variability. For example, Mo isotope anomalies are coupled with Ru isotope anomalies (e.g., Dauphas et al., 2004). By studying the extent to which this Mo-Ru cosmic correlation holds for a wide variety of cosmochemical materials, it may be possible to elucidate the natures of the presolar carriers of nucleosynthetic anomalies. Further, the position of the Earth

relative to the cosmic Mo-Ru correlation may help to elucidate the nature of late accreted materials versus the major contributors of mass to Earth (e.g., Dauphas et al., 2004).

The Mo isotopic composition of lunar impact melt rocks may reflect the isotopic composition of the impactors that generated them, as do Os isotopes in lunar impact melt breccias (Puchtel et al., 2008). The characterization of a late impacting population using the Mo isotopic system may elucidate the source and type of material(s) which may have seeded the Earth and other terrestrial planetary bodies with the HSE, water, and/or organics (e.g., Tingle et al., 1992; Cooper et al., 2001; Kring and Cohen, 2002).

Finally, Archean terrestrial rocks derived from a mantle source that has been contaminated with late accreted material may contain a Mo isotopic signature inherited from the foreign material. Such scenarios have been suggested to explain isotopically anomalous W in certain komatiites (e.g., Willbold et al., 2011; Touboul et al., 2012).

The potential for large-scale mantle heterogeneity and the efficiency of mantle mixing in the Earth from the Archean to the modern day may be evaluated using Mo isotopes. Because late accretion to the Earth was likely dominated by a few large impactors after the cessation of core formation (Bottke et al., 2010), it is possible that some impactors transmitted unique genetic signatures to distinct mantle domains. It is unclear whether, or on what time scales, mantle mixing and convection homogenized the isotopic signatures imparted during the later stages of the growth of the Earth. Future work using Mo and W isotopic compositions of ancient and modern terrestrial rocks to investigate signatures that may have been left by those impactors will be important to provide constraints on the efficiency of mantle mixing and the nature of the late accreted materials.

Bibliography

Achterbergh E. V., Ryan C. G., Jackson S. E., and Griffin W. L. (2001) Appendix 3: Data reduction software for LA-ICP-MS. In *Laser Ablation-ICP-MS in the Earth Sciences*, vol. 29 (ed. P. Sylvester). Mineralogical Association of Canada, Short Course Series, 243pp.

Aggarwal S. K., Wang B. -S., You C. -F., and Chung C. -H. (2009) Fractionation correction methodology for precise and accurate isotopic analysis of boron by negative thermal ionization mass spectrometry based on BO_2^- ions and using the $^{18}O/^{16}O$ ratio from ReO_4^- for internal normalization. *Anal. Chem.* **81**, 7420-7427.

Albarède F., Bouchet R. A., and Blichert-Toft J. (2013) Siderophile elements in IVA irons and the compaction of their parent asteroidal core. *Earth Planet Sc. Lett.* **362**, 122-129.

Allègre C. J. and Luck J.-M. (1980) Osmium isotopes as petrogenetic and geological tracers. *Earth Planet. Sci. Lett.* **48**, 148-154.

Amelin Y., Krot A. N., Hutcheon I. D., and Ulyanov A. A. (2002) Lead isotopic ages of chondrules and calcium–aluminum-rich inclusions. *Science* **297**, 1678–1683.

Anbar A. D., Knab K. A., and Barling J. (2001) Precise determination of mass-dependent variations in the isotopic composition of molybdenum using MC-ICPMS. *Anal. Chem.* **73**, 1425-1431.

Anbar, A.D. (2004) Molybdenum stable isotopes: Observations, interpretations and directions. *Rev. Min. Geochem.* **55**, 429-454.

Anders E., and Grevesse N. (1989) Abundances of the elements: Meteoritic and solar. *Geochim. Cosmochim. Acta* **53**, 197-214.

Andreasen R. and Sharma M. (2006) Solar nebula heterogeneity in p-process samarium and neodymium isotopes. *Science* **314**, 806-809.

Andreasen R. and Sharma M. (2007) Mixing and homogenization in the early solar system: Clues from Sr, Ba, Nd, and Sm isotopes in meteorites. *Astrophys. J.* **665**, 874-883.

Archer G. J., Ash R. D., Bullock E. S., and Walker R. J. (2014) Highly siderophile elements and ^{187}Re-^{187}Os isotopic systematics of the Allende meteorite: Evidence for primary nebular processes and late-stage alteration. *Geochim. Cosmochim. Acta* **131**, 402-414.

Archer G. J., Mundl A., Walker R. J., Worsham E.A., and Bermingham K.R. (2016) High-precision analysis of $^{182}W/^{184}W$ and $^{183}W/^{184}W$ by negative thermal ionization mass spectrometry: Per-integration oxide corrections using measured $^{18}O/^{16}O$. *Int. J. Mass. Spectrom.* **In Review**.

Arlandini C., Käppeler F., Wisshak K., Gallino R., Lugaro M., Busso M., and Straniero O. (1999) Neutron capture in low-mass asymptotic giant branch stars: Cross sections and abundance signatures. *Astrophys. J.* **525**, 886-900.

Asphaug E. (2010) Similar-sized collisions and the diversity of planets. *Chem. Erde-Geochem.* **70**, 199-219.

Asphaug E., Agnor C. B., and Williams Q. (2006) Hit-and-run planetary collisions. *Nature* **439**, 155-160.

Asphaug E., Collins G., and Jutzi M. (2015) Global scale impacts. In *Asteroids IV* (P. Michel et al., eds.) pp. 661-677. Univ. of Arizona, Rucson, DOI: 10.2458/azu_uapress_9780816532131-ch034

Baertschi P. (1976) Absolute ^{18}O content of standard mean ocean water. *Earth Planet. Sci. Lett.* **31**, 341-344.

Bandi W. R., Buyok E. G., Lewis L. L., and Melnick L. M. (1961) Anion exchange separation of zirconium, titanium, niobium, tantalum, tungsten, and molybdenum. *Anal. Chem.* **33**, 1275-1278.

Barling, J., Arnold, G. L., and Anbar, A. D. (2001) Natural mass-dependent variations in the isotopic composition of molybdenum. *Earth Planet. Sc. Lett.* **193**, 447-457.

Becker H., Morgan J. W., Walker R. J., MacPherson G. L., and Grossman J. N. (2001) Rhenium–osmium systematics of calcium–aluminum-rich inclusions in carbonaceous chondrites. *Geochim. Cosmochim. Acta* **65**, 3379–3390.

Becker, H. and Walker, R. J. (2003) Efficient mixing of the solar nebula from uniform Mo isotopic composition of meteorites. *Nature* **425**, 152-155.

Benedix G. K., McCoy T. J., Keil K., and Love S. G. (2000) A petrologic study of the IAB iron meteorites: Constraints on the formation of the IAB-Winonaite parent body. *Meteorit. Planet. Sci.* **35,** 1127-1141.

Benedix G. K., Lauretta D. S., and McCoy T. J. (2005) Thermodynamic constraints on the formation conditions of winonaites and silicate-bearing IAB irons. *Geochim. Cosmochim. Acta* **69**, 5123-5131.

Bermingham K. R., Mezger K., Scherer E. E., Horan M. F., Carlson R. W., Upadhyay D., Magna T., and Pack A. (2016a) Barium isotope abundances in meteorites and their implications for early solar system evolution. *Geochim. Cosmochim. Acta* **175**, 282-298.

Bermingham K. R., Walker R. J., and Worsham E. A. (2016b) Refinement of high precision Ru isotope analysis using negative thermal ionization mass spectrometry. *Int. J. Mass Spec.* **403**, 15-26.

Bild R.W. (1977) Silicate inclusions in group IAB irons and a relation to the anomalous stones Winona and Mt. Morris (Wis). *Geochim. Cosmochim. Acta* **41**, 1439-1456.

Birck J.-L., Roy-Barman M., and Capmas F. (1997) Re-Os isotopic measurements at the femtomole level in natural samples. *Geostand. Newslett.* **20**, 9-27.

Bogard D.D., Garrison D.H., and Takeda H. (2005) Ar-Ar and I-Xe ages and the thermal history of IAB meteorites. *Meteorit. Planet. Sci.* **40(2),** 207-224.

Bottke, W. F., Walker, R. J., Day, J. M. D., Nesvorny, D., and Elkins-Tanton, L., (2010) Stochastic Late Accretion to Earth, the Moon, and Mars. *Science* **330**, 1527-1530.

Bouvier A. and Wadhwa M. (2010) The age of the Solar System redefined by the oldest Pb–Pb age of a meteorite inclusion. *Nat. Geosci.* **3**, 637–641.

Buchwald V.F. (1975) *Handbook of Iron Meteorites.* University of California Press. 1418 pp.

Bunch T. E., Keil K., and Huss G. I. (1972) The Landes meteorite. *Meteoritics* **7**, 31-38.

Burbidge E. M., Burbidge G. R., Fowler W. A., and Hoyle F. (1957) Synthesis of the elements in stars. *Rev. Mod. Phys.* **29**, 547-650.

Burkhardt C., Kleine, T., Oberli F., Pack A., Bourdon B., and Wieler, R. (2011) Molybdenum isotope anomalies in meteorites: Constraints on solar nebula evolution and origin of the *Earth. Earth Planet. Sc. Lett.* **312**, 390-400.

Burkhardt C., Kleine T., Dauphas N., and Wieler R. (2012) Origin of isotopic heterogeneity in the solar nebula by thermal processing and mixing of nebular dust. *Earth Planet. Sci. Lett.* **357**, 298-307.

Burkhardt C., Hin R. C., Kleine T., and Bourdon B. (2014) Evidence for Mo isotope fractionation in the solar nebula and during planetary differentiation. *Earth Planet. Sc. Lett.* **391**, 201-211.

Cameron A. G. W. (1957) *Stellar evolution, nuclear astrophysics and nucleogenesis*. In Chalk River Report, pp. CRL-41. AELC (Atomic Energy of Canada, Ltd.).

Cameron, A. G. W. and Truran, J. W. (1977) Supernova Trigger for Formation of Solar-System. *Icarus* **30**, 447-461.

Campbell A. J., Humayun M., and Weisberg M. K. (2002) Siderophile element constraints on the formation of metal in the metal-rich chondrites Bencubbin, Weatherford, and Gujba. *Geochim. Cosmochim. Acta* **66**, 647-660.

Campbell A. J. and Humayun M. (2005) Compositions of group IVB iron meteorites and their parent melt. *Geochim. Cosmochim. Acta* **69**, 4733-4744.

Chabot N.L. and Jones J.H. (2003) The parameterization of solid metal-liquid metal partitioning of siderophile elements. *Meteorit. Planet. Sci.* **38**, 1425-1436.

Chabot N.L., Campbell A.J., Jones J.H., Humayun M., and Lauer, Jr., H.V. (2006) The influence of carbon on trace element partitioning behavior. *Geochim. Cosmochim. Acta* **70**, 1322-1335.

Chabot N.L., Wollack E.A., McDonough W.F., and Ash R.D. (2014) The effect of light elements in metallic liquids on partitioning behavior. *Lunar Planet. Sci.* XLV. Lunar Planet. Inst., Houston. #1165 (abstr.).

Chambers, J. E., (2004) Planetary accretion in the inner Solar System. *Earth Planet. Sc. Lett.* **223**, 241-252.

Chatterjee R. and Lassiter J. C. (2015) High precision Os isotopic measurement using N-TIMS: Quantification of various sources of error in $^{186}Os/^{188}Os$ measurements. *Chem. Geol.* **396**, 112-123.

Chen J. H., Papanastassiou D. A. and Wasserburg G. J. (1998) Re–Os systematics in chondrites and the fractionation of the platinum group elements in the early Solar System. *Geochim. Cosmochim. Acta* **62**, 3379–3392.

Chen J. H., Papanastassiou D. A., and Wasserburg G. J. (2010) Ruthenium endemic isotope effects in chondrites and differentiated meteorites. *Geochim. Cosmochim. Acta* **74**, 3851-3862.

Choi B. G., Ouyang X. W., and Wasson J. T. (1995) Classification and Origin of IAB and IIICD Iron-Meteorites. *Geochim. Cosmochim. Acta* **59**, 593-612.

Chu Z. -Y., Li C. -F., Chen Z., Xu J. -J., Di Y. -K., and Guo J. -H. (2015) High-precision measurement of $^{186}Os/^{188}Os$ and $^{187}Os/^{188}Os$: Isobaric oxide corrections with in-run measured oxygen isotope ratios. *Anal. Chem.* **87**, 8765-8771.

Clayton, R. N. (1993) Oxygen Isotopes in Meteorites. *Annu. Rev. Earth Pl. Sc.* 21, 115-149.

Clayton R. N. and Mayeda T. K. (1996) Oxygen isotope studies of achondrites. *Geochim. Cosmochim. Acta* **60**, 1999-2017.

Clayton, R. N., Onuma, N., and Mayeda, T. K. (1976) Classification of Meteorites Based on Oxygen Isotopes. *Earth Planet. Sc. Lett.* **30**, 10-18.

Clayton R. N., Mayeda T. K., Goswami J. N., and Olsen E. J. (1991) Oxygen isotope studies of ordinary chondrites. *Geochim. Cosmochim. Acta* **55**, 2317-2337.

Cohen A. S. and Waters F. J. (1996) Separation of osmium from geological materials by solvent extraction for analysis by thermal ionization mass spectrometry. *Anal. Chim. Acta* **332**, 269-275.

Cook D. L., Walker R. J., Horan M. F., Wasson J. T., and Morgan J. W. (2004) Pt-Re-Os systematics of group IIAB and IIIAB iron meteorites. *Geochim. Cosmochim. Acta* **68**, 1413-1431.

Cooper, G., Kimmich, N., Belisle, W., Sarinana, J., Brabham, K., and Garrel, L. (2001) Carbonaceous meteorites as a source of sugar-related organic compounds for the early Earth. *Nature* **414**, 879-883.

Creaser R. A. Papanastassiou D. A., and Wasserburg G. J. (1991) Negative thermal ion mass spectrometry of osmium, rhenium and iridium. *Geochim. Cosmochim. Acta* **55**, 397-401.

Crocket J. H. (1972) Some aspects of the geochemistry of Ru, Os, Ir, and Pt in iron meteorites. *Geochim. Cosmochim. Acta* **36**, 517-535.

Dauphas N., Reisberg L., and Marty B. (2001) Solvent extraction, ion chromatography, and mass spectrometry of molybdenum isotopes. *Anal. Chem.* **73**, 2613-2616.

Dauphas N., Marty B., and Reisberg L. (2002a) Molybdenum evidence for inherited planetary scale isotope heterogeneity of the protosolar nebula. *Astrophys. J.* **565**, 640-644.

Dauphas N., Marty B., and Reisberg L. (2002b) Molybdenum nucleosynthetic dichotomy revealed in primitive meteorites. *Astrophys. J.* **569**, L139-L142

Dauphas N., Davis A. M., Marty B., and Reisberg L. (2004) The cosmic molybdenum-ruthenium isotope correlation. *Earth Planet. Sci. Lett.* **226**, 465-475.

Dauphas N., Remusat L., Chen J. H., Roskosz M., Papanastassiou D., Stodolna J., Guan Y., Ma C., and Eiler J. M. (2010) Neutron-rich chromium isotope anomalies in supernova nanoparticles. *Astrophys. J.* **720**, 1577-1591.

Davison T. M., Collins G. S., and Ciesla F. J. (2010) Numerical modelling of heating in porous planetesimal collisions. *Icarus* **208**, 468-481.

Davison T. M., O'Brien D. P., Ciesla F. J., and Collins G. S. (2013) The early impact histories of meteorite parent bodies. *Meteorit. Planet. Sci.* **48**, 1894-1918.

Dodson R. W., Forney G. J., and Swift E. H. (1936) The extraction of ferric chloride from hydrochloric acid solutions by isopropyl ether. *J. Am. Chem. Soc.* **58**, 2573-2577.

Fischer-Gödde M., Burkhardt C., Kruijer T. S., and Kleine T. (2015) Ru isotope heterogeneity in the solar protoplanetary disk. *Geochim. Cosmochim. Acta* **168**, 151-171.

Fischer-Gödde M., Render J., Budde G., Burkhardt C., and Kleine T. (2016) Molybdenum isotope dichotomy of meteorites. *Goldschmidt Conference Abstract 822.*

Fish R.A., Goles G.G., and Anders E. (1960) The record in the meteorites. III. on the development of meteorites in asteroidal bodies. *Astrophys. J.* **132**, 243.

Franchi I. A. (2008) Oxygen isotopes in asteroidal materials. *Rev. Mineral. Geochem.* **68**, 345-397.

Fujii, T., Moynier, F., Telouk, P., and Albarède, F. (2006) Mass-independent isotope fractionation of molybdenum and ruthenium and the origin of isotopic anomalies in Murchison. *Astrophys. J.* **647**, 1506-1516.

Giussani A., Hansen Ch., Nüsslin F., and Werner E. (1995) Application of thermal ionization mass spectrometry to investigations of molybdenum absorption in humans. *Int. J. Mass Spec. Ion Proc.***148**, 171-178.

Goderis S., Brandon A. D., Mayer B., and Humayun M. (2015) s-Process Os isotope enrichment in ureilites by planetary processing. *Earth Planet. Sci. Lett.***431**, 110-118.

Goldberg E., Uchiyama A., and Brown H. (1951) The distribution of nickel, cobalt, gallium, palladium and gold in iron meteorites. *Geochim. Cosmochim. Acta* **2**, 1-25.

Goldstein J. I. and R. E. Ogilvie (1965) The growth of the Widmanstätten pattern in metallic meteorites. *Geochim. Cosmochim. Acta* **29**, 893-920.

Goldstein J. I. and Short J.M. (1967) The iron meteorites, their thermal history and parent bodies. *Geochim. Cosmochim. Acta* **31**, 1733-1770.

Goldstein J. I., Scott E. R. D., and Chabot N. L. (2009) Iron meteorites: Crystallization, thermal history, parent bodies, and origin. *Chem. Erde-Geochem.* **69**, 293-325.

Goldstein J. I., Scott E. R. D., Winfield T., and Yang J. (2013) Thermal histories of group IAB and related iron meteorites and comparison with other groups of irons and stony iron meteorites. *Lunar Planet. Sci. XLIV.* Lunar Planet. Inst., Houston. #1394 (abstr.)

Greenwood R. C., Franchi I. A., Jambon A., Barrat J. A., and Burbine T. H. (2006) Oxygen isotope variation in stony-iron meteorites. *Science* **313**, 1763-1765.

Greenwood R. C., Franchi I. A., Gibson J. M., and Benedix G. K. (2012) Oxygen isotope variation in primitive achondrites: The influence of primordial, asteroidal and terrestrial processes. *Geochim. Cosmochim. Acta* **94**, 146-163.

Grossman, L. (1972) Condensation in the primitive solar nebula. *Geochim. Cosmochim. Acta* **36**, 297-619.

Harper C. L. and Jacobsen S. B. (1996) Evidence for ^{182}Hf in the early Solar System and constraints on the timescale of terrestrial accretion and core formation. *Geochim. Cosmochim. Acta* **60**, 1311-1153.

Hermann F., Kiesl W., Kluger F., and Hecht F. (1971) Neutronenaktivierungsanalytische bestimmung einiger spurenelemente in meteoritischen phasen. *Mikrochim. Acta* **2**, 225-240

Herpfer M. A., Larimer J. W., and Goldstein J. I. (1994) A comparison of metallographic cooling rate methods used in meteorites. *Geochim. Cosmochim. Acta* **58**, 1353-1365.

Heumann K. G., Eisenhut S., Gallus S., Hebeda E. H., Nusko R., Vengosh A., and Walczyk T. (1995) Recent developments in thermal ionization mass spectrometric techniques for isotope analysis. *Analyst* **120**, 1291-1299.

Hirata T. and Masuda A. (1992) Rhenium and osmium systematics on iron and stony iron meteorites. *Meteoritics* **27**, 568-575.

Hirata T. and Nesbitt R. W. (1997) Distribution of platinum group elements and rhenium between metallic phases of iron meteorites. *Earth Planet. Sc. Lett.* **147**, 11-24.

Hoashi M., Brooks R.R., and Reeves R.D. (1993) Palladium, platinum, and ruthenium in iron meteorites and their taxonomic significance. *Chem. Geol.* **106**, 207-218.

Horan M. F., Smoliar M. I., and Walker R. J. (1998) ^{182}W and ^{187}Re-^{187}Os systematics of iron meteorites: Chronology for melting, differentiation, and crystallization in asteroids. *Geochim. Cosmochim. Acta* **62**, 545-554.

Horan M. F., Walker R. J., Morgan J. W., Grossman J. N., and Rubin A. E. (2003) Highly siderophile elements in chondrites. *Chem. Geol.* **196**, 5-20.

Horan M. F., Alexander C. M. O'D., and Walker R. J. (2009) Highly siderophile element evidence for early Solar System processes in components from ordinary chondrites. *Geochim. Cosmochim. Acta* **73**, 6984-6997.

Hsu W., Huss G. R., and Wasserburg G. J. (2000) Ion probe measurements of Os, Ir, Pt, and Au in individual phases of iron meteorites. *Geochim. Cosmochim. Acta* **64**, 1133-1147.

Humayun M., Davis F. A., and Hirschmann M. M. (2010) Major element analysis of natural silicates by laser ablation ICP-MS. *J. Anal. Atom. Spectrom.* **25**, 998-1005.

Javoy M. (1995) The integral enstatite chondrite model of the earth. *Geophys. Res. Lett.* **22**, 2219-2222.

Jones J.H. and Drake M.J. (1983) Experimental investigations of trace element fractionation in iron meteorites. II: The influence of sulfur. *Geochim. Cosmochim. Acta* **47**, 1199-1209.

Jones J.H. and Malvin D.J. (1990) A nonmetal interaction model for the segregation of trace metals during solidification of Fe-Ni-S, Fe-Ni-P, and Fe-Ni-S-P alloys. *Metall. Mater. Trans. B* **21B**, 697-706.

José, J. and Iliadis, C. (2011) Nuclear astrophysics: the unfinished quest for the origin of the elements. *Reports on Progress in Physics* **74**. 1-48.

Kelly W. R. and Larimer J. W. (1977) Chemical fractionations in meteorites – VIII. Iron meteorites and the cosmochemical history of the metal phase. *Geochim. Cosmochim. Acta* **41**, 93-111.

Keil K., Stöffler D., Love S. G., and Scott E. R. D (1997) Constraints on the role of impact heating and melting in asteroids. *Meteorit. Planet. Sci.* **32**, 349-363.

Kleine T., Mezger K., Münker C., Palme H., Bischoff A. (2004) ^{182}Hf–^{182}W isotope systematics of chondrites, eucrites, and Martian meteorites: Chronology of core formation and mantle differentiation in Vesta and Mars, *Geochim. Cosmochim. Acta* **68**, 2935–2946.

Koornneef J. M., Bouman C., Schwieters J. B., and Davies G. R. (2013) Use of $10^{12}\Omega$ current amplifiers in Sr and Nd isotope analyses by TIMS for application to sub-nanogram samples. *J. Anal. At. Spectrom.* **28**, 749-754.

Koornneef J. M., Bouman C., Schwieters J. B., and Davies G. R. (2014) Measurement of small ion beams by thermal ionization mass spectrometry using new 10^{13} Ohm resistors. *Anal. Chim. Acta* **819**, 49-55.

Kracher A. (1985) The evolution of partially differentiated planetesimals: Evidence from iron meteorite groups IAB and IIICD. *J. Geophys. Res.* **90 (S02)**, C689-C698.

Kracher A., Willis J., and Wasson J. T. (1980) Chemical classification of iron meteorites-IX. A new group (IIF), revision of IAB and IIICD, and data on 57 additional irons. *Geochim. Cosmochim. Acta* **44**, 773-787.

Kring, D. A. and Cohen, B. A. (2002) Cataclysmic bombardment throughout the inner solar system 3.9-4.0 Ga. *J Geophys Res-Planet* **107**(E2), 5009.

Kruijer T. S., Fischer-Gödde M., Kleine T., Sprung P., Leya I., and Wieler R. (2013) Neutron capture on Pt isotopes in iron meteorites and the Hf-W chronology of core formation in planetesimals. *Earth Planet. Sc. Lett.* **361**, 162-172.

Kruijer T. S., Touboul M., Fischer-Gödde M., Bermingham K. R., Walker R. J., and Kleine T. (2014a) Protracted core formation and rapid accretion of protoplanets. *Science* **344**, 1150-1154.

Kruijer T. S., Kleine T., Fischer-Gödde M., Burkhardt C., and Wieler R. (2014b) Nucleosynthetic W isotope anomalies and the Hf-W chronometry of Ca–Al-rich inclusions. *Earth Planet. Sc. Lett.* **403**, 317-327.

Kuroda, P. K. and Sandell, E. B. (1954) Geochemistry of molybdenum. *Geochim. Cosmochim. Ac.* **6**, 35-63.

Lee T., Papanastassiou D. A., and Wasserburg G. J. (1977) Aluminum-26 in the early solar system: Fossil or Fuel? *Astrophys. J.* **211**, L107-L110.

Lee D. C. and Halliday A. N. (1995) Precise determinations of the isotopic compositions and atomic weights of molybdenum, tellurium, tin and tungsten using ICP magnetic sector multiple collector mass spectrometry. *Int. J. Mass. Ion Proc.* **31**, 35-46.

Lee D.-C. and Halliday A. N. (1996) Hf-W isotopic evidence for rapid accretion and differentiation in the early solar system. *Science* **274**, 1876–1879.

Lewis C. F. and Moore C. B. (1971) Chemical analyses of thirty-eight iron meteorites. *Meteoritics* **6**, 195-205.

Li W. -J., Jin D., Chang T. -L. (1988) *Kexue Tinboa* **33**, 1610.

Liu Y., Huang M., Masuda A., and Inoue M. (1998) High-precision determination of osmium and rhenium isotope ratios by in situ oxygen isotope ratio correction using negative thermal ionization mass spectrometry. *Int. J. Mass Spectrom.* **173**, 163-175.

Liu J. and Pearson D. (2014) Rapid, precise and accurate Os isotope ratio measurements of nanogram to sub-nanogram amounts using multiple Faraday collectors and amplifiers equipped with $10^{12}\Omega$ resistors by N-TIMS. *Chem. Geol.* **363**, 301-311.

Lodders K. (2003) Solar System abundances and condensation temperatures of the elements. *Astrophys. J.* **59**, 1220-1247.

Lovering J. F. (1957) Differentiation in the iron-nickel core of a parent meteorite body. *Geochim. Cosmochim. Acta* **12**, 238-252.

Lovering J. F., Nichiporuk W., Chodos A., and Brown H. (1957) The distribution of gallium, germanium, cobalt, chromium, and copper in iron and stony-iron meteorites in relation to nickel content and structure. *Geochim. Cosmochim. Acta* **11**, 263-278.

Lu Q. and Masuda A. (1992) High accuracy measurement of isotope ratios of molybdenum in some terrestrial molybdenites. *J. Am. Soc. Mass Spectrom.* **3**, 10-17.

Lu Q. and Masuda A. (1994) The isotopic composition and atomic weight of molybdenum. *Int. J. Mass Spectrom. Ion Proc.* **130**, 65–72.

Ludwig K. R. (2003) User's Manual for Isoplot 3.00. Berkeley Geochronology Center Special Publication No. 4, Berkeley, CA, 70pp.

Luguet A., Nowell G. M., and Pearson G. (2008) $^{184}Os/^{188}Os$ and $^{186}Os/^{188}Os$ measurements by negative thermal ionization mass spectrometry (N-TIMS): Effects of interfering element and mass fractionation corrections on data accuracy and precision. *Chem. Geol.* **248**, 342-362.

Markowski A., Quitté G., Halliday A. N., and Kleine T. (2006) Tungsten isotopic compositions of iron meteorites: Chronological constraints vs. cosmogenic effects. *Earth Planet. Sci. Lett.* **242**, 1-15.

Masarik J. (1997) Contribution of neutron-capture reactions to observed tungsten isotopic ratios. *Earth Planet. Sci. Lett.* **152**, 181-185.

McCoy T. J., Keil K., Scott E. R. D, and Haack H. (1993) Genesis of the IIICD iron meteorites: Evidence from silicate-bearing inclusions. *Meteoritics* **28**, 552-560.

McCoy T. J., Ehlmann A. J., Benedix G. K., Keil K., and Wasson J. T. (1996) The Lueders, Texas, IAB iron meteorite with silicate inclusions. *Meteorit. Planet. Sci.* **31**, 419-422.

McCoy T. J., Walker R. J., Goldstein J. I., Yang J., McDonough W. F., Rumble D., Chabot N. L., Ash R. D., Corrigan C. M., Michael J. R., and Kotula P. G. (2011) Group IVA irons: New constraints on the crystallization and cooling history of an asteroidal core with a complex history. *Geochim. Cosmochim. Acta* **75**, 6821-6843.

McDonough W. F., Horn I., Lange D., and Rudnick R. L. (1999) Distribution of platinum group elements between phases in iron meteorites. *Lunar Planet. Sci.* XXX, Lunar Planet. Inst., Houston. #2062 (absr.)

Meija J., Coplen T. B., Berglund M., Brand W. A., De Bièvre P., Gröning M., Holden N. E., Irrgeher J., Loss R. D., Walczyk T., and Prohaska T. (2016) Isotopic compositions of the elements 2013 (IUPAC technical report). *Pure Appl. Chem.* **88**, 293-306.

Moore C. B., Lewis C. F., and Nava D. (1969) Superior analyses of iron meteorites. In *Meteorite Research* (ed. P. M. Millman), pp. 738-748. Reidel, Dodrecht, Holland.

Mughabghab S. F. (2003) Thermal neutron capture cross sections, resonance integrals, and G-factors. International Nuclear Data Committee INDC(NDS)-440 Distr. PG+R.

Nagai Y. and Yokoyama T. (2014) Chemical separation of Mo and W from terrestrial and extraterrestrial samples via anion exchange chromatography. *Analytical Chem.* **86**, 4856-4863.

Nagai Y. and Yokoyama T. (2016a) Molybdenum isotopic analysis by negative thermal ionization mass spectrometry (N-TIMS): Effects on oxygen isotopic composition. *J. Anal. At. Spectrom.* **29**, 1090-1096.

Nagai Y. and Yokoyama T. (2016b) Molybdenum isotope anomalies in non-carbonaceous meteorites. *Lunar Planet. Sci. Conf.* **47**, 1888.

Nicolussi G. K., Pellin M. J., Lewis R. S., Davis A. M., Amari S., and Clayton R. N. (1998) Molybdenum isotopic composition of individual presolar silicon carbide grains from the Murchison meteorite. *Geochim. Cosmochim. Acta* **62**, 1093–1104.

Nier A. O. (1950) A redetermination of the relative abundances of the isotopes of carbon, nitrogen, oxygen, argon, and potassium. *Phys. Rev.* **77**, 789–793.

Niemeyer S. and Lugmair G. W. (1984) Titanium isotopic anomalies in meteorites. *Geochim. Cosmochim. Acta* **48**, 1401-1416.

Nittler, L. R. (2003) Presolar stardust in meteorites: recent advances and scientific frontiers. *Earth Planet. Sc. Lett.* **209**, 259-273.

Ohtani H. and Nishizawa T. (1986) Calculation of Fe-C-S ternary phase diagram. *Trans. Iron Steel Inst. Japan* **26(7)**, 655-663. In: *ASM Alloy Phase Diagram Database* (eds. P. Villars, H. Okamoto, and K. Cenzual), ASM International, Materials Park OH, 2006.

Okamoto H. (1990) C-Fe (carbon-iron), second ed., In: *Binary alloy phase diagrams* **1** (ed. T. B. Massalaski), ASM International, pp. 842-848.

Pernicka E. and Wasson J.T. (1987) Ru, Re, Os, Pt, and Au in iron meteorites. *Geochim. Cosmochim. Acta* **51**, 1717-1726.

Pietruszka A. J., Walker R. J., and Candela P. A. (2006) Determination of mass-dependent molybdenum isotopic variations by MC-ICP-MS: An evaluation of matrix effects. *Chem. Geol.* **225**, 121-136.

Pilski A. S., Wasson J. T., Muszyński A., Kryza R., Karwowski Ł., and Nowak M. (2013) Low-Ir IAB irons from Morasko and other locations in central Europe: One fall, possibly distinct from IAB-MG. *Meteorit. Planet. Sci.* **48**, 2531-2541.

Puchtel, I. S., Walker, R. J., James, O. B., and Kring, D. A. (2008) Osmium isotope and highly siderophile element systematics of lunar impact melt breccias: Implications for the late accretion history of the Moon and Earth. *Geochim. Cosmochim. Ac.* **72**, 3022-3042.

Qin L., Dauphas N, Wadhwa M., Masarik J., and Janney P. E. (2008a) Rapid accretion and differentiation of iron meteorite parent bodies inferred from ^{182}Hf-^{182}W chronometry and thermal modeling. *Earth Planet. Sci. Lett.* **273**, 94-104.

Qin L., Dauphas N, Wadhwa M., Markowski A., Gallino R., Janney P.E., and Bouman C. (2008b) Tungsten nuclear anomalies in planetesimal cores. *Astrophys. J.* **674**, 1234–1241.

Qin, L. P., Alexander, C. M. O., Carlson, R. W., Horan, M. F., and Yokoyama, T. (2010) Contributors to chromium isotope variation of meteorites. *Geochim. Cosmochim. Ac.* **74**, 1122-1145.

Ranen M. C. and Jacobsen S. B. (2006) Barium isotopes in chondritic meteorites: Implications for planetary reservoir models. *Science* **314**, 809-812.

Rasmussen K. L., Malvin D. J., Buchwald V. F., and Wasson J. T., (1984) Compositional trends and cooling rates of group IVB iron meteorites. *Geochim. Cosmochim. Acta* **48**, 805-813.

Rasmussen K. L., Malvin D. J., and Wasson J. T. (1988) Trace element partitioning between taenite and kamacite; Relationship to the cooling rates of iron meteorites. *Meteoritics* **23**, 107-112.

Rasmussen K.L. (1989) Cooling rates and parent bodies of iron meteorites from group IIICD, IAB, and IVB. *Physica Scripta* **39**, 410-416.

Regelous M., Elliott T., and Coath C. D. (2008) Nickel isotope heterogeneity in the early solar system. *Earth Planet. Sci. Lett.* **272**, 330-338.

Rehkämper M., and Halliday A. N. (1997) Development and application of new ion-exchange techniques for the separation of the platinum group and other siderophile elements from geological samples. *Talanta* **44**, 663-672.

Rizo H., Walker R. J., Carlson R. W., Touboul M., Horan M. F., Puchtel I. S., Boyet M., and Rosing M. T. (2016) Early Earth differentiation investigated through ^{142}Nd, ^{182}W, and highly siderophile element abundances in samples from Isua, Greenland. *Geochim. Cosmochim. Acta* **175**, 319-336.

Russell W. A., Papanastassiou D. A., Tombrello T. A. (1978) Ca isotope fractionation in the Earth and other solar system materials. *Geochim. Cosmochim. Acta* **42**, 1075–1090.

Ruzicka A. (2014) Silicate-bearing iron meteorites and their implications for the evolution of asteroidal parent bodies. *Chem. Erde-Geochem.* **74**, 3-48.

Ruzicka A. and Hutson M. (2010) Comparative petrology of silicates in the Udei Station (IAB) and Miles (IIE) iron meteorites: Implications for the origin of silicate-bearing iron meteorites. *Geochim. Cosmochim. Acta* **74**, 394-433.

Ruzicka A., Hutson M., and Floss C. (2006) Petrology of silicate inclusions in the Sombrerete ungrouped iron meteorite: Implications for the origins of IIE-type silicate-bearing irons. *Meteorit. Planet. Sci.* **41**, 1797-1831.

Ryan D. E., Holzbecher J., and Brooks R. R. (1990) Rhodium and osmium in iron meteorites. *Chem. Geol.* **85**, 295-303.

Sahoo S. K. and Masuda A. (1997) Precise measurement of zirconium isotopes by thermal ionization mass spectrometry. *Chem. Geol.* **141**, 117-126.

Scheiderich K., Helz G. R., and Walker R. J. (2010) Century-long record of Mo isotopic composition in sediments of a seasonally anoxic estuary (Chesapeake Bay). *Earth. Planet. Sci. Lett.* **289**, 189-197.

Schulz T., Upadhyay D., Münker C., and Mezger K. (2012) Formation and exposure history of non-magmatic iron meteorites and winonaites: Clues from Sm and W isotopes. *Geochim. Cosmochim. Acta* **85**, 200-212.

Scott E. R. D. (1972) Chemical Fractionation in Iron-Meteorites and Its Interpretation. *Geochim. Cosmochim. Acta* **36**, 1205-1236.

Scott E. R. D. and Wasson J. T. (1975) Classification and Properties of Iron-Meteorites. *Rev. Geophys.* **13**, 527-546.

Scott E. R. D., Wasson J. T., and Buchwald V. F. (1973) The chemical classification of iron meteorites – VII. A reinvestigation of irons with Ge concentrations between 25 and 80 ppm. *Geochim. Cosmochim. Acta* **37**, 1957-1983.

Seitner H., Kiesl W., Kluger F., and Hecht F. (1971) Wet-chemical analysis and determination of trace elements by neutron activation in meteorites. *J. Radioanal. Chem.* **7**, 235-248.

Shen J. J., Papanastassiou D. A., and Wasserburg G. J. (1996) Precise Re-Os determinations and systematics in iron meteorites. *Geochim. Cosmochim. Acta* **60**, 2887-2900.

Siebert, C., Nägler, T. F., von Blanckenburg, F., and Kramers, J. D. (2003) Molybdenum isotope records as a potential new proxy for paleoceanography. *Earth Planet. Sc. Lett.* **211**, 159-171.

Smales A. A., Mapper D., and Fouche K. F. (1967) The distribution of some trace elements in iron meteorites as determined by neutron activation. *Geochim. Cosmochim. Acta* **31**, 673-720.

Smoliar M. I., Walker R. J., and Morgan J. W. (1996) Re-Os ages of group IIA, IIIA, IVA, and IVB iron meteorites. *Science* **271**, 1099-1102.

Sutton S. R., Delaney J. S., Smith J. V., and Prinz M. (1987) Copper and nickel partitioning in iron meteorites. *Geochim. Cosmochim. Acta* **51**, 2653-2662.

Takeda H., Bogard D.D., Mittlefehldt D.W., and Garrison D.H. (2000) Mineralogy, petrology, chemistry, and ^{39}Ar–^{40}Ar and exposure ages of the Caddo County IAB iron: Evidence for early partial melt segregation of a gabbro area rich in plagioclase–diopside. *Geochim. Cosmochim. Acta* **64**, 1311-1327.

Theis K.J., Schönbächler M., Benedix G.K., Rehkämper M., Andreasen R., and Davies C. (2013) Palladium-silver chronology of IAB iron meteorites. *Earth Planet. Sc. Lett.* **361**, 402-411.

Tingle, T. N., Tyburczy, J. A., Ahrens, T. J., and Becker, C. H. (1992) The Fate of Organic-Matter during Planetary Accretion - Preliminary Studies of the Organic-Chemistry of Experimentally Shocked Murchison Meteorite. *Origins of Life and Evolution of the Biosphere* **21**, 385-397.

Tomkins A.G., Mare E.R., and Reveggi M. (2013) Fe-carbide and Fe-sulfide liquid immiscibility in IAB meteorite, Campo del Cielo: Implications for iron meteorite chemistry and planetesimal core compositions. *Geochim. Cosmochim. Acta* **117**, 80-98.

Touboul M. and Walker R. J., (2012) High precision tungsten isotope measurement by thermal ionization mass spectrometry. *Int. J. Mass Spec.* **309**, 109-117.

Touboul, M., Puchtel, I. S., and Walker, R. J. (2012) W-182 Evidence for Long-Term Preservation of Early Mantle Differentiation Products. *Science* **335**, 1065-1069.

Trinquier A., Birck J. –L., and Allègre C. J (2007) Widespread ^{54}Cr heterogeneity in the inner solar system. *Astrophys. J.* **655**, 1179-1185.

Trinquier A., Elliott T., Ulfbeck D., Coath C., Krot A. N., and Bizzarro M. (2009) Origin of nucleosynthetic isotope heterogeneity in the solar protoplanetary disk. *Science* **324**, 374-376.

Trinquier A. (2016) Fractionation of oxygen isotopes by thermal ionization mass spectrometry inferred from simultaneous measurement of ^{17}O/^{16}O and ^{18}O/^{16}O ratios and implications for the ^{182}Hf-^{182}W systematics. *Anal Chem.* **88**, 5600-5604.

Trinquier A., Touboul M., and Walker R. J. (2016) High-precision tungsten isotopic analysis by multicollection negative thermal ionization mass spectrometry based on simultaneous measurement of W and ^{18}O/^{16}O isotope ratios for accurate fractionation correction. *Anal. Chem.* **88**, 1542-1546.

Turnlund J. R., Keyes W. R., and Peiffer G. L. (1993) Isotope ratios of molybdenum determined by thermal ionization mass spectrometry for stable isotope studies of molybdenum metabolism in humans. *Anal. Chem.* **65**, 1717-1722.

Vogel N. and Renne P.R. (2008) ^{40}Ar-^{39}Ar dating of plagioclase grain size separates from silicate inclusions in IAB iron meteorites and implications for the thermochronological evolution of the IAB parent body. *Geochim. Cosmochim. Acta* **72**, 1231-1255.

Volkening J., Köppe M., and Heumann K. G. (1991) Tungsten isotope ratio determinations by negative thermal ionization mass spectrometry. *Int. J. Mass Spectrom.* **107**, 361-368.

Walker R. J., Horan M. F., Morgan J. W., Becker H., Grossman J. N., and Rubin A. E. (2002) Comparative ^{187}Re-^{187}Os systematics of chondrites: Implications regarding early Solar System processes. *Geochim. Cosmochim. Acta* **66**, 4187-4201.

Walker R. J., McDonough W. F., Honesto J., Chabot N. L., McCoy T. J., Ash R. D., and Bellucci J.J. (2008) Modeling fractional crystallization of group IVB iron meteorites. *Geochim. Cosmochim. Acta* **72**, 2198-2216.

Walker R. J. (2012) Evidence for homogenous distribution of osmium in the protosolar nebula. *Earth Planet. Sc. Lett.* **351**, 36-44.

Wasson J. T. (1967) The chemical classification of iron meteorites: I. A study of iron meteorites with low concentrations of gallium and germanium. *Geochim. Cosmochim. Acta* **31**, 161-180.

Wasson J. T. (1969) The chemical classification of iron meteorites – III. Hexahedrites and other irons with germanium concentrations between 80 and 200 ppm. *Geochim. Cosmochim. Acta* **33**, 859-876.

Wasson J. T. (1970) The chemical classification of iron meteorites – IV. Irons with Ge concentrations greater than 190 ppm and other meteorites associated with group I. *Icarus* **12**, 407-423.

Wasson J. T. (1974) *Meteorites: Classification and Properties.* Springer-Verlag.

Wasson J. T. (1999) Trapped melt in IIIAB irons; solid/liquid elemental partitioning during the fractionation of the IIIAB magma. *Geochim. Cosmochim. Acta* **63**, 2875-2889.

Wasson J. T. (2011) Relationship between iron-meteorite composition and size: Compositional distribution of irons from North Africa. *Geochim. Cosmochim. Acta* **75**, 1757-1772.

Wasson J. T. and Kallemeyn G. W. (2002) The IAB iron-meteorite complex: A group, five subgroups, numerous grouplets, closely related, mainly formed by crystal segregation in rapidly cooling melts. *Geochim. Cosmochim. Acta* **66**, 2445-2473.

Wasson J. T. and Richardson J. W. (2001) Fractionation trends among IVA iron meteorites: Contrasts with IIIAB trends. *Geochim. Cosmochim. Acta* **65**, 951-970.

Wasson J. T. and Schaudy R. (1971) The chemical classification of iron meteorites – V. Groups IIIC and IIID and other irons with germanium concentrations between 1 and 25 ppm. *Icarus* **14**, 59-70.

Wasson J. T., Willis J., Wai C. M., and Kracher A. (1980) Origin of iron meteorite groups IAB and IIICD. *Z. Naturforsch.* **35**, 781-795.

Wasson J. T., Huber H., and Malvin D. J. (2007) Formation of IIAB iron meteorites. *Geochim. Cosmochim. Acta* **71**, 760-781.

Wieser M. E. and De Laeter J. R. (2000) Thermal ionization mass spectrometry of molybdenum isotopes. *Int. J. Mass Spec.* **197**, 253-261.

Wieser M. E. and De Laeter J. R. (2009) Molybdenum isotope mass fractionation in iron meteorites. *Int. J. Mass Spec.* **286**, 98-103.

Wieser M. E., De Laeter J. R., and Varner M. D. (2007) Isotope fractionation studies of molybdenum. *Int. J. Mass Spec.* **265**, 40-48.

Willbold M., Elliott T., and Moorbath S. (2011) The tungsten isotopic composition of the Earth's mantle before the terminal bombardment. *Nature* **477**, 195–198.

Willis J. (1981) Antimony in iron meteorites. *Earth Planet. Sc. Lett.* **53**, 1-10.

Willis J. and Goldstein J. I. (1982) The effects of C, P, and S on trace element partitioning during solidification in Fe-Ni alloys. *Proc. 13th Lunar and Planet. Sci. Conf., J. Geophys. Res.* **87**, A435-A445.

Wittig N., Humayun M., Brandon A. D., Huang S., and Leya I. (2013) Coupled W-Os-Pt isotope systematics in IVB iron meteorites: In situ neutron dosimetry for W isotope chronology. *Earth Planet. Sci. Lett.* **361**, 152-161.

Worsham E. A., Bermingham K. R., and Walker R. J. (2016a) Siderophile element systematics of IAB complex iron meteorites: New insights into the formation of an enigmatic group. *Geochim. Cosmochim. Acta* **188**, 261-283.

Worsham E. A., Walker R. J., and Bermingham K. R. (2016b) High-precision molybdenum isotope analysis by negative thermal ionization mass spectrometry. *Int. J. Mass Spectrom.* **407**, 51-61.

Yang C. W., Williams D. B., and Goldstein J. I. (1996) A revision of the Fe-Ni phase diagram at low temperature. *J. Phase Equilib.* **17**, 522–531.

Yang J., Goldstein J. I., and Scott E. R. D. (2007) Iron meteorite evidence for early formation and catastrophic disruption of protoplanets. *Nature* **446**, 888-891.

Yin Q. Z. (1995) N-TIMS technique for the Re-Os and Ru isotopic systems and its application to selected geochemical and cosmochemical problems. PhD thesis, University of Mainz and Max Planck Institute for Chemistry.

Yin, Q. Z., Jacobsen, S. B., and Yamashita, K., (2002) Diverse supernova sources of pre-solar material inferred from molybdenum isotopes in meteorites. *Nature* **415**, 881-883.

Yokoyama T. and Walker R. J. (2016) Nucleosynthetic isotope variations of siderophile and chalcophile elements in the solar system. *Rev. Mineral. Geochem.* **81**, 107-160.

Zhang J., Dauphas N., Davis A. M., Leya I., and Fedkin A. (2012) The proto-Earth as a significant source of lunar material. *Nat. Geosci.* **5**, 251-255.

.